

# **A Numerical Study on the Viscous Fingering Instability of Immiscible Displacement in Hele-Shaw Cells**

Samuel James Jackson MEng (Hons)

Thesis submitted to the University of Nottingham  
for the degree of Doctor of Philosophy

February 2017

*To my Granddad, who would have said "A good job, jobbed"*

# Abstract

In this thesis, the viscous fingering instability of radial immiscible displacement is analysed numerically using novel mesh-reduction and interface tracking techniques. Using a reduced Hele-Shaw model for the depth averaged lateral flow, viscous fingering instabilities are explored in flow regimes typical of subsurface carbon sequestration involving supercritical  $CO_2$  - brine displacements, i.e. with high capillary numbers, low mobility ratios and inhomogeneous permeability/temperature fields.

A high accuracy boundary element method (BEM) is implemented for the solution of homogeneous, finite mobility ratio immiscible displacements. Through efficient, explicit tracking of the sharp fluid-fluid interface, classical fingering processes such as spreading, shielding and splitting are analysed in the late stages of finger growth at low mobility ratios and high capillary numbers. Under these conditions, large differences are found compared with previous high or infinite mobility ratio models and critical events such as plume break-off and coalescence are analysed in much greater detail than has previously been attempted.

For the solution of inhomogeneous mobility problems, a novel meshless radial basis function-finite collocation method is developed that utilises a dynamic quadtree dataset and local enforcement of interface matching conditions. When coupled with the BEM, the numerical scheme allows the analysis of variable permeability effects and the transition in (de)stabilising mechanisms that occurs when the capillary number is increased with a fixed, spatially varying permeability. Finally, thermo-viscous fingering is explored in the context of immiscible flows, with a detailed mechanistic study presented to explain, for the first time, the immiscible thermo-viscous fingering process.

# Publications

## Journal Articles

- S.J. Jackson, D. Stevens, H. Power, and D. Giddings. A boundary element method for the solution of finite mobility ratio immiscible displacement in a Hele-Shaw cell. *International Journal for Numerical Methods in Fluids*, 78(9), 521 – 551, 2015.
- S.J. Jackson, D. Stevens, D. Giddings and H. Power. Dynamic-wetting effects in finite-mobility-ratio Hele-Shaw flow. *Physical Review E*, 92(2), 023021, 2015.
- S.J. Jackson, D. Stevens, D. Giddings and H. Power. An adaptive RBF finite collocation approach to track transport processes across moving fronts. *Computers & Mathematics with Applications*, 71(1), 278-300, 2016.
- S.J. Jackson, H. Power, D. Giddings and D. Stevens. The stability of immiscible viscous fingering in Hele-Shaw cells with spatially varying permeability. *Submitted to Computer Methods in Applied Mechanics and Engineering*.
- S.J. Jackson, H. Power and D. Giddings. Immiscible Thermo-Viscous fingering in Hele-Shaw Cells. *Invited for ICCFD9 special issue of Computers & Fluids*.

## Conference proceedings

- S.J. Jackson, D. Stevens, H. Power, and D. Giddings. A direct boundary element approach for the numerical simulation of finite mobility ratio immiscible displacement in a Hele-Shaw cell. *Boundary Elements and Other Mesh Reduction Methods XXXVII*, New Forest, UK, 279 - 288, 2014.
- S.J. Jackson, D. Stevens, D. Giddings and H. Power. The effect of thermocapillary motion during Hele-Shaw flow. *10th UK Conference on Boundary Integral Methods*, Brighton, UK, 46 - 58, 2015.

- H. Power, S.J. Jackson, D. Stevens, and D. Giddings. A high resolution RBF local meshless tracking approach for moving boundary transport problems, *ICOME and Trefftz/MFS*, Hangzhou, China, 2015.
- S.J. Jackson, H. Power and D. Giddings. Temperature dependent viscosity effects in immiscible Hele-Shaw flow, *IHTS & HPC 2016*, Nottingham, UK, IHTS-HPC 1254, 2016.
- S.J. Jackson, H. Power, and D. Giddings. Numerical modelling of Immiscible Hele-Shaw Flow with Inhomogeneous Viscosity, *ICCFD9*, Istanbul, Turkey, ICCFD9-2016-175, 2016.
- S.J. Jackson, H. Power, D. Giddings and N. Johnson. The effect of inhomogeneous mobility on immiscible Hele-Shaw flow, *ICTAM 2016*, Montreal, Canada, PO.FM06-1.17.101, 2016.

# Acknowledgements

Firstly, I would like to thank Professor Henry Power and Dr. Donald Giddings for their unwavering support and patience, and the countless hours spent discussing even the smallest of curiosities. I am very grateful to Dr. David Stevens for the many technical discussions and advice on all things numerical.

Thanks go to all the students and staff in the Thermo-Fluids group at the University of Nottingham who made my Ph.D. so enjoyable, especially those whom I have become close friends with in L4.

Finally, I would like to thank my family and friends who have supported me throughout. Special thanks go to Megan, for keeping me sane and for all of your love and support.

# Contents

<b>Abstract</b>	<b>ii</b>
<b>Publications</b>	<b>iii</b>
<b>Acknowledgements</b>	<b>v</b>
<b>Nomenclature</b>	<b>ix</b>
<b>1 Introduction</b>	<b>1</b>
1.1 Background and motivation . . . . .	1
1.2 Thesis aims and objectives . . . . .	6
1.3 Thesis Structure . . . . .	7
<b>2 Finite mobility ratio immiscible displacement in Hele-Shaw cells</b>	<b>9</b>
2.1 Introduction . . . . .	10
2.2 The flow in a Hele-Shaw cell . . . . .	15
2.2.1 Radial immiscible displacement . . . . .	18
2.3 Finite mobility ratio formulation . . . . .	21
2.4 Boundary element method . . . . .	24
2.4.1 Boundary integral formulation . . . . .	24
2.4.2 B-Spline representation . . . . .	28
2.4.3 Local curvature evaluation . . . . .	30
2.4.4 Hypersingular integral treatment . . . . .	31
2.4.5 Numerical performance . . . . .	35
2.4.6 Numerical stability and convergence analysis . . . . .	38
2.5 Mobility ratio effects . . . . .	43
2.6 Capillary number effects . . . . .	46
2.7 Long time scale evolution . . . . .	51
2.7.1 Coalescence and breaking . . . . .	56
2.8 Conclusion . . . . .	60
<b>3 Dynamic wetting effects</b>	<b>62</b>
3.1 Introduction . . . . .	62
3.2 Mathematical formulation . . . . .	66
3.3 Numerical results and discussion . . . . .	69
3.3.1 Local capillary number effects . . . . .	69
3.3.2 Global capillary number effects . . . . .	72
3.3.3 Late stage interfacial displacement . . . . .	74
3.4 Conclusion . . . . .	79

<b>4</b>	<b>A local RBF method for moving multi-zone transport problems</b>	<b>80</b>
4.1	Introduction . . . . .	81
4.1.1	Polynomial methods for multi-zone transport . . . . .	83
4.1.2	RBF methods for multi-zone transport . . . . .	86
4.2	The multi-zone RBF-FC method . . . . .	89
4.3	Adaptive quadtree datasets . . . . .	95
4.3.1	Quadtree grading criteria . . . . .	98
4.3.2	Quadtree dataset generation . . . . .	99
4.4	Stencil configuration . . . . .	102
4.5	Transient verification . . . . .	111
4.6	Multi-zone verification . . . . .	120
4.6.1	Steady-state fixed interface . . . . .	121
4.6.2	Transient fixed interface . . . . .	123
4.6.3	Transient moving interface . . . . .	127
4.7	Conclusion . . . . .	132
<b>5</b>	<b>Immiscible displacement with inhomogeneous mobility</b>	<b>134</b>
5.1	Introduction . . . . .	135
5.2	Mathematical model . . . . .	139
5.3	Numerical methods . . . . .	143
5.3.1	Homogeneous pressure solution . . . . .	145
5.3.2	Perturbed pressure solution . . . . .	147
5.3.3	Coupled solution algorithm . . . . .	149
5.4	Mass conservation verification . . . . .	150
5.5	Numerical results and discussion . . . . .	155
5.5.1	Uniformly converging/diverging Hele-Shaw cells . . . . .	156
5.5.1.1	Sharply converging/diverging geometry . . . . .	167
5.5.2	Highly anisotropic Hele-Shaw cells . . . . .	169
5.5.2.1	Radially periodic cells . . . . .	171
5.5.2.2	Cartesian periodic cells . . . . .	173
5.5.2.3	Channelled cells . . . . .	175
5.6	Conclusion . . . . .	178
<b>6</b>	<b>Immiscible thermo-viscous fingering</b>	<b>180</b>
6.1	Introduction . . . . .	181
6.2	Mathematical model . . . . .	185
6.3	Numerical methods . . . . .	190
6.3.1	Transient heat transfer solution . . . . .	191
6.3.2	Steady-state pressure solution . . . . .	193
6.3.3	Coupled solution algorithm . . . . .	195
6.4	Fluid properties . . . . .	197
6.5	Mass conservation verification . . . . .	198
6.5.1	Artificial diffusion and smoothing . . . . .	201
6.5.2	Shape parameter relaxation . . . . .	202
6.6	Thermo-viscous fingering results . . . . .	202
6.6.1	General system behaviour . . . . .	203
6.6.2	Thermal evolution & bifurcation modes . . . . .	207
6.6.3	Thermo-viscous fingering with a continuous viscosity profile . . . . .	212
6.6.4	Thermal diffusivity effects . . . . .	215
6.7	Conclusion . . . . .	220

<b>7</b>	<b>Conclusions &amp; future work</b>	<b>222</b>
7.1	Conclusions . . . . .	222
7.2	Future work . . . . .	227
7.2.1	Parallelisation . . . . .	227
7.2.2	Interface capturing . . . . .	229
7.2.3	Marangoni & other temperature effects . . . . .	230

# Nomenclature

Here, common variables used throughout the thesis are presented. Other variables may appear, but will be locally defined.

## Acronyms

BEM	Boundary Element Method
$CO_2$	Carbon dioxide
DC	Diffusivity Case
FD	Finite Difference
LHS/RHS	Left Hand Side/Right Hand Side
LSA	Linear Stability Analysis
LU	Lower Upper
MQL	Maximum Quadtree Level
PDE	Partial Differential Equation
RBF-FC	Radial Basis Function - Finite Collocation
NaCl	Sodium Chloride

## Greek

$\phi^*$	2D fundamental solution of Laplace's equation
$\theta$	Azimuthal angle
$\alpha$	Converging/diverging cell gradient
$\rho$	Density
$\psi$	Double layer potential density
$\sigma_a$	Growth rate - analytical linear
$\sigma_i/\sigma_t$	Growth rate - numerical linear/numerical non-linear
$\eta$	Hypersingular point
$\epsilon_0$	Initial perturbation amplitude

---

$\Omega_1/\Omega_2$	Inner/outer zone
$\xi$	Interface coordinate
$\epsilon$	Interface perturbation
$\Delta x$	Mesh or nodal separation
$\beta$	Mobility ratio
$\Delta L_n$	Normal distance moved in a single time step
$\delta$	Ratio between small and large length scales
$\phi$	RBF field variable solution
$\Psi$	RBF Hardy multiquadric interpolant
$\tau$	RBF weighting function
$\lambda$	Reduced mobility ratio
$\hat{\phi}$	Surface potential pressure
$\gamma$	Surface tension
$\Delta t$	Time step size
$\mu$	Viscosity
<b>Latin lowercase</b>	
$x, y, z$	Cartesian coordinates
$k$	Curvature
$g_l$	Dirichlet boundary operator value
$f$	Interface flux matching value
$h$	Interface solution matching value
$k$	Intrinsic permeability
$f_s$	Modified capillary pressure jump
$g$	Non-homogeneous boundary term
$n$	Normal direction
$b$	Plate separation
$r, R$	Radial distance
$d_s$	RBF local data vector
$c, c^*$	RBF Shape parameter
$q$	Surface potential flux
$t$	Time

---

$r_0$	Unperturbed interface radius
$u, U$	Velocity
$k_{as}$	Zero flux condition constant
$l$	Zone
<b>Latin uppercase</b>	
$W(\theta)$	Bifurcation parameter
$B$	Boundary operator
$L_c$	Critical length scale of bifurcation
$D$	Diffusivity
$W$	Double layer potential
$Ca_g/Ca_l$	Global/Local capillary number
$F, F_{-1}, F_{-2}$	Hypersingular function
$\hat{S}$	Inhomogeneous Crank-Nicholson right hand side
$V$	Integral function
$Q_1, Q_2$	Interface flux matching operator
$C_1, C_2$	Interface solution matching operator
$S$	Interface surface
$J$	Jacobian
$L_0, L_1, L_2, L_{inf}$	L error norms
$L$	Length
$M/m$	Mobility/modified mobility
$U_n$	Normal interfacial velocity
$N$	Number (boundary elements, series terms etc.)
$L, \hat{L}, \bar{L}$	PDE operators
$Pe$	Peclet number
$B_t$	Quadtree band thickness
$Diag$	Quadtree cell diagonal length
$Q$	Radial injection source flux
$A_s$	RBF local collocation matrix
$H$	RBF Reconstruction vector
$K$	Regular kernel

---

$S_w$	Saturation index
$N^a$	Shape function
$T$	Temperature
$V_a$	Total volume of fluid
$P, \bar{p}, \tilde{p}$	Total, homogeneous and perturbed pressure
$J_0$	Wetting layer constant

# 1. Introduction

## 1.1 Background and motivation

Interfacial instabilities may arise and subsequently evolve at the interface between displacing fluids due to the growth of perturbations, forming complex interface topologies. These perturbations will grow and compete with one another in a non-linear fashion, altering the overall fluid flow and resulting displacement characteristics. A common interfacial instability, induced by a disparity in the fluids' viscosity is the viscous fingering instability. During the displacement of a high viscosity fluid by a low viscosity fluid, perturbations greater than a certain wavelength create instabilities along the fluid interface and promote the growth of long fingers which penetrate into the more viscous fluid [1] (see Figure 1.1).

The viscous fingering process is an important feature in many practical applications, particularly those involving the flow through porous media, such as enhanced oil recovery [2], geothermal heat extraction [3] and carbon sequestration [4]. In these flows, the 'solutal' front marks the compositional transition from the injected fluid to the resident fluid and can occur in a smooth or sharp fashion. In immiscible displacements the transition is sharp and controlled by capillary forces, where the fluid properties exhibit discontinuous profiles, whilst in miscible displacements the front is smoothed as dispersion and molecular diffusion mix the fluid properties of the injected and resident fluid [5].

During immiscible displacement in porous media, the flow regime depends greatly on the capillary number at the interface between the fluids, describing the ratio of viscous driving forces to capillary forces [6]. The capillary number  $Ca$  is defined as  $\mu U/\gamma$ , where  $\mu$  is the dynamic viscosity of the displaced fluid,  $U$  is the interfacial velocity and  $\gamma$  is the surface tension. At capillary numbers above roughly  $1 \times 10^{-4}$  with an unfavourable

viscosity contrast, viscous fingering can occur, where long fingers extend into the porous domain [7]. At capillary numbers lower than  $1 \times 10^{-4}$ , capillary fingering can occur, where the plume advances in a ‘random walk’ fashion, and disconnected globules of the displaced fluid can remain trapped in the pores of the porous media.

By assuming that the fluid properties vary sharply over the fluid-fluid interface, the displacement in the porous media can be considered completely immiscible. One such flow, and the motivation behind the current work is the injection and storage of supercritical carbon dioxide ( $CO_2$ ) in deep subsurface aquifers, known as  $CO_2$  sequestration. In this process,  $CO_2$  is captured from industrial processes and stored in a variety of natural geological structures in supercritical form, in an attempt to reduce greenhouse gas emissions and rising global temperatures. Suitable geological structures include depleted oil/gas reservoirs and deep saline aquifers containing brine and mineral deposits, with storage capacity and safety being of primary importance when assessing the suitability of an injection site [8]. To have any impact on atmospheric concentration levels, the  $CO_2$  must be stored at least until the end of the fossil fuel era, meaning an expected storage life of around 100-1000 years [9].

For the site to be suitable for geological storage, the presence of a large enough formation with high permeability at suitable depth is required. To avoid the loss of injected  $CO_2$ , the target formation needs to be overlain by a layer of very low permeability (cap rock), thus creating both a permeability barrier and a capillary barrier to the upwards migrating  $CO_2$ . As the rising  $CO_2$  plume reaches the cap rock a layer of the injected  $CO_2$  spreads under the cap rock at some distance from the injection well, of almost constant thickness.

The lateral spreading and structural trapping of  $CO_2$  represents a large proportion of the  $CO_2$  injection and storage life, with complex interfacial interaction occurring between the  $CO_2$ , brine and porous media. As the  $CO_2$  spreads through a deep saline geological formation, it will replace the indigenous fluid (brine), thus creating a two-phase flow system. At the depth of the target formation considered as appropriate for injection, the injected  $CO_2$  is in a supercritical condition with a temperature of the order of  $35^\circ C$ , pressure ranging from 10 to 20 MPa and having a density between 0.4 to 0.8 times that of the surrounding brine. The mobility ratio (inverse of the viscosity ratio) between the  $CO_2$  and brine is typically of the order 10-30 [10]. Under these conditions in a deep

subsurface aquifer, the  $CO_2$  - Brine displacement is immiscible [11]. There is inherent instability at the interface in the  $CO_2$  spreading, due to the difference in fluid properties, which can give rise to the viscous fingering phenomenon.

The injection of supercritical  $CO_2$  will typically occur at a temperature different to that of the resident brine, creating temperature gradients in the domain that will alter mechanical fluid quantities such as diffusivity, viscosity, density and surface tension. The  $CO_2$  can be injected at a colder temperature than the resident brine, due to heat loss en-route to the downhole injection site [12], or through very deep subsurface injection where the resident brine temperature is very high (typically at depths  $> 3\text{km}$ ), e.g. the In Salah formation in Algeria [13].  $CO_2$  can also be used for combined storage and extraction in geothermal reservoirs, in which very high temperature brine ( $T > 150^\circ\text{C}$ ) can be extracted for energy use [14]. The  $CO_2$  may also be injected at a higher temperature than the resident brine, for pre-conditioning purposes [15] or for plume evolution monitoring [16]. These temperature gradients can create a process known as thermo-viscous fingering, whereby the thermal dependence of viscosity affects the underlying mechanisms of the fingering process.

The structural properties of the aquifer can also dramatically affect the  $CO_2$  plume evolution and viscous fingering process. A typical subsurface aquifer will have an inhomogeneous permeability that varies in space as a consequence of the way it has been formed and re-shaped over many millions of years, altering the natural stress state of the aquifer [17]. Abrupt changes in aquifer permeability can exist due to fault lines and changes in the aquifer material [17]. As well as pre-existing variations in permeability, the  $CO_2$  injection process itself can alter the permeability of the aquifer. During  $CO_2$  injection, formation dry-out and precipitation of minerals (such as salt from pre-existing brine) near the injection well can reduce the porosity and permeability of the aquifer [18]. The formation of carbonic acids in the brine due to reactions with the injected  $CO_2$  can dissolve the calcite in sandstone aquifers, increasing the permeability [19]. Injection pressures over the formation pressure of the aquifer can also induce fracturing and fault slip, which can increase the permeability in a region surrounding the injection well [20]. Understanding the effect of these permeability variations on the flow regime and interfacial evolution of injected  $CO_2$  is critical in understanding the long term storage capabilities of supercritical  $CO_2$ .

Due to the uncertainty associated with deep geological injection, numerical models are often used to predict the movement of  $CO_2$ , to back-up experimental observations and assess the life-cycle of the  $CO_2$  [4]. Since the structural trapping regime accounts for the majority of the storage capacity in a subsurface aquifer, the viscous fingering process that can occur during the lateral spreading of the  $CO_2$  under the cap rock must be fully understood in order to predict the life cycle of the  $CO_2$ . In recent years there have been significant breakthroughs in understanding the viscous fingering process, however, there still exist many unknown factors associated with the fingering process, especially under the conditions found in  $CO_2$  sequestration.

Due to the practical difficulties associated with monitoring the viscous fingering process in detail in a subsurface aquifer, there has been extensive research on viscous fingering occurring in Hele-Shaw cells, where the fluid flows between two thinly separated plates [21]. The mobility of a fluid within a Hele-Shaw cell is defined by the cell separation and the viscosity, giving rise to an intrinsic permeability, analogous to that in porous media flows. The study of viscous fingering in Hele-Shaw cells is often used to provide insight into the more complex problem in porous media, allowing reduced models to shed light on the mechanisms controlling the viscous fingering regime [1]. As well as analytical and numerical models of the flow, detailed experimentation is possible under laboratory conditions using a relatively simple Hele-Shaw cell setup [22].

There is substantial experimental evidence previously reported in the literature, where it is shown that the core immiscible viscous fingering processes of shielding, spreading, and splitting are present during displacements in both Hele-Shaw cells and porous media, determining the pattern of the fluids' interface (see for example [1, 22, 23]). Chouke et al. observed the formation of fingering patterns in immiscible displacement in porous media, which show variation of the length scales with increasing velocity and viscosity contrast, i.e. with increasing capillary number [24]. Fingering takes place on many scales, including a macroscopic one, suggesting the existence of a characteristic macroscopic length scale or wavelength.

The analysis of the immiscible viscous fingering process in a Hele-Shaw cell although not directly analogous to the two-phase flow in porous media ([1]) can be used to provide insight into the basic fingering mechanisms that could occur during the flow in porous media. The immiscible Hele-Shaw system is a member of Stefan-type moving boundary

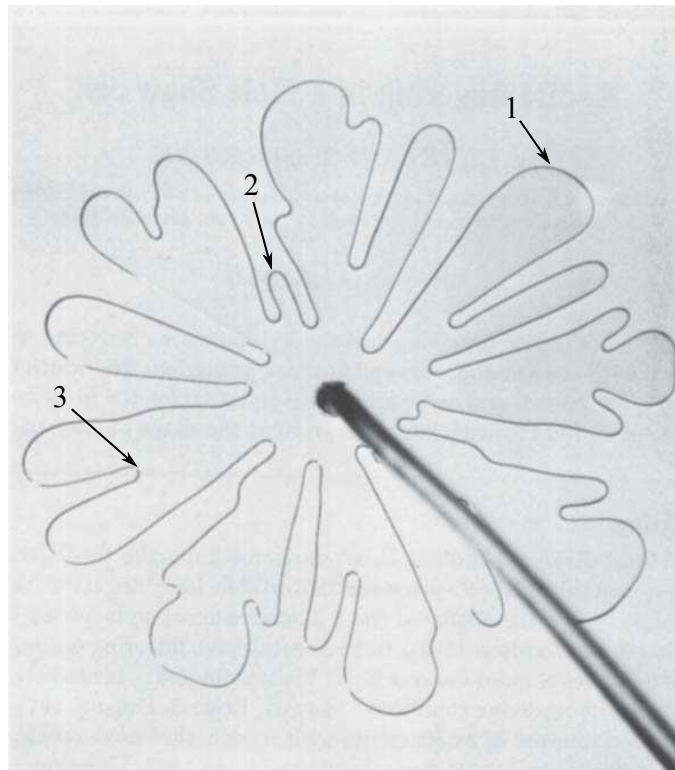


Figure 1.1: Viscous fingering occurring during the radial injection of air into a Hele-Shaw cell filled with glycerine. Numbers correspond to the three basic fingering mechanisms: 1 - Spreading; 2 - Shielding; 3 - Splitting. Figure reproduced from [22].

problems (at the quasi-static limit), which occur in many other natural processes (such as dendritic solidification [25]), making the study of the fingering process in Hele-Shaw cells of fundamental interest in its own right [23].

The three main mechanisms governing the immiscible viscous fingering process are shown in Figure 1.1, namely: spreading, shielding and splitting. As a finger grows due to the injection of an inner, less viscous (more mobile) fluid, the front of the advancing finger is spread continuously, creating a fan like structure with an increasingly flat front. The early stages of finger growth occur in a linear regime, where perturbations greater than the critical wavelength form into separate fingers. The fastest growing fingers have a wavelength proportional to the square root of the capillary number of the flow [22, 26, 27]. Linear stability analysis gives good correspondence with both radial and channel flows, during the early stages of finger growth. However, when the coupling of the different modes of perturbation becomes significant, the regime becomes weakly non-linear and processes such as shielding and splitting occur [28]. By including second order terms in the Fourier decomposition of the modes of perturbation, [28] shows that

harmonic and sub-harmonic perturbation modes are responsible for tip splitting and finger competition respectively.

Past the weakly non-linear stage, during the later stages of finger evolution, finger growth is only fully described by the full coupling of modes in the Fourier decomposition of the perturbation. When flat sections at the front of the advancing finger become larger than the critical length scale of bifurcation, tip-splitting occurs, whereby the tip will bifurcate into smaller fingers creating a more convoluted surface. These fingers will grow and compete with each other, with larger fingers shielding the growth of smaller fingers in a non-linear regime controlled by interfacial dynamics. The non-linear finger evolution is key to predicting the late stage interfacial behaviour and controls the extent to which the injected plume displaces in the domain. Since current stability analyses are valid only in the linear or weakly non-linear stages of finger growth, it is necessary to use numerical methods to fully explore the non-linear regime and describe the resulting finger growth and interaction.

This thesis aims to explore the non-linear stages of the viscous fingering instability in immiscible flows, furthering understanding of the underlying mechanisms and shedding light on the various processes that can occur during the  $CO_2$  - brine displacement process. By studying the problem in Hele-Shaw cells using advanced numerical methods, the mechanisms for the instability in the non-linear stages of finger growth can be explicitly studied and the different thermal and structural effects explored in detail. The thesis does not aim to model the full, complex 3D evolution of the  $CO_2$  plume in porous media, instead exploring certain aspects of the displacement regime and viscous instability to better understand the underlying mechanisms that control the immiscible viscous fingering process.

## 1.2 Thesis aims and objectives

The study of immiscible viscous fingering in this thesis is motivated by the interfacial processes and conditions that are found during the injection and storage of supercritical  $CO_2$  in brine filled subsurface aquifers. The type of viscous fingering that occurs in these injection scenarios has not been explored in detail and there is a lack of knowledge regarding the key mechanisms that control the flow in these regimes. In order to study

the viscous fingering phenomena at these conditions, a Hele-Shaw approach will be used to reduce the complexity of the full porous media problem and focus on the key mechanisms that govern the immiscible viscous fingering process.

The main objective of this work is to develop a suitable model and numerical methods to track two-phase interfacial flows in a Hele-Shaw cell at finite mobility ratios and capillary numbers typical of  $CO_2$  injection and storage. This will allow the exploration of mobility ratio, capillary number and dynamic wetting layer effects on the late stage non-linear viscous finger growth, specifically under the conditions found in subsurface aquifers during  $CO_2$  injection.

This study also aims to provide insight into the thermal and structural effects that are likely to occur during the injection and storage of  $CO_2$  in subsurface aquifers, using the Hele-Shaw model. Through development of novel numerical methods, the effects of inhomogeneous permeability and temperature dependent viscosity should be quantified and their relative importance in the immiscible viscous fingering regime assessed.

Although this study concerns the viscous fingering problem in Hele-Shaw cells, the numerical methods are developed with general applicability to moving multi-zone transport problems in fluid mechanics. All numerical methods in this study are programmed by the author using the FORTRAN language for both regular desktop PC architectures and high performance computing clusters.

### 1.3 Thesis Structure

In each chapter, a summary is first given, followed by a detailed literature review pertaining specifically to the content of the chapter. At the end of each chapter a brief conclusion is also presented. References for each chapter are included in a single bibliography at the end of the thesis.

In chapter 2 finite mobility ratio immiscible displacement in Hele-Shaw cells is explored. A novel boundary element method is implemented which utilises a hypersingular integral subtraction technique, in order that high order cubic B-Spline boundary elements can be employed. The effects of finite mobility ratio and high capillary number on the viscous fingering regime are explored at the early and late stages of finger growth. The chapter

concludes with long time scale simulation results of viscous fingering using realistic  $CO_2$  injection conditions and asymmetric initial conditions.

Chapter 3 introduces a Picard iteration scheme to evaluate the non-linear capillary pressure associated with dynamic wetting layers in Hele-Shaw cells. This allows the analysis of wetting layer effects, and their contribution to the late stage tip-splitting instability of viscous fingering.

For the solution of moving boundary transport problems with a multi-zone interface (for use in chapter 5 & 6), an adaptive radial basis function-finite collocation (RBF-FC) numerical method is developed in chapter 4. The method is validated on several transport problems, including steady-state and transient convection-diffusion problems both with single and multi-zone representations.

The embedded multi-zone RBF-FC method is used in chapter 5 in conjunction with the BEM from chapter 2 to solve immiscible displacement in Hele-Shaw cells with inhomogeneous mobility. Specifically, the case of inhomogeneity arising from a variable plate separation (cell permeability) is explored, with detailed analysis on the effects of variable cell permeability on the viscous fingering evolution.

In chapter 6, the adaptive multi-zone RBF-FC method is used with the BEM to solve the problem of transient heat transfer between immiscible fluids at different temperatures in a Hele-Shaw cell. The transient heat transfer is solved using the auxiliary multi-zone method presented in chapter 4 in order to evaluate the temperature dependent viscosity. This model and the numerical methods allow thermo-viscous fingering to be explored for the first time in the context of immiscible flows, at the conditions apparent in  $CO_2$  injection.

Finally, in chapter 7 the thesis is concluded, and recommendations for future work are given.

## 2. Finite mobility ratio immiscible displacement in Hele-Shaw cells

### Summary

In this chapter, the interaction between two immiscible fluids with a finite mobility ratio is investigated numerically within a Hele-Shaw cell. Fingering instabilities initiated at the interface between a low viscosity fluid and a high viscosity fluid are analysed at varying capillary numbers and mobility ratios using a finite mobility ratio model.

Firstly, the governing lubrication model and the specific radial injection Hele-Shaw case are formulated for use throughout the thesis. A boundary element numerical scheme is then presented for the finite mobility ratio case, based on the work of [29]. The original work is extended to allow the solution of finite mobility ratio flows through the direct evaluation of a hypersingular integral. The boundary integral equation is solved using a Neumann convergent series with cubic B-Spline boundary discretisation, exhibiting 6<sup>th</sup> order spatial convergence. The convergent series allows the long term non-linear dynamics of growing viscous fingers to be explored accurately and efficiently.

Simulations are presented in low mobility ratio regimes, revealing large differences in fingering patterns compared to those predicted by previous high (and infinite) mobility ratio models. Most significantly, classical finger shielding between competing fingers is inhibited. Secondary fingers can possess significant velocity, allowing greater interaction with primary fingers compared to high mobility ratio flows. Eventually, this interaction can lead to base thinning and the breaking of fingers into separate bubbles.

## 2.1 Introduction

Viscous fingering occurs during the displacement of a high viscosity fluid by a low viscosity fluid, in which instabilities may evolve to form complex interface topologies. Perturbations greater than a certain wavelength create instabilities along the fluid interface and promote the growth of long fingers which penetrate into the more viscous fluid. The fingering regime under consideration in this work stems from the immiscible displacement of  $CO_2$  and brine in a deep subsurface aquifer, in which the mobility ratio between the fluids is low and the characteristic capillary number is high, creating highly ramified structures.

Since the work of Saffman and Taylor in 1958 [21], there has been extensive research on viscous fingering occurring in Hele-Shaw cells, where the fluid flows between two thinly separated plates. The mobility of a fluid within a Hele-Shaw cell is defined by the cell plate separation and the viscosity, giving rise to an intrinsic permeability, analogous to that in porous media flows.

The case of immiscible displacement is characterised by a sharp interface, across which the properties of the fluids (such as viscosity and density) vary discontinuously [1]. The first attempt to provide a theoretical analysis of the onset of immiscible viscous fingering in porous media was by Chouke et al. in 1959 [24]. They assumed that there was complete displacement of one fluid by the other, using the similarity between Hele-Shaw and porous media flows and ignoring the zone of partial saturation or volume concentration of the displacing fluid behind the front. In the case of two dimensional immiscible displacement in a porous medium, the finger characteristic width scale predicted by a Hele-Shaw approximation under predicts the experimental observations. This has led to the hypothesis of an effective surface tension, larger than the molecular surface tension and function of the wetting conditions, that varies with the large-scale curvature at the macro-scale (see [30]). The use of a modified jump condition in terms of the effective surface tension is known as Chouke's boundary condition and the resulting interface instability analysis is referred to Hele-Shaw-Chouke theory (for more details see the review article [1]).

An alternative approach to study the viscous fingering instability of the displacement of immiscible fluids in a porous media can be obtained from the classical porous

media formulation of multiphase flows in terms of the saturation index,  $S_w$ , where an overlapping region between the fluids is considered for  $0 \leq S_w \leq 1$ , without definition of the fluid interface. This type of formulation is now one of the most popular approaches used in the numerical solution of immiscible displacement in porous media (see [10] and [31]).

In the multiphase flow approach, the variation in saturation in the overlapping region results in a gradual change of the mobility of both phases. This type of analysis is closely related to the stability of graded mobility processes, see [32] and [33], where depending upon the mobility function a displacement that has an unfavourable viscosity ratio may still be linearly stable, even at infinite capillary number.

Both types of models for immiscible displacement in porous media, i.e. the saturation index (multiphase flow) and sharp front (Hele-Shaw-Chouke), are consistent with the main hypothesis of Darcy flow, i.e. seepage average flow. In the saturation index approach, the flow field of both fluids in the region near the front is averaged in a representative elementary volume (REV) resulting in a type of fluid mixture characterised by the saturation index,  $S_w$ . On the other hand, in the sharp front approach, the irregular and complex interface at the porous media is averaged in a representative smooth surface.

In this thesis, a 2D Darcy model is used to analyse the simplified problem of viscous fingering in a Hele-Shaw cell, using a sharp front approach. By considering that the flow between the plates in the Hele-Shaw cell follows a Poiseuille profile, the Stokes equations can be reduced to a Darcy equation by depth-averaging across the gap. The immiscible displacement of the fluids is then described by 2D potential flow in the plane of the Hele-Shaw cell.

The sharp front Hele-Shaw approach is used in preference to the saturation index approach in order to better characterise the basic fingering mechanisms that occur at the immiscible interface between two fluids. Since the saturation approach uses a smooth approximation for the interface location, some details of the fingering process may be lost at the smaller lengthscales. The approach used in this work does not intend to analyse the full complexity of the 3D porous media flow, instead providing insight into the basic mechanisms for the viscous fingering instability between two immiscible fluids, which

is inherent in many physical situations - beyond those found solely in porous media. The Hele-Shaw approximation allows the fundamental characteristics of the fingering regime to be explored in greater detail than is possible with a large scale simulation of the analogous flow in a porous medium. The full porous media problem requires the solution of a different set of partial differential equations (PDEs) that are beyond the scope and intent of this work.

During immiscible displacement, the advancing front is defined by kinematic and dynamic matching conditions at the interface of the two fluids. The surface tension and curvature cause a jump in the pressure which along with continuity of normal velocities at the interface must be matched by the solutions in both fluid domains. Detailed and robust analyses of immiscible displacement in Hele-Shaw cells have been the subject of many publications in the literature including the review article “Surprises in viscous fingering” by Tanveer [26].

Most previous work in the literature has focussed on flow regimes where the mobility ratio of the fluids is typically very large, such as gas-oil displacement occurring in enhanced oil recovery. Therefore, most numerical approaches consider only the external fluid, with an injected fluid of negligible viscosity, resulting in an infinite mobility ratio model [34–36]. Immiscible displacement with finite mobility ratio (occurring in  $CO_2$  injection) has not been as extensively explored, mainly due to difficulties associated with matching the conditions for both internal and external flows at the interface.

Boundary element methods (BEMs) are one of the most popular techniques for solving immiscible displacement in a Hele-Shaw cell, whereby the dimensionality of the problem is reduced by one and accurate representation of the surface is provided, explicitly tracking it through time. Although only the surface of the problem has to be discretised, a fully populated collocation matrix is generated due to the integral equations being used. This can lead to very slow solution times and poor scaling. Li [36] uses scaling techniques to rescale time and space so that the interface can evolve significantly faster without changing the interface, allowing much longer simulated times to be run.

In addition to BEMs for use in the limit of infinite mobility ratio, BEMs have also been applied for finite mobility ratio flows, where the viscosity of both fluids is considered, resulting in a finite mobility ratio. These methods typically solve immiscible

displacement between fluids with high mobility ratio, effectively reducing the model to that of an infinite mobility ratio [35, 37, 38]. Utilising a direct boundary integral approach, [37] and [38] are able to solve directly for the surface velocity to create a finite mobility ratio model applicable in both fluid domains. [37] evaluates a set of integral equation systems expressing the internal and external fluid domains in terms of their corresponding integral equation formulations with an auxiliary external boundary enclosing the outer fluid domain. Using an auxiliary external boundary introduces additional error into the solution, which can be reduced by moving the boundary far into the external domain at the expense of increased computational cost.

The auxiliary external boundary can be evaluated analytically in the limit that the boundary tends to infinity. When the external boundary is evaluated asymptotically at infinity, it gives rise to the solvability condition for the unique solution of the infinite mobility ratio problem [39]. An alternative approach to deal with the external boundary is presented in [38], in which the integral equation is transformed using a Green's function and periodic boundary conditions, meaning the evaluation of an auxiliary external boundary ( $S_\infty$ ) can be avoided. This comes at the expense of introducing a periodic solution in the domain and the need to solve a Cauchy weakly singular integral.

Some authors propose the use of an indirect boundary integral approach, whereby a fictitious density variable is computed before the velocity is reconstructed at the interface between the two fluids [36, 40]. By utilising an indirect approach solely in terms of double layer potentials, the need to evaluate an auxiliary external boundary is avoided due to the double layer potential asymptotic condition at infinity.

To ease the computational cost imposed by the front tracking methods above, alternative approaches can be used whereby the interface is captured implicitly, such as the volume of fluid method [41], the diffuse interface method [42] and the level set method [43]. In these works, long term dynamics can be efficiently modelled as fully populated matrices are not encountered. However, as the interface is not explicitly tracked, events that occur at a length scale smaller than the volume size or transition region cannot be accurately captured.

Experimental results from [44], along with numerical results from [42] and [41] suggest that the basic fingering mechanisms such as shielding, spreading and tip-splitting that

occur in low mobility ratio flows are vastly different to those in infinite (or very high) mobility ratio flows. Due to the small fingers in the domain (typically those that have branched from the side of a primary finger) possessing significant velocity compared to those in infinite mobility ratio models, finger interaction becomes much more prominent and the resulting competition can lead to coalescence and breaking [41].

To study the interaction processes and the long term evolution of low mobility ratio flows characteristic of  $CO_2$  sequestration, a non-dimensional finite mobility ratio model is formulated based on a direct boundary element approach first presented in [29]. The finite mobility ratio formulation proposed by Power and Wrobel [29] has not been previously implemented in the literature with high order boundary elements. Previous work has focused on indirect methods with constant boundary elements, or infinite mobility ratio approaches [29, 40]. In the proposed method, the hypersingular integral arising from the single integral equation is evaluated explicitly, resulting in a second kind Fredholm equation, which can be solved through the use of an analytical Neumann series. Numerically, the Neumann series is truncated using a finite number of terms, giving rise to a convergent series solution with good agreement to the analytical Neumann series.

The need to evaluate an auxiliary external boundary is present in all direct formulations. However, in the proposed method, by evaluating the auxiliary external boundary asymptotically at infinity, the resulting integral equation avoids direct surface integration of the auxiliary external boundary, whilst maintaining solvability of the internal and external domains. Using explicit interface tracking, the velocity of the interface can be accurately computed allowing high capillary number flows to be explored. The computational cost of the convergent series scales with the square of the number of boundary elements (quadratic scaling), meaning the long term effects of finger interaction can be examined more efficiently than previous direct numerical approaches that exhibit cubic scaling [37]. The resulting numerical method allows the effective modelling of a moving interface in a Hele-Shaw cell, using a physically realistic mobility ratio.

In this chapter, the mathematical model for Hele-Shaw flow is first presented, followed by the model for radial immiscible displacement and the boundary element method. Numerical performance and validation studies of the numerical scheme are then performed. After validation of the numerical method, results for varying mobility ratio

and capillary number are shown, concluding in simulations focusing on longer term interface evolution to showcase the new finite mobility ratio approach.

## 2.2 The flow in a Hele-Shaw cell

In this section, the lubrication equations for the flow in a Hele-Shaw cell will be derived. Throughout this thesis, the indices  $i, j, k$  are used for spatial coordinates and are summed in the usual Einstein notation convention, the index  $l$  is used to indicate the fluid zone.

A schematic representation of a typical Hele-Shaw cell is shown in Figure 2.1, where the fluid-fluid interface is shown by the blue line. The three dimensional flow in each fluid region in the Hele-Shaw cell is governed by the incompressible Navier-Stokes equation for the conservation of momentum and the equation governing conservation of mass, in Cartesian coordinates given as:

$$\rho \left( \frac{\partial u_i}{\partial t} + u_j \frac{\partial u_i}{\partial x_j} \right) = - \frac{\partial P}{\partial x_i} + \mu \frac{\partial^2 u_i}{\partial x_j \partial x_j} \quad (2.1)$$

$$\frac{\partial u_i}{\partial x_i} = 0 \quad (2.2)$$

Where,  $P$  is the pressure,  $u$  is the fluid velocity,  $\rho$  is the density and  $\mu$  is the viscosity. Gravitational body accelerations have been neglected due to the very small variation in the vertical direction. To derive the lubrications equations, the following non-dimensional scalings are used:

$$\begin{aligned} x_1 &= Lx'_1, & x_2 &= Lx'_2, & x_3 &= \delta Lx'_3 \\ u_1 &= Uu'_1, & u_2 &= Uu'_2, & u_3 &= \delta Uu'_3 \\ b &= \delta Lb', & P &= \frac{\mu U}{\delta^2 L} P', & t &= \frac{L}{U} t' \end{aligned} \quad (2.3)$$

Here,  $L$  and  $U$  are the long wave length and velocity scales respectively, which are chosen based on the problem being solved. For example, in the rectilinear Hele-Shaw cell (akin to that shown in Figure 2.1), the length and velocity scale could be  $L = W$ ,  $U = U_n$  where  $W$  is the cell width, and  $U_n$  is the normal front velocity. However in radial injection problems, they may be chosen as  $L = R$ ,  $U = Q/R$  where  $R$  is the interfacial radius and  $Q$  is the injection flux. For this derivation however, it is adequate to consider

them purely as long wave scales in the problem domain. At the smaller scale,  $b$  is the plate separation with the ratio  $\delta = b/L$  defining the relative magnitude of the small and large length scale variations in the domain.  $t$  is the time, and  $P$  is the pressure. The pressure length scale is chosen to balance viscous and pressure terms that will become apparent later in the derivation. Substituting the non-dimensional variables

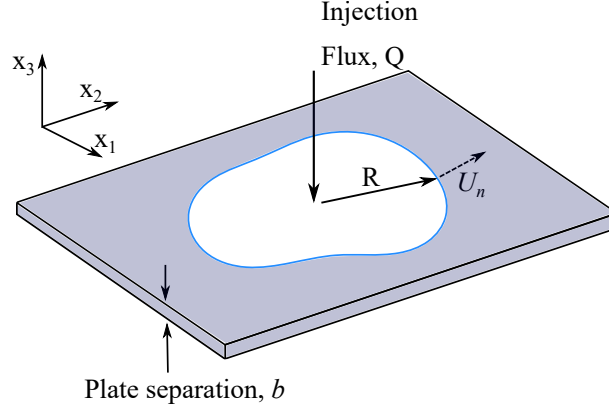


Figure 2.1: Sketch of a typical Hele-Shaw cell and injected fluid, the blue line represents the fluid-fluid interface.

into the original equations (2.1) and (2.2), after rearranging the following equations can be formed:

$$\delta Re \left( \frac{\partial u'_1}{\partial t'} + u'_1 \frac{\partial u'_1}{\partial x'_1} + u'_2 \frac{\partial u'_1}{\partial x'_2} + u'_3 \frac{\partial u'_1}{\partial x'_3} \right) = -\frac{\partial P'}{\partial x'_1} + \delta^2 \frac{\partial^2 u'_1}{\partial x'^2_1} + \delta^2 \frac{\partial^2 u'_1}{\partial x'^2_2} + \frac{\partial^2 u'_1}{\partial x'^2_3} \quad (2.4)$$

$$\delta Re \left( \frac{\partial u'_2}{\partial t'} + u'_1 \frac{\partial u'_2}{\partial x'_1} + u'_2 \frac{\partial u'_2}{\partial x'_2} + u'_3 \frac{\partial u'_2}{\partial x'_3} \right) = -\frac{\partial P'}{\partial x'_2} + \delta^2 \frac{\partial^2 u'_2}{\partial x'^2_1} + \delta^2 \frac{\partial^2 u'_2}{\partial x'^2_2} + \frac{\partial^2 u'_2}{\partial x'^2_3} \quad (2.5)$$

$$\delta^3 Re \left( \frac{\partial u'_3}{\partial t'} + u'_1 \frac{\partial u'_3}{\partial x'_1} + u'_2 \frac{\partial u'_3}{\partial x'_2} + u'_3 \frac{\partial u'_3}{\partial x'_3} \right) = -\frac{\partial P'}{\partial x'_3} + \delta^4 \frac{\partial^2 u'_3}{\partial x'^2_1} + \delta^4 \frac{\partial^2 u'_3}{\partial x'^2_2} + \delta^2 \frac{\partial^2 u'_3}{\partial x'^2_3} \quad (2.6)$$

$$0 = \frac{\partial u'_1}{\partial x'_1} + \frac{\partial u'_2}{\partial x'_2} + \frac{\partial u'_3}{\partial x'_3} \quad (2.7)$$

Where,  $Re = \rho Ub/\mu$  is the Reynolds number that quantifies the relative importance of inertial and viscous forces in the flow using the plate separation as the characteristic length. The lubrication approximation assumes that the reduced Reynolds number  $Re' = \delta Re$  and  $\delta$  are both small, i.e.,  $Re' \ll 1$ ,  $\delta \ll 1$ . At the first order of approximation for small  $\delta$ , and returning back to dimensional form, the above equations

reduce to:

$$\mu \frac{\partial^2 u_1}{\partial x_3^2} = \frac{\partial P}{\partial x_1} \quad (2.8)$$

$$\mu \frac{\partial^2 u_2}{\partial x_3^2} = \frac{\partial P}{\partial x_2} \quad (2.9)$$

$$0 = \frac{\partial P}{\partial x_3} \quad (2.10)$$

$$0 = \frac{\partial u_1}{\partial x_1} + \frac{\partial u_2}{\partial x_2} + \frac{\partial u_3}{\partial x_3} \quad (2.11)$$

It is worth noting, that in equations (2.8) to (2.11) the pressure has been kept in the formulation due to the viscosity scaling used in (2.3). If the pressure had been scaled with inertial terms, as in common in high Reynolds number flows, the pressure would have been lost in the formulation, resulting in a trivial solution. Integrating equations (2.8) and (2.9) across the cell gap from  $0 \leq x_3 \leq b$ , using the boundary conditions  $u_1 = u_2 = 0$  at  $x_3 = 0$  and  $x_3 = b$ , the following equations are formed:

$$u_1 = -\frac{1}{2\mu} \frac{\partial P}{\partial x_1} (bx_3 - x_3^2) \quad (2.12)$$

$$u_2 = -\frac{1}{2\mu} \frac{\partial P}{\partial x_2} (bx_3 - x_3^2) \quad (2.13)$$

The average velocities  $\bar{u}_i$  are given by:

$$\bar{u}_i = \frac{1}{b} \int_0^b u_i dx_3 \quad (2.14)$$

Using the average velocity and integrating equations (2.12), (2.13) and (2.11) across the cell gap, the following lubrication equations are formed:

$$\bar{u}_1 = -\frac{b^2}{12\mu} \frac{\partial P}{\partial x_1} \quad (2.15)$$

$$\bar{u}_2 = -\frac{b^2}{12\mu} \frac{\partial P}{\partial x_2} \quad (2.16)$$

$$\frac{\partial (b\bar{u}_1)}{\partial x_1} + \frac{\partial (b\bar{u}_2)}{\partial x_2} = 0 \quad (2.17)$$

Equations (2.15) to (2.17) represent the average flow field in the gap, i.e. the Darcy flow in a Hele-Shaw cell. Note, to form equation (2.17), Leibniz's rule was used assuming the cell plates are not moving. Using scalings appropriate to the thin cell, slow flow problem, inertial effects are removed from the original Navier-Stokes equations and by

depth-averaging in the vertical direction, velocity dependence through the thin film is removed. These equations will be used in the rest of the thesis as the basis behind the different Hele-Shaw models. Although the equations describe the fluid flow in each flow region, they also require suitable conditions at the interface between the two fluids and at the  $x_1$ - $x_2$  plane boundaries to close the problem.

### 2.2.1 Radial immiscible displacement

In this thesis, a circular Hele-Shaw cell of infinite radius is considered, in which high viscosity fluid is displaced by the injection of a less viscous fluid. The low viscosity invading fluid (such as  $CO_2$ ) occupies region  $\Omega_1$  whilst a high viscosity fluid (such as brine) occupies the external region  $\Omega_2$ , shown in Figure 2.2. The initial interface has a perturbation given in Figure 2.2 as  $\epsilon = r_0 \epsilon_0 \cos(6\theta)$  where  $r_0$  is the unperturbed interface radius,  $\epsilon_0$  is the perturbation amplitude and  $\theta$  is azimuthal angle around the interface. A symmetric perturbation is shown in Figure 2.2, which is used as the

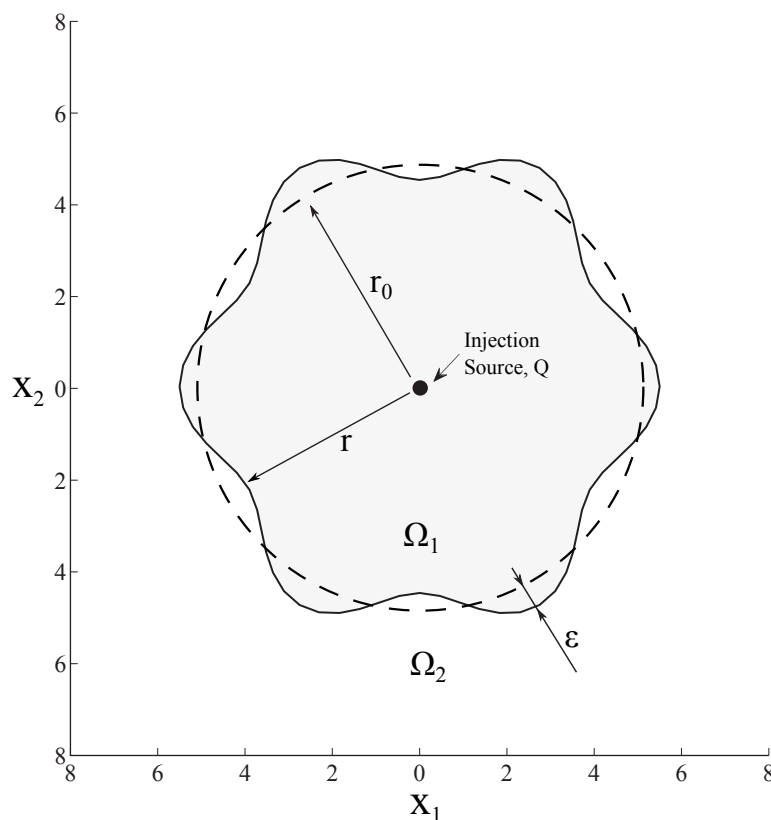


Figure 2.2: Planar view of the radial injection Hele-Shaw configuration. The initial interface here has a radius given by  $r = r_0 + \epsilon$

initial interface conditions in this chapter. The symmetric perturbation acts to initiate instability so that fingering effects can be seen at several locations on the interface. An asymmetric perturbation is used later in section 2.7, to mimic naturally occurring noise and disturbance within the system.

The fluid mobility in region  $l$  at a point  $\mathbf{x} = (x_1, x_2)$  is related to the Hele-Shaw plate separation  $b(\mathbf{x})$  and the fluid viscosity  $\mu_l(\mathbf{x})$  by:

$$M_l(\mathbf{x}) = \frac{b(\mathbf{x})^2}{12\mu_l(\mathbf{x})} \quad (2.18)$$

The  $b(\mathbf{x})^2/12$  term in the mobility refers to the intrinsic permeability of the Hele-Shaw cell, defined by the plate separation. Note, that in (2.18), both the plate separation and viscosity can vary in space, which is important for the analyses in chapter 5 and 6. For the flow between two thinly separated plates in a Hele-Shaw cell, the depth averaged pressure  $P_l$  and two dimensional cross-sectional average Darcy velocity  $u_i^l$  in each fluid region  $l$  can be expressed through Darcy's law:

$$u_i^l(\mathbf{x}) = -M_l(\mathbf{x}) \frac{\partial P_l(\mathbf{x})}{\partial x_i} \quad (2.19)$$

Note, the over-bar on the average velocity has been dropped here for convenience, since the depth averaged velocities are used throughout this thesis as the velocities in the two-dimensional Hele-Shaw problem. The flow field satisfies conservation of mass that can be written in terms of the Darcy velocity and the plate separation as:

$$\frac{\partial(b(\mathbf{x})u_i^l(\mathbf{x}))}{\partial x_i} = 0 \quad (2.20)$$

Substituting the Darcy velocity (2.19) into the conservation of mass equation (2.20):

$$\frac{\partial}{\partial x_i} \left( b(\mathbf{x})M_l(\mathbf{x}) \frac{\partial P_l(\mathbf{x})}{\partial x_i} \right) = 0 \quad \mathbf{x} \in \Omega_l, \quad l = 1, 2 \quad (2.21)$$

At a boundary point  $\boldsymbol{\xi} = (\xi_1, \xi_2)$  on the fluid interface  $S$  between  $\Omega_1$  and  $\Omega_2$ , there are two matching conditions (kinematic and dynamic) that must be met by the advancing interface. Firstly, the kinematic condition requires the continuity of normal velocity

$u_i(\boldsymbol{\xi})n_i(\boldsymbol{\xi})$ , i.e.

$$-M_1(\boldsymbol{\xi})\frac{\partial P_1(\boldsymbol{\xi})}{\partial n} = -M_2(\boldsymbol{\xi})\frac{\partial P_2(\boldsymbol{\xi})}{\partial n} \quad (2.22)$$

Secondly, the dynamic condition describes the pressure jump across the interface:

$$P_1(\boldsymbol{\xi}) - P_2(\boldsymbol{\xi}) = \gamma \left( \frac{2}{b(\boldsymbol{\xi})} + k(\boldsymbol{\xi}) \right) \quad (2.23)$$

Where  $\gamma$  is the surface tension and  $k(\boldsymbol{\xi})$  is the curvature.  $k(\boldsymbol{\xi})$  is considered a continuous function on the interface surface. The pressure jump condition above represents one of the most basic forms of the Young-Laplace equation. Numerous studies use the curvature representation given above, with some also including a  $\pi/4$  scaling term for consistency with the asymptotic analysis of [45]. In this thesis, various forms of the pressure jump condition are considered, to compare with previous works. In all forms, the contact angle of the meniscus has been assumed to be zero, to be consistent with the limit that the outer fluid (brine) is perfectly wetting, and the inner fluid ( $CO_2$ ) is perfectly non-wetting. Dynamic wetting effects have not been shown in equation (2.23), but can have a considerable effect on the interfacial displacement in a Hele-Shaw cell at high capillary numbers [46–48]. Specific wetting effects are considered explicitly in the formulation in chapter 3.

The displacement of the outer fluid is initiated by the injection of the inner fluid with a point source of strength  $Q$  at the origin, with velocity given by:

$$u_i = \frac{Qx_i}{2\pi r^2} \quad (2.24)$$

Here,  $r$  is the distance from the collocation point,  $\boldsymbol{x}$ , to the source point located at the origin; i.e.  $r = |\boldsymbol{x}|$ . The far field pressure tends to that generated by the source at a distance  $\boldsymbol{x} \rightarrow \infty$ :

$$P_2(\boldsymbol{x}) \xrightarrow{\boldsymbol{x} \rightarrow \infty} -\frac{Q}{2\pi M_2(\boldsymbol{x})} \ln \left( \frac{r}{r_0} \right) \quad (2.25)$$

Equation (2.21), subject to matching conditions (2.22, 2.23), and asymptotic conditions (2.24) and (2.25) represents a well posed problem that can be solved with a variety of numerical methods in order to find the pressure in the domain and subsequently the interface velocity. This model represents the basis to analyse the different processes in

this work, with any necessary alterations included in the relevant chapter formulations.

## 2.3 Finite mobility ratio formulation

Here, a non-dimensional Hele-Shaw model is presented specific to the radial injection case with a constant mobility in each region, allowing simplification of the equations described in the previous section. Utilising the characteristic length, time, velocity and pressure of the radial injection problem, the field variables can be represented in non-dimensional form:

$$(\mathbf{x}, \mathbf{y}, r) = r_0 (\mathbf{x}', \mathbf{y}', r') \quad (2.26)$$

$$t = \frac{r_0^2}{Q} t' \quad (2.27)$$

$$u_i^l = \frac{Q}{r_0} u_i^{l'} \quad l = 1, 2 \quad (2.28)$$

$$(P, \hat{\phi})_l = \frac{Q}{M_2} (P', \hat{\phi}')_l \quad l = 1, 2 \quad (2.29)$$

In equalities (2.26) - (2.29), apostrophes identify non-dimensional variables.  $t, u, P$  and  $\hat{\phi}$  represent time, two-dimensional velocity, depth averaged pressure and surface potential pressure respectively. The parameters  $Q$  and  $M_2$  are the radial injection flux and the mobility of the displaced fluid respectively. The depth averaged pressure and two dimensional velocity in each fluid region can be expressed through Darcy's law along with the conservation of mass in non-dimensional form as:

$$u_i^{1'}(\mathbf{x}) = -\beta \frac{\partial P_1'(\mathbf{x})}{\partial x_i'} \quad (2.30)$$

$$u_i^{2'}(\mathbf{x}) = -\frac{\partial P_2'(\mathbf{x})}{\partial x_i'} \quad (2.31)$$

$$\frac{\partial u_i^{l'}}{\partial x_i'} = 0 \quad \mathbf{x} \in \Omega_l, \quad l = 1, 2 \quad (2.32)$$

Note that the plate separation  $b$  does not appear in (2.32) due its constant value in this model. In equation (2.30),  $\beta$  is the ratio of mobilities between the two fluids:

$$\beta = \frac{M_1}{M_2} \quad (2.33)$$

For  $\beta$  values greater than 1, the inner fluid is less viscous than the external fluid. For infinite mobility ratio models  $\beta = \infty$ . With a constant, finite  $\beta$ , equations (2.30) - (2.32) can be reduced to Laplace's equation:

$$\frac{\partial^2 P'_l(\mathbf{x})}{\partial x_i'^2} = 0 \quad \mathbf{x} \in \Omega_l, \quad l = 1, 2 \quad (2.34)$$

From this point on in the chapter, the apostrophe of all dimensionless variables will be dropped for clarity, and every variable will be assumed to be in its non-dimensional form, unless otherwise stated. In this chapter, a boundary element method is constructed to solve the Laplace equation above. Firstly, to form a boundary integral equation, the pressure field can be represented as a sum of the pressures due to an injection potential source  $Q$  and a surface potential term  $\hat{\phi}_l$ :

$$P_1(\mathbf{x}) = \hat{\phi}_1 - \frac{1}{2\pi\beta} \ln(r) \quad (2.35)$$

$$P_2(\mathbf{x}) = \hat{\phi}_2 - \frac{1}{2\pi} \ln(r) \quad (2.36)$$

Note,  $Q$  does not appear on the far right term in equations (2.35) and (2.36) due to the non-dimensional scaling of the pressure. At a boundary point  $\boldsymbol{\xi}$  on the fluid interface  $S$  between  $\Omega_1$  and  $\Omega_2$ , the matching conditions can now be described as continuity of normal potential fluxes:

$$q = \beta \frac{\partial \hat{\phi}_1}{\partial n} = \frac{\partial \hat{\phi}_2}{\partial n} \quad (2.37)$$

and secondly, the pressure jump across the interface due to the surface tension,  $\gamma$ :

$$\hat{\phi}_1 - \hat{\phi}_2 = \frac{1}{Ca_g} \left( \frac{2r_0}{b} + k(\boldsymbol{\xi}) \right) - \left( \frac{\beta - 1}{2\pi\beta} \right) \ln(r) = (1 + \beta) f_s \quad (2.38)$$

Where:

$$f_s = \frac{1}{Ca_g(1 + \beta)} \left( \frac{2r_0}{b} + k(\boldsymbol{\xi}) \right) - \frac{1}{1 + \beta} \left( \frac{\beta - 1}{2\pi\beta} \right) \ln(r) \quad (2.39)$$

In equations (2.38) and (2.39), the global capillary number  $Ca_g$  has been introduced, which describes the ratio of viscous driving forces to surface tension forces. Classically, a modified capillary number can be used to completely describe infinite mobility ratio rectilinear Hele-Shaw flow [1]. Due to the the radial setup of the Hele-Shaw injection,

this modified capillary number must be adapted to adequately describe the flow regime. The capillary number produced from the dimensional analysis of the radial Hele-Shaw flow above and that presented by [1] are shown below, with the classical rectilinear version shown with an apostrophe.

$$Ca_g = \frac{12\mu_2 Q}{\gamma r_0} \left(\frac{r_0}{b}\right)^2 = \frac{r_0 Q}{\gamma M_2} \quad Ca' = \frac{12\mu_2 U_n}{\gamma} \left(\frac{L}{b}\right)^2 \quad (2.40)$$

In the modified capillary number for rectilinear flow  $Ca'$ , the half Hele-Shaw cell width  $L$  is used as the macroscopic length scale, with the cell plate separation  $b$  used as the microscopic length scale. For radial flow, the initial unperturbed radius  $r_0$  is chosen as the macroscopic length scale as there is no characteristic cell width in the fully circular domain. The initial source injection velocity,  $Q/r_0$  is chosen as the characteristic velocity of the problem. The capillary number presented here for radial Hele-Shaw flow, and that presented by [1] are equivalent, with a difference only in the macroscopic length scale of the problem and the characteristic velocity.

The  $r_0/b$  scaling term in equation (2.40) relates the initial unperturbed bubble radius to the Hele-Shaw plate separation, which modifies the physical capillary number to include the effective permeability of the cell. The capillary number together with the mobility ratio uniquely describe radial Hele-Shaw flow, and as such are the main parameters used to analyse and describe different flow regimes in this chapter.

The signed curvature,  $k$  is considered a continuous function on the parametric interface surface  $S(t) = S(x(t), y(t))$ , given by equation (2.41) below.

$$k = r_0 \frac{(x_t y_{tt} - y_t x_{tt})}{\left[(x_t)^2 + (y_t)^2\right]^{\frac{3}{2}}} \quad (2.41)$$

Where  $y_{tt}$  refers to the dimensional second derivative with respect to  $t$ . The final condition required to close the system is given by the far field pressure condition:

$$P_2(\mathbf{x}) \xrightarrow{\mathbf{x} \rightarrow \infty} -\frac{1}{2\pi} \ln r \quad (2.42)$$

The Laplace equation (2.34), subject to matching conditions (2.37) and (2.38) and the far field condition (2.42) represents a well posed problem, that can be solved directly using a boundary element approach. This formulation is possible due to the constant, finite

mobility in each region that reduces the elliptic PDE (2.21) to the simplest form of elliptic PDE in (2.34); the Laplace equation. This mathematical model forms the basis to form a boundary integral equation which can be discretised with a B-Spline boundary element method with hypersingular integral treatment, presented in the following sections.

## 2.4 Boundary element method

### 2.4.1 Boundary integral formulation

Following from the pressure field representation in Equation (2.35) and (2.36), the surface potentials in zone 1 and zone 2,  $\hat{\phi}_1$  and  $\hat{\phi}_2$  respectively can be expressed in terms of their corresponding Green's formulae at the fluid interface [39], using the two dimensional fundamental solution,  $\phi^*$ .

$$\begin{aligned} & \int_{S_\infty} \phi^*(\boldsymbol{\xi}, \mathbf{y}) \frac{\partial \hat{\phi}_2(\mathbf{y})}{\partial n_y} dS_y - \int_{S_\infty} \hat{\phi}_2(\mathbf{y}) \frac{\partial \phi^*(\boldsymbol{\xi}, \mathbf{y})}{\partial n_y} dS_y \\ & + \int_s \hat{\phi}_2(\mathbf{y}) \frac{\partial \phi^*(\boldsymbol{\xi}, \mathbf{y})}{\partial n_y} dS_y - \int_s \phi^*(\boldsymbol{\xi}, \mathbf{y}) \frac{\partial \hat{\phi}_2(\mathbf{y})}{\partial n_y} dS_y = \frac{1}{2} \hat{\phi}_2(\boldsymbol{\xi}) \end{aligned} \quad (2.43)$$

$$\int_s \hat{\phi}_1(\mathbf{y}) \frac{\partial \phi^*(\boldsymbol{\xi}, \mathbf{y})}{\partial n_y} dS_y - \int_s \frac{\partial \hat{\phi}_1(\mathbf{y})}{\partial n_y} \phi^*(\boldsymbol{\xi}, \mathbf{y}) dS_y = -\frac{1}{2} \hat{\phi}_1(\boldsymbol{\xi}) \quad (2.44)$$

The difference in sign between the two equations is due to the direction of the outward facing normal  $\vec{n}$  with respect to the domain. In the above equation  $n_y$  refers to the normal direction at field point  $y$ . The continuity and discontinuity properties of the single-layer and double-layer potential are used to evaluate the integrals along the curve  $S$ . For the external problem in equation (2.43), both the internal boundary at the interface and the auxiliary external boundary at infinity  $S_\infty$  must be considered. The external boundary can be evaluated at a fixed location in the far field and treated as a regular surface integral, introducing extra computation and constraining the interior fluid to the region inside the external boundary [37]. The evaluation of the external surface can be removed by utilising a Green's function with periodic boundary conditions [38].

The external boundary at infinity can also be evaluated asymptotically, considering the perturbation flux to approach zero as the radial distance from the source approaches

infinity. This allows the fluid domain to extend to infinity, so the evolution of the inner fluid interface can continue unrestricted, without having to re-scale an exterior bounding surface. Batchelor [49] has shown that asymptotic evaluation introduces a constant into the equation, replacing the external boundary surface integral:

$$\frac{k_{as}}{2\pi} + \int_s \hat{\phi}_2(\mathbf{y}) \frac{\partial \phi^*(\boldsymbol{\xi}, \mathbf{y})}{\partial n_y} dS_y - \int_s \frac{\partial \hat{\phi}_2(\boldsymbol{\xi}, \mathbf{y})}{\partial n_y} \phi^*(\boldsymbol{\xi}, \mathbf{y}) dS_y = \frac{1}{2} \hat{\phi}_2(\boldsymbol{\xi}) \quad (2.45)$$

The constant  $k_{as}$  becomes an unknown variable to be found, which along with the zero-flux condition of the surface potential pressure across the interface ensures the solvability of the exterior problem:

$$\int_s q(\boldsymbol{\xi}) dS_\xi = 0 \quad (2.46)$$

Equations (2.45) and (2.46) represent an infinite mobility ratio model for the exterior problem, considering solely the displaced fluid in region two. This model has been implemented by [40] and more recently by [50] including a dissolution velocity at the interface. To combine the interior and exterior boundary integral equations to produce a finite mobility ratio model applicable in both domains, the limiting value of the normal derivatives of equations (2.44) and (2.45) can be taken:

$$\int_s \hat{\phi}_2(\mathbf{y}) \frac{\partial^2 \phi^*(\boldsymbol{\xi}, \mathbf{y})}{\partial n_\xi \partial n_y} dS_y - \int_s \frac{\partial \hat{\phi}_2(\mathbf{y})}{\partial n_y} \frac{\partial \phi^*(\boldsymbol{\xi}, \mathbf{y})}{\partial n_\xi} dS_y = \frac{1}{2} \frac{\partial \hat{\phi}_2(\boldsymbol{\xi})}{\partial n_\xi} \quad (2.47)$$

$$\int_s \hat{\phi}_1(\mathbf{y}) \frac{\partial^2 \phi^*(\boldsymbol{\xi}, \mathbf{y})}{\partial n_\xi \partial n_y} dS_y - \int_s \frac{\partial \hat{\phi}_1(\mathbf{y})}{\partial n_y} \frac{\partial \phi^*(\boldsymbol{\xi}, \mathbf{y})}{\partial n_\xi} dS_y = -\frac{1}{2} \frac{\partial \hat{\phi}_1(\boldsymbol{\xi})}{\partial n_\xi} \quad (2.48)$$

Subtracting the above two equations and using the matching conditions (2.37) and (2.38), the following second kind Fredholm integral equation can be formed [29]:

$$-\frac{1}{2} q(\boldsymbol{\xi}) + \left( \frac{1-\beta}{\beta+1} \right) \int_s K(\mathbf{y}, \boldsymbol{\xi}) q(\mathbf{y}) dS_y = g(\boldsymbol{\xi}) \quad (2.49)$$

The regular kernel,  $K(\mathbf{y}, \boldsymbol{\xi})$  in equation (2.49) is given by:

$$K(\mathbf{y}, \boldsymbol{\xi}) = \frac{1}{2\pi} \frac{\partial}{\partial n_\xi} \left( \ln \frac{1}{R(\boldsymbol{\xi}, \mathbf{y})} \right) = \frac{1}{2\pi} \frac{y_j - \xi_j}{R^2} n_j(\boldsymbol{\xi}) \quad (2.50)$$

Noting from [29] that,

$$\lim_{\mathbf{y} \rightarrow \boldsymbol{\xi}} K(\mathbf{y}, \boldsymbol{\xi}) = -\frac{k(\boldsymbol{\xi})}{2} \quad (2.51)$$

The  $R$  term in the regular kernel is the non-dimensional absolute distance from the collocation point  $\boldsymbol{\xi}$  to the point of integration on the surface  $\mathbf{y}$ . The non-homogeneous boundary term  $g(\boldsymbol{\xi})$  is given by the following hypersingular integral.

$$g(\boldsymbol{\xi}) = \frac{\beta}{2\pi} \int_s f_s(\mathbf{y}) \frac{\partial^2}{\partial n_\xi \partial n_y} \left( \ln \frac{1}{R(\boldsymbol{\xi}, \mathbf{y})} \right) dS_y \quad (2.52)$$

The second kind Fredholm equation in (2.49) permits an analytical Neumann series solution, owing to the fact that it is the adjoint of the corresponding indirect equation, which has been proven to have an analytical Neumann series solution (for more details see [29]). Before the solution technique for equation (2.49) is given, it is worth noting that by combining the two integral equations for the different fluid domains, (2.47) and (2.48), the constant  $k_{as}$  obtained from the asymptotic limit of the surface integral at infinity in equation (2.45) does not need to be evaluated. To show that the no-flux condition of the surface potential across the interface is still met by equation (2.49), without the need to explicitly include it in the equation, firstly the potential flux can be integrated over the interface surface:

$$\int_s -\frac{1}{2} q(\boldsymbol{\xi}) dS_\xi + \left( \frac{1-\beta}{\beta+1} \right) \int_s q(\mathbf{y}) \int_s K(\mathbf{y}, \boldsymbol{\xi}) dS_\xi dS_y = \int_s g(\boldsymbol{\xi}) dS_\xi \quad (2.53)$$

The integral of the kernel  $K(\mathbf{y}, \boldsymbol{\xi})$ , over the surface has a value of 1/2 meaning equation (2.53) can be simplified to:

$$\frac{\beta}{\beta+1} \int_s q(\boldsymbol{\xi}) dS_\xi = \int_s g(\boldsymbol{\xi}) dS_\xi \quad (2.54)$$

The right hand side of equation (2.54), can be written as:

$$\begin{aligned} \int_s g(\boldsymbol{\xi}) dS_\xi &= \frac{\beta}{2\pi} \int_s f_s(\mathbf{y}) \int_s \frac{\partial^2}{\partial n_\xi \partial n_y} \left( \ln \frac{1}{R(\boldsymbol{\xi}, \mathbf{y})} \right) dS_\xi dS_y \\ &= \frac{\beta}{2\pi} \int_s f_s(\mathbf{y}) \int_s \frac{\partial}{\partial n_\xi} K(\boldsymbol{\xi}, \mathbf{y}) dS_\xi dS_y = 0 \end{aligned} \quad (2.55)$$

Since,

$$\int_s \frac{\partial}{\partial n_\xi} K(\boldsymbol{\xi}, \mathbf{y}) dS_\xi = 0 \quad (2.56)$$

Using the above expressions and equation (2.54), it follows that the no-flux condition of the surface potential at the interface has been met:

$$\int_s q(\boldsymbol{\xi}) dS_\xi = 0 \quad (2.57)$$

The above analysis shows that the no-flux condition at the interface is met by equation (2.49). By combining the integral equations for each fluid domain into one single equation, the need to explicitly evaluate the no-flux condition at the interface has been avoided, at the expense of introducing a hypersingular integral.

Equation (2.49) can be solved using a convergent series for  $q$ , as long as  $0 \leq \beta < \infty$  [29]. Using infinitely many terms results in an analytical Neumann convergent series solution. The series can be simplified by taking  $\lambda = \frac{(1-\beta)}{(\beta+1)}$  and using a discrete number of terms,  $m$ , to truncate the solution of equation (2.49).

$$q(\boldsymbol{\xi}) = q_0(\boldsymbol{\xi}) + \lambda q_1(\boldsymbol{\xi}) + \cdots + \lambda^m q_m(\boldsymbol{\xi}) \quad (2.58)$$

The terms in equation (2.58) can be calculated recursively, via the following formulae:

$$q_0(\boldsymbol{\xi}) = -2g(\boldsymbol{\xi}) \quad (2.59)$$

$$q_m(\boldsymbol{\xi}) = 2 \int_s K(\boldsymbol{\xi}, \mathbf{y}) q_{m-1}(\mathbf{y}) dS_y \quad m \neq 0 \quad (2.60)$$

The movement of the fluid-fluid interface is then calculated via a forward Euler time stepping approach, where  $\Delta L_n(\boldsymbol{\xi})$  represents the dimensionless distance moved by a boundary point in a single time-step:

$$U_n = \frac{\Delta L_n(\boldsymbol{\xi})}{\Delta t} = -q(\boldsymbol{\xi}) + \frac{x_i(\boldsymbol{\xi}) n_i(\boldsymbol{\xi})}{2\pi r^2} \quad (2.61)$$

Where  $U_n$  is the total normal interface velocity.

### 2.4.2 B-Spline representation

The surface integrals in the boundary integral equations in the previous section are solved by discretising the boundary using uniform cubic B-Spline boundary elements, first shown in [51]. Every variable that requires interpolation along the interface can be represented by a B-Spline, using the following equations [51].

$$q(\mathbf{x}) = N^c(t(\mathbf{x}))q^c \quad c = 1, 2, 3, 4 \quad (2.62)$$

In equation (2.62), the surface potential flux  $q$  has been used to represent a continuous scalar field along the interface, with corresponding control points  $q^c$ .  $t(\mathbf{x})$  is the intrinsic coordinate of the element of length  $0 \leq t \leq 1$ . The continuous field can be any scalar or vector component with corresponding control points, e.g.  $x$ ,  $y$ ,  $\hat{\phi}_1$  etc. The shape functions  $N^c$  over each element are given by:

$$\begin{aligned} N^0(t) &= \frac{-t^3}{6} + \frac{t^2}{2} - \frac{t}{2} + \frac{1}{6} \\ N^1(t) &= \frac{t^3}{2} - t^2 + \frac{2}{3} \\ N^2(t) &= \frac{-t^3}{2} + \frac{t^2}{2} + \frac{t}{2} + \frac{1}{6} \\ N^3(t) &= \frac{t^3}{6} \end{aligned} \quad (2.63)$$

Equation (2.62) can be formed for each nodal location along the boundary, producing a system of equations that may be solved to find the control points for each element. To close the curve of the control points, the following conditions must be met at the start and end of the elements:

$$\begin{aligned} N^0 &= N^{N_b} \\ N^{N_b+1} &= N^1 \end{aligned} \quad (2.64)$$

Here,  $N_b$  is the total number of boundary elements. The system of equations for the control points can be solved to find the control points for the variable in question. This has to be done at each time step to find the new  $x$  and  $y$  control points, given the new interface that has been calculated. The resulting cyclic tri-diagonal system is efficiently solved utilising the Sherman-Morrison formula [52]. Given the shape functions and control points, the discretised form of equation (2.60) can be written in terms of a

boundary element formulation as:

$$q_m(\boldsymbol{\xi}) = \sum_{k=1}^{N_b} \sum_{j=1}^{N_g} \sum_{i=1}^{N_c} \left( W_j K(\boldsymbol{\xi}, \mathbf{y}(t_j)) N^{ki}(\mathbf{y}(t_j)) q_{m-1}^{ki} J(\mathbf{y}(t_j)) \right) \quad (2.65)$$

Where,  $N_b$  are the number of boundary elements,  $N_g$  are the number of Gaussian integration points and  $N_c$  are the number of control points (here taken as 4).  $W_j$  are the Gaussian quadrature weighting functions at intrinsic locations  $t_j$ .  $J$  is the Jacobian transforming the surface integral into the local element integral over the range of the intrinsic coordinate, i.e.  $0 \leq t_j \leq 1$ .  $q^{ki}$  is the  $i^{th}$  control point for element  $k$ , with corresponding shape function  $N^{ki}(\mathbf{y}(t_j))$  at the field points of integration ( $\mathbf{y}(t_j)$ ). The sum over all elements represents all elements that don't coincide with the collocation point  $\boldsymbol{\xi}$ ; for these two elements a hypersingular integral technique has to be used, discussed in detail later.

The B-spline boundary elements are adaptively fitted to the interface as it grows at each time step. A target element size (arc length) is fed into the program, which is maintained at each time step. At each time step, with the new interface position, the control points for the B-Spline curve can be calculated. With this, the total arc length of the interface can be calculated, and the number of elements that are needed can be evaluated from the desired element size. This number is always an integer multiple of the number of fingers in a symmetric simulation, to maintain symmetry.

With the desired number of elements, an iterative Newton-Raphson scheme is implemented using the current elements to locate the new element nodal positions. This takes a guess at the correct nodal position using the midpoint of the current element and compares it to the desired element length. Based on this, and the Jacobian of the surface derivatives, the guess can be updated and moved along the element. When the error between the desired arc length and the arc length using the new nodal position is less than  $1 \times 10^{-12}$  the iteration stops, and the next nodal point can be calculated. With the new nodal points, the new control points for the B-Spline can be calculated and the discretised form of the integral equations can be solved.

### 2.4.3 Local curvature evaluation

Along with the B-Spline representation of the curve, a 4<sup>th</sup> order Lagrangian polynomial is used to compute the local curvature,  $k(\xi)$  at a nodal point. A Lagrangian polynomial accurately represents second derivatives at nodal points, which are second order accurate with a B-Spline representation. The Lagrangian polynomial is adaptively fitted to the B-spline curve, reconstructing locally using the surrounding nodal points. A non-uniform polynomial was tested, but since the locations must be reconstructed using the B-Spline rather than the raw nodal positions, the accuracy was only as good as the B-spline itself.

Table 2.1 shows the 4<sup>th</sup> order Lagrangian polynomial and cubic B-Spline schemes used to calculate the curvature of a test function,  $y = \frac{1}{2} + \frac{3}{10}\sin(2\pi x)$ , which was also presented in [41] and [53] with a 20x20 grid. There are  $N$  elements used to approximate the function, with  $N + 1$  nodal points. The Lagrangian polynomial has a much better approximation to the curvature than the cubic B-Spline scheme, which when centred on the nodal points is second order accurate. The  $L_1$  error norm between the 4<sup>th</sup> order Lagrangian polynomial and the analytical solution using 20 elements is 0.003%, with the numerical points being indistinguishable from the analytical function when viewed graphically. This is a much better approximation than the schemes used in [41] and [53], in which the numerical approximation shows noticeable discrepancy from the analytical function graphically.

Number of elements, N		20	40	60	80
$L_1$ Error Norm	B-Spline	$1.18 \times 10^{-3}$	$3.00 \times 10^{-4}$	$1.34 \times 10^{-4}$	$7.58 \times 10^{-5}$
	Lagrangian	$3.03 \times 10^{-5}$	$1.80 \times 10^{-6}$	$3.61 \times 10^{-7}$	$1.15 \times 10^{-7}$
$L_2$ Error Norm	B-Spline	$1.76 \times 10^{-3}$	$4.42 \times 10^{-4}$	$1.97 \times 10^{-4}$	$1.11 \times 10^{-4}$
	Lagrangian	$3.58 \times 10^{-5}$	$2.18 \times 10^{-6}$	$4.32 \times 10^{-7}$	$1.37 \times 10^{-7}$
$L_2$ Conv rate	B-Spline	–	1.98	1.98	1.99
	Lagrangian	–	4.07	3.97	3.97

Table 2.1:  $L_1$  and  $L_2$  error norms and convergence rate of the 4<sup>th</sup> order Lagrangian polynomial and B-Spline approximations to the curvature of  $y = \frac{1}{2} + \frac{3}{10}\sin(2\pi x)$ .

After discretising the boundary into B-Splines, and effectively evaluating the curvature, the hypersingular integral in equation (2.52) must be handled numerically. In [29], the surface integral could be simplified by using constant elements. This allowed the hypersingular integral to be equated to the integral over the remaining elements making up the surface. However, in the present scheme using non-linear B-Spline elements,

the hypersingular integration must be handled explicitly. B-spline boundary elements are favoured over constant, linear or quadratic elements, due to their accuracy when approximating highly curved surfaces, which are typical of the ramified patterns seen in viscous fingering phenomena.

#### 2.4.4 Hypersingular integral treatment

The hypersingular integral in (2.52) is treated using a semi-analytical approach implemented in [54], first proposed by Mikhlin in 1957 [55]. The limiting process will not be performed here due to its length; only the resulting formulae final will be presented, for thorough details of the derivation see [54]. The hypersingular integral in equation (2.52) becomes an issue when the field points of integration,  $\mathbf{y}$  lie close to a collocation point,  $\boldsymbol{\xi}$ . This is most significant on elements that coincide with the collocation point, shown in Figure 2.3. The hypersingular integral must be evaluated in the sense of Hadamard finite parts in order to guarantee its existence over the two elements where the hypersingular point  $\eta$  coincides [56], i.e., for a hypersingular integral  $I_h$  on an element with intrinsic limits  $0 \leq t \leq 1$  the integral can be represented in finite parts as:

$$I_h = \int_0^1 \frac{f(t)}{(t-\eta)^2} dt = \lim_{\epsilon \rightarrow 0^+} \left( \int_0^{\eta-\epsilon} \frac{f(t)}{(t-\eta)^2} dt + \int_{\eta+\epsilon}^1 \frac{f(t)}{(t-\eta)^2} dt - \frac{2f(\eta)}{\epsilon} \right) \quad (2.66)$$

The Hadamard finite parts representation forms the basis behind evaluating the hypersingular integral. The hypersingular integrals of equation (2.52) that must be evaluated on the two elements coinciding with each collocation point are defined here as  $g_h$ :

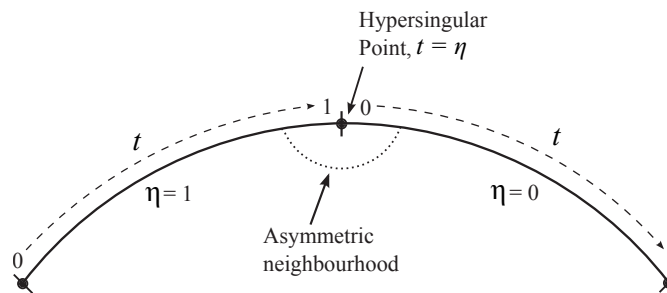


Figure 2.3: Collocation point  $\boldsymbol{\xi}$  on the same elements as the quadrature points  $\mathbf{y}$  creating a hypersingular point  $\eta$  and corresponding hypersingular integral over these elements. Unbold  $t$  and  $\eta$  represent intrinsic locations along the element of integration.

$$g_h(\boldsymbol{\xi}) = \frac{\beta n_i(\boldsymbol{\xi}) f_s^a(\boldsymbol{\xi})}{2\pi} \sum_{m=1}^2 \left( \int_0^1 V_i(\boldsymbol{\xi}, t(\mathbf{y})) N^a(t(\mathbf{y})) J(t(\mathbf{y})) dt \right) \quad (2.67)$$

Where,  $J$  is the Jacobian to transform from the global surface to the intrinsic coordinate  $t$  of the elements  $J(t(\mathbf{y})) = |dy_i/dt|$ . The summation in (2.67) is used to compute the total hypersingular integral from both elements.  $N^a$  are the shape functions in (2.63) which are non-zero at the hypersingular point, using corresponding function control points  $f_s^a$ . Only shape functions that are non-zero at  $\eta$  are considered here since the remainder of the integral  $g_r(\boldsymbol{\xi}) = g(\boldsymbol{\xi}) - g_h(\boldsymbol{\xi})$  for equation (2.52) includes the components from the shape functions that tend to zero at  $\eta$ . These shape functions produce regular integrands on the two hypersingular elements and are included in the normal integration scheme, along with the other elements that do not coincide with the hypersingular point. In (2.67) the specific hypersingular component of the expression is given by:

$$V_i(\boldsymbol{\xi}, t(\mathbf{y})) = \frac{\partial^2}{\partial \xi_i \partial n_y} \left( \ln \frac{1}{R(\boldsymbol{\xi}, t(\mathbf{y}))} \right) = \frac{1}{R^2} \left( -2 \frac{\partial R}{\partial \xi_i} \frac{\partial R}{\partial n} + n_i(t(\mathbf{y})) \right) \quad (2.68)$$

In order to perform the limiting process in (2.66), the integral expression in (2.67) can be expanded in terms of a Laurent power series about  $\eta$  [54].

$$V_i(\boldsymbol{\xi}, t(\mathbf{y})) N^a(t(\mathbf{y})) J(t(\mathbf{y})) = F_i(\eta, t) = \frac{F_{-2}(\eta)}{(t - \eta)^2} + \frac{F_{-1}(\eta)}{t - \eta} + O(1) \quad (2.69)$$

The  $F_{-2}$  and  $F_{-1}$  terms depend only on the derivatives of the B-spline shape functions  $N^a$  that are non-zero at the hypersingular point, i.e.:

$$F_{-2}(\eta) = \frac{n_i(\boldsymbol{\xi}) N^a(\eta)}{J(\eta)} \quad F_{-1}(\eta) = \frac{n_i(\boldsymbol{\xi})}{J(\eta)} \frac{dN^a}{dt} \Big|_{t=\eta} \quad (2.70)$$

By introducing the power series (2.69) into the hypersingular integral (2.67), the limits may be evaluated analytically in order to remove unbounded terms. This results in a regular integral and analytical expression.

$$g_h(\boldsymbol{\xi}) = \frac{\beta n_i(\boldsymbol{\xi}) f_s^a(\boldsymbol{\xi})}{2\pi} \sum_{m=1}^2 \left( \int_0^1 \left[ F^m(\eta, t) - \left( \frac{F_{-2}^m(\eta)}{(t - \eta)^2} + \frac{F_{-1}^m(\eta)}{t - \eta} \right) \right] dt \right. \\ \left. + F_{-1}^m(\eta) \ln \left| \frac{1}{\beta_m(\eta)} \right| \operatorname{sgn}(t - \eta) - F_{-2}^m(\eta) \left[ \operatorname{sgn}(t - \eta) \frac{\gamma_m(\eta)}{\beta_m^2(\eta)} + 1 \right] \right) \quad (2.71)$$

The terms  $F_{-2}^m$ , represent those given by  $F_{-2}$  in equation (2.70) evaluated on element  $m$ . In equation (2.71), the  $\beta_m$  and  $\gamma_m$  terms account for any possible distortion from an asymmetric neighbourhood around the hypersingular point:

$$\beta_m = \frac{1}{J(\eta)}, \quad \gamma_m = -\frac{1}{J^4(\eta)} \frac{dy_i}{dt} \frac{d^2 y_i}{dt^2} \Big|_{t=\eta} \quad i = 1, 2 \quad (2.72)$$

In Figure 2.4 the hypersingular function and the subtraction terms have been evaluated over two B-Spline elements. The hypersingular function,  $F^m$  and the power series terms tend towards infinity when nearing the hypersingular point at  $t - \eta = 0$ . However, the regular function produced by subtracting the power series terms from the hypersingular function is finite and regular at all points in the domain, meaning it can be integrated using standard Gaussian quadrature techniques. The regular integrands are evaluated using 10 quadrature points for each element, with further quadrature points not improving the accuracy of the scheme significantly.

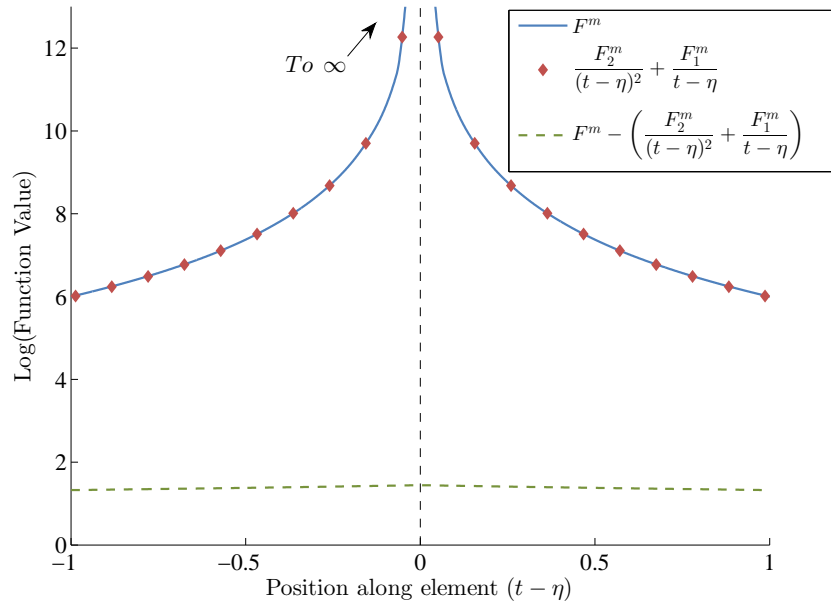


Figure 2.4: Hypersingular integrand, power series and resulting regular function over two elements coinciding with the collocation point.

A simple test of the validity of the hypersingular scheme is to evaluate the integrals on a circle. Here, due to the constant curvature and radius of the circle  $f(\mathbf{y})$  is a constant, meaning that the integrals are effectively evaluating the normal derivative of a double layer potential with a constant density, which is identically zero everywhere. It has been

verified that the sum of the hypersingular integrals is equal to the negative sum of the remaining element integrals, giving a net zero potential flux  $q = 0$ . This means the circle radius  $r(t)$  evolves solely with the potential source velocity,  $r(t) = ((\pi + t)/\pi)^{0.5}$  as expected.

Due to the lack of finite mobility ratio boundary element schemes using a low mobility ratio, a classical viscous fingering example is presented to verify the new finite mobility ratio model. In the classical fingering case presented in [29, 34, 50], air displaces oil in a fully circular Hele-Shaw cell, with a capillary number  $Ca_g = 2000$  and mobility ratio  $\beta = \infty$ .

To compare the infinite mobility ratio schemes in [29, 34, 50], with the finite mobility ratio method developed here, the mobility ratio of the two fluids is varied between 1 and 1000. By varying the mobility ratio, the viscosity of the injected fluid is changed whilst keeping the resident oil viscosity the same. The different mobility ratio cases are compared with an infinite mobility ratio solution in Figure 2.5. The infinite mobility ratio result was created using equations (2.45) and (2.46), which is identical (and produces identical results) to those presented in [29]. The solutions shown in Figure 2.5 are both mesh and time independent (see the next section for verification), with  $\Delta x \approx 0.06$ ,  $\Delta t = 0.02$ .

Note that the global coordinates used in the interface plot (and all others throughout the thesis) are  $x$  and  $y$  for clarity, i.e.  $x = \xi_1$ ,  $y = \xi_2$ .

In Figure 2.5 the finite mobility ratio solutions tend to the infinite mobility ratio solution when the mobility ratio is increased. The base and front of the fingers for the  $\beta = 1000$  case agree very well with the  $\beta = \infty$  case, with an  $L_1$  error of 0.9%. This shows that the finite mobility ratio model with hypersingular integral evaluation is tending to that of the infinite mobility case that does not require hypersingular evaluation, verifying the numerical scheme. If the mobility ratio is raised further to  $\beta = 10000$  (not shown here) the results are graphically indistinguishable. The case of  $\beta = 10$  has a somewhat different shape to the infinite case, with the finger base extending much further into the liquid domain. This is due to the significant velocity possessed by the inner fluid, working to push the bases out. This process is explored more in section 2.5, where mobility ratio effects are examined.

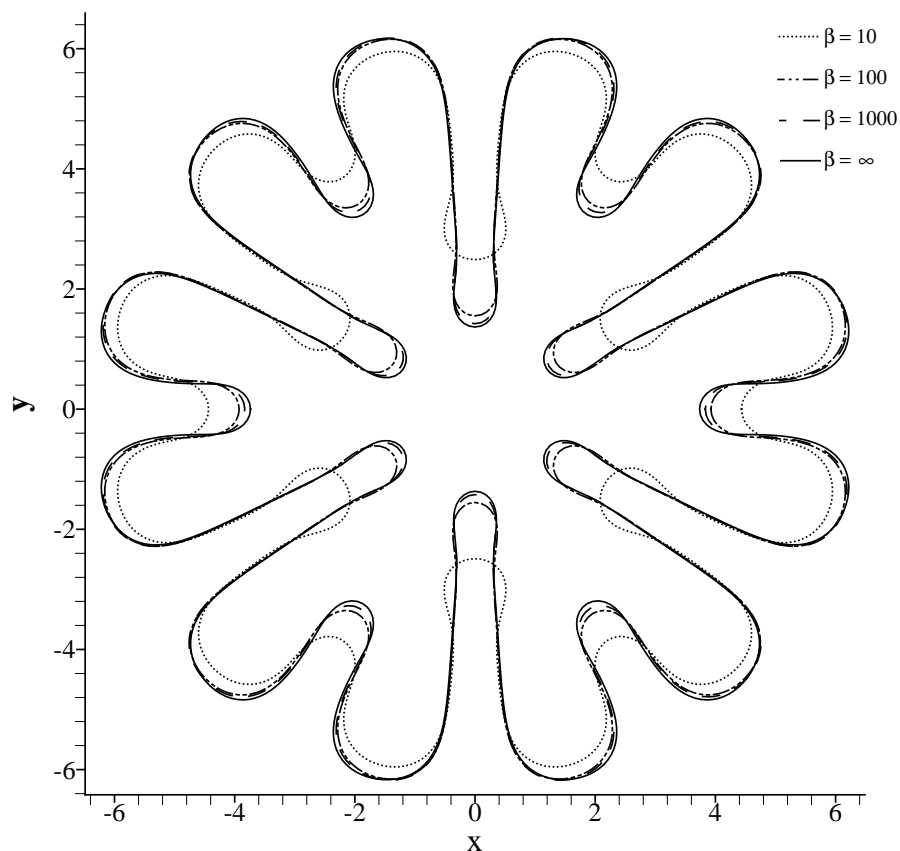


Figure 2.5: Interface of an infinite mobility ratio gas injection at  $t=80$ , showing the classical fingering problem presented in [29, 34, 50], and the interfaces of finite mobility injections utilising the new finite mobility ratio model.

By verifying that the finite mobility ratio scheme tends to the infinite mobility ratio scheme when  $\beta$  is raised, the numerical scheme effectively reproduces the well known results from [29, 34, 50]. This verifies that both the hypersingular integral is contributing correctly to the potential flux calculation and that the other numerical techniques are working correctly to track and update the interface. With this, the finite mobility ratio scheme can be used to explore effects that are not accessible when  $\beta = \infty$ . In the next section, specific performance issues of the finite mobility ratio scheme are discussed before presenting results using the new scheme.

#### 2.4.5 Numerical performance

Here, the numerical performance of the finite mobility ratio model is examined using various small scale simulations. From equations (2.58) - (2.60), it can be seen that the computational cost scales with  $N_p N_b^2$ , where  $N_p$  is the number of terms in the convergent

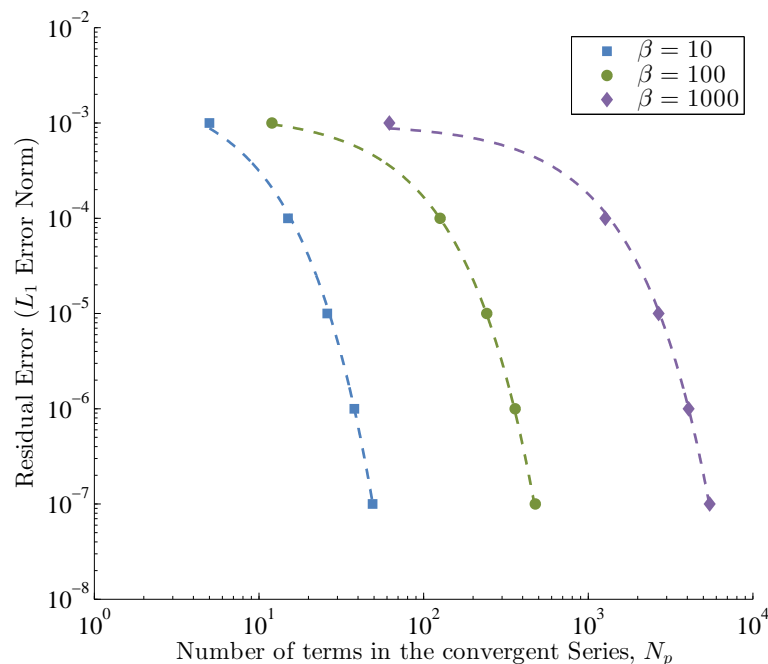


Figure 2.6: Residual error convergence with number of terms in the convergent series and varying mobility ratio.

series, and  $N_b$  is the number of boundary elements. Therefore, for a fixed  $N_p$  the scheme will exhibit close to second order scaling. This is much better than direct solvers for the corresponding matrix system (typically LU decomposition), which exhibit cubic scaling.

During the early stages of interfacial evolution in which the number of boundary elements is low (typically  $<1000$ ), a direct LU solver can outperform the convergent series. However, as the size of the dataset grows, the convergent series will eventually run faster than a direct LU solver due to the second order scaling.

The number of terms used in the convergent series plays an important role in the accuracy and speed of solution. Figure 2.6 shows that as the mobility ratio of the two fluids becomes larger, the number of terms required by the convergent series to reach a desired error increases. This is because the value of  $\lambda$  approaches  $-1$ , and successive terms in the convergent series do not decay as rapidly. When  $\lambda = -1$  there is no unique solution to equation (2.49), due to a singular value in the corresponding spectrum of the integral operator. For most simulations, a residual error of  $10^{-6}$  provides an acceptable convergence level. This typically gives an  $L_1$  error between the interface positions obtained from the series solver and direct matrix solver of less than 0.05%.

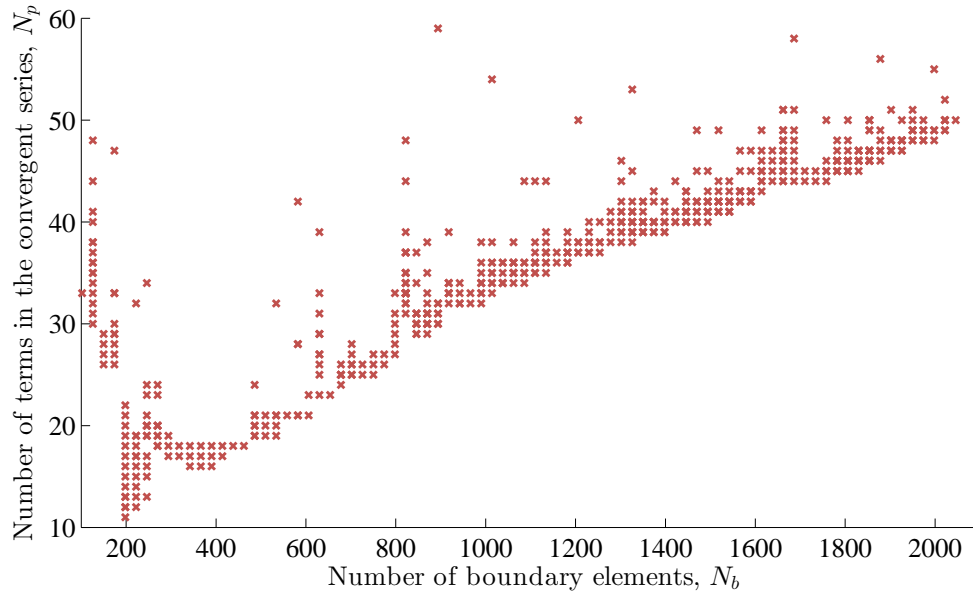


Figure 2.7: Number of terms ( $N_p$ ) needed in the convergent series to produce an  $L_1$  residual error of  $1 \times 10^{-6}$ , with varying numbers of boundary elements.

When the mobility ratio increases beyond 100, the number of terms required in the convergent series to get a low residual error becomes much larger ( $> 500$ ) than the number of starting elements used ( $\sim 100$ ). This means that for high mobility ratios, the convergent series solution can be significantly slower than a corresponding direct matrix solver, showing that this method is much more applicable for the solution of low mobility ratio flows. In simulations when the mobility ratio  $\beta \geq 1000$ , a direct LU solver is used in favour of the series solver, due to solution speed. The resulting interfacial displacements are almost identical between the two methods (i.e. graphically indistinguishable), as long as the residual error in the series solution is maintained below  $10^{-6}$ .

The convergence of the series solution is determined by the residual error between successive terms and is therefore largely independent from the number of boundary elements. Figure 2.7 shows the number of series terms ( $N_p$ ) needed to achieve a  $L_1$  residual error of  $1 \times 10^{-6}$  as the number of boundary elements  $N_b$  increases during the evolution of the interface in the  $\beta = 10$  case in Figure 2.5. Multiple points at the same value of  $N_b$  correspond to outputs from different time steps in the simulation that used the same number of boundary elements in the interface profile. As the interface grows the number of elements are adaptively increased to maintain a target size. However, as the growth rate is so small per time step, the same number of elements can be used for

several steps whilst still maintaining an element size under the target maximum size, resulting in several points with the same value of  $N_b$ . It can be seen that the number of terms needed in the convergent series varies between 30-50 as the number of elements is increased from 100-2000. The number of terms in the series is generally much lower than the number of boundary elements required to accurately compute the solution.

Due to the small number of terms required in low mobility cases, this method is particularly well-suited to solving low mobility ratio regimes, compared to previous direct matrix solutions. As the number of terms in the series solution is typically several orders of magnitude less than the number of boundary elements, long time evolutions can be analysed quickly in comparison to direct matrix solver approaches and as such are one of the main focuses of this work.

#### 2.4.6 Numerical stability and convergence analysis

Along with the number of terms in the convergent series, the number of boundary elements, and time step size also affect the accuracy of the resulting solution. To investigate mesh and time independence, the model was tested under various capillary number regimes.

Figure 2.8 shows the relationship between the capillary number and the solution discretisation. At certain values of mesh spacing and time step size, the solution becomes numerically unstable, with the solution quickly blowing up after only a few time steps. The proposed numerical approach is conditionally stable, as expected by the use of the explicit forward Euler time integration scheme (equation (2.61)). When the capillary number is decreased, the solution becomes more numerically unstable as the equations become stiff, and a lower  $\frac{\Delta t}{\Delta x^3}$  must be used so that the solution does not blow up, as can be seen in Figure 2.8.

The expression represented by the line in Figure 2.8 relates the capillary number to the mesh spacing and time step size. Equation (2.73) for the instability limit shows similarities with a Courant - Friedrichs - Lewy condition in finite difference approximation. The cubic mesh dependence comes from the cubic B-Spline discretisation that is used, with the Euler time stepping technique producing first order temporal

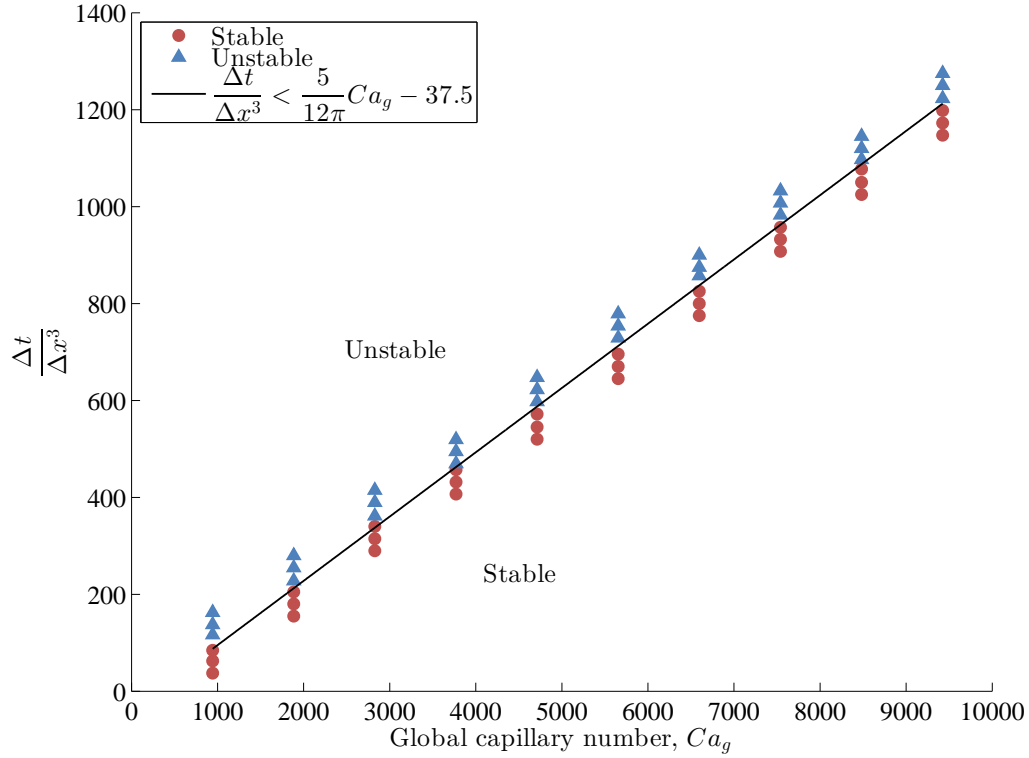


Figure 2.8: Numerical stability of the finite mobility ratio solution with least squares best fit curve giving the limit of stability.

dependence.

$$\frac{\Delta t}{\Delta x^3} < \frac{5}{12\pi} Ca_g - 37.5 \quad (2.73)$$

Numerical experiments were performed to produce Figure 2.8, whereby many simulations were run with varying values of  $\Delta t/\Delta x^3$ , until the observed stability criterion became apparent. Although only six points per capillary number are shown in Figure 2.8, many trial cases were used around the limit of stability to explicitly define the limiting value of stability. The instability expression can be used for all simulations as a check to ensure that the solution is stable under the  $\Delta t/\Delta x^3$  value being used. Fortunately, as the capillary number increases, the restriction of  $\Delta t/\Delta x^3$  for a stable solution slackens and a more refined data set can be used without the solution becoming numerically unstable. As most of the flows and mechanisms under investigation in this work occur at higher capillary numbers, the instability limit is generally not encountered frequently, but is a defining feature of the numerical method.

To illustrate the physical instability of the problem caused by a high capillary number,

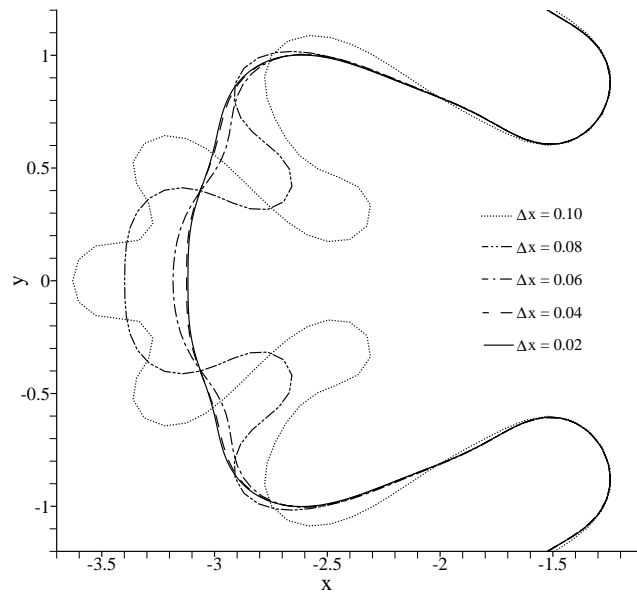


Figure 2.9: Unstable interface shown at  $t = 20$  with differing mesh resolutions.  $Ca_g = 10000$ .

a test case was run with identical conditions to that as the  $\beta = 10$  case in Figure 2.5, but with the volume flux,  $Q$  increased by a factor of 5, producing a capillary number of 10000. When using an element size of  $\Delta x = 0.1$ , it can be seen in Figure 2.9 that the boundary has become highly convoluted, compared to the stable shape of the solution with  $\Delta x = 0.02$ . The problem has become much more sensitive with the increase in capillary number, and as such large number of elements are required to accurately capture the interface. By increasing the number of elements, the solution becomes more stable and flattens out. With a factor of 2.5 decrease in the element size, the solution has effectively converged to a mesh independent solution, with no change to the boundary position. Care has to be taken when solving high capillary number systems as the highly unstable nature of the problem can permit a very different solution if the element density is not sufficiently high.

In Figure 2.10, the spatial convergence of the solutions can be seen. The  $L_1$  error norm quoted is the error between the position of the boundaries of the numerical solution and a mesh independent, pseudo analytical case. This pseudo analytical case was obtained using a very small time step ( $\Delta t < 0.005$ ) and element size ( $\Delta x < 0.02$ ), meaning that using any lower time step or element size did not change the position of the interface. To compare interfacial positions, the nodal positions (in the azimuthal direction around

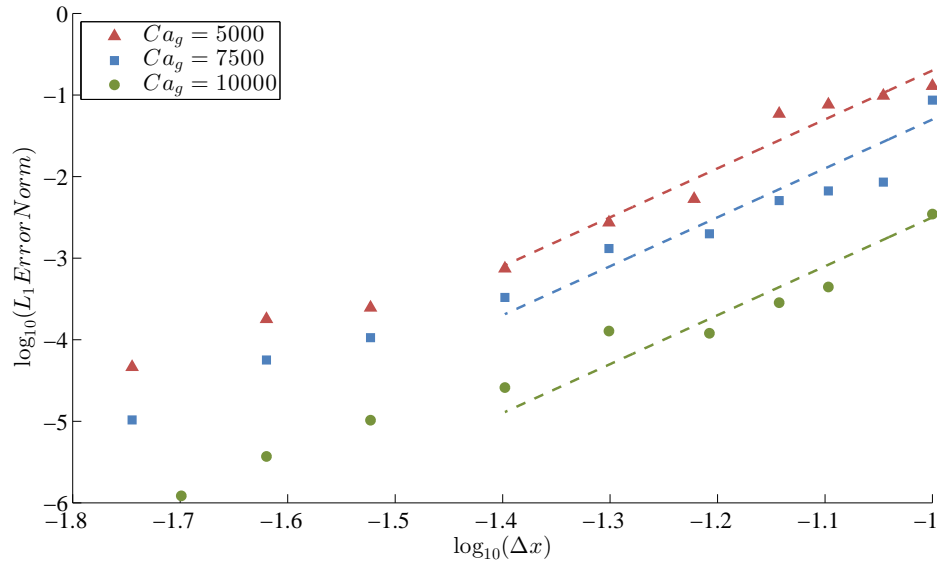


Figure 2.10: Mesh independence study, showing the effect of mesh resolution on the  $L_1$  error norm between the numerical solution and a mesh independent (pseudo analytical) case. Dashed lines show 6<sup>th</sup> order convergence.

the solution interface) were reconstructed at the same location on the pseudo analytical case, and then the radial extents of the nodes compared.

Spatially, the solution seen in Figure 2.10 converges very quickly; for large  $\Delta x$  roughly 6<sup>th</sup> order is observed. This accounts for the mesh independence in Figure 2.9 whereby doubling the number of elements has produced a mesh independent solution. This excellent spatial convergence means that relatively few elements can be used to begin the simulation, with very high accuracies being achieved.

Temporally the solutions converge linearly, as expected from the forward Euler time stepping scheme. Higher order time integration schemes were considered, such as the midpoint and Runge-Kutta methods, however, the spatial resolution was found to be much more of a limiting factor in the overall solution accuracy than the temporal resolution. The Darcy flow model is quasi-static, meaning that the velocity does not vary significantly between time steps. A relatively low temporal resolution could therefore be used without affecting the solution quality, and hence much greater attention was paid to the spatial resolution; in which a small change in the number of elements could create a large difference in the interface position.

The small gain in accuracy from the higher order integration schemes was deemed

unnecessary when considering the extra computation required to sub-divide the time steps and calculate the weighted average of the resulting interfacial velocities to calculate the subsequent interface position.

Through the numerical testing and convergence analysis above, the spatial and temporal resolutions of the scheme can be quantified, and practical limits put in place for subsequent runs. These limits are both to avoid the numerical instability at low capillary numbers, and ensure an accurate solution at high capillary numbers. For the cases in this chapter (and as a general rule of thumb for the rest of boundary element simulations) a spatial resolution of  $\Delta x \approx 0.03$  and temporal resolution of  $\Delta t = 0.02$  is sufficient to achieve a mesh and time step independent solution when  $Ca_g = 4000$ . For different values of capillary number, the spatial and temporal resolutions can be changed proportionally from these values, in order that a spatially and temporally independent solution is achieved.

When testing the very high capillary number regimes, and those involving bubble break-off in the following sections, several runs were performed at varying discretisations to ensure that the results were independent of mesh and time step discretisation. This involved testing up to a 4 four-fold increase in the number of elements and time steps (with simulation times changing from several hours to a week), to ensure a fully accurate solution had been obtained.

As well as mesh and time step analysis above, the number of Gaussian quadrature points were varied to check the integration accuracy. The same number of quadrature points are used for each element, even though significantly less could be used on elements far away from the collocation point. This is done in order to maintain simplicity within the numerical program. It was found that once  $N_g \geq 8$ , the integration accuracy was invariant to increases in the number of Gaussian points. For this reason,  $N_g = 10$  integration points are used for the simulations in this work.

At points in the simulation where elements grow very close to each, such as breaking and coalescing events, the number of integration points is increased. If the distance between nodal points  $r$  is  $0.25r_d \leq r \leq 0.5r_d$ , where  $r_d$  is the element arc length, then the number of integration points is increased to 50 on the corresponding elements. If the distance gets closer, 100 integration points will be used when  $0.1r_d \leq r < 0.25r_d$ . Below

$r < 0.1r_d$ , the interface points have effectively coincided, and the interface should either coalesce or break, discussed in more detail in the long time scale evolution section.

## 2.5 Mobility ratio effects

This work is motivated by  $CO_2$  injection and storage during carbon sequestration, in which the injection is performed supercritically, with the mobility ratio between supercritical  $CO_2$  and brine of the order 10-30 [10].

The finite mobility ratio model developed in this chapter allows the efficient solution of low mobility ratio flows, and can be used to characterise the transition through a range of mobility ratios. Several finite mobility ratios are presented in Figure 2.11, in which the capillary number is 4000. With the mobility ratio as  $\beta = 1$ , the initially perturbed solution stabilises after around  $t = 20$  and expands to form a stable circle as there is no critical length scale for which bifurcation will occur due to there being no difference in viscosities. At all mobility ratios above 1, the interface eventually evolves to form a complex viscous fingering pattern, with higher mobility ratios promoting the onset of viscous fingering.

With a relatively low mobility ratio, such as the  $\beta = 10$  case, the bases of the fingers continue to advance with time. However, once the mobility is taken higher, the finger base evolution slows as the base position approaches a near constant radius. During the  $\beta = 1000$  case, the finger bases effectively become stagnation points, where the interface velocity at the base drops to near zero. This characteristic is a well known feature of high mobility ratio displacement, causing highly convoluted surfaces and a much lower swept volume of the higher viscosity fluid. A consequence of the slowed base evolution and quickly growing primary fingers is that competing fingers' growth is hindered by the larger primary fingers and shielding occurs [1].

However, in the low mobility ratio regime, the growing finger bases allow secondary growing fingers to be fed by fluid, meaning that they can possess significant velocity. Shielding between competing fingers is inhibited as the fluid flow is not forced from the secondary finger into the primary finger, meaning much greater interaction and non-linear dynamics are seen between growing fingers.

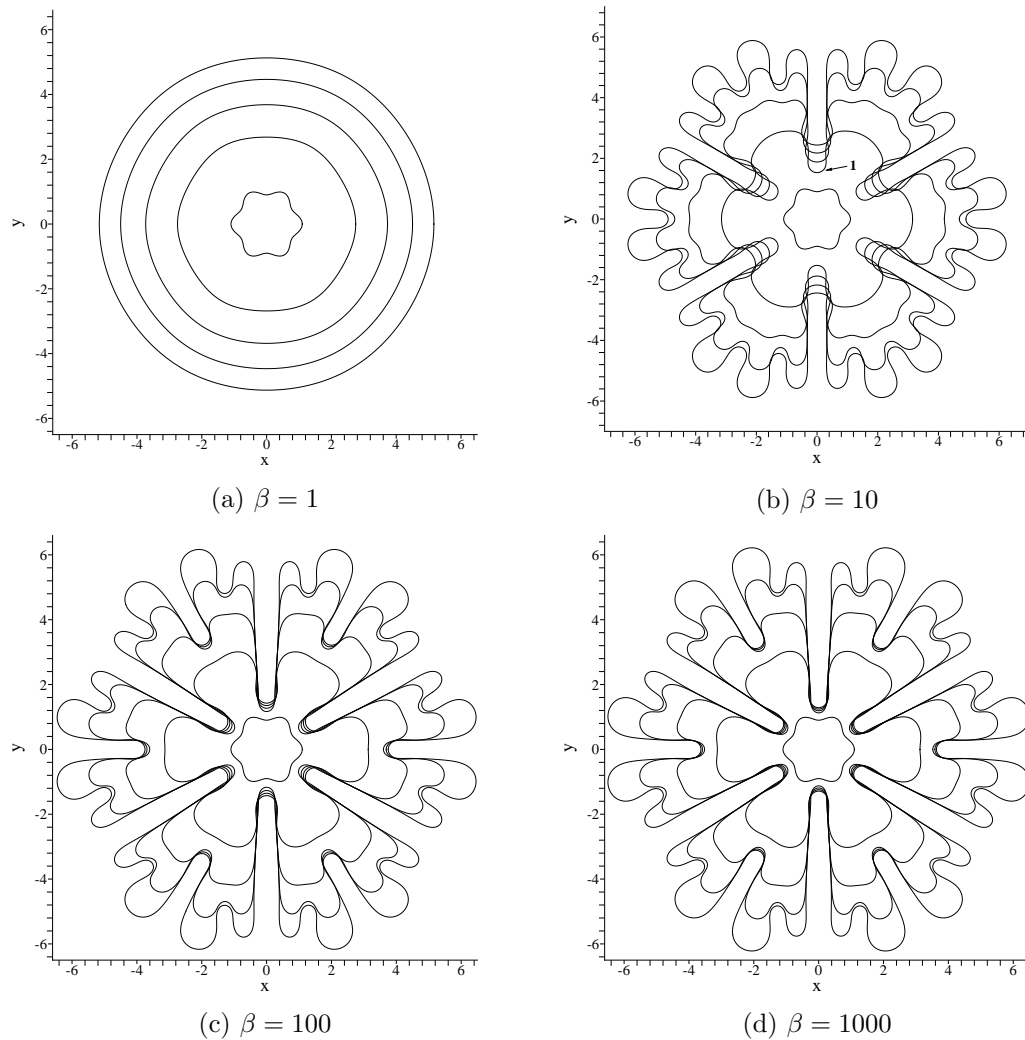


Figure 2.11: Interface evolution plots showing the effect of varying the mobility ratio,  $\beta$ . Each sub-plot shows the interface every  $\Delta t = 20$  from  $t = 0 - 80$ . Location 1 shows the finger base used for the velocity field analysis in Figure 2.13.

By explicitly tracking the base position of the fingers for varying mobility ratio runs, the radial extent of the finger bases can be seen to reach an almost constant value for high mobility cases in Figure 2.12. The lower mobility ratio cases show a much greater evolution of the base position once the profile of the interface has developed. This evolution continues until the non-linear regime, where the fingers interact significantly with each other affecting the base position.

To further emphasise the difference between the base profiles and the velocity of the fluid at the base regions, a velocity field can be generated at grid points throughout the domain. Utilising Green's formulae for the surface potential in the fluid domain (as opposed to at the fluid interface, equation (2.43)), the surface potential can be

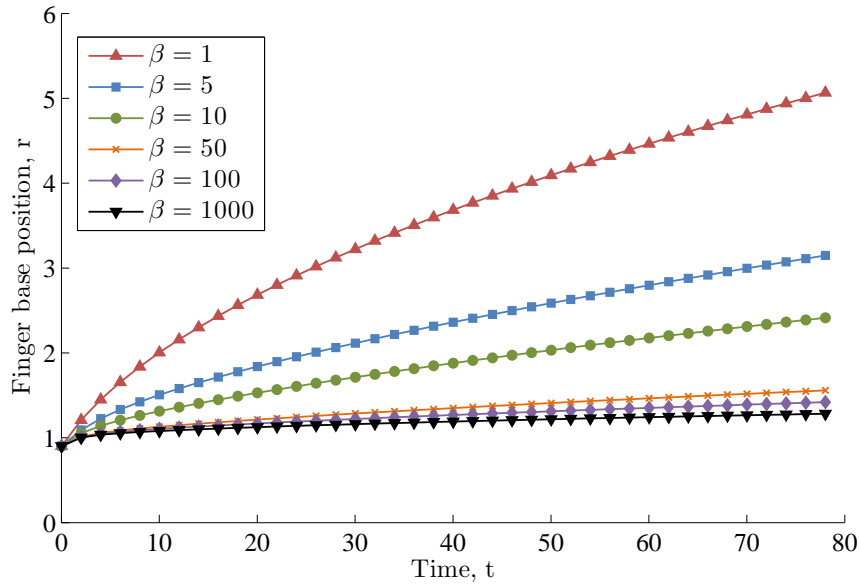


Figure 2.12: Evolution of the finger bases with time and varying mobility ratio.

reconstructed using the known interface values. Using equations (2.35), (2.36), (2.31) and (2.30) the velocity at any point in the interior or exterior domains can then be reconstructed, once the surface potential and flux is known at the interface.

Figure 2.13 shows the velocity field generated around the finger base at location 1 in Figure 2.11, for the  $\beta = 10$  and  $\beta = 1000$  mobility ratio cases. In both plots, there is significant velocity in the interior domain, with the fluid flowing preferentially around the finger base, due to the high surface tension and curvature at the bottom of the base. However, in the  $\beta = 1000$  case, the fluid velocity drops much more significantly in the exterior fluid close to the finger base, than in the  $\beta = 10$  case. The finger base in the higher mobility example has a higher curvature which makes it harder for the fluid to displace the surface, and as such the velocity drops to near zero in the exterior fluid. This explains the near stagnation of the finger bases found in the high mobility ratio examples in Figures 2.11 and 2.12.

In Figure 2.13, the velocity of the inner fluid just inside the finger base has been labelled, along with the  $x, y$  position of the vector. The velocity is approximately 7 times less in the  $\beta = 1000$  case than the  $\beta = 10$  case. It can also be seen that the velocity vectors immediately adjacent (left and right) to the base velocity are much larger in the  $\beta = 1000$ , and in a tangential direction to the base profile, showing the preferential movement of the fluid around the base in higher mobility ratio flows. The velocity

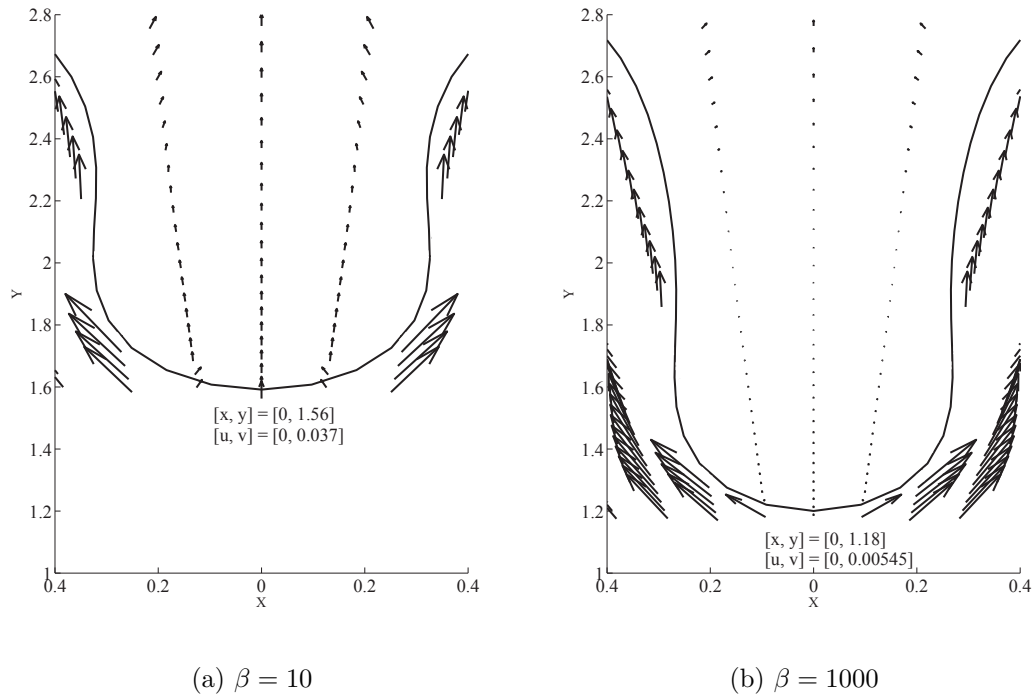


Figure 2.13: Fluid velocity vector  $\vec{u}$  plots at the base of a finger in the  $\beta = 10$  and  $\beta = 1000$  cases in Figure 2.11 at  $t = 20$ .

vectors close to the finger base in the low mobility regime have a large component in the normal direction, which gives rise to the movement of the base.

The significant velocity possessed by the finger base and the exterior fluid close to it in Figure 2.13(a) causes the finger base to displace and not stagnate near the starting profile. This velocity explains the greater finger interaction between competing fingers in the low mobility ratio regime, and finger breaking/coalescing mechanisms, that will be discussed in section 2.7.

## 2.6 Capillary number effects

As a consequence of the  $N_b^2$  scaling of the convergent series numerical method, high capillary number cases can be accurately resolved using many elements. High injection rates typically found in  $CO_2$  sequestration processes give rise to large capillary numbers that promote finger instability. In section 2.4.6, large capillary numbers were found to create highly unstable interfaces between the fluids, requiring many elements to accurately solve.

Several high capillary number flows are shown in Figure 2.14 with a mobility ratio of 10. The number of fingers created on the first bifurcation increases from two to six through the range of capillary numbers due to a decrease in critical length at which bifurcation occurs. The dimensional critical length scale of bifurcation of a finger growing into a parallel flow is given by [57]:

$$L_c = \pi b \sqrt{\frac{\gamma}{\mu U_n}} \quad (2.74)$$

Where,  $U_n$  represents the normal interface velocity. The critical length scale was originally obtained in the linear stability of [24], and represents the most unstable wavelength, i.e., the lengthscale which must be overcome by a ‘flat’ front perpendicular to the flow for a bifurcation to occur. The term bifurcation refers to the point at which the interface curvature changes in sign.

Observations confirm that generally the number of fingers at the first bifurcation increase with capillary number, although there are several different modes of bifurcation that can occur. This means that bifurcations such as side branching can occur in preference to generating more primary fingers at several values of capillary number, as can be seen in Figure 2.14.

An important point about the position of the profiles shown in Figures 2.14(a) to 2.14(f) is that the base positions show almost exactly the same radial evolution with time, but their fronts show vastly differing profiles. In Figure 2.15, the evolution of the base of the fingers is shown for varying capillary number where it can be seen that as the capillary number is increased, the base position starts to converge to the same value.

As the capillary number is increased, preferential movement of the inner fluid causes the finger fronts to exhibit vastly different profiles, while the base positions remain fairly constant. The convergence of the base position is due to the relatively large, smooth curvature of the finger base profile acting to stabilise the flow. As the driving force of the fluid increases with capillary number, the lower curvature finger front becomes more likely to destabilise and the flow is forced to this region in preference to the finger base, leaving it unaffected.

It should be noted, that for the late stage displacements in highly ramified cases, as seen in Figure 2.14(f) (and Figure 2.20 in the next section), many boundary elements have

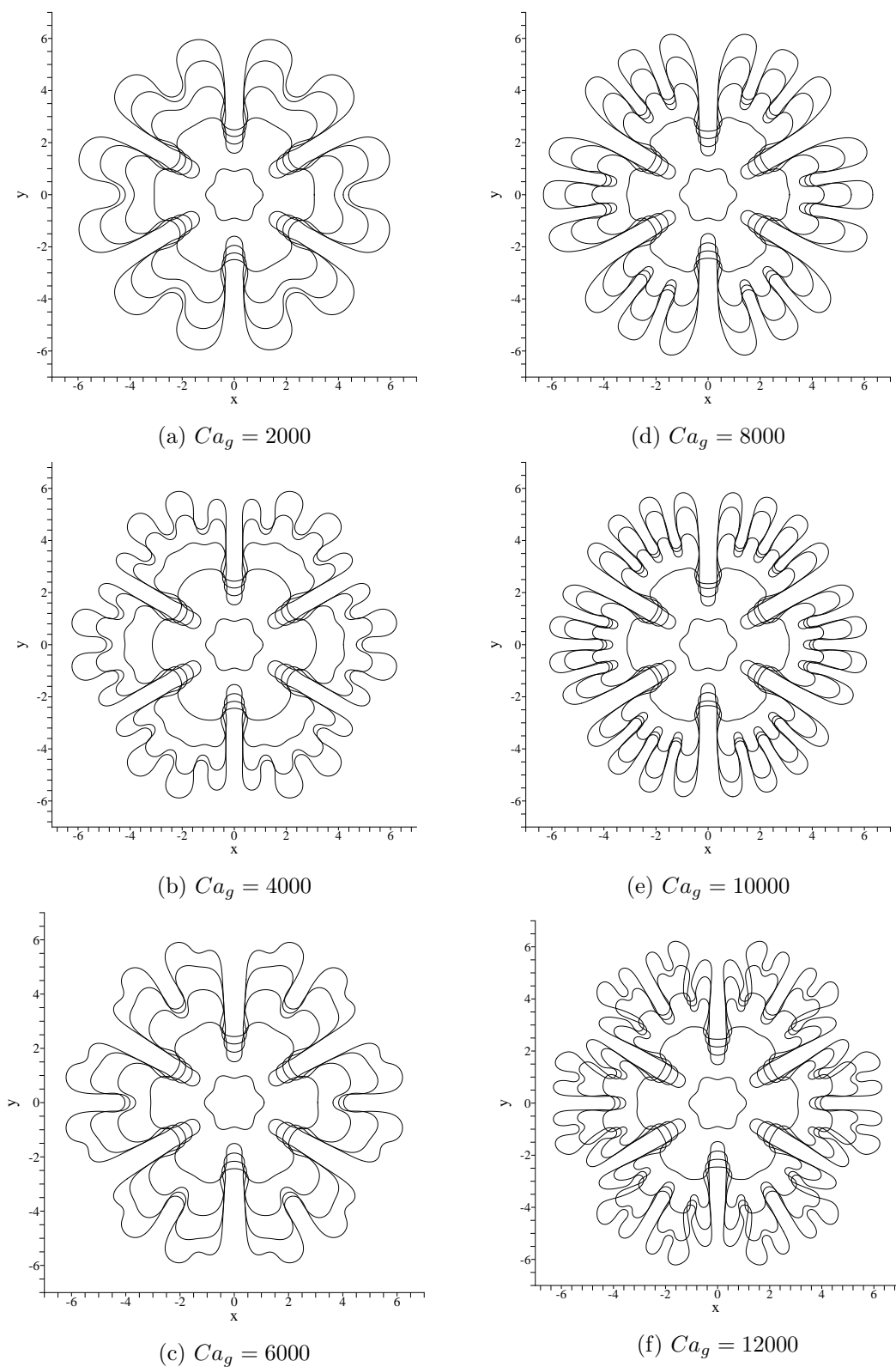


Figure 2.14: Interfacial evolution plots showing the effect of varying capillary number. Each sub-plot shows the interface every  $\Delta t = 20$  from  $t = 0 - 80$ .

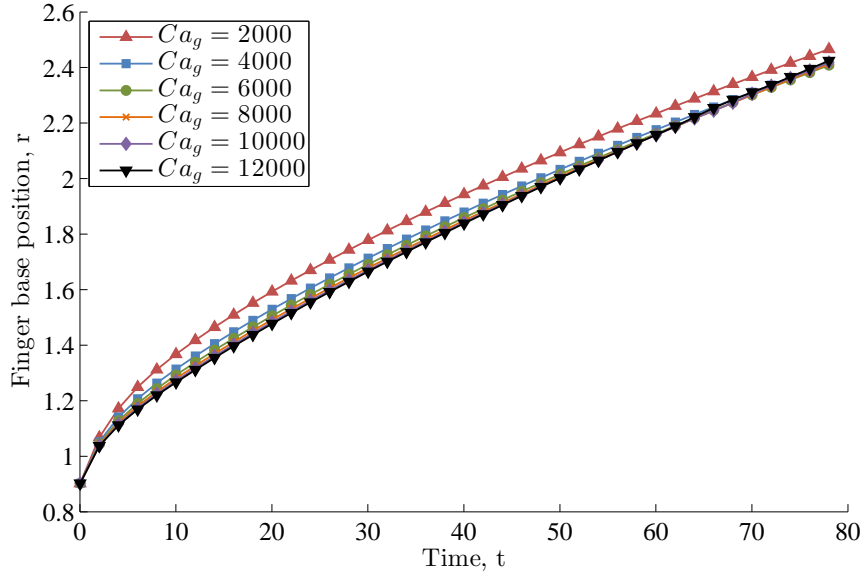


Figure 2.15: Position of the finger base with time and varying capillary number

to be used. For  $t > 70$ , this is generally in the range  $4000 < N_b < 6000$  depending on the capillary number of the flow. The simulation time for these runs on an Intel Core i3-4130 CPU, with 8GB RAM takes several hours ( $< 10$ ).

The different finger front profiles in the two cases presented in Figure 2.14 are caused by the critical length of bifurcation being smaller for the higher capillary number case. At the point of the first bifurcation, there are more ‘flat’ sections of the finger larger than the critical length and hence more fingers are able to form.

Once the front velocity  $U_n$  reaches a low enough speed and there is a flat section in the interface that exceeds the critical length scale, the front starts to destabilise and bifurcate. The exact point of bifurcation is difficult to identify, due to the small length scale at which bifurcation initiates. Therefore, a dimensionless parameter,  $W(\theta)$  can be used to provide a robust measure of the point at which the first bifurcation occurs in radial Hele-Shaw flow [57]. This parameter defines when bifurcation occurs based on the interior angle occupied by the finger  $\theta_r$ , the radial extent of the finger  $r$ , and the critical length of bifurcation  $L_c$ . These parameters are shown in Figure 2.16, at the first bifurcation of a radial viscous finger.

$$W(\theta) = \frac{\theta_r r}{L_c} \quad (2.75)$$

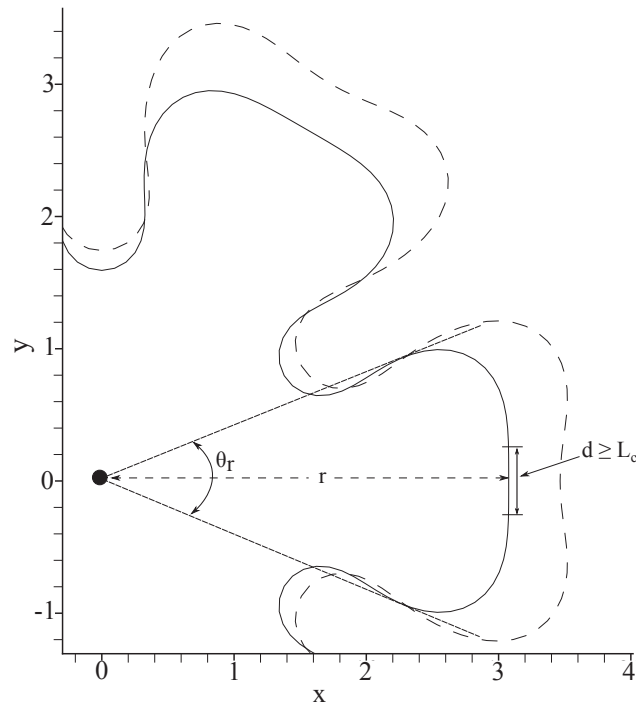


Figure 2.16: Initial bifurcation of two viscous fingers, showing critical length scales. Dashed line shows the interface position  $\Delta t = 20$  after the solid line interface.

The value of  $W(\theta)$  at which bifurcation occurs shows much less variance than the critical length scale, hence, if the time at which bifurcation first occurs is misjudged slightly, the value of  $W(\theta)$  changes by only a fraction of a percent.

By performing similar tests to [57] at varying capillary numbers, the first point of bifurcation may be measured. In the results of [57], the front velocity was kept constant unlike the simulations run here that have a constant volume flux injection and hence decreasing front speed with increasing radial distance from the source. Also, [57] used a wedge shaped cell with only one finger, compared to the fully circular cell with multiple fingers used here.

In Figure 2.17 the value of  $W(\theta)$  increases with increasing capillary number, as expected due to the critical length scale decreasing. However the mobility ratio does not alter the value of  $W(\theta)$  at which bifurcation occurs. In [57] the value of  $W(\theta)$  is constant for all capillary numbers, however by having a non-constant front velocity, this value is able to change with capillary number. In Figure 2.17 the bifurcation value of  $W(\theta)$  follows an

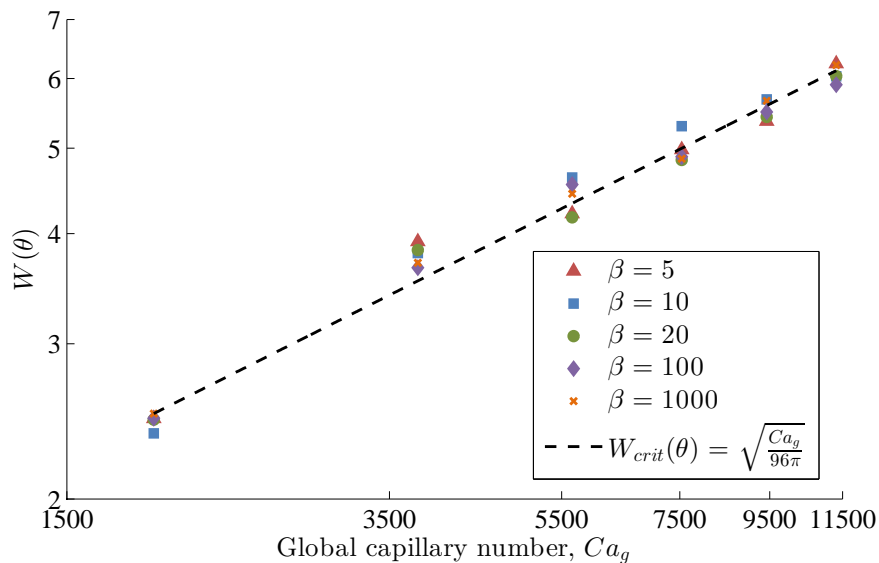


Figure 2.17: Variance of  $W(\theta)$  with capillary number and mobility ratio.

explicit trend given by:

$$W_{crit}(\theta) = \sqrt{\frac{Ca_g}{96\pi}} \quad (2.76)$$

At any point in the simulation, if the front velocity and internal angle of the finger is great enough to cause  $W(\theta)$  to be above the critical value defined in equation (2.76), bifurcation will occur. This expression holds for all capillary numbers up until the first bifurcation, after which the fingers can grow non-linearly and interact significantly with each other.  $W(\theta)$  does not predict the type of bifurcation that will occur, only the point at which a bifurcation will occur. Whether the front splits into 2 fingers or 5 fingers is determined by the critical length scale at that point in time and the number of flat sections running perpendicular to the flow that are longer than this length scale.

## 2.7 Long time scale evolution

The work presented in this thesis is motivated by the need to investigate low mobility ratio, high capillary number flows that occur in supercritical  $CO_2$  sequestration in deep subsurface aquifers. While the current model cannot predict the full complexity of the  $CO_2$  plume evolution in the injected porous media aquifer, it can provide qualitative understanding of the mechanisms and plume growth that can occur due to the low

Property	Value (SI Units)
Gaseous injection depth	100m
Supercritical injection depth	1000m
$T_{CO_2(sc)}$	50 °C
$T_{CO_2(g)}$	25 °C
$P_{CO_2(sc)}$	20 MPa
$P_{CO_2(g)}$	1 MPa
NaCl concentration in brine	0.5 mol/kg
$\mu_{Brine}$	$7.60 \times 10^{-4}$ Pa.s
$\mu_{CO_2(sc)}$	$7.00 \times 10^{-5}$ Pa.s
$\mu_{CO_2(g)}$	$1.52 \times 10^{-5}$ Pa.s
$M_{Brine}$	$0.1827 \times 10^{-6}$ m <sup>3</sup> .s/kg
$M_{CO_2(sc)}$	$1.9834 \times 10^{-6}$ m <sup>3</sup> .s/kg
$M_{CO_2(g)}$	$9.1342 \times 10^{-6}$ m <sup>3</sup> .s/kg
$\beta_{CO_2(sc) - brine}$	10.86
$\beta_{CO_2(g) - brine}$	50
$\beta$ Infinite mobility ratio model	$\infty$
Intrinsic permeability, k	$1.4 \times 10^{-10}$ m <sup>2</sup>
$\gamma$	$0.03$ kg/s <sup>2</sup>
$Ca_g$	4561

Table 2.2: Injection Properties of gaseous and supercritical  $CO_2$ 

mobility ratio, high capillary number flow regime, using the assumption of a perfectly sharp interface between the  $CO_2$  and brine.

To understand the long term mechanisms that occur during low mobility ratio flows, long time evolutions of the interface are presented in this section, in order to see the effect of finger interaction when shielding is inhibited. [44] and [58] show that mechanisms such as finger coalescing and finger break-off could be observed under certain flow regimes. In reaction models and diffuse-interface models, similar mechanisms have also been observed [42, 50, 59]. However with truly immiscible models with sharp fronts, these mechanisms have not been explored, due to most former models concentrating on cases of high mobility ratio (generally using very viscous displaced fluids) where shielding inhibits break-off and coalescing [35, 37]. These mechanisms will be explored by studying long term interface growth using realistic injection parameters.

Presented in Figures 2.18 - 2.22 are long time evolutions of three different injection scenarios using fluid parameters defined for supercritical  $CO_2$ , gaseous  $CO_2$  injection and an infinite mobility ratio brine displacement. All simulations use brine as the displaced fluid, with a suitable deep aquifer salinity, and only differ by the mobility of the injecting

fluid. Table 2.2 shows the fluid properties for the test cases, with supercritical  $CO_2$  properties calculated using [60]. The brine salinity, viscosity and surface tension were calculated using standard chemical data tables, under deep subsurface aquifer ambient conditions [61, 62].

To investigate the complex interfacial dynamics and non-linear growth that could occur in an injection, asymmetry can be introduced into the starting perturbed interface. By including different wavelengths of perturbation along the interface, multiple length scales are produced, mimicking that which would be found in reality due to random noise and disturbance. The initial displacement of the interface is given by the asymmetric condition below.

$$r = 1 + \epsilon_0 \cos \left( 6\sqrt{\frac{\theta^3}{2\pi}} \right) \quad (2.77)$$

Equation (2.77) allows different wavelengths of perturbation to be produced along the interface in a controlled manner, in contrast to using a randomly generated noise function. By utilising the asymmetric condition, the effect of different wavelengths of perturbation can be analysed in a reproducible manner, allowing the specific effects of the low mobility ratio environment to be studied accurately. In equation (2.77)  $\epsilon_0 = 0.1$ .

Similar to porous media, the flow in a Hele-Shaw cell has an intrinsic permeability, given by the ratio  $b^2/12$ . In table 2.2, the intrinsic permeability of the Hele-Shaw cell configuration being used corresponds to that of oil reservoir/fractured rock in porous media flow [63]. The three simulations utilising the injection parameters outlined in table 2.2 can be seen in Figures 2.18, 2.19 and 2.20, with dotted lines showing the initial interface perturbation.

In Figures 2.18, 2.19 and 2.20, differences in interface patterns can be seen, due to the different mobility ratios in each simulation. The infinite mobility ratio and gaseous injection cases share several similarities, most prominently the near stagnant finger bases that have not moved significantly from their starting positions. This is a common feature of infinite mobility ratio models, and due to the relatively high mobility ratio of the gaseous injection, the finger bases show considerable likeness. This is further emphasised by Figure 2.21, where the base position of the finger at location 1 in Figure 2.18 has been tracked with time for the three different injection scenarios. For the infinite mobility ratio case, the base can be seen to move very little once the initial profile has

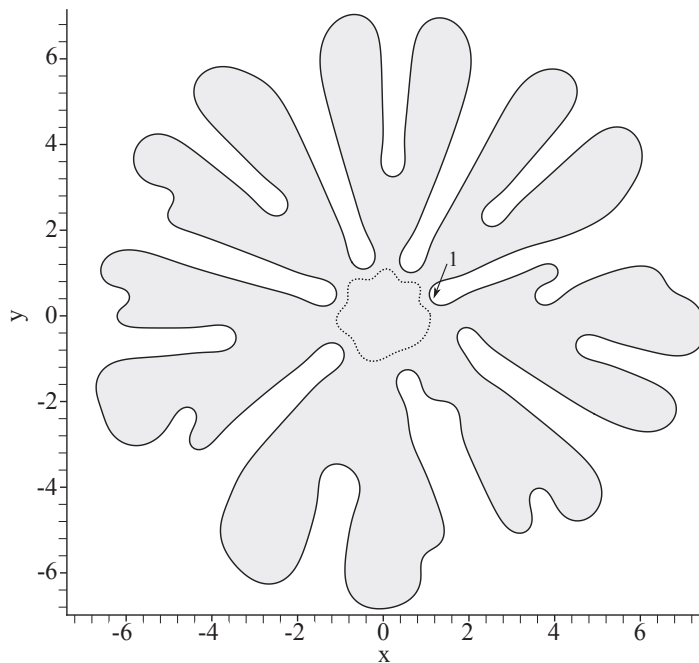


Figure 2.18: Interface plot of the asymmetric, infinite mobility ratio injection at  $t = 90$ ,  $\beta = \infty$ . 1 shows base tracking location in Figure 2.21.

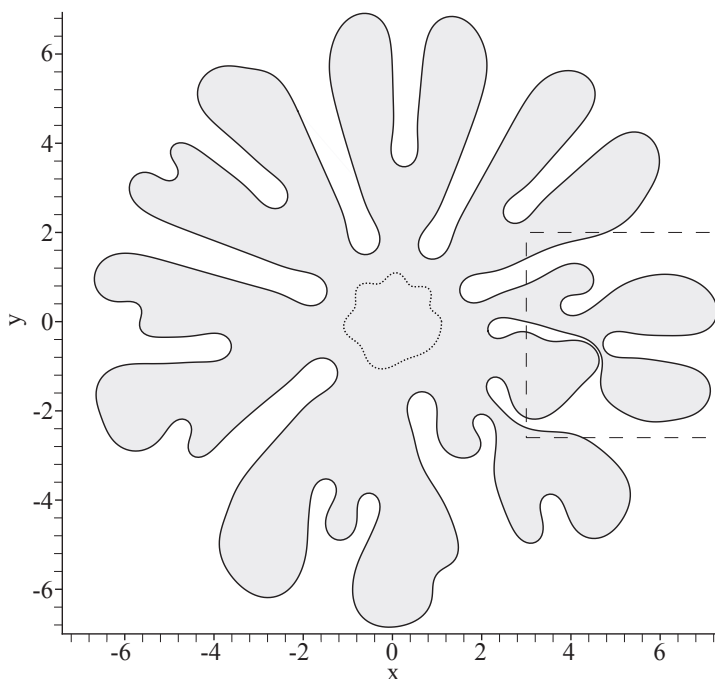


Figure 2.19: Interface plot of the asymmetric gaseous  $CO_2$  injection at  $t = 90$ ,  $\beta = 50$ . Dashed box shows zoomed area for subfigures (a) - (c) in Figure 2.22.

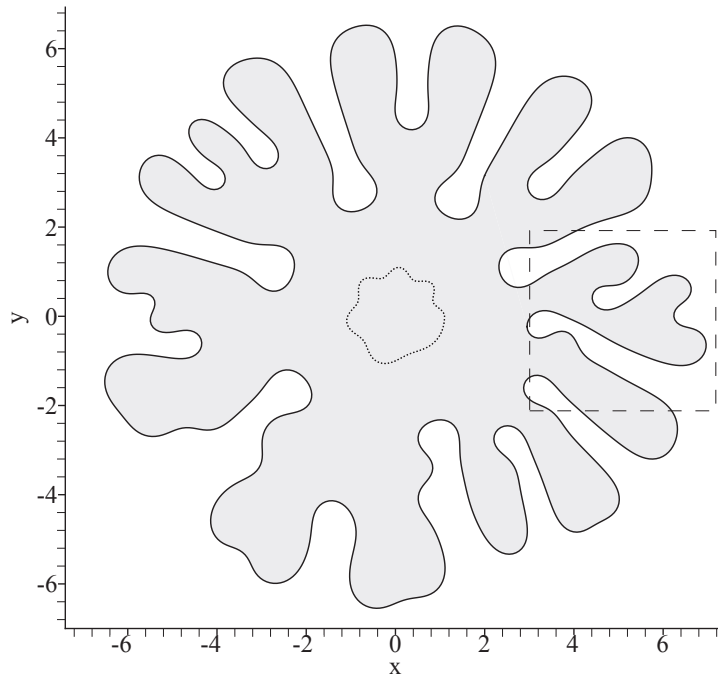


Figure 2.20: Interface plot of the asymmetric supercritical  $CO_2$  injection at  $t = 90$ ,  $\beta = 10.86$ . Dashed box shows zoomed area for subfigures (d) - (f) in Figure 2.22.

been set up, however, both the  $CO_2(g)$  and  $CO_2(sc)$  injection cases show considerable base movement.

At the moderate mobility ratio of 50, the gaseous injection can be seen to exhibit significant finger interaction in Figure 2.19. The finger shielding effect present in the infinite mobility ratio case has not occurred as significantly in the gaseous injection case and the fingers shown in the dashed box in Figure 2.19 are moving into each other. At the moderate mobility ratio of gaseous  $CO_2$  injection, the inner fluid still possesses some velocity, and hence shielding is inhibited. It is therefore inadequate to use an infinite mobility ratio model for gaseous  $CO_2$  injection into brine, with infinite mobility ratio models only being applicable for cases of mobility ratio of 100 or more, common in gas-oil displacements.

The supercritical  $CO_2$  injection case shown in Figure 2.20 shows less shielding than the gaseous injection case. The smallest wavelength fingers on the right of the domain have a large interaction with each other, with severe base thinning occurring at two different locations. Due to the relatively large capillary number, the critical length scale is small, allowing side branching to form on some of the larger fingers. More fingers have been

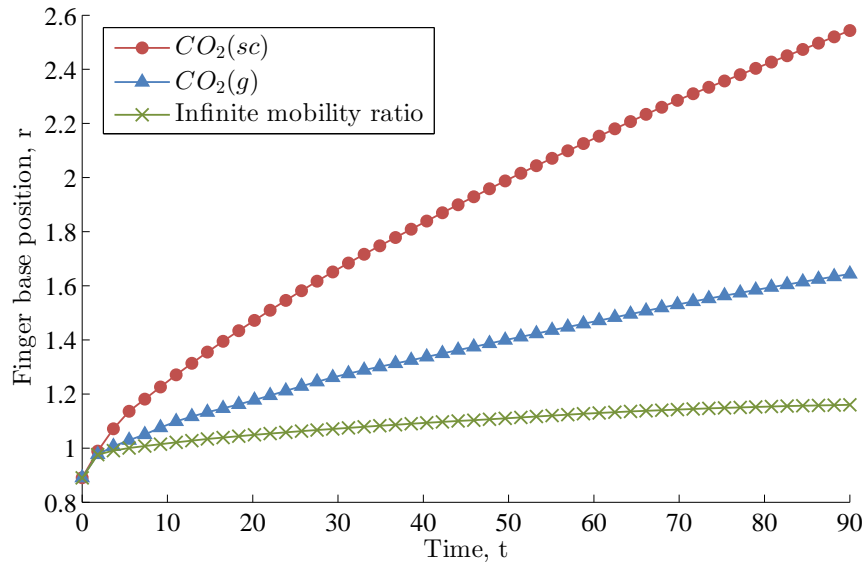


Figure 2.21: Evolution of finger bases (at location 1 in Figure 2.18) for infinite mobility ratio ( $\beta = \infty$ ), gaseous ( $\beta = 50$ ) and supercritical ( $\beta = 10.86$ )  $CO_2$  injection.

allowed to develop, unhindered by the growth of larger fingers, resulting in a larger number of fingers present in the domain.

In both the gaseous and supercritical  $CO_2$  injection cases, competing fingers can grow very close to each other, creating a small immiscible lubrication layer between them. This kind of interaction needs to be monitored closely to study what happens when the fingers are separated by a very small distance. There are two possible outcomes when the fingers grow very close to each other, either the two fingers merge together creating one finger and the inclusion of a brine bubble, or one finger causes the base of the other to thin to such an extent that the finger breaks off.

### 2.7.1 Coalescence and breaking

A rudimentary breaking algorithm was developed that detects the separation between adjacent sections in the viscous fingers. These sections can be external (i.e two fingers are travelling into each other) or internal (i.e the finger's base is thinning). By constructing local B-spline curves, the separation can be analysed efficiently to see whether fingers are likely to collide and coalesce, or if a finger's base is thinning and the finger will break off. The algorithm then pinches off fingers that have a sufficiently thin base, or merges fingers that are sufficiently close to each other, forming new B-spline curves

around each of the disconnected domains. The integral equation formulation allows easy extension of surface integrals over the new disconnected bubbles. As discussed in the previous section, for nodal points that displace very close to each other, the number of integration points is increased from 10 – 100 over the affected elements, to evaluate the near-hypersingular integrands.

The specific time that the interfaces are captured in Figures 2.18, 2.19 and 2.20 allows the interaction between fingers to be seen and the difference in mobility ratio assessed. After this time, the interaction between fingers in the finite mobility ratio cases becomes highly complex, in particular from fingers that have evolved from the small wavelength perturbations, shown in the dashed boxes. To analyse this interaction and the effect of the lubrication layer between the competing fingers, zoomed in plots of several events have been shown in Figure 2.22.

Figure 2.22 shows the breaking mechanism of two events in the gaseous and supercritical  $CO_2$  injection cases. These occur at different stages in the overall interface evolution due to the difference in finger shielding between the cases. In the gaseous injection, there is still significant finger shielding present, which has caused the finger growing into the base of the primary finger in Figure 2.22(a) to be hindered in its early growth, meaning it did not develop into a primary finger advancing at the forefront of the evolution. However, as it still possesses some velocity, the finger has continued to grow, and eventually thins the base of the primary finger causing it to break off, seen in Figure 2.22(b). This breaking is a combined effect of shielding and the velocity of the inner fluid. If the mobility ratio were pushed much higher, the shielding would have been more significant and the finger would have been almost completely hindered in its early growth and would never have grown to any scale to affect the primary finger.

After the primary finger has broken off in Figure 2.22(c), the secondary finger grows towards it. The breaking of the fingers occurs in a ‘snapping’ reaction, whereby the fingers break back from each other very rapidly. As the secondary finger is still being fed by the inner fluid, it continues to grow with a significant rate, which is faster than the detached finger. However, a small immiscible lubrication layer of the resident brine separates the two, which is maintained throughout the subsequent evolution and prevents the two fingers from coalescing. The two fingers are immiscible with the brine, and as such cannot transfer mass across the interface and coalesce if this layer is maintained.

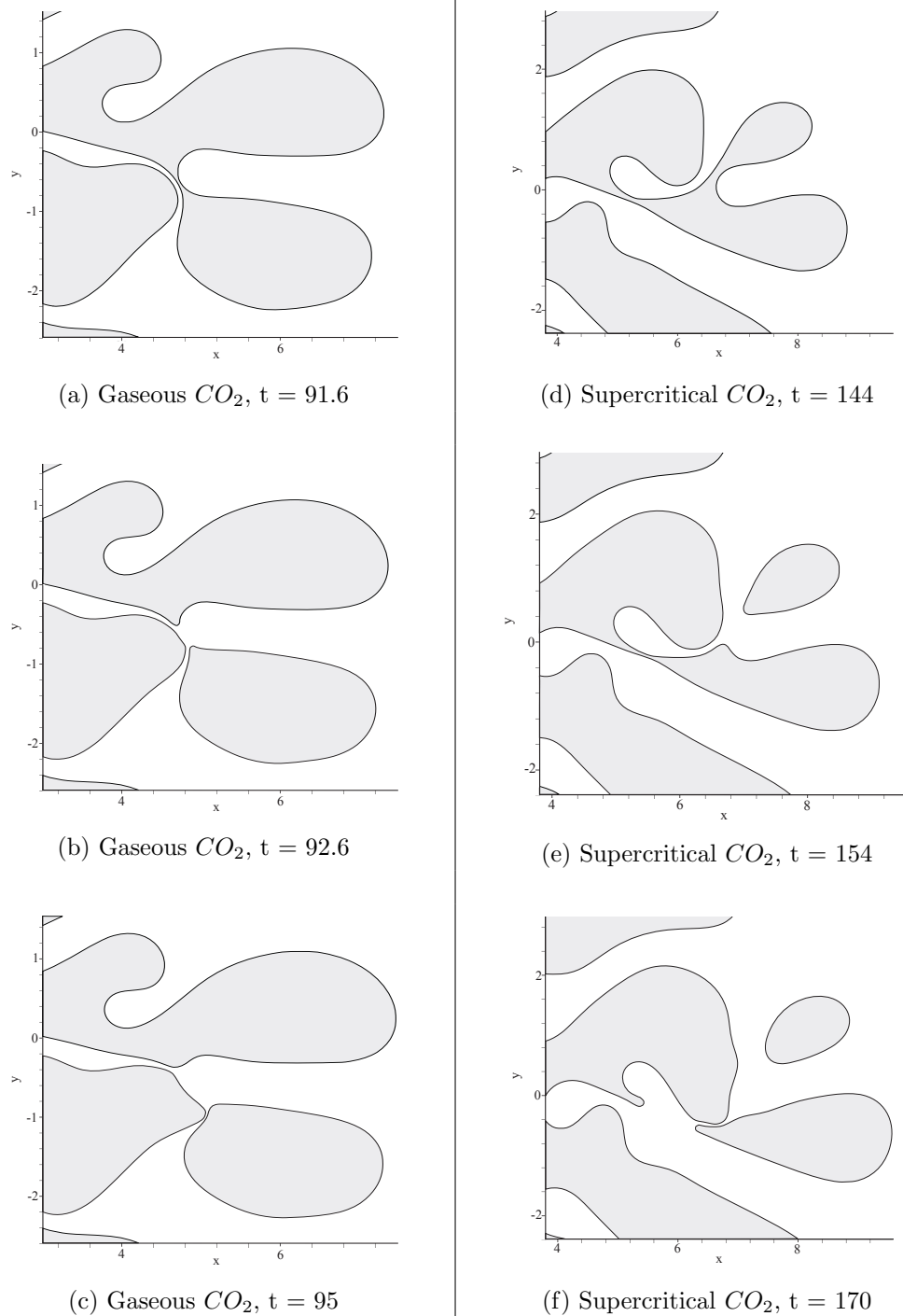


Figure 2.22: Zoomed in plots of finger break-off for the gaseous  $CO_2$  injection (left),  $\beta = 50$  and supercritical  $CO_2$  injection (right),  $\beta = 10.86$

The secondary finger continues to distort the detached bubble, which will eventually cause it to split. This mechanism is very difficult to capture, due to the very large amount of elements needed to maintain the lubrication layer.

A similar process occurs in the supercritical injection case shown in Figures 2.22(d) - 2.22(f), in which two fingers detach from the main injection plume. The first finger to detach is caused by the primary finger growing behind it, however the second finger break-off is due to a combination of thinning caused by fingers growing into the left and right side of it. After the second break-off, the finger that is still attached to the main plume acts to push the trailing edge of the detached bubble, which along with surface tension quickly forms it to a droplet shape. The attached finger left from the second break-off quickly recedes due to the very high curvature and re-stabilising effect of surface tension.

This kind of breaking has been reported before in [42] and [41], however using a diffuse interface model or volume tracking technique does not as accurately resolve the interface between the fluids, introducing a level of uncertainty about the exact position. As the interface is captured implicitly, the lubrication layer between advancing fingers cannot be as accurately defined, meaning that the preference of coalescing or breaking of fingers is unclear. The lubrication layer is vital in defining the movement of fingers in the sharp interface model and as such needs to be accurately resolved. With the current method, the lubrication layer between fingers can be maintained efficiently, allowing the breaking to be seen in much greater detail, with events being explicitly tracked.

In all simulations run, if a sufficiently high element density was used, finger break-off would always occur in preference to coalescence. Both mechanisms occur due to the same process of finger interaction and the inhibition of shielding, but as long as the immiscible lubrication layer between the two fluids is maintained, breaking will always occur in preference. The breaking algorithm will detach bubbles that have a neck width under a certain prescribed 'breaking distance'. If this breaking distance is decreased to a very small value much smaller than the element size, the point of separation occurs just before the two surfaces of the interface actually overlap in the next time step, indicating clearly that a break should have occurred.

Experimentally in [44], coalescing and breaking of fingers are reported for immiscible flows. Due to the large aspect ratio of the channel being used, there is considerable interaction between fingers, and breaking is found with air injection into resident silicone oil. The finger interaction is promoted by the aspect ratio rather than a low mobility ratio of the fluids, as is the case in the results presented here. Also, in [44] coalescing occurs between competing fingers under certain conditions after they initially broke. This is due to the fluids having some small amount of miscibility with each other, allowing the rapidly growing finger to coalesce with the bubble that had just detached.

Due to the microscopic scale of fluid interaction that occurs experimentally, and the fact that the fluids under consideration in [44] have a small level of miscibility with each other, there will be a very small miscible region between the fluids. If the fingers are moving with sufficient speed the fingers could overcome the miscible region separating the fingers, and coalesce. However, as there is no microscopic miscible layer in the sharp interface model presented here, coalescing cannot occur at the macroscopic scale. The sharp interface model assumes the displacement of the resident fluid occurs much faster than the miscible mixing of the fluids and that there is a discontinuity of properties over the fluid interface. The fluids are considered to be completely immiscible and therefore no coalescence should occur, as a lubrication layer should always separate the two fluids.

## 2.8 Conclusion

A BEM formulation for solving finite mobility ratio flows has been used to investigate radial viscous fingering mechanisms in a Hele-Shaw cell. The Hele-Shaw model was used to investigate the mechanisms and plume evolution associated with viscous fingering that could occur during  $CO_2$  injection and storage in deep porous media aquifers, during carbon sequestration.

The finite mobility ratio model allowed investigation into the effects that a low mobility ratio and high capillary number have on the plume evolution. When the mobility ratio of the two fluids is of order 10 - 50, the fingering characteristics are vastly different to those predicted by infinite mobility ratio models. Finger base movement was found to be independent of capillary number, but strongly dependent on mobility ratio, with the bases moving significantly away from their starting positions. The near stagnation

points on the bases of the fingers found in infinite mobility ratio flows were not found when using the finite mobility ratio model for low mobility ratio flows.

The validity and the numerical performance of the BEM was studied in detail, showing its applicability to finite mobility ratio flows. The quadratic scaling of the solution time shows large improvements over traditional matrix solvers and lifts the restriction of previous models on short time scale solutions. The numerical stability of the solution has been shown to rely heavily on the temporal and spacial discretisation, providing an upper limit for stability. Similarly, the physical instability of bifurcating fingers was analysed with an expression found to predict the point at which the first bifurcation of a finger will occur.

Long time interface evolutions were run to showcase the numerical method for predicting the large time scale dynamics of viscous fingering. Finger interaction was found to be much more significant than in infinite mobility ratio models, and on small wavelength perturbations could lead to base thinning and eventual finger breaking. After breaking, the detached bubbles would continue with the velocity of the surrounding fluid. The numerical method allowed the resolution of the immiscible lubrication layer between fingers meaning the finger breaking and coalescing mechanisms could be explored more explicitly than in previous models.

The results obtained in this chapter indicate that the low mobility ratio flows present during supercritical  $CO_2$  injection could significantly alter the storage capacity compared to gaseous  $CO_2$  injection. The base movement is much more prominent, meaning the overall surface area is less for supercritical injections, which would lead to less storage through dissolution. The amount of  $CO_2$  structurally trapped for the gaseous and supercritical cases would be equal, but dissolution trapping would be increased in the gaseous case through increased surface area. The bubble break off mechanisms found under low mobility ratio regimes in a supercritical injection would be beneficial from a  $CO_2$  injection standpoint, since the detached bubbles would slowly dissolve in the surrounding brine and increase the total amount of trapped  $CO_2$ .

## 3. Dynamic wetting effects

### Summary

In this chapter the effects of dynamic wetting on the immiscible displacement of a high viscosity fluid subject to the radial injection of a less viscous fluid in a Hele-Shaw cell are studied. The displaced fluid in a Hele-Shaw cell can leave behind a trailing film that coats the cell walls, dynamically affecting the pressure drop at the fluid interface. By considering the non-linear pressure drop in the direct boundary element formulation, a Picard scheme is implemented to iteratively predict the interfacial velocity and subsequent displacement in finite mobility ratio flow regimes.

Dynamic wetting is found to delay the onset of finger bifurcation in the late stages of interfacial growth, and at high local capillary numbers can alter the fundamental mode of bifurcation, producing vastly different finger morphologies. In low mobility ratio regimes, finger interaction is reduced and characteristic finger breaking mechanisms are delayed but never fully inhibited. In high mobility ratio regimes, finger shielding is reduced when dynamic wetting is present. Finger bifurcation is delayed which allows the primary fingers to advance further into the domain before secondary fingers are generated, reducing the level of competition.

### 3.1 Introduction

During immiscible displacement in porous media, the flow regime depends greatly on the capillary number at the interface between the fluids, describing the ratio of viscous driving forces to capillary forces [6]. As well as the capillary number, the wetting conditions of the fluids in the porous media play a crucial role in defining the capillary

pressure at the interface between the fluids and the resulting interfacial displacement [30, 64]. The contact angle of the displaced fluid with respect to the porous media affects the viscous finger width, which is comparable to the pore size if the displaced fluids wets the medium [65]. The displaced fluid can also leave behind a trailing film of finite thickness that wets the porous medium, resulting in the capillary pressure having a non-linear dependence on the interfacial velocity in a process known as dynamic wetting [30].

To provide analysis of the  $CO_2$  injection process and explore the dynamic wetting effects above, a detailed study of the wetting layer effects and flow in a Hele-Shaw cell are presented in this chapter. By considering fluid properties that are directly analogous to those found in supercritical  $CO_2$  injection, and cell geometry that mimics the continuum length scales in a typical subsurface aquifer, dynamic wetting effects can be explored in the context of immiscible viscous fingering.

At the interface between the fluids in a potential flow Hele-Shaw model, two boundary conditions must be met; the capillary pressure jump and the continuity of normal interface velocity. In the previous chapter, and classically in many viscous fingering works, the capillary pressure jump is given by Young-Laplace theory, which describes the pressure jump as the sum of the in-plane curvature and the curvature of the fluid meniscus, multiplied by the surface tension. By assuming that the displaced fluid is perfectly wetting, the meniscus curvature is proportional to  $2/b$ , where  $b$  is the plate spacing. While this boundary condition has been used by many authors and proved successful in matching theory with experiment in the limit of low capillary number flows, in the case of higher capillary number flows the condition must be modified to take into account non-linear wetting terms [45].

A non-linear term appears in the pressure jump condition due to the trailing film left behind by the displaced fluid (see Figure 3.1). In the pioneering experimental work by Fairbrother and Stubbs in 1935 for air displacing water in circular capillary tubes, they observed a wetting water film with thickness of the order of  $Ca_l^{1/2}$  in the range  $7.5 \times 10^{-5} < Ca_l < 0.014$  [66]. Here,  $Ca_l$  is defined as the local capillary number given by  $Ca_l = \mu_2 U_n / \gamma$ . Bretherton (1961) studied two phase flow displacement in a two dimensional channel by using a patching analytical approach between the Stokes flow describing the displaced fluid and a lubrication approximation of the thin film left behind

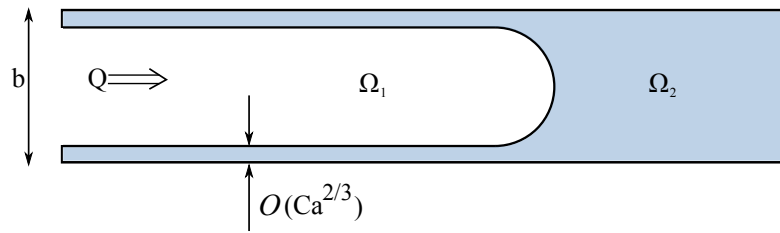


Figure 3.1: Side view of the Hele-Shaw cell showing trailing film of displaced brine (in blue).

the moving interface, as shown in Figure 3.1. In the limit of small capillary number, Bretherton found a film thickness of the order of  $Ca_l^{2/3}$  instead of the  $Ca_l^{1/2}$  value found experimentally by Fairbrother and Stubbs [67].

A formal double asymptotic expansion approach for three dimensional disturbances of a planar flow between two plates was presented by Park and Homsy in 1984, formally proving that in the limit of small capillary number Bretherton's wetting film thickness of the order of  $Ca_l^{2/3}$  is obtained [45]. Besides, the Park and Homsy asymptotic analysis also shows that until order  $Ca_l^{1/3}$ , the wetting film thickness does not have a correction term even though the profile of the transition region at the front tip does have a correction at this order. Bretherton infers that a possible explanation for the discrepancy between the theory and the experimental values is the existence of small impurities on the experiments [67]. Recently several works have addressed this issue theoretically and experimentally, showing the possibility of thicker films when small impurities (surfactants) are included in the analysis; see [68, 69]. As pointed out by Park and Homsy, the effect of the trailing wetting film can be taken into account in the cross average Hele-Shaw cell approximation (Darcy flow) by including in the pressure jump condition across the fluid interface a term linearly proportional to the wetting film thickness, see equation (3.5) [45].

Since the work of Park and Homsy in 1984, there has been considerable research comparing this modified boundary condition with experimental findings. Early channel flow stability analyses by Schwartz in 1986 and Reinelt in 1987 find that including a non-linear velocity term in the pressure jump improves the agreement between theory and experiment [70, 71]. Schwartz also shows that the linear growth rate of the fingers is reduced when dynamic wetting is included. Later, Maxworthy compares various theoretical boundary conditions for predicting the wavelength of the most unstable

wave in a radial Hele-Shaw cell under different capillary numbers and compares these to experimental findings [27]. His results indicate that for high capillary number flows, 3D effects can become significant and could account for the discrepancy between theory and experiment.

More recently, there has been renewed interest in the stability analysis of the radial injection case [47, 72, 73]. [72] and [73] deal with the linear regime of finger growth, deriving dispersion relations for the growth rate. Without wetting effects, the fastest growing fingers have a wavelength proportional to the square root of the capillary number [22]. However, [73] find that dynamic wetting effects stabilise perturbations and decrease the growth rate of fingers, similar to the findings of [27]. [47] takes the analysis further and explores the weakly non-linear regime of finger splitting and competition. They investigate the pattern forming mechanism of the problem, finding that dynamic wetting effects stabilise the fingers and lead to the formation of short stubby fingers in contrast to the classical fan-like patterns [47].

Several papers also exist for the radial injection cases with rotating Hele-Shaw cells [46, 74] and lifting Hele-Shaw cells [75], showing similar stability analyses and wavelength selection for the linear and weakly non-linear growth regimes. To the author's knowledge, there does not exist any analysis on the highly non-linear regime occurring after finger bifurcation in radial injection whereby finger competition is prominent and mechanisms such as finger break-off can occur in low mobility ratio flows, as shown in the previous chapter.

In this chapter, a numerical scheme using the boundary element method presented previously is developed, to study the morphological changes that occur due to dynamic wetting in the late stages of interfacial evolution. To include the effects of dynamic wetting, a Picard iteration scheme is utilised that iteratively improves the pressure jump boundary condition and subsequent interfacial velocity calculation at each time step. This scheme allows the effective evaluation of the non-linear term, and the prediction of the late stage pattern forming mechanisms due to dynamic wetting in low mobility ratio regimes found in  $CO_2$  injection.

### 3.2 Mathematical formulation

The dynamic wetting formulation follows from the finite mobility ratio model in the previous chapter, with modifications to take into account the wetting layer present in Figure 3.1. Due to the constant plate separation, the Laplace equation is again solved using the non-dimensional parameters in (2.26) - (2.29):

$$\frac{\partial^2 P_l(\mathbf{x})}{\partial x_i^2} = 0 \quad \mathbf{x} \in \Omega_l, \quad l = 1, 2 \quad (3.1)$$

The pressure is represented as that due to an injection potential source and a surface potential:

$$P_1(\mathbf{x}) = \hat{\phi}_1 - \frac{1}{2\pi\beta} \ln(r) \quad (3.2)$$

$$P_2(\mathbf{x}) = \hat{\phi}_2 - \frac{1}{2\pi} \ln(r) \quad (3.3)$$

The matching conditions at the interface have to be changed to take into account the wetting layer. Firstly, continuity of normal fluxes:

$$q = \beta \frac{\partial \phi_1}{\partial n} = \frac{\partial \phi_2}{\partial n} \quad (3.4)$$

Secondly, the pressure jump across the interface due to the Hele-Shaw meniscus ( $2r_0/b$  term), the dynamic wetting layer ( $Ca_l$  term) and the in-plane curvature ( $k(\boldsymbol{\xi})$ ) term:

$$P_1(\boldsymbol{\xi}) - P_2(\boldsymbol{\xi}) = \frac{1}{Ca_g} \left( \frac{2r_0}{b} (1 + J_0 |Ca_l|^{2/3}) + \frac{\pi}{4} k(\boldsymbol{\xi}) \right) \quad (3.5)$$

The pressure jump in equation (3.5) includes both the Hele-Shaw meniscus and the dynamic wetting film layer, with  $J_0$  being a constant derived in [45] as 3.8. In the above equations, the global capillary number  $Ca_g$  has been used in the non-dimensional scaling, whilst the local capillary number  $Ca_l$  modifies the effective out of plane curvature term (Hele-Shaw meniscus). The two forms of capillary number are repeated here:

$$Ca_g = \frac{r_0 Q}{\gamma M_2} \quad Ca_l = \frac{\mu_2 U_n}{\gamma} \quad (3.6)$$

Without any wetting effects, the global capillary number and mobility ratio uniquely describe the radial Hele-Shaw flow. However, with the non-linear dynamic wetting term,

$J_0|Ca_l|^{2/3}$  given in equation (3.5), the problem now also depends on the local capillary number at the interface of the two fluids.

In the present two dimensional Hele-Shaw flow problem, the injected fluid spreads radially through the space with an interface velocity that decreases with time as the fluid interface evolves. It follows that the local capillary number also decreases as time progress. The defined global capillary number is prescribed by the initial value of the local capillary number along the unperturbed bubble radius:

$$Ca_g = Ca_l(0, r_0) \left( \frac{r_0}{b} \right)^2 24\pi \quad (3.7)$$

Where  $Ca_l(0, r_0)$  represents the local capillary number at time  $t = 0$  along the unperturbed bubble radius,  $r_0$ . The  $24\pi$  comes from the definition of the mobility and the velocity from the source injection. Due to the controversy between the experimental results and theoretical values, in the present work the Park and Homsy (1984) pressure jump condition is used, since it corresponds to the theoretical value at small capillary number [45]. Besides, as previously mentioned, in the present radial injection problem with a constant injection flux, the local capillary number reduces in magnitude as time progresses, reaching the limit of a small value at a short time in the evolution. This is in contrast with the cases of flow in a capillary pipe or channel where the finger tip velocity remains constant with an associated constant capillary number.

Following from the pressure field representation in equations (3.2) and (3.3), the surface potentials  $\hat{\phi}_1$  and  $\hat{\phi}_2$  can be expressed in terms of their corresponding Green's formulae at the fluid interface using the two dimensional fundamental solution,  $\phi^*$ . Taking the limiting value of the normal derivatives of these equations and subtracting the results from one another, the following second kind Fredholm integral equation can be formed as in the previous chapter:

$$-\frac{1}{2}q(\boldsymbol{\xi}) + \left( \frac{1-\beta}{\beta+1} \right) \int_s K(\mathbf{y}, \boldsymbol{\xi}) q(\mathbf{y}) dS_y = g(\boldsymbol{\xi}) \quad (3.8)$$

$$g(\boldsymbol{\xi}) = \frac{\beta}{2\pi} \int_s f_s(\mathbf{y}) \frac{\partial^2}{\partial n_\xi \partial n_y} \left( \ln \frac{1}{R(\boldsymbol{\xi}, \mathbf{y})} \right) dS_y \quad (3.9)$$

Where,

$$f_s(\mathbf{y}) = \frac{1}{1 + \beta} \left( (P_1(\mathbf{y}) - P_2(\mathbf{y})) - \left( \frac{\beta - 1}{2\pi\beta} \right) \ln(r) \right) \quad (3.10)$$

Now, the boundary term (3.9) depends on the  $(P_1 - P_2)$  given by equation (3.5), which includes the dynamic wetting component. Equation (3.8) can be solved using a convergent series for  $q$  in exactly the same manner as presented previously, using the same hypersingular integral evaluations and numerical procedures, giving the interfacial displacement as:

$$U_n(\boldsymbol{\xi}) = \frac{\Delta L_n(\boldsymbol{\xi})}{\Delta t} = -q(\boldsymbol{\xi}) + \frac{x_i(\boldsymbol{\xi})n_i(\boldsymbol{\xi})}{2\pi r^2} \quad (3.11)$$

The major difference between the solution of (3.11) and that of (2.61) is the appearance of the interfacial velocity in the non-homogeneous boundary term in (3.9). As the normal velocity for use in  $f_s(\mathbf{y})$  and hence  $g(\boldsymbol{\xi})$  is not known *a priori*, a guessed value is used initially, so that the capillary number can be predicted.  $U_n(\boldsymbol{\xi})$  can then be calculated based on the predicted boundary term  $g(\boldsymbol{\xi})$ . After calculation of this new velocity, the local capillary number can be updated and the process repeated until the updated interface velocity does not change from one iteration to the next. At each Picard iteration,  $k$ , the normal interface velocity is updated using:

$$\tilde{U}_n^k = \tilde{U}_n^{k-1} + \lambda_r \left( U_n^k - \tilde{U}_n^{k-1} \right) \quad (3.12)$$

Where  $U_n^k$  represents the value of  $U_n$ , calculated using (3.11), at Picard step  $k$ . The relaxation factor,  $\lambda_r$  in equation (3.12) ensures that the velocity does not vary too dramatically with each Picard iteration in highly non-linear cases, where  $Ca_l$  is large. After each Picard iteration, the updated velocity is used to calculate the local capillary number for the next Picard step, i.e:

$$Ca_l = \frac{\mu_2 \tilde{U}_n^{k-1}}{\gamma} \quad (3.13)$$

The scheme converges once the  $L_2$  relative error norm between successive velocity updates is less than a specified tolerance. In all cases, a tolerance of  $1 \times 10^{-3}$  was found to be low enough that any further updates to the velocity field were negligible at each time step, generally requiring around 10-50 Picard iterations. Relaxation factors in

the range of 0.1 - 0.5 were used to ensure convergence in high  $Ca_l$  cases. On the first time step, the initial guessed velocity is taken as zero. In subsequent time steps, the initial guessed velocity can be taken as the final converged velocity value from the previous time step. As the surface grows at each time step according to equation (3.11), the number of boundary elements along the interface are adaptively increased to maintain a target element size. The target element size varies with each case (as higher capillary number flows require a finer dataset), but is typically of the order 0.05.

This numerical method forms the basis to investigate the effects of dynamic wetting on viscous fingering morphologies during the non-linear stages of finger bifurcation and competition. By setting  $J_0$  to zero in the pressure jump condition, the dynamic wetting term can be removed, and the usual viscous fingering regime will be recovered. In the next section the effects of dynamic wetting are numerically investigated by varying the local capillary number, the global capillary number and the mobility ratio between the fluids.

### 3.3 Numerical results and discussion

#### 3.3.1 Local capillary number effects

The trailing film left by the displaced fluid in the Hele-Shaw cell has a thickness proportional to  $Ca_l^{2/3}$ . To investigate how the local capillary number affects the interfacial displacement after bifurcation,  $Ca_l$  can be varied whilst maintaining the same global capillary number and mobility ratio. If the viscosity of both the injected fluid and displaced fluid are increased by the same factor, and the Hele-Shaw plate separation  $b$  is increased by the square root of this factor, the global capillary number can be kept constant whilst varying the local capillary number. In effect, the wetting layer thickness is increased by using more viscous fluids, but the mobility of those fluids is the same through the cell, so the effect of dynamic wetting can be evaluated independently. Without wetting effects, having the same  $Ca_g$  and mobility ratio would produce exactly the same interfacial displacement.

Several different fluids are injected under the same global capillary number and mobility ratio regime, producing different local capillary numbers. In the results that follow, the

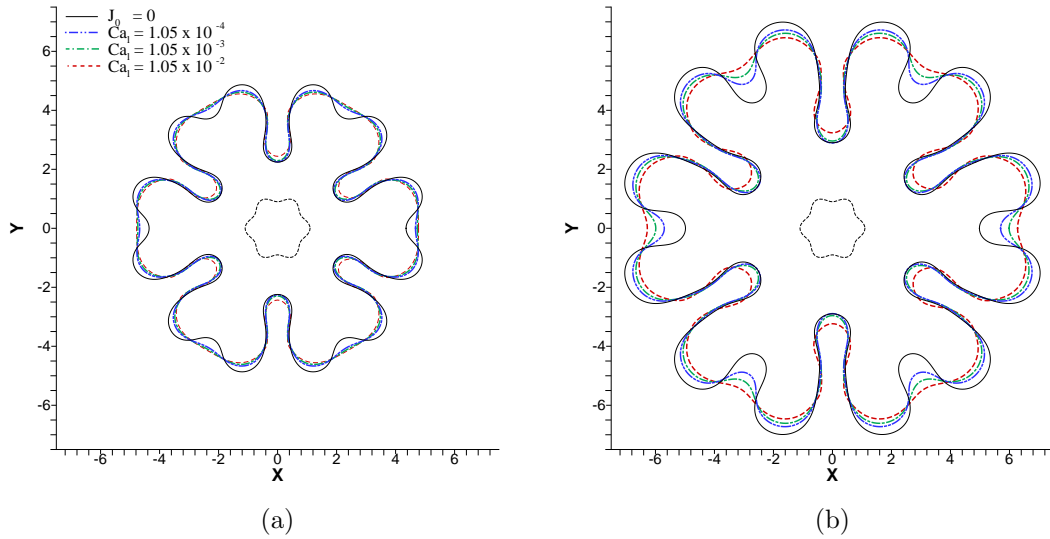


Figure 3.2: Effect of varying the local capillary number on interfacial displacement. (a)  $t = 55$ , (b)  $t = 110$ .  $Ca_g = 1000$ ,  $\beta = 10$ .

local capillary number that is stated in the figures is the maximum found along the interface at  $t = 0$ , i.e.  $|Ca_l(0, r)|_{max}$ .

The local capillary number will decay as the radial distance of the interface from the source point increases, but it is convenient to use this initial value for discussion purposes as the local capillary number can vary significantly around the interface at later stages in time. The initial value gives an indication of the level of dynamic wetting that will be present in the regime. By ensuring that  $Ca_l$  is above  $1 \times 10^{-4}$  initially, insight can be provided into the viscous fingering regime that would occur in a corresponding porous medium subject to the same capillary number flow.

By altering the viscosity of the fluids, the local capillary number for each simulation is changed. Brine, low viscosity oil and high viscosity oil are used as the resident fluids and in each simulation, a fluid with a viscosity an order of magnitude lower than the resident fluid is injected, giving a mobility ratio of 10. When testing capillary number dependence, an initial 6 perturbation symmetric interface is used shown in Figure 2.2, with an initial perturbation amplitude of  $\epsilon_0 = 0.1$ .

In Figure 3.2, the  $J_0 = 0$  interface represents a simulation where the effect of dynamic wetting has been excluded. It can be seen that by including the effect of dynamic wetting ( $J_0 = 3.8$ ), the onset of bifurcation has been delayed. With an increasing local capillary number the thickness of the wetting film increases, which causes the point of

bifurcation to be delayed, as a small pressure jump is generated that works to stabilise the interface (Figure 3.2(a)). The increase in wetting layer thickness causes an increase in the capillary pressure ( $P_c = P_1 - P_2$ ), which makes it harder for the fluids to displace and smooths the advancing interface. This is because the injected non-wetting fluid is effectively trying to displace a wetting fluid out of a ‘smaller’ capillary tube, which requires more force. At this low global capillary number, the solution is reasonably stable, generating just two fingers at the first bifurcation due to the relatively large critical length scale of bifurcation.

Dynamic wetting effects also alter the evolution of the finger bases, and can be seen to push the bases further into the domain in Figure 3.2(b). At low values of  $Ca_l$ , the bases follow a very similar evolution to that with no dynamic wetting effects, however, above  $Ca_l = 1.05 \times 10^{-3}$ , the base is pushed significantly away. The effect of dynamic wetting in the  $Ca_l = 1.05 \times 10^{-2}$  case is very significant. The finger fronts are displaced less and have a much smaller perturbation in comparison to the other cases, causing the bases of the fingers to be pulled much further forwards into the domain.

It is worth noting that in this model, dynamic wetting has no historical hysteresis, that is, if the finger moves back into a region it has previously been, the wetting layer behaves exactly the same as if the finger had never been there (hence the absolute value of  $Ca_l$  in the pressure jump condition). This assumption has been discussed in [46] concluding that thorough experimental work is needed to test the validity of this assumption.

The results in Figure 3.2 show very similar properties to the analytical results of Anjos and Miranda [47]. In their case, several modes of perturbation are analysed, with displacement computed for the early stages of finger growth and the weakly non-linear stage of bifurcation (finger splitting). They use local capillary numbers in the order of  $0.01 - 0.1$  (initially), and find that the dynamic wetting layer hinders finger growth and can almost completely inhibit bifurcation, creating short stubby fingers. Similar results are found here, however, in the later stages of finger growth, bifurcation can still occur even with large values of local capillary number.

The local capillary number decreases with time, meaning in later stages it can be small enough that the usual viscous fingering dynamics occur and bifurcation will proceed.

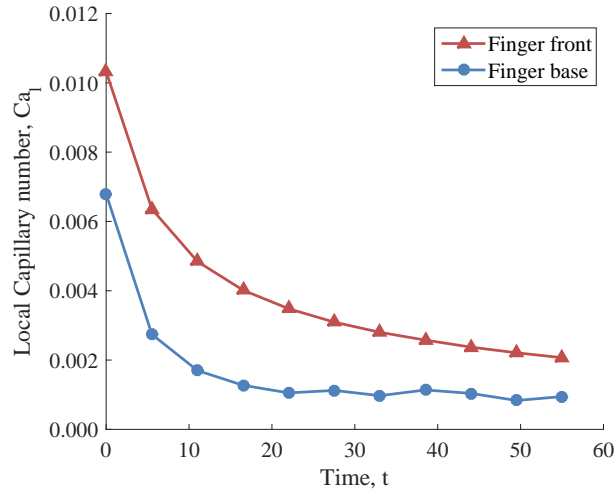


Figure 3.3: Local Capillary number variation with time for the dashed line case ( $Ca_l$  initial =  $1.05 \times 10^{-2}$ ) in Figure 3.2.

If the bifurcation is delayed significantly, the mode of bifurcation can change and the resulting interface can be significantly different.

In Figure 3.3, it is reported how the local capillary number changes with time for the highest initial  $Ca_l$  case from Figure 3.2. The local capillary number decreases quickly, and reaches the small capillary number limit of the Park and Homsy correction used in equation (3.5) early in the simulation. Even in the highest initial  $Ca_l$  case, the Park and Homsy small capillary number limit is quickly reached, showing the applicability of the correction term for the radial injection cases presented here.

### 3.3.2 Global capillary number effects

In this section, the effect of changing the global capillary number and resulting wetting layer is investigated. Increasing the global capillary number lowers the critical length scale of bifurcation and generally means that more fingers are generated on the first bifurcation, leading to a more convoluted interface. With an increase in  $Ca_g$ , the local capillary number  $Ca_l$  is also increased, meaning the effects of both a more unstable solution globally, and an increased thickness of dynamic wetting layer can be seen.

The changing global capillary number results are presented in Figure 3.4. A mobility ratio of 10 is used in all cases, with brine as the displaced fluid, and supercritical  $CO_2$  as the injected fluid. To increase the global capillary number, the surface tension between

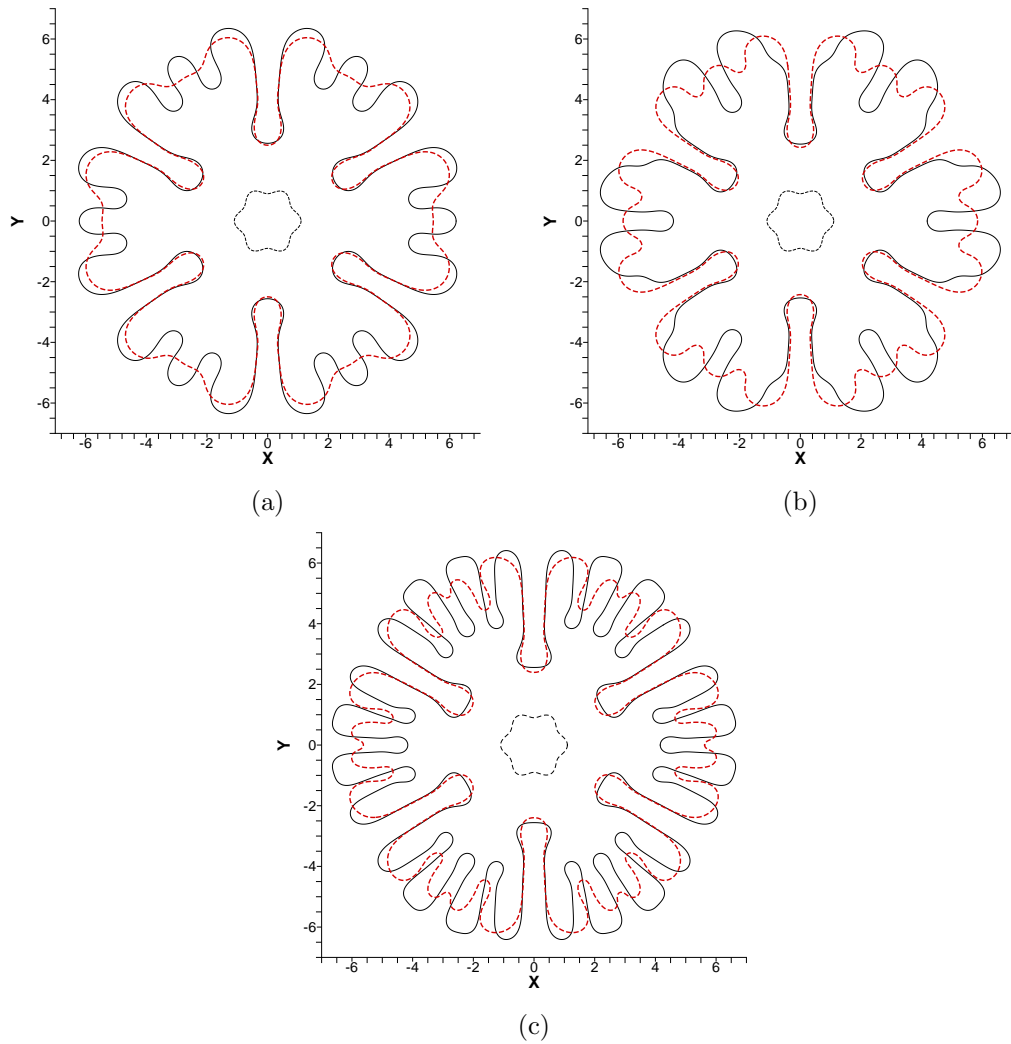


Figure 3.4: Effect of varying  $Ca_l$  and  $Ca_g$  on interfacial evolution,  $t = 88$ . (a)  $Ca_g = 2000$ , initial  $Ca_l = 2.19 \times 10^{-4}$ . (b)  $Ca_g = 4000$ , initial  $Ca_l = 4.47 \times 10^{-4}$ . (c)  $Ca_g = 8000$ , initial  $Ca_l = 9.04 \times 10^{-4}$ . —  $J_0 = 0$ , - - -  $J_0 = 3.8$ .  $\beta = 10$ .

the fluids is correspondingly decreased (equally the injection flux could be increased for the same change in global capillary number). The local capillary number stated in each figure refers to the initial maximum along the interface calculated at  $t = 0$ .

With the relatively high local and global capillary numbers tested in Figure 3.4 it can be seen that bifurcation is delayed and the fundamental mode can be changed when dynamic wetting effects are included ( $J_0 = 3.8$ ). It should be noted that due to the inclusion of the  $\pi/4$  pre-factor in the in-plane curvature term here (equation (3.5)), the base cases without wetting layer effects ( $J_0 = 0$ ) show different bifurcation regimes to the corresponding cases in Figure 2.14 in chapter 2. The inclusion of the  $\pi/4$  term in the capillary pressure (to be consistent with the Park and Homsy analysis [45]) has

effectively reduced the surface tension in comparison to the cases in Figure 2.14, meaning the interfaces are more unstable and exhibit more fingers on bifurcation.

In the  $Ca_g = 2000$  case in Figure 3.4, the three finger split has been inhibited, and only two primary fingers form from the first bifurcation through the inclusion of the dynamic wetting layer. The bifurcation has been delayed, and in doing so the fundamental splitting mode has been changed due to the inhibition of the middle finger.

Similar effects are seen at higher global capillary numbers, although the number of fingers that form on the first bifurcation is not always reduced due to dynamic wetting. The critical length scale of bifurcation decreases at higher capillary numbers, meaning it is easier for more fingers to form upon bifurcation. However, as the interface is generally ‘smeared’ and made more uniform by the inclusion of dynamic wetting, there can be more parts of the interface greater than the critical length scale of bifurcation. This means more fingers can sometimes be formed due to the presence of the dynamic wetting layer (see Figure 3.4(b)).

When the global capillary number is increased, the overall stability of the solution is reduced. The interface becomes more ramified and an increased number of boundary elements must be used to accurately capture the displacement. However, the stabilising effect of dynamic wetting also increases with global capillary number, meaning that there is competition between the destabilising effect of increasing the viscous driving force and the stabilising effect of increasing the thickness of the dynamic wetting layer. Through many numerical experiments, it was observed that even at very large local capillary numbers, bifurcation could never be completely inhibited. The system would eventually become unstable due to the viscosity contrast between the fluids and the fact that the wetting layer thickness reduces with time.

### **3.3.3 Late stage interfacial displacement**

Here the late stage interfacial evolution is considered, given an asymmetric starting interface in order to more closely mimic the different perturbation wavelengths that may occur naturally in a real injection scenario. An asymmetric boundary is used,

which is similar to that presented previously with a radius defined by:

$$r = 1 + \epsilon_0 \cos \left( 6 \sqrt{\frac{\theta^{3.5}}{2\pi^{2.5}}} \right) \quad (3.14)$$

Equation (3.14) with  $\epsilon_0 = 0.1$  is a slightly different asymmetric form to equation (2.77). The form in (3.14) is used in order to create perturbations of longer wavelength around the interface, which create more fingers on bifurcation where dynamic wetting effects can be analysed. The displaced fluid is taken as brine with suitable deep aquifer properties as per the previous chapter (i.e. injection depth 1000m,  $P_{amb} = 10MPa$ ,  $T = 35^\circ C$ ,  $\gamma = 0.03kg.s^{-2}$ ,  $\mu = 7.6 \times 10^{-4}Pa.s$ ). Supercritical  $CO_2$  is injected into the system with a pressure of  $20MPa$ , and a viscosity ten times lower than that of the resident brine. This gives a global capillary number of 5000, with a initial local capillary number of  $5.33 \times 10^{-4}$ . The plate separation is 0.0123cm, giving an intrinsic permeability of  $1.26 \times 10^{-5}cm^2$  equivalent to highly fractured porous rock [63].

Time plots of the injection can be seen in Figure 3.5. The onset of fingering has been delayed significantly in the dynamic wetting case, especially on the more stable fingers in the left of the domain. At  $t = 20$ , the interfaces show considerable likeness, with only minor deviation from each other. However, as time progresses, the effects of the dynamic wetting layer can be seen, whereby the bifurcation of fingers are inhibited significantly. In the areas where small fingers have formed with a large curvature, dynamic wetting has only slightly hindered the growth and subsequent bifurcation (mainly in the right of the domain). The large curvature means that the effects of dynamic wetting are proportionally less pronounced compared to areas with a small curvature.

Due to the very flat interface at the bottom right of the domain and the relatively large global capillary number, many small fingers are able to form at the first bifurcation. Dynamic wetting has delayed the fingers from forming, but the bifurcation mode is very similar. The bases of the newly generated fingers have been pushed further into the domain due to the dynamic wetting layer.

In Figure 3.6 the zoomed in area from the dashed box in Figure 3.5 can be seen. This plot highlights the finger interaction occurring between several small fingers with large curvature and rapid growth rates. The solid line shows that without dynamic wetting, the side branching finger is thinning the base of the other primary finger significantly.

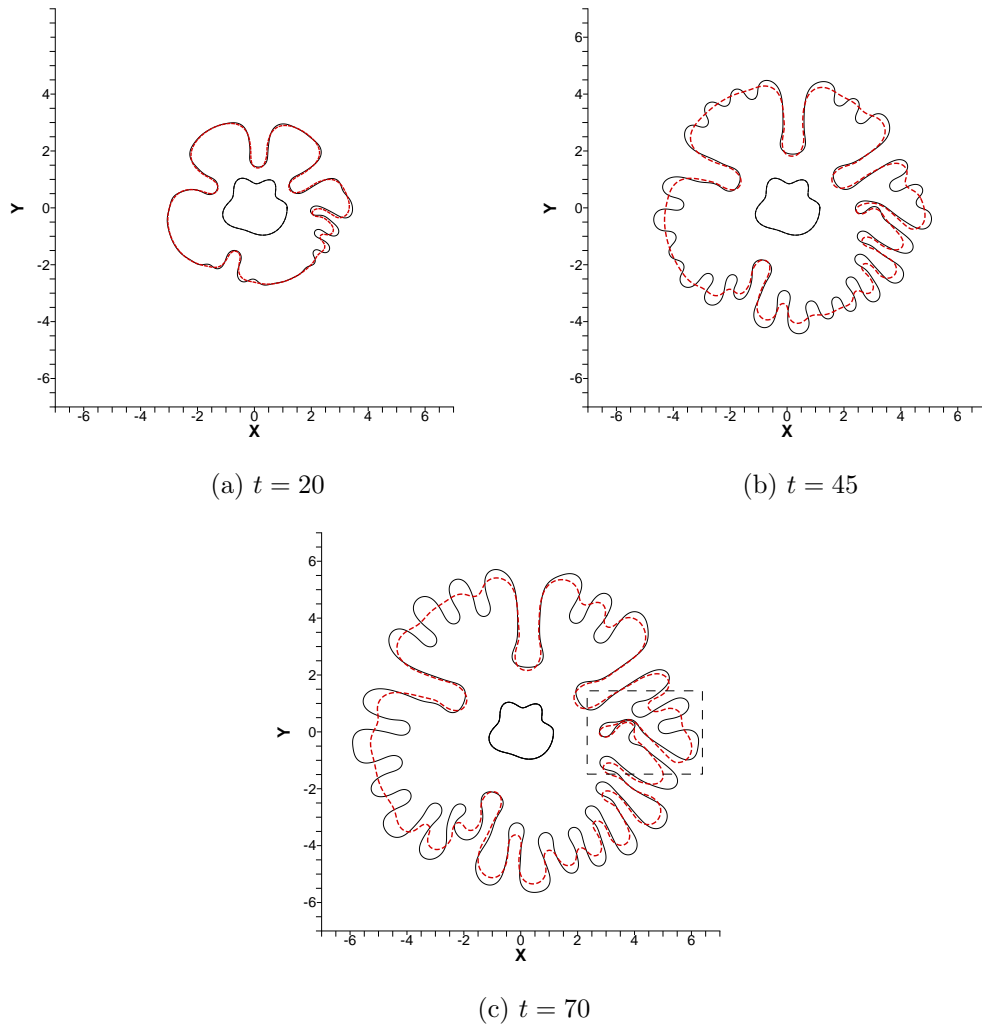


Figure 3.5: Asymmetric interfacial displacement with a mobility ratio of 10 at different times. Dashed box represents zoomed in area for Figure (3.6). —  $J_0 = 0$ , ---  $J_0 = 3.8$

This will eventually lead to finger breaking, shown in the previous chapter as a result of the small immiscible lubrication layer separating the fingers and the significant velocity possessed by the side branching finger. The base thinning is only slightly inhibited when dynamic wetting effects have been included (dashed line). The side branching finger is less defined than the case without dynamic wetting, but it is still advancing at nearly the same rate, and thinning the base of the other primary finger significantly. Both cases lead to finger break-off, with dynamic wetting effects delaying the base thinning mechanism but still having the same overall outcome once time has progressed.

To compare the above case with a classical negligible viscosity injection, the same simulations are run but the mobility ratio between the two fluids is increased to 250. This case is presented purely for comparison purposes, as most previous work in the

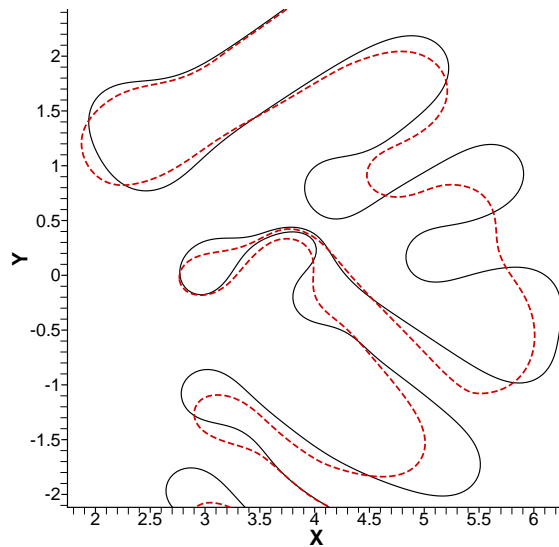


Figure 3.6: Zoomed in plot of finger interaction in Figure 3.5. —  $J_0 = 0$ , ---  $J_0 = 3.8$  field (when wetting effects are not considered) show flow regimes where the inner fluid has negligible viscosity.

Comparing the non-dynamic wetting cases in Figure 3.5 and Figure 3.7 the effect of increasing the mobility ratio between the fluids can be seen. Classical effects such as finger shielding are present in the high mobility ratio case, in which the secondary and side branching fingers' growth has been inhibited by the growth of primary fingers.

The combination of finger shielding and dynamic wetting have a noticeable effect on the number of fingers that are able to form in Figure 3.7(c). There are several fingers (notably those appearing after bifurcation on the far right primary finger) that advance more significantly into the domain than in the non-dynamic wetting case. Dynamic wetting hinders the bifurcation of the finger, which means that the initial growth of the primary finger to the side is unable to shield its growth (shown by the note in Figure 3.7(c)). This means that later on in time when the finger does eventually bifurcate, the primary finger has already grown beyond it, and there is much less competition. The smaller finger can then grow relatively unhindered, and become a primary finger advancing at the forefront of the plume.

Raising the mobility ratio has introduced the shielding effect to the viscous fingering problem, but this has been somewhat inhibited by the inclusion of the dynamic wetting layer. The delaying of bifurcation means that several previously competing fingers are

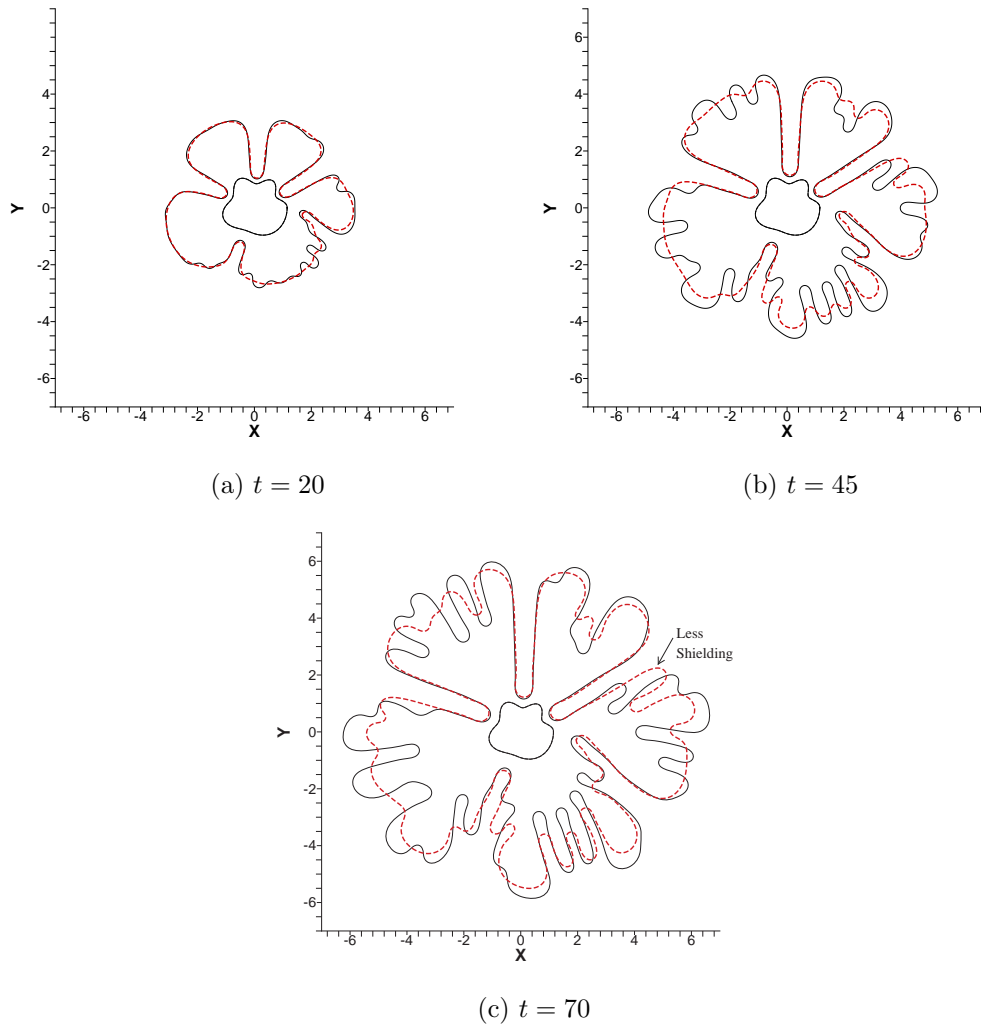


Figure 3.7: Asymmetric interfacial displacement with a mobility ratio of 250 at different times. —  $J_0 = 0$ , ---  $J_0 = 3.8$

not present until later in the simulation, when the primary fingers have advanced much further into the domain. The primary fingers do not compete as directly with these newly formed fingers, as the fronts are further into the domain and not advancing at the same rate as the new fingers.

Finger competition was also found to be reduced by Anjos and Miranda in the weakly non-linear stages of finger growth [47]. They measure finger variability in the domain and find that dynamic wetting produces fingers with a more uniform radial extent, i.e., competition has been reduced. Similar features are observed here in the non-linear stages of finger growth, whereby the shielding effect is reduced due to delayed bifurcation. Fingers compete less with each other and the difference in radial extent of the different finger fronts is reduced.

Figure 3.5 and 3.7 show considerable likeness to the experimental results presented in Figure 2 of [76]. Ward and White analyse the trailing film thickness left by a glycerol-water mix displaced by air, studying the bursting time, average film thickness and total area. Although finger morphology is not the focus of the paper, their qualitative results show remarkably similar fingering patterns to those found here, especially at the high mobility ratios presented in Figure 3.7.

### 3.4 Conclusion

In this chapter, a direct boundary element method and Picard iteration scheme have been developed for the solution of immiscible displacement in a Hele-Shaw cell with non-linear wetting effects. The numerical method allows accurate and efficient evaluation of the interface velocity, permitting long term exploration of the effects of dynamic wetting in the non-linear regime of viscous finger bifurcation and competition.

During the non-linear stages of interfacial evolution, dynamic wetting delays the onset of finger splitting and changes the fundamental mode of bifurcation. Dynamic wetting smooths the interface, creating a less convoluted surface that takes longer to bifurcate. The smoothing of the interface also means that, once bifurcation starts to occur, the number of fingers produced is generally different to that when no dynamic wetting is included.

Asymmetric interface simulations reveal that finger interaction is reduced by the inclusion of dynamic wetting in low mobility regimes and that previously found finger breaking mechanisms can be delayed but can never be completely inhibited. The dynamic wetting layer thickness decreases with time, meaning that eventually classical viscous fingering patterns emerge in the solution.

When the mobility ratio is raised to simulate negligible viscosity, finger shielding is less prominent. Secondary and side branching fingers appear later in the simulation due to delayed bifurcation meaning less competition is encountered with the primary growing fingers.

## 4. A local RBF method for moving multi-zone transport problems

### Summary

This chapter develops a local radial basis function - finite collocation method (RBF-FC) that utilises an adaptive quadtree dataset to cluster nodes around critical features in the domain, for the solution of transport processes occurring in moving front problems. This method is developed specifically for the viscous fingering problem when the mobility varies inhomogeneously in the domain, requiring the solution of convection-diffusion type multi-zone problems with a moving interface.

The numerical method utilises an adaptive quadtree dataset to generate an improved distribution of solution centres in the domain, around which local Hermitian collocation systems are formed. In these local systems, the governing PDE and boundary operators of the problem are enforced by collocation. Globally, the systems are linked via reconstruction of the solution variable in terms of the solution value at neighbouring nodes producing a sparse global matrix with a solution cost that scales linearly with the number of nodes in the domain. Two new multi-zone methods are developed; an embedded method which enforces the multi-zone matching conditions globally in the sparse matrix system, and an auxiliary method which enforces the matching conditions in the local RBF systems.

The RBF-FC method with adaptive quadtree dataset and new multi-zone formulations are verified on several steady-state and transient test cases. Stencil configurations are analysed on a steady-state boundary layer problem, highlighting the most optimal PDE centre location using the adaptive dataset. Transient single-zone testing using an

infinite Peclet number advection problem is performed to analyse the most effective way to update the inhomogeneous PDE term at each time step, showing the basic stencil configuration to perform best in transient cases.

The multi-zone methods are demonstrated on a steady-state fixed interface problem showing very similar performance attributes and consistent 3<sup>rd</sup> order convergence for both schemes. In the transient fixed interface case, the embedded method performs significantly better due to the enforcing of the PDE from both zones on the interface, however the auxiliary method is still able to achieve 2<sup>nd</sup> order convergence. Final testing on a full moving boundary problem with the auxiliary method highlights the robustness of the scheme and the accuracy that can be achieved without the need for ghost-node extrapolation.

## 4.1 Introduction

Interfacial displacements involve transport processes such as mass, heat and momentum transfer occurring across the interface, which generate solution fields that vary sharply through the domain. In this work, the effects of inhomogeneous mobility arising from variable cell permeability and thermally dependent viscosity are to be considered under the conditions found in  $CO_2$  injection. To this end, in order to evaluate the effect of an inhomogeneous mobility on immiscible viscous fingering, two convection-diffusion transport problems have to be considered. Firstly, equation (2.21) can be expanded considering a non-constant  $b(\mathbf{x})$  and  $\mu_l(\mathbf{x})$  as:

$$\frac{\partial}{\partial x_i} \left( \frac{b^3(\mathbf{x})}{12\mu_l(\mathbf{x})} \right) \frac{\partial P_l}{\partial x_i} + \left( \frac{b^3(\mathbf{x})}{12\mu_l(\mathbf{x})} \right) \frac{\partial^2 P_l}{\partial x_i^2} = 0 \quad \mathbf{x} \in \Omega_l, \quad l = 1, 2 \quad (4.1)$$

The plate separation  $b(\mathbf{x})$  in equation (4.1) can vary in space, either subject to a known analytical function (as in chapter 5) or using physical point data. The viscosity  $\mu_l(\mathbf{x})$  can also vary in space due to an imposed temperature field, i.e.  $\mu_l(\mathbf{x}) = f(T_l(\mathbf{x}, t))$ , and can change dramatically in a small range of temperatures (especially in  $CO_2$  injection scenarios). It is therefore necessary to evaluate the heat transfer in each fluid zone  $l$  to

calculate the transient temperature field and viscosity for equation (4.1):

$$\frac{\partial T_l(\mathbf{x}, t)}{\partial t} = D_l \frac{\partial^2 T_l(\mathbf{x}, t)}{\partial x_i^2} - u_i^l(\mathbf{x}, t) \frac{\partial T_l(\mathbf{x}, t)}{\partial x_i} \quad l = 1, 2 \quad (4.2)$$

Where,  $D_l$  is the thermal diffusivity,  $T_l$  is the temperature and  $u_i^l$  is the fluid velocity. The expanded form of the elliptic equation (4.1) and the heat transfer equation (4.2) represent multi-zone convection diffusion type transport problems, in which appropriate solution and flux matching conditions have to be imposed on the moving interface. Suitable boundary conditions also need to be applied to fully close the system. The effective solution of the above equations introduces two main issues:

1. The transport of mass in equation (4.1) and temperature in (4.2) involves several length scales throughout the domain [77], requiring a numerical scheme that can accurately and efficiently capture sharply varying profiles near the interface and smooth details in the outer regions of the domain.
2. Both equations have discontinuities in the effective diffusivity at the interface, as well as rapidly varying (discontinuous in (4.1)) velocity fields, creating a sharp multi-zone representation of the problem that cannot be solved using smooth interpolating functions. The multi-zone interface is explicit and forms an integral part of the solution that may not necessarily be known *a - priori*.

Developing a suitable numerical technique that can effectively handle the issues above is challenging, and has been the focus of many recent works. The two issues can arise separately, as in single-zone convection-diffusion problems [78–80], or in a coupled manner in moving boundary transport problems [81–83]. The moving interface must be accurately represented, with many previous works focusing on level set methods to implicitly capture the interface location [77, 84, 85] or boundary element methods, as are used in this work, to explicitly track the interface [36, 37, 86].

Since an accurate boundary element method has been presented in chapter 2, which can be adapted to suit the problems above, this chapter focuses on developing a technique to capture the rapidly varying solution profile in fixed and moving multi-zone convection-diffusion problems where the sharp interface location is known. The developed method will then be used alongside the BEM in chapters 5 and 6 for the solution of inhomogeneous mobility viscous fingering problems.

### 4.1.1 Polynomial methods for multi-zone transport

When considering convection-diffusion type problems in general, numerical methods that employ polynomial interpolations are typically used to find approximate solutions to the governing equations, e.g. the finite difference (FD), finite volume (FV) or finite element (FE) methods. When the solution is strongly convective, these numerical methods generally use some form of upwinding, where the polynomial interpolation is biased in the upstream direction [78, 79, 87]. This helps to damp numerical oscillations that can grow over time and destroy the solution [87]. However, using purely upwinded stencils for convective situations can introduce significant numerical diffusion over time, smearing sharp solution profiles. Also, extra complexity is introduced into the numerical scheme since stencils must be properly aligned with the flow direction; a task which is non-trivial in two or three dimensional problems, or if the velocity is computed as part of the solution.

A common technique to minimise numerical smearing whilst maintaining stability in the solution is to use a combination of different stencils; biasing between centrally-defined stencils and upwind-biased stencils depending on the flow regime, minimising the variation in the solution. See for example total variation diminishing (TVD) methods [88] or weighted essentially non-oscillatory (WENO) methods [89]. In WENO methods various large stencils (with a range of spatial accuracy's) are formed around the rapidly varying solution profile, with the most optimal stencil being chosen to minimise oscillations and capture sharp solution profiles very accurately.

Although there has been significant progress in creating non-diffusive, high-accuracy stable polynomial based techniques for single-zone convection-diffusion problems, there are still significant drawbacks when the approaches are considered for multi-zone problems. When meshed based methods are explicitly conformed to an interface, either through coordinate transforms or by directly deforming mesh points to coincide with the interface, the resulting solution quality is strongly dependent on the mesh quality [90]. For moving interface problems with highly deformable interfaces, the resulting mesh can be highly skewed leading to inaccurate solutions. Also, the mesh has to be updated at each time step, which is non-trivial when the mesh quality is of prime importance and the interface can experience large deformations.

Multi-zone matching conditions in conformed meshes can be enforced using a variety of techniques that vary in their order of approximation. Non-overlapping alternative Schwarz iteration procedures can be implemented, whereby the two zones use different boundary conditions at the interface that are iteratively updated from the solution of the alternate zone [91]. Neumann or Robin boundary conditions may be employed in one zone to represent the surface flux, whilst the other zone may use a corresponding Dirichlet condition to enforce the surface solution. The procedure then iterates between each zone, with the first zone reconstructing the solution on the interface for use as the second zone Dirichlet condition, and the second zone reconstructing the surface flux for use as the Neumann or Robin boundary condition for the first zone. Once the variation in flux and solution drops below a prescribed tolerance the procedure ends, with the matching conditions enforced globally.

Another technique is to use fictitious points in each zone, extending the solution of each domain over the interface, allowing the use of Taylor series expansions [92]. Since a Taylor series expansion is only valid for continuous data, by extending the inner and outer zone solution to a small region outside the interface, the expansion can be completed. This technique also forms the basis behind many immersed boundary and interface type problems, see [93–95]. The expansion of the solution using the inner and outer fictitious points allows two equations to be formed for the interface solution, which when coupled with a suitable flux matching condition equation can close the problem. Three equations are formed, with three unknowns: the interface solution and two fictitious point solutions. Note that if the interface solution is constructed using polynomial interpolations coming from a single zone without fictitious points (i.e. using backward or forward differences), only one matching condition equation can be enforced without solving an overdetermined system.

Due to the issues associated with mesh generation and quality in conformal methods, improvements can be made by using regular Cartesian meshes with an underlying representation of the boundary, as in common in Stefan and Dendritic solidification heat transfer problems [81, 96, 97]. Here, at locations where the interface cuts the regular mesh, a similar procedure to the fictitious point method above can be implemented whereby the solution is extended in a small band out of the zone [96]. For grid points next to the interface, the solution can be extrapolated to the grid point past the interface

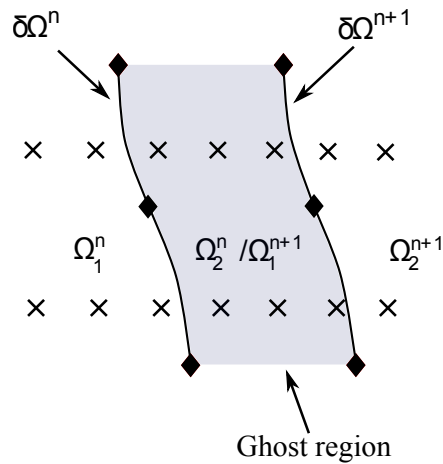


Figure 4.1: Diagram showing the ghost region.  $\partial\Omega$  refers to the interface at time steps  $n$  and  $n + 1$ .  $\Omega_1/\Omega_2$  are the interior and exterior zones respectively. Crosses show a regular Cartesian grid, with diamonds representing the underlying interface points.

in terms of the interface solution and inner zone nodes. When this is done for both grid points on either side of the interface two equations are produced with three unknowns. The flux matching condition can then be used to close the system. The extrapolation can be performed to various orders [98], allowing the extension of the sharp interface problem to regular grids with arbitrarily complicated interfaces.

As well as the extrapolation procedure to approximate the interface solution, a further issue associated with the transient multi-zone problem using fixed Cartesian grids is that of ghost nodes, illustrated in Figure 4.1 [81, 99]. This problem occurs when the moving interface travels over a regular interior node, and the zone switches from 2 to 1 between time step  $n$  and  $n + 1$ . This means the value of previous time step data needs to be calculated for the node, but at time step  $n$  the node was positioned in zone 2; no data exists for the node in zone 1 at time step  $n$ . Transport data such as the fluid velocity and temperature are only known in the specified zones at a specified time step, and do not exist outside of these regions, meaning the zone 1 fluid velocity at time step  $n$  cannot be reconstructed accurately by the numerical method in zone 2. Since the mesh nodal points cluster in a rigid orthogonal manner around the interface, and do not sit explicitly on the interface location, points frequently pass through the ghost region shown in Figure 4.1. Extrapolation schemes can again be used to reconstruct the data needed from the previous time step in a small band outside of the interior zone [98]. However, this limits the convergence and accuracy of the numerical method to that of

the extrapolation scheme, which can be very poor when the data varies sharply over the interface.

### 4.1.2 RBF methods for multi-zone transport

Natural alternatives to the mesh based polynomial techniques described above are meshless techniques that don't require explicit meshes to be created at each time step. One prominent technique, and the basis behind this work is the strong form, radial basis function (RBF) collocation technique [100–103]. Here, polynomial interpolating functions are replaced with radial basis functions, which use the radial distance between points  $r = |\mathbf{x}|$  to construct interpolating functions between nodal points. Since partial derivatives can be reconstructed simply based on the derivatives of  $r$ , there are no restrictions on orthogonality as in methods based on Taylor expansions, and extending the method to higher dimensions is relatively straightforward. This makes RBF methods highly suited to tackle problems using scattered, irregular datasets with high dimensionality, requiring no formal mesh connectivity.

There exist many global implementations of RBF schemes, in which the entire dataset is interpolated and used to reconstruct the solution, where exponential convergence rates (spectral accuracy) can be observed producing highly accurate solutions [104]. However as the size of the dataset grows the resulting matrix systems suffer from severe ill-conditioning and since the cost of solving the fully populated global matrix grows with  $N^3$ , there is a practical limit to the dataset size and accuracy that can be achieved using standard hardware (8 or 16 byte precision) arithmetic. Although arbitrary-precision arithmetic ( $> 100$  decimal points) can be implemented in software to solve the ill-conditioned matrices, the solution time can increase significantly for practical problems [105].

To alleviate the global issues above, the RBFs can be formed locally on small overlapping systems that are linked via global reconstruction of appropriate operators [106]. A straightforward localised implementation of RBFs can be found in the finite difference style approach - RBF-FD. The polynomial interpolants in regular finite difference schemes are replaced by radial basis functions, with the same global differencing procedure applied to reconstruct the PDE at the global level at solution nodes (see

[107–110]). Since the principle is the same as traditional finite differences (albeit with significantly increased accuracy and flexibility), upwinded stencils can also be employed for highly convective regimes [111, 112]. In [113, 114] improved accuracy and stability is achieved through the use of auxiliary PDE points. The auxiliary PDE points appear solely in the local interpolation, having no global context, giving rise to an implicit upwinding effect and improved solution stability.

Since the solution is meshless, nodal points can be placed directly on the interface with relative ease, and grouped into local stencils. Multi-zone matching conditions can be applied at the global level utilising the flux as an operator in the RBF interpolation at the local level. This means that the flux and solution can appear as unknowns in the resulting global system. By reconstructing the PDE from the two different zones at the same interface point, two equations are formed in the global system with 4 unknowns. By equating the flux and solution variables to each other using the matching conditions, the problem is reduced to 2 equations in the global matrix with 2 unknowns. This global multi-zone reconstruction was performed in [113] on various steady-state and transient cases, demonstrating the robustness of the method and accuracy when capturing discontinuous multi-zone interfaces, with large changes in fluid properties.

A further extension to the RBF-FD methods described above are RBF-finite collocation (RBF-FC) schemes that allow non-oscillatory solutions to highly convective regimes, even in the presence of discontinuous shocks [115]. Here, the local interpolation uses the boundary operators and PDE centres in a similar way to the auxiliary nodes in [113] producing similar implicit upwinding effects. However, instead of global differencing, the systems are linked through reconstructing of the field variable in terms of the field value at neighbouring nodes producing a sparse global matrix [116]. The PDE is only enforced locally, and does not appear at the global level, meaning that the resulting global matrix is well conditioned, and scales linearly with the number of nodes in the domain. In this way, the RBF-FC method is a direct analogue to the global RBF method applied at the local scale, where small boundary value problems are formed that are then linked via global solution collocation.

The RBF-FC method has been previously demonstrated on various steady and transient convection-diffusion problems using uniform, geometrically refined and scattered irregular datasets, showing consistent spatial and temporal convergence [115, 116]. Local

stencil configuration and spatial refinement play a crucial role in the overall accuracy of the scheme, with uniform datasets showing much more predictable scaling properties and lower solution errors than their scattered irregular counterparts [116]. However, uniform datasets generally use many more points than are necessary in areas where the solution profile is varying gradually, in the outer limits of the domain in moving front problems. To maintain the regular systems present in uniform datasets whilst allowing significant spatial refinement throughout the domain, a quadtree data structure can be implemented that clusters the nodal points of the RBF-FC method around critical features in the domain.

Quadtree datasets are typically used as mesh pre-processors for finite difference or finite volume schemes, where mesh orthogonality is crucial, particularly for the finite difference scheme, where unless special treatment is to be given to spatial derivatives, orthogonality is a binding restriction. When the FD method is coupled with a level set front capturing technique, quadtree meshes have effectively been used to solve the well known Stefan problem and other heat transfer problems [77, 99]. However, these methods generally have limited spatial convergence (typically supra-linear). Similar schemes have also been implemented using quadtree datasets with a volume of fluid front capturing technique, showing considerable improvement over their uniform dataset counterparts [117].

By utilising a quadtree data set for the nodal point generation for the RBF-FC scheme, a sparse global dataset can be created that alleviates issues with convergence and upwinding criteria. Consistent nodal refinement can be achieved, that allows local systems to maintain regularity and consistency, whilst grading from a coarse discretisation in the far field to a fine discretisation near the interface.

In this chapter the RBF-FC method described above is developed for use with adaptive quadtree datasets that cluster and ‘snap’ directly to the moving interface. Two new multi-zone methods are also introduced, one which follows the same procedure as the global formulation in [113], collocating two systems at each interface point, and a second method which only collocates the matching conditions locally in a fashion in keeping with the original boundary value style of the RBF-FC scheme. These new schemes are suited to different forms of the problems presented at the start of this chapter, and are developed specifically for different tasks.

In the following sections, the new RBF-FC multi-zone formulations are first presented for general moving multi-zone transport problems, followed by stencil configuration testing and transient verification. The chapter concludes with multi-zone verification on three test problems.

## 4.2 The multi-zone RBF-FC method

The RBF-FC method presented in this section covers new formulations for moving multi-zone problems, with adaptive multi-zone features added to the original RBF-FC method first presented in [116]. For more details on the base RBF-FC method, along with comparison to other RBF schemes, see [115, 116]. The convection-diffusion problems under consideration in this work can be described generally as initial boundary value problems of the form:

$$\frac{\partial \phi_l(\mathbf{x}, t)}{\partial t} = L_l[\phi_l(\mathbf{x}, t)] + S_l(\mathbf{x}, t) \quad \mathbf{x} \in \Omega_l \quad (4.3)$$

$$\phi_l(\mathbf{x}, 0) = p_l(\mathbf{x}) \quad \mathbf{x} \in \Omega_l \quad (4.4)$$

$$B_l[\phi_l(\mathbf{x}, t)] = g_l(\mathbf{x}) \quad \mathbf{x} \in \partial\Omega_l \quad (4.5)$$

$$C_1[\phi_1(\mathbf{x}, t)] - C_2[\phi_2(\mathbf{x}, t)] = h(\mathbf{x}) \quad \mathbf{x} \in \partial\Omega_{int} \quad (4.6)$$

$$Q_1[\phi_1(\mathbf{x}, t)] - Q_2[\phi_2(\mathbf{x}, t)] = f(\mathbf{x}) \quad \mathbf{x} \in \partial\Omega_{int} \quad (4.7)$$

Here,  $\Omega_l$  is the interior of zone  $l$ ,  $\partial\Omega_l$  is the boundary of zone  $l$  and  $\partial\Omega_{int}$  is the fluid-fluid interface.  $\phi_l$  represents the field variable solution in zone  $l$ .  $L$  and  $B$  are linear partial differential operators on the domain  $\Omega_l$  and the boundary  $\partial\Omega_l$  respectively.  $C$  and  $Q$  are solution and flux operators acting at the interface  $\partial\Omega_{int}$  with corresponding matching conditions  $h(\mathbf{x})$  and  $f(\mathbf{x})$ . If  $h(\mathbf{x}) = f(\mathbf{x}) = 0$ , the solution and flux are continuous across the interface. Equation (4.4) represents the initial conditions of the problem in each zone. A Crank-Nicholson approximation can be applied to the time derivative:

$$\frac{\phi_l^{n+1} - \phi_l^n}{\Delta t} = \theta L[\phi_l^{n+1}] + (1 - \theta) L[\phi_l^n] + S_l \quad (4.8)$$

From (4.8), modified PDE governing operators can be obtained:

$$\begin{aligned}\bar{L} &= I - \theta \Delta t L \\ \hat{L} &= I + (1 - \theta) \Delta t L\end{aligned}\quad (4.9)$$

such that

$$\bar{L}_l [\phi_l^{n+1}] = \hat{L}_l [\phi_l^n] + S_l = \hat{S}_l \quad (4.10)$$

In the equations above,  $I$  is the identity matrix (dimension 1 here). By using this type of time stepping algorithm, the transient problem is reduced to a series of inhomogeneous steady-state problems, with the inhomogeneous term  $\hat{S}_l$  a function of the solution at the previous time step. Steady-state problems are achieved by setting  $\hat{L}_l$  to zero and  $\bar{L}_l = L_l$  in the above equations.

The Hermitian collocation approach constructs the value of the solution  $\phi$  as a weighted sum of partial differential operators applied to a set of radial basis functions that are centred on nodes  $\mathbf{y}_j$  (here  $j$  refers to the specific node in the summation, not the spatial components  $y_1/y_2$  of  $\mathbf{y}$ ). In the Hermitian RBF interpolation in equation (4.11), the boundary operator  $B$  is applied at the domain boundary, the governing PDE  $\bar{L}$  operator is applied at the domain interior, and the flux and solution operators  $Q$  and  $C$  are applied at the multi-zone interface:

$$\begin{aligned}\phi_l^{n+1}(\mathbf{x}) &= \sum_{j=1}^{NB} \tau_j B_{l,y} \Psi(\|\mathbf{x} - \mathbf{y}_j\|) + \sum_{j=NB+1}^{NB+NI+1} \tau_j \bar{L}_{l,y} \Psi(\|\mathbf{x} - \mathbf{y}_j\|) \\ &+ \sum_{j=NB+NI+2}^{NB+NI+NF+2} \tau_j C_{l,y} \Psi(\|\mathbf{x} - \mathbf{y}_j\|) + \sum_{j=NB+NI+NF+3}^{NB+NI+2NF+3} \tau_j Q_{l,y} \Psi(\|\mathbf{x} - \mathbf{y}_j\|)\end{aligned}\quad (4.11)$$

In equation (4.11),  $NB$  is the number of boundary nodes,  $NF$  is the number of flux (interface) nodes and  $NI$  is the number of internal nodes.  $\tau_j$  are the unknown RBF weights. For operators with two subscripts, i.e.  $B_{l,y}$ , the  $l$  refers to the zone, whilst the  $y$  refers to the node at which the operator is applied, i.e. they are not Einstein notation subscripts representing spatial or temporal components. The RBF operators in equations (4.11) are Hardy Multiquadric RBF interpolants:

$$\Psi(r) = (r^2 + c^2)^{\frac{1}{2}} \quad (4.12)$$

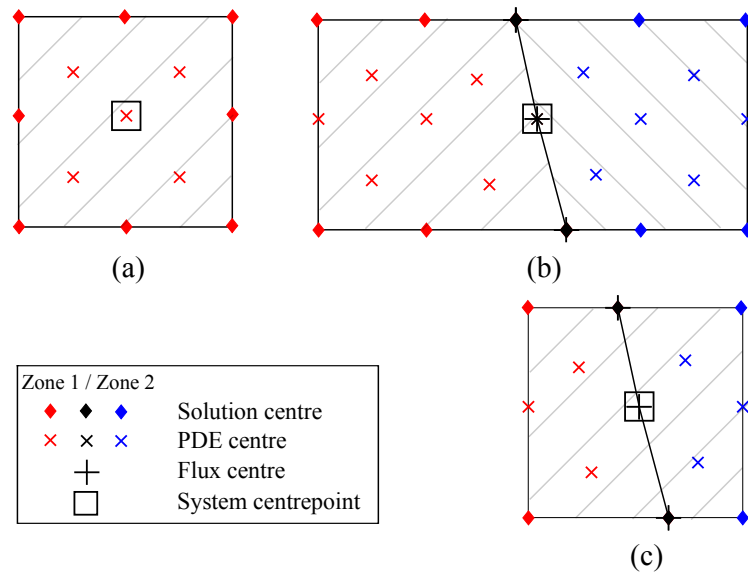


Figure 4.2: Typical RBF-FC stencil types. (a) Interior stencil. (b) Two Embedded multi-zone stencils collocated on the interface. (c) A single Auxiliary multi-zone stencil collocated on the interface. Black diagonal lines indicate the fluid-fluid interface. The grey hatching highlights separate RBF stencils.

The  $c$  term in (4.12) is known as the shape parameter, and describes the relative ‘flatness’ of the RBF functions about their centres. In this work, a non-dimensional version given as  $c^* = c/\Delta$  is used.  $\Delta$  is the average nodal separation in the local stencil.

The value of  $c^*$  has been investigated previously in [115, 116]. Values of  $c^*$  that are too small can lead to a loss of accuracy, however sufficiently large values of  $c^*$  are found to provide a solution of consistent accuracy. The use of extremely flat basis functions is therefore desirable; however, this leads to more poorly conditioned local collocation systems which may require high-precision arithmetic. Throughout this work, a relatively high shape parameter ( $c^* \geq 50$ ) is coupled with quad precision arithmetic to ensure high solution accuracy and numerical stability.

In the RBF-FC method, the global domain is broken down into a series of overlapping local stencils. These stencils are formed at every interior node  $\mathbf{x}$  in the domain, with three examples shown in Figure 4.2. Enforcing the PDE system (4.3 - 4.7) at a set of test locations, equal to the set of functional centres  $\mathbf{y}_j$  in a local stencil in zone  $l$ , a collocation matrix can be formed. The node around which the stencil is formed is identified as the centrepoint for the stencil, see Figure 4.2.

For a general interior stencil in zone  $l$  shown in Figure 4.2(a), that does not coincide with the interface, the following system of equations is formed:

$$\begin{bmatrix} B_{l,x}B_{l,y}[\Psi_{ij}] & B_{l,x}\bar{L}_{l,y}[\Psi_{ij}] \\ \bar{L}_{l,x}B_{l,y}[\Psi_{ij}] & \bar{L}_{l,x}\bar{L}_{l,y}[\Psi_{ij}] \end{bmatrix} \tau_j = \begin{bmatrix} g_{l,i} \\ \hat{S}_{l,i} \end{bmatrix} \quad (4.13)$$

In the above matrix equation, the operators with  $y$  subscript are applied to the functional centres, and the operators with  $x$  subscript are applied to the test locations. The RBF  $\Psi_{ij}$  is given by  $\Psi_{ij} = \Psi(\|x_i - y_j\|)$ .

For stencils with centrepoints on the interface, the two multi-zone methods have slightly different formulations. For the embedded multi-zone method, two stencils are formed at each interface point (shown in 4.2(b)), with the interface flux and boundary field variables (including those on the interface) appearing as unknowns in the corresponding data vector. At the stencil centrepoint the corresponding zone PDE value  $\bar{L}_l$  is enforced, giving rise to the following system for zone 1 and zone 2 respectively:

$$\begin{bmatrix} B_{1,x}B_{1,\xi} & B_{1,x}\bar{L}_{1,\xi} & B_{1,x}C_{1,\xi} & B_{1,x}Q_{1,\xi} \\ \bar{L}_{1,x}B_{1,\xi} & \bar{L}_{1,x}\bar{L}_{1,\xi} & \bar{L}_{1,x}C_{1,\xi} & \bar{L}_{1,x}Q_{1,\xi} \\ C_{1,x}B_{1,\xi} & C_{1,x}\bar{L}_{1,\xi} & C_{1,x}C_{1,\xi} & C_{1,x}Q_{1,\xi} \\ Q_{1,x}B_{1,\xi} & Q_{1,x}\bar{L}_{1,\xi} & Q_{1,x}C_{1,\xi} & Q_{1,x}Q_{1,\xi} \end{bmatrix} \tau_j = \begin{bmatrix} g_{1,i} \\ \hat{S}_{1,i} \\ C_1[\phi(\mathbf{x}, t)] \\ Q_1[\phi(\mathbf{x}, t)] \end{bmatrix} \quad (4.14)$$

$$\begin{bmatrix} B_{2,x}B_{2,\xi} & B_{2,x}\bar{L}_{2,\xi} & B_{2,x}C_{2,\xi} & B_{2,x}Q_{2,\xi} \\ \bar{L}_{2,x}B_{2,\xi} & \bar{L}_{2,x}\bar{L}_{2,\xi} & \bar{L}_{2,x}C_{2,\xi} & \bar{L}_{2,x}Q_{2,\xi} \\ C_{2,x}B_{2,\xi} & C_{2,x}\bar{L}_{2,\xi} & C_{2,x}C_{2,\xi} & C_{2,x}Q_{2,\xi} \\ Q_{2,x}B_{2,\xi} & Q_{2,x}\bar{L}_{2,\xi} & Q_{2,x}C_{2,\xi} & Q_{2,x}Q_{2,\xi} \end{bmatrix} \tau_j = \begin{bmatrix} g_{2,i} \\ \hat{S}_{2,i} \\ C_1[\phi(\mathbf{x}, t)] - h_i \\ Q_1[\phi(\mathbf{x}, t)] - f_i \end{bmatrix} \quad (4.15)$$

Note, the RBF functions  $[\Psi_{ij}]$  have been left out to save space. The data vectors (on the RHS of the equations) contain the unknown interior solution values  $g_{l,i}$  and the unknown interface solution and flux values  $C_1[\phi(\mathbf{x}, t)]$  and  $Q_1[\phi(\mathbf{x}, t)]$  respectively. From these the corresponding zone 2 interface solution and flux values can be calculated using equation (4.6) and (4.7).

In contrast to the embedded method, the auxiliary multi-zone method collocates only one stencil at each interface point (see 4.2(c)), enforcing operators from zone 1 and zone

2 in the same matrix system, i.e.:

$$\begin{bmatrix} B_{1,x}B_{1,\xi} & 0 & B_{1,x}\bar{L}_{1,\xi} & 0 & B_{1,x}C_{1,\xi} & B_{1,x}Q_{1,\xi} \\ 0 & B_{2,x}B_{2,\xi} & 0 & B_{2,x}\bar{L}_{2,\xi} & B_{2,x}C_{2,\xi} & B_{2,x}Q_{2,\xi} \\ \bar{L}_{1,x}B_{1,\xi} & 0 & \bar{L}_{1,x}\bar{L}_{1,\xi} & 0 & \bar{L}_{1,x}C_{1,\xi} & \bar{L}_{1,x}Q_{1,\xi} \\ 0 & \bar{L}_{2,x}B_{2,\xi} & 0 & \bar{L}_{2,x}\bar{L}_{2,\xi} & \bar{L}_{2,x}C_{2,\xi} & \bar{L}_{2,x}Q_{2,\xi} \\ C_{1,x}B_{1,\xi} & -C_{2,x}B_{2,\xi} & C_{1,x}\bar{L}_{1,\xi} & -C_{2,x}\bar{L}_{2,\xi} & C_{1,x}C_{1,\xi} - C_{2,x}C_{2,\xi} & C_{1,x}Q_{1,\xi} - C_{2,x}Q_{2,\xi} \\ Q_{1,x}B_{1,\xi} & -Q_{2,x}B_{2,\xi} & Q_{1,x}\bar{L}_{1,\xi} & -Q_{2,x}\bar{L}_{2,\xi} & Q_{1,x}C_{1,\xi} - Q_{2,x}C_{2,\xi} & Q_{1,x}Q_{1,\xi} - Q_{2,x}Q_{2,\xi} \end{bmatrix} \tau_j = \begin{bmatrix} g_{1,i} \\ g_{2,i} \\ \hat{S}_{1,i} \\ \hat{S}_{2,i} \\ h_i \\ f_i \end{bmatrix} \quad (4.16)$$

In the auxiliary system, the unknown solution fluxes do not appear in the data vector, with  $f_i$  instead enforcing the flux matching condition locally. Similarly, the field variable matching condition appears locally in the form  $h_i$ . The auxiliary system only enforces corresponding zone operators on each other, so that the interpolation is valid in a particular zone. A smooth interpolation cannot be performed using a single interpolating function if there are discontinuities in the operators, hence the need for zone specific interpolations that creates a block structure in (4.16). The PDE centres present at the system centrepoints of the two embedded systems are not apparent in the auxiliary system. This is because the local enforcement of the matching conditions provides a strong collocation at the centrepoint, which already takes into account the multi-zone transport scalars that appear in the PDE centres, so there is no need for a third/fourth collocation here.

If interface points fall on the periphery of an interior stencil (i.e. not at the actual centrepoint of the stencil), then the embedded method collocates both flux and solution around the periphery in keeping with the rest of the formulation (with the flux and solution appearing globally). In the auxiliary method however, only solution points are collocated on the boundary of interior stencils, with the matching conditions only enforced in the system that has a centrepoint directly on the interface. This is because a block structure would be introduced with only a limited number of flux and solution points, without any points in the interior of the alternative zone. This weakens the matrix system, making it more beneficial to use a standard interior collocation system with points solely from the zone in which the centrepoint exists.

Given known data vectors (the right hand side of (4.13)-(4.16))  $\tau_j$  can be found, which may be used to obtain the value of  $\phi_l$  at any location  $x$  within the domain or on its boundary via equation (4.11).

Around each internal node a local stencil is formed, which connects the node to its neighbours (specific stencil configuration is explored in section 4.4). An RBF collocation is formed over each of the  $N$  stencils using (4.13)-(4.16) depending on the centrepoint location in the domain, leading to [116]:

$$A_s^{(k)} \tau^{(k)} = d_s^{(k)} \quad k = 1, \dots, N \quad (4.17)$$

Where  $A_s$  are the local RBF collocation systems and  $d_s$  are the corresponding local data vectors (the right hand side of (4.13)-(4.16)). Here,  $d_s$  contains both known values, i.e.  $\hat{S}_l^n$  and unknown solution values, i.e.  $\phi_l^{n+1}$ .

To link the systems together in a global manner,  $\phi_l^{n+1}$  can be reconstructed at each system centrepoint  $x_c^{(k)}$  using (4.11) [116], i.e.:

$$\phi_l^{(k)n+1} \left( x_c^{(k)} \right) = H_l^{(k)} \left( x_c^{(k)} \right) \left[ A_s^{(k)} \right]^{-1} d_s^{(k)} \quad k = 1, \dots, N \quad (4.18)$$

where the reconstruction vector corresponds to that given in (4.11). For example, the reconstruction vector  $H_l^{(k)}$  of a point on the interface is given by:

$$H_l^{(k)} \left( x_c^{(k)} \right) = [B_{l,x} [\Psi], \bar{L}_{l,x} [\Psi], C_{l,x} [\Psi], Q_{l,x} [\Psi]] \quad (4.19)$$

By performing the reconstruction (4.18) at the centrepoint of each local system  $k$ , a sparse global system can be formed expressing the  $N$  unknown values of  $\phi^{n+1}$  at the system centrepoints:

$$A_g [\phi^{n+1}] = D_g \quad (4.20)$$

In the global system (4.20) above,  $A_g$  is the sparse global matrix formed of  $N$  rows/columns from the multiplication of the reconstruction vectors  $H_l^{(k)}$  and local system matrices  $A_s^{(k)}$  for each system centrepoint.  $D_g$  is the global data vector containing only known values. The unknown values of  $\phi^{n+1}$  appearing in each local data vector  $d_s$  are retained on the LHS of (4.20), with the known values (such as the boundary values and matching conditions etc.) moved to the RHS to form  $D_g$ .

Solving the sparse global system (4.20), the value of  $\phi^{n+1}$  are obtained at the  $N$  internal nodes. The newly computed nodal values of  $\phi^{n+1}$  may then be fed back into the the

local data vectors,  $d_s^{(k)}$ , allowing the value of  $\hat{L}_l[\phi_l^{n+1}]$  or any other operators to be reconstructed at the end of each time step.

The sparse global system is well conditioned and contains only several values on each row (equal to the number of unknowns in the local systems), meaning it can be solved with any standard sparse LU solver. A direct sparse LU solver adapted for quad-precision arithmetic is used (developed by D. Stevens at the University of Nottingham), which has been tested in many instances (see for examples [86, 113, 115, 116]). A non-sparse version is used for the factorisation of the fully populated local systems.

It should be noted that for each node that lies on the interface between the fluids, two reconstructions are performed for the embedded method, one for each RBF system with a centrepoint at that node. Since the PDE operators are different in each zone, the reconstructions will form two linearly independent rows in the global matrix. By solving this sparse global system the values of  $\phi_l^{n+1}(\mathbf{x})$  are obtained at the  $N$  internal nodes as well as  $Q_{l,x}(\phi_l^{n+1}(\mathbf{x}))$  at each interface point. For the auxiliary method, since the unknown flux terms do not appear in the data vectors, only the values of  $\phi_l^{n+1}(\mathbf{x})$  are obtained from the solution of the sparse global system and any other operators have to be reconstructed using appropriate reconstruction vectors.

At the first time step the value of  $\hat{L}_l^0$  and hence  $\hat{S}_l^0$  is unknown, and must be approximated from the initial solution field. The most straightforward way to obtain this estimate is to perform an initialisation time step of zero size; i.e. setting  $\Delta t = 0$  and utilising the existing local systems and reconstruction algorithms to perform a simple RBF interpolation of the initial data field in order to obtain  $\hat{S}_l^0(\mathbf{x}, 0)$ .

### 4.3 Adaptive quadtree datasets

The RBF-FC method described previously requires a distribution of nodal points over the domain. These can be distributed uniformly, using a geometric refinement or randomly scattered (see [113, 114, 116]). Alternatively, the nodal points can be distributed in a more optimal way in the domain to reduce the global solution error, whilst maintaining a low number of overall points. One popular method is the Greedy algorithm, demonstrated in [118]. Here the nodal points are iteratively moved until a

dataset that shows the smallest residual error is achieved. This technique along with other optimising methods are best suited to very smooth problems (particularly elliptic PDEs) and are generally computationally expensive due to their full-domain application. Since the critical areas of computation are known in the moving interface problems here, an alternative method can be employed that clusters nodal points around the interface based on a quadtree data structure. Although this method might not produce an optimal dataset with a minimal amount of nodal points as per the greedy algorithm, it should dramatically reduce the number of nodal points in the domain whilst maintaining a low solution error in comparison to uniform or geometrically refined datasets.

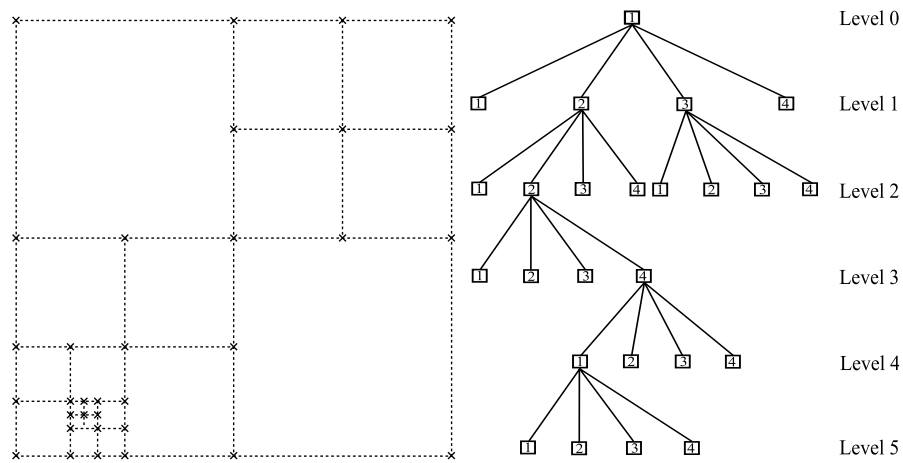


Figure 4.3: An example of a quadtree data set with corresponding levels. Dashed lines represent quadtree cell boundaries, crosses represent quadtree dataset points. Figure adapted from [99].

The quadtree data structure provides an efficient way of recursively subdividing a domain into smaller and smaller cells, based on a simple splitting criterion, such as the distance away from a critical feature, or the value of the solution gradient [119]. The process starts with a simple cell (level zero) bounding the entire domain, which is split into four level one children. In turn, each of these four children are split if they pass the splitting criterion, and splitting continues until the smallest cell size allowable in the domain is reached. The tree structure and numbering scheme used in this quadtree implementation are shown in Figure 4.3.

Each quadtree cell has a bounding domain represented by the dotted lines in Figure 4.3, where the original domain is embedded. As the bounding domain is a square in 2D, the

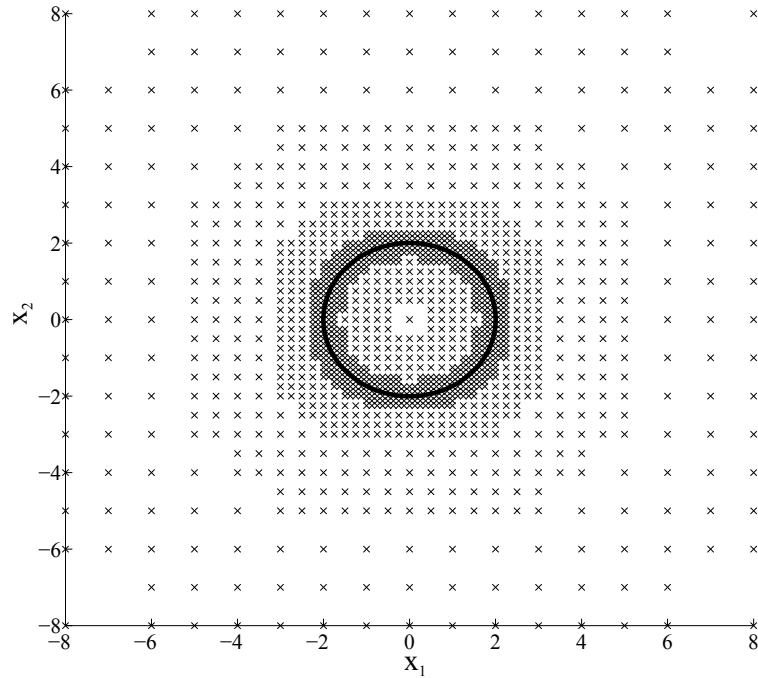


Figure 4.4: Example quadtree dataset formed around a circle with distance based grading. Circular interface shown by the bold line. Crosses represent nodal points.

side length of each cell is given by:

$$\Delta = \frac{(x_{max} - x_{min})}{2^n} \quad (4.21)$$

Where,  $x_{max}$  and  $x_{min}$  are the bounds of the global domain, and  $n$  is the level that the cell exists at. At each recursive split, the level increments by one. By recursively splitting each cell, the data set can be stored in a linked list, where each parent cell points dynamically to its child cells (if it has them). The list can be followed down the tree until leaf cells are reached which have no further children. Leaf cells are used to produce the nodal points for the RBF-FC method.

An example of a typical quadtree dataset is shown in Figure 4.4 where a simple distance based criterion has been applied to split the tree around a circle. The splitting criterion in this example works by comparing the diagonal length of the cell to the radial distance to the circle interface; if the diagonal is greater than the distance, the cell will split into four.

The quadtree data structure can easily be extended to 3D where it is known as an octree,

and cells are recursively split into 8 children. The splitting of a cell into geometrically equal children creates a data set in which the aspect ratio of cells is maintained at unity, unlike a geometrically refined data set, where cells far from the refinement can have very poor aspect ratios, which is undesirable to achieve a stable, accurate solution.

The quadtree dataset used in this work has cells representing parents and children at various levels in the tree, however, there is no explicit mesh being generated by the quadtree itself. There is no line connectivity between nodes, and no flux conditions etc imposed through the boundaries connecting the nodes together to form cells. The cells are used purely to generate discrete data points at their vertices and centres, which are passed to the strong form local RBF-FC method as nodal points.

Although the RBF-FC method can work on completely scattered irregular datasets, it is desirable to try and keep the local stencils as uniform and consistent throughout the domain as possible in order to maximise spatial convergence and accuracy [116]. The quadtree data structure provides an efficient way of generating nodal points throughout the domain with varying spatial discretisation whilst maintaining local system regularity. Fast tree searching algorithms and neighbour finding routines can be used to effectively traverse the tree and pull out the required information for the nodal points of the RBF-FC method.

Using linked lists to represent the parents and children in the tree, removal or addition of cells is straightforward from a programming context in comparison to dynamically allocating array structures. Using the cells as user defined objects, key features such as fluid velocity and PDE values can be stored directly at the cell level and accessed easily, making the program structure simple and easy to extend to very large problems.

### 4.3.1 Quadtree grading criteria

For the quadtree dataset examined in this work several requirements are imposed to maintain consistency throughout the domain, to ensure that the stencils used for the local RBF systems have nodal points of similar spatial refinement within them. To do this, certain restrictions are enforced on the quadtree data set:

1. The number of cells directly neighbouring any cell side must be no greater than two.
2. The difference in level between a cell and a neighbouring corner cell must be no greater than one.
3. Any cell that neighbours a leaf cell and is at the same grading level must not contain any children that are not leaf cells.

The above three grading criteria limit the variance of nodal separation throughout the domain, and ensure that the difference in nodal separation in an RBF stencil can be a maximum of one grading level. These restrictions are in place to ensure nodal separation consistency in the local stencils, as well as in the whole domain. These grading criteria will become apparent later in the stencil configuration section, whereby changing the uniformity of nodal separation within a stencil can have a dramatic effect on the resulting solution error.

The grading criteria enforce that the quadtree is graded and cannot jump more than one level between adjacent cells. Although non-graded quadtree datasets have been used by various authors, notably [77], a less severe grading is required here compared to their level set implementation due to the convection-diffusion problem being solved. The level set problem depends almost entirely on information very close to the interface, meaning it can grade very quickly down to very coarse cell sizes. However, for the case of convection-diffusion problems, the solution may still be changing in areas away from the interface and hence still requires a reasonably fine nodal distribution, limiting the amount of grading that can occur. Although this puts a limit on how quickly the scheme can refine from coarse cells to fine cells, the ability to jump more than one level between cells does not dramatically increase the number of nodal points in the domain compared to a non-graded quadtree.

### 4.3.2 Quadtree dataset generation

To generate the quadtree one of two splitting criteria are utilised; a distance based scheme and a solution gradient based scheme. The distance scheme checks each cell

recursively and splits a cell if the following equality is met:

$$Diag \times B_t > R_t \quad (4.22)$$

In (4.22),  $Diag$  refers to the diagonal length of the cell,  $R_t$  is the distance from the cell centre to the closest point on the critical feature and  $B_t$  is the band thickness. By increasing  $B_t$ , it is easier for the cells to be split, creating larger ‘bands’ of constant cell size in the solution domain. The critical feature could be a fluid-fluid interface, solid boundary etc. The cells can be checked at their centre, or at the centre location of the four children that could potentially be created.

The distance based scheme is efficient and simple to implement, but has a relatively slow refining rate. This is because the distance  $R_t$  changes linearly through the domain and hence splitting occurs gradually, meaning that there are sometimes more cells than required in areas of small solution gradient. To contrast this, a solution gradient scheme can be used, whereby the following criteria must be met for cells to split:

$$\left| \frac{\partial \phi}{\partial x_i} \right| \times Diag \times 10^{B_t} > \left| \frac{\partial \phi}{\partial x_i} \right|_{max} \times Diag_{min} \quad (4.23)$$

In (4.23),  $Diag_{min}$  refers to the minimum diagonal length in the domain (defined by the maximum grading level the user specifies).  $\left| \frac{\partial \phi}{\partial x_i} \right|_{max}$  is the magnitude of the maximum solution gradient in the domain (can be approximated on the first set-up initialisation time step, or is known analytically). This splitting criteria produces a much sharper refinement (if the solution gradient changes rapidly) than the distance based refinement, but requires more post-processing to ensure that the three grading criteria have been met.

The solution gradient scheme will add more nodal points than the distance based scheme in areas of high solution gradient, which do not necessarily coincide with the interface. The solution gradient scheme is therefore more applicable to general transport problems, that may have areas of rapidly changing solution away from the interface.

Both of the splitting schemes also have two more criteria for splitting a cell. Firstly, if the cell level is below the minimum specified by the user, the cell will automatically split. Secondly, if the cell is at the maximum level specified by the user, no further splitting of that cell is possible. Using either of the two splitting equalities along with

the maximum and minimum level criteria, the quadtree dataset specific for the RBF-FC scheme can be constructed using the following algorithm:

1. Generate the root cell (level 0) that bounds the solution domain.
2. Check the splitting criteria at each of the cell centre locations for the four possible children of the Root cell.
3. If a split is required, split the cell and create four new children. Perform the splitting check on each of the four children in turn.
4. Repeat step three until the criterion for splitting is not met and a leaf cell is created. The splitting is performed recursively, i.e. upon creation of new cells, each new cell is checked before checking the next cell in the level above. After checking the 4<sup>th</sup> child, the system will then go up a level and check the next child of the parent cell.
5. When all cells have been checked and no further children can be created the algorithm ends.

Upon completion of the algorithm detailed above, there will exist a simple quadtree data structure specific to the problem. The three grading criteria are then performed in order for the quadtree to meet the constraints of the RBF-FC local stencils. Firstly, the tree is graded based on its neighbours using grading criteria one and two from Section 4.3.1. If either of these criteria are not matched, the cell in question will be continually split with the four children being checked recursively until the criteria are matched. Finally as a last check the most stringent constraint is applied. This constraint requires that any neighbouring cell of a leaf cell must not have any cells within it (children, grandchildren etc.) that are more than one level different to the leaf cell. If this constraint is not met, the cell in question will be split, and the process repeated. This final constraint makes sure that the RBF stencils only contain nodes that are separated by a maximum of one cell level.

After the quadtree has been generated, the nodal points for the RBF-FC local systems can be created based on the vertices and cell centres of the leaf cells. A simple tree search can be performed, with nodal locations picked out as the tree is recursively traversed, and grouped into local stencil configurations. The stencil configuration has a significant

effect on the resulting solution, and care has to be taken with auxillary PDE centres, which will be investigated in the next section.

## 4.4 Stencil configuration

The local stencils that form the basis for the Hermitian interpolation systems in the RBF-FC method can contain a number of additional PDE points to increase the accuracy and stability of the resulting solution [120]. The inclusion of these additional points in the local stencils formed using the quadtree data structure will be explored in this section. To test various stencil configurations, a steady-state convection-diffusion-reaction (CDR) problem is considered:

$$\frac{\partial^2 \phi}{\partial x_i^2} - \left( u_1 x_1 \frac{\partial \phi}{\partial x_1} + u_2 x_2 \frac{\partial \phi}{\partial x_2} \right) - (u_1 + u_2) \phi = 0 \quad (4.24)$$

Equation (4.24) has a particular solution given by:

$$\phi_a = e^{\left( \frac{u_1 x_1^2}{2} + \frac{u_2 x_2^2}{2} \right)} \quad (4.25)$$

To create a sharp solution profile simulating that which could be found in a 2D boundary layer problem, a high velocity and large reaction term are used to push the field variable into the corner of the domain, with  $u_1 = 6$  and  $u_2 = -2$ . This produces a large drop in the field variable over a small space, shown in Figure 4.5(a).

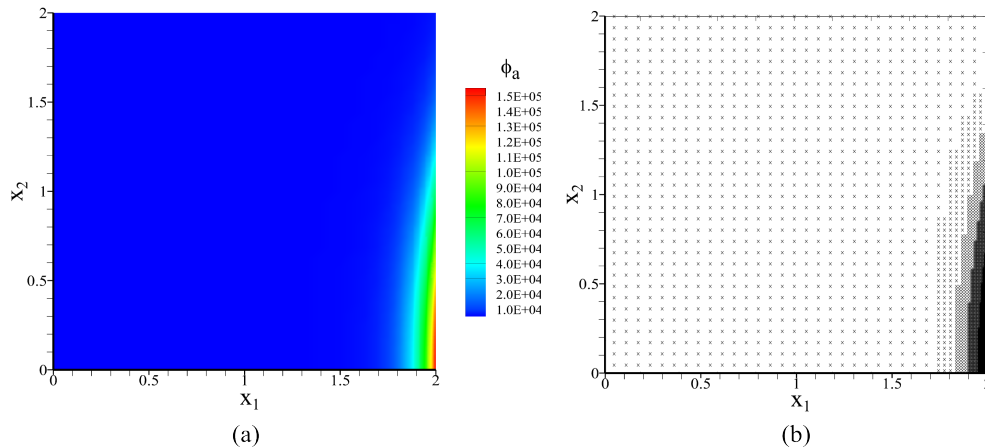


Figure 4.5: (a) Particular solution contours for the 2D CDR PDE. (b) Quadtree dataset for stencil configuration testing for the 2D CDR PDE.

For boundary operators the Dirichlet solution value is imposed over the top and left boundary, along with the normal gradient of (4.25) as a Neumann condition over the bottom and right boundaries. This means that the maximum field value in the domain occurring at  $(2,0)$  is not given by a boundary operator and instead must be predicted by the solution. Before different quadtree grading configurations are given and compared with uniform datasets, the different stencil configurations will be analysed. One specific quadtree grading is used for this test, given in Figure 4.5(b).

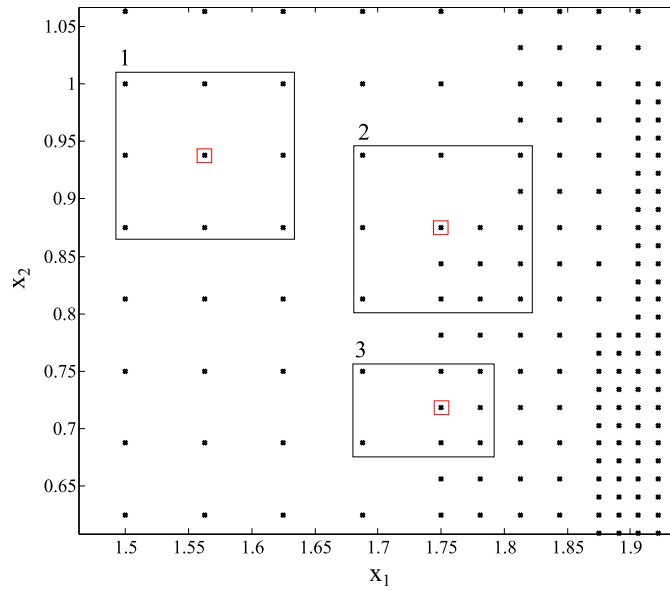


Figure 4.6: Zoomed in display of the quadtree dataset in Figure 4.5(b), showing the different stencil configurations. 1 - Normal 3x3 stencil. 2 - Crossover stencil. 3 - T-junction stencil. Red boxes indicate the stencil centrepoint.

The quadtree dataset in Figure 4.5(b) has a  $B_t$  value of 4.3 with the analytical value of the solution gradient used as the splitting criteria. In general the analytical value of the solution gradient is unknown, in which case the solution gradient can be approximated numerically, or a combination of distance based splitting and solution gradient approximation can be used to refine the dataset. The minimum cell level in the domain is 5, with a maximum of 9. The quadtree sharply transitions from level 5 - 9, due to the low  $B_t$  value combined with the solution gradient splitting criteria.

Throughout all simulations in this section and the transient performance section, a non-dimensional shape parameter  $c^*$  value of 90 is used, providing a good balance between matrix conditioning and accuracy. Increasing the shape parameter increases the basis function flatness and hence the solution accuracy. However taking the

shape parameter too high creates collocation matrices which are poorly conditioned and require high-precision arithmetic to solve accurately. Using a relatively high non-dimensional shape parameter of 90, the solution accuracy is invariant to increases in shape parameter, and the collocation matrices are well conditioned enough to be solved using quad-precision arithmetic (see [115, 116] for more detail on  $c^*$ ). The shape parameter  $c$  used for each RBF collocation system is found by scaling the non-dimensional shape parameter with the average side length of the cells used to generate the nodal points in the corresponding local stencil. This means that the shape parameter varies throughout the domain based on the local nodal separation.

Using the quadtree dataset there is the possibility of three different kinds of local stencils using the base 3x3 node configuration. The stencil configurations form the basis of the RBF-FC collocation systems, which use the points from the corresponding stencils to form local Hermitian interpolation systems centred at the stencil centrepoint. The 3x3 local stencil is used as the base throughout, as no special truncation or extension needs to be applied at the boundary of the domain, and the solution time of the resulting local systems is very small. Using larger 5x5 stencils would also require the grading to transition more gradually from coarse to fine.

A typical 3x3 stencil generally sits at the centre of four quadtree cells (stencil 1 in Figure 4.6). The standard 3x3 stencil is used when all surrounding cells are of the same level, in the interior of a band. When crossing from one level to the next at a band boundary, there will be two further types of stencils: crossover stencils, and T-junction stencils shown in Figure 4.6. No PDE centres or solution centres are shown in Figure 4.6, only the raw quadtree nodal points.

Crossover stencils cover four cells, some of which have children associated with them. This leads to a stencil containing nodes with varying spatial discretisation, unlike the standard 3x3 node stencil. T-junction stencils on the other hand cover only three cells, and as such have a hanging node where there is no direct neighbour. These stencils have the smallest number of nodes and are generally the weakest part of the solution. The T-junction and crossover stencils can include a varying number of additional PDE centres to increase solution stability and to try and maintain consistent accuracy with the standard 3x3 stencils. The different configurations that can be used for the crossover and T-junction stencils are shown in Figure 4.7 and 4.8 respectively.

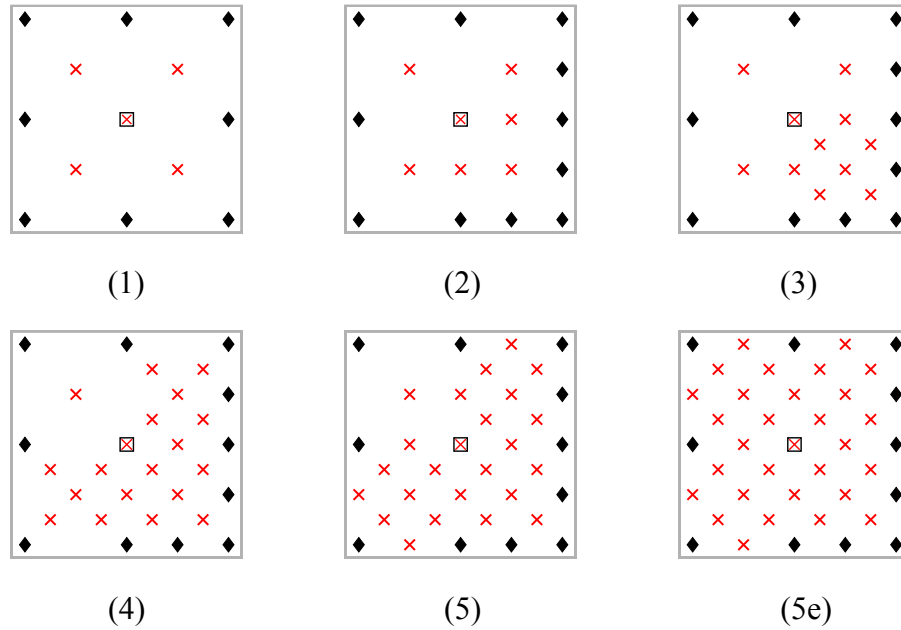


Figure 4.7: Different crossover stencil configurations. Diamonds represent solution centres. Crosses represent PDE centres. The black box indicates the system centrepoint.

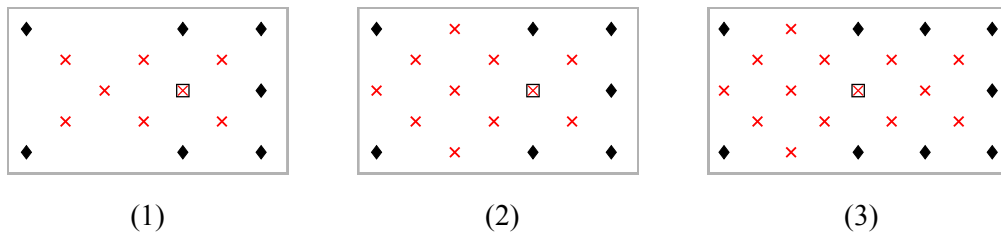


Figure 4.8: Different T-junction stencil configurations. Diamonds represent solution centres. Crosses represent PDE centres. The black box indicates the system centrepoint.

The PDE points shown as crosses in Figures 4.7 and 4.8 are added into the local stencils when they are formed from the raw nodal points of the quadtree dataset. PDE points are not included in the global system and instead act solely at the local interpolation level, as in the enhanced RBF-FD method. To highlight the differences in the stencil configurations, and their effect on the overall solution error, results are presented from the 2D convection-diffusion-reaction test case shown above in Figure 4.5. The dataset in Figure 4.5(b) is used, with 3508 solution centres in the domain. To compare the different global solutions errors, the  $L_1$ ,  $L_2$  and  $L_{inf}$  relative error norms are used:

$$L_1 \text{ error} = \frac{\sum_1^N (\phi - \phi_a)}{N(\phi_{a,max} - \phi_{a,min})} \quad (4.26)$$

Crossover Stencil type	T-junction Stencil type	$L_2$ Relative Error Norm	$L_{inf}$ Relative Error Norm
Uniform dataset, Lvl 6		$1.22 \times 10^{-4}$	$1.24 \times 10^{-3}$
1	1	$9.22 \times 10^{-5}$	$1.28 \times 10^{-3}$
2	2	$5.72 \times 10^{-4}$	$2.86 \times 10^{-3}$
3	2	$5.94 \times 10^{-4}$	$2.95 \times 10^{-3}$
4	2	$1.06 \times 10^{-4}$	$1.22 \times 10^{-3}$
5	2	$7.57 \times 10^{-5}$	$7.99 \times 10^{-4}$
5	3	$1.80 \times 10^{-5}$	$2.99 \times 10^{-4}$
5e	1	$2.38 \times 10^{-4}$	$1.32 \times 10^{-3}$
5e	2	$1.04 \times 10^{-4}$	$1.22 \times 10^{-3}$
5e	3	$1.40 \times 10^{-5}$	$2.74 \times 10^{-4}$

Table 4.1:  $L_2$  and  $L_{inf}$  relative error norms for various stencil configurations on the 2D CDR problem using the 3508 solution centre dataset in Figure 4.5(b).

$$L_2 \text{ error} = \sqrt{\frac{\sum_1^N (\phi - \phi_a)^2}{N(\phi_{a,max} - \phi_{a,min})^2}} \quad (4.27)$$

$$L_{inf} \text{ error} = \frac{\text{Max}|\phi - \phi_a|}{\phi_{a,max} - \phi_{a,min}} \quad (4.28)$$

Here,  $\phi$ ,  $\phi_a$ ,  $\phi_{a,max}$  and  $\phi_{a,min}$  represent the calculated solution value, the analytical solution value and the maximum and minimum analytical solution value in the domain respectively.  $N$  is the number of solution centres in the domain. The various stencil configuration  $L_2$  and  $L_{inf}$  errors for the 2D CDR problem are shown in table 4.1, with the corresponding uniform dataset shown for comparison.

From table 4.1, it can be seen that the  $L_2$  and  $L_{inf}$  errors can vary by one order of magnitude depending on the stencil configuration used, according to how the points are distributed in the stencils. Although all the non-uniform distributions have at least the same order of accuracy as the uniform stencil, some errors are slightly higher whilst other datasets have an order of magnitude lower error.

Generally, by increasing the number of points within a stencil the  $L_2$  error drops. However, this is not always the case, especially when extra PDE points are introduced into some parts of the stencil but not others. If a disparity in length scales exists within the stencil (for example crossover stencil types 3, 4 and 5) then the error can be increased. This is due to the global reconstruction of the solution at the centre of the stencil.

Locally, increasing the number of PDE points in the stencil always gives a more accurate reconstruction of the solution. However, in the global reconstruction of the system centrepoint, several overlapping stencils use the same point, with the point appearing as a solution centre for several systems, a boundary point for several systems and an internal PDE point for several other systems. The number of overlapping systems can be as high as 10, meaning the accuracy of that one point affects the accuracy of many others. It is therefore paramount that the point exists within stencils that have as near to a uniform nodal discretisation as possible to maintain uniformity with overlapping stencils. If overlapping stencils use the same point but the stencils have different length scales within them then the crossover systems hold back the solution error, even though there are some stencils with very fine uniform nodal discretisation using that same point, for example in the 3-2 stencil configuration. The 3-2 stencil configuration refers to a quadtree dataset using crossover stencils of type 3 and T-junction stencils of type 2.

By keeping the length scale within the local systems uniform, and making sure that overlapping systems are all using a similar nodal discretisation, the  $L_2$  error is kept to a minimum. This can be seen with the 1-1, 5-3 and 5e-3 configurations in Table 4.1. Using the extended T-junction system type 3 makes the T-junctions become much more accurate as their range of influence is extended. This is highlighted by the drop in  $L_{inf}$  error, which indicates that the maximum error found in the domain (generally located around the T-junction stencils) is reduced by around an order of magnitude compared to the cases with T-junction system type 2. For the steady-state case presented here, the 5e-3 configuration is preferred.

The crossover stencils can contain as many as 41 points (equivalent to a regular 5x5 node stencil), however, the global solution time does not increase significantly compared to a case with much smaller system sizes. The crossover and T-junction stencils only represent around 10% of the total number of stencils, and as such the solution of the local collocation systems and weights vectors uses a very small proportion of the overall solution time. Introducing extra PDE points does not affect the number of global solution centres and hence the solution time of the sparse global matrix remains unchanged.

To compare different refinements, various quadtree datasets are used to compute the solution to the 2D CDR equation (4.24). Changing the maximum and minimum cell

levels within the domain and the band thickness creates different quadtree datasets which can be compared to uniform datasets. In Figure 4.9, the error from different dataset configurations can be seen. The a and b datasets refer to cases that differ only in  $B_t$  value, in which b datasets have larger  $B_t$  values than a, creating more nodal points in the domain. All of the configurations use the  $5e-3$  stencil set-up shown previously, and all show a much lower solution error than the corresponding uniform dataset. The average nodal separation was calculated by taking the number of solution centres in the quadtree dataset and equating the average separation to that of the equivalent uniform case with the same total number of solution centres, i.e. solutions with the same average separation have the same total number of solution centres.

The error in Figure 4.9 can be seen to be largely dominated by the maximum cell level in the domain. The maximum cell level dictates the smallest nodal separation, with the maximum level occurring in the bottom right of the domain. As the maximum cell level in the domain increases (denoted by the numbers next to the data-points in Figure 4.9), the error reduces.

It is worth noting, that some datasets, specifically those with a minimum cell level 5, exhibit lower error than a corresponding dataset with the same maximum level but with a higher minimum level (i.e. the dataset with levels 5-10 compared to 6-10). This is because the dataset with levels 5-10 exhibits a more strongly varying dataset, with more nodes at the level 10 refinement than in the 6-10 dataset. In the level 6-10 dataset, there are more nodal points in the outer regions of the domain where the solution is not varying significantly. Therefore the level 6 nodal points do not improve the solution accuracy, but decrease the average nodal spacing in the domain. However, in the level 5-10 dataset, there is a similar average nodal separation, but there are significantly more nodes at the higher refinement, leading to an improved solution.

In Figure 4.9 there appears to be optimum datasets for the domain size and problem being solved; those with a minimum cell level of 5. In these cases the solution exhibits around eight times lower error than the corresponding uniform datasets with the same number of solution centres. When comparing to a higher resolution uniform dataset (such as the level 7 uniform case), there is roughly the same solution error but only 3508 solutions centres (Minimum level 5, maximum level 9 dataset in Figure 4.9) compared to the 16129 solution centres used by the uniform case, a factor of 4.6 less. The

---

minimum level 5 datasets give a good range of nodal discretisations in the domain, whilst maintaining an accurate coarse representation of the solution, resulting in more optimal performance than the minimum level 3, 4 or 6 datasets. The difference between the maximum and minimum cell level within the domain is largely controlled by the domain size and the sharpness of the solution. For this test case, a maximum difference of around five levels could be achieved in the domain.

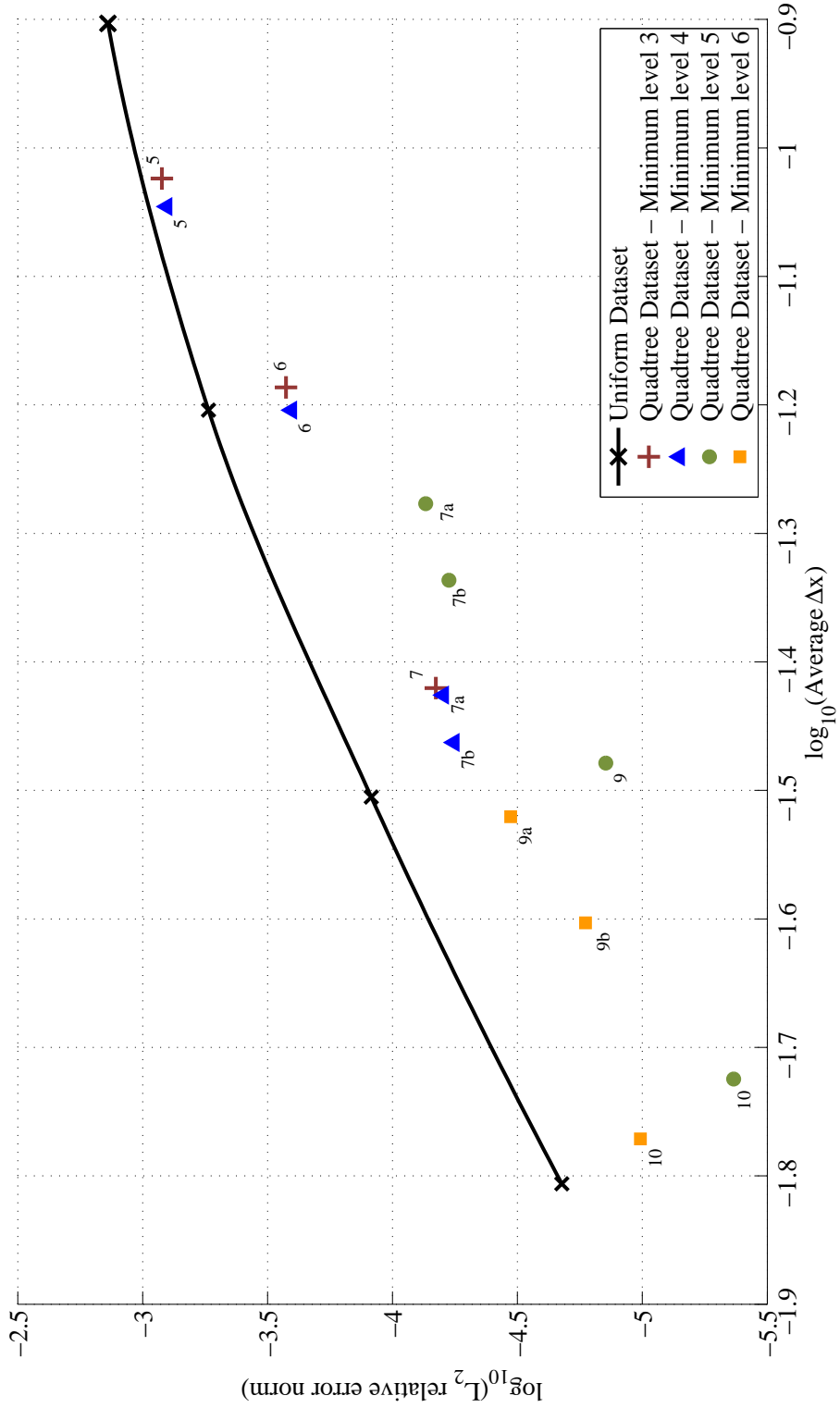


Figure 4.9: Steady-state  $L_2$  relative error norm for various uniform and quadtree datasets. Numbers next to data points refer to the maximum cell level in the domain. b datasets have larger  $B_t$  values than a, creating more nodal points in the domain.

## 4.5 Transient verification

The quadtree dataset has been shown to work well for a steady-state 2D CDR PDE, with the solution exhibiting a boundary layer type profile. Although the quadtree dataset shows significant improvements over the uniform dataset for steady-state problems, even greater benefits can be found in transient cases.

The transient time stepping algorithm proceeds as a series of inhomogeneous steady-state problems, with the inhomogeneous term storing information from the previous time step. Therefore, using a quadtree dataset can bring significant reductions to the wall clock time for each time step whilst still maintaining an accurate solution. In this section the evolution of a two-dimensional advection problem is analysed, described by the first order hyperbolic equation:

$$\frac{\partial \phi}{\partial t} + u_i \frac{\partial \phi}{\partial x_i} = 0 \quad (4.29)$$

In the case of a constant velocity (along a specific curve), the initial condition should be advected by the hyperbolic PDE without a change of shape. To compare the quadtree dataset to uniform cases, the rotation of a Gaussian packet is studied in 2D, subject to an irrotational velocity field. The advection of a Gaussian packet is considered in the absence of diffusion at infinite pecllet number using equation (4.29) above. The initial condition of the Gaussian packet is defined in the interior of the domain  $\mathbf{x} = (x_1, x_2)$  with  $-1 \leq x_1 \leq 1$ ,  $-1 \leq x_2 \leq 1$  by:

$$\phi(\mathbf{x}, 0) = e^{-\alpha_g \|\mathbf{x} - \hat{\mathbf{x}}\|^2} \quad (4.30)$$

Where,  $\hat{\mathbf{x}}$  is the centrepoint of the Gaussian packet at  $t = 0$  and  $\alpha_g$  is the relative width of the packet about the centrepoint. Dirichlet boundary conditions are enforced around the edge of the domain, which must be updated at each iteration based on the analytical position of the Gaussian packet. The irrotational convective field is given by:

$$\vec{u} = (x_2, -x_1) \quad (4.31)$$

The Gaussian packet is centred initially at  $\hat{\mathbf{x}} = (0.5, 0.0)$  and allowed to rotate for  $t = 2\pi$ , completing one full revolution. The irrotational convective field means the flow is not aligned with the direction of the dataset. The centre of the Gaussian packet

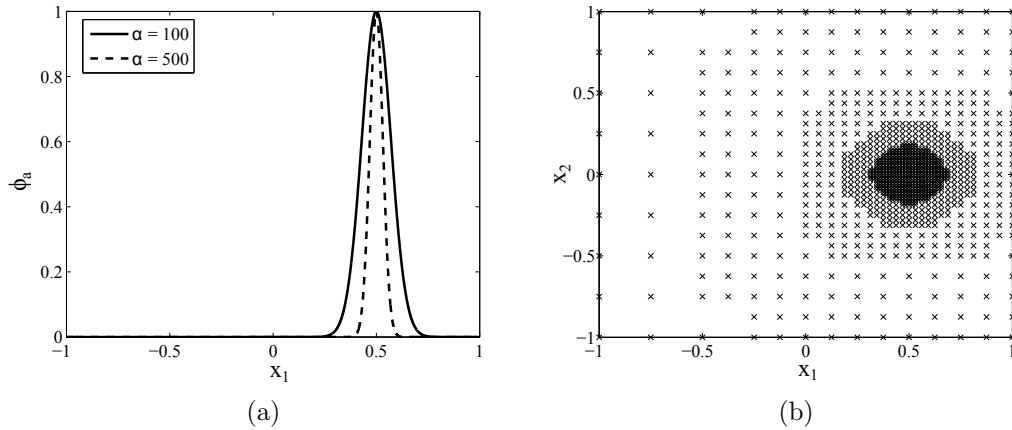


Figure 4.10: (a) 1D Cross-section along  $y = 0$  for two different Gaussian packet initial conditions. (b) Typical graded quadtree dataset for a Gaussian packet with  $\alpha_g = 500$  at  $t = 0$ .

should translate along the arc of a circle centred at the origin with radius  $r = |\hat{\mathbf{x}}|$ . In this transient example, two different values of  $\alpha_g$  will be demonstrated, showing the quadtree dataset on a relatively smooth function with  $\alpha_g = 100$ , and a very sharp function with  $\alpha_g = 500$ , shown as a 1D cross-section through the domain in Figure 4.10(a).

Figure 4.10(b) shows a typical quadtree dataset used in the transient simulations, refining from levels 3-7 around an  $\alpha_g = 500$  Gaussian packet. The transient nature of the problem introduces several extra steps in the quadtree generation and updating at each time step. These steps have been summarised below:

1. At the first time step, perform the initial grading, interpolate the value of  $\hat{L}$  using a time step size of zero and then perform the first time step. Advance time by  $\Delta t$ .
2. Using the analytical solution gradient of the Gaussian packet at the current time step, update the quadtree dataset. Firstly, perform the splitting check for gradient based refinement on each cell centre. If any cells are above the minimum permitted cell level but fail the splitting criteria, the cell can be removed and all associated nodes removed from the domain. If the cell is below the maximum level permitted and passes the splitting check, split the cell and create new nodes at the cell centres and cell vertices according to the stencil configuration being used.
3. For all nodes in the domain, reconstruct the value of  $\hat{L}$  using the existing local systems with updated RHS vectors containing the corresponding field values at the current time.

4. Solve for the next time step. Advance time by  $\Delta t$ .
5. Repeat steps 2 - 4 until the required number of time steps have been performed.

In the above procedure, the cost of  $NT$  time steps, with  $N_{sys}$  local systems of size  $N_m$  is approximately equal to [115]:

$$COST \approx NT \left( \sum_{k=1}^{N_{sys}} \beta_c N_m^{(k)} + \sum_{k=1}^{N_{changed}} \left[ \alpha_c \left( N_m^{(k)} \right)^2 + \frac{2}{3} \left( N_m^{(k)} \right)^3 \right] + SPARSE \right) \quad (4.32)$$

Where,  $\alpha_c$  represents the number of operations to compute each entry in the collocation matrix and  $\beta_c$  represents the number of reconstructions (there can be as many as 10 overlapping systems) required to compute each inhomogeneous PDE value. SPARSE refers to the cost of solving the global matrix at each time step, which varies linearly with the number of local systems. Both  $N_{sys}$  and  $N_{changed}$  can vary between time steps, as nodal points are added or removed from the domain. On the first time step,  $N_{changed} = N_{sys}$ . Equation (4.32) does not include the cost of initialising or updating the quadtree dataset, as these operations are typically orders of magnitude quicker than solving the local systems or sparse global matrix.

In equation (4.32), there is the cost of changing local systems at each time step, due to the changing geometry of the quadtree given by the  $N_{changed}$  summation. If nodes are added or removed from the domain, the collocation systems must be reformed and solved. This introduces extra cost compared to a fixed spatial discretisation of nodes if the velocity and diffusivity fields remain constant (i.e  $N_{changed} = 0$  after the first time step). However, this extra cost is typically very small as  $N_{changed}$  is generally smaller than  $N_{sys}$  by more than an order of magnitude. Also, in practical problems, where the velocity/diffusivity field will likely change between time steps, the local systems must be re-formed and solved at each time step, meaning there is no additional cost penalty for changes in geometry of the local systems.

The updating of the inhomogeneous PDE value at the end of each time step (step 3 above) in preparation for the next time step is critical to the performance of the scheme, and must be performed accurately to ensure information is propagated through time. The inhomogeneous PDE term,  $\hat{L}$  can be reconstructed from several stencils that overlap the node in question, using a weighted average of the stencils. The weighted

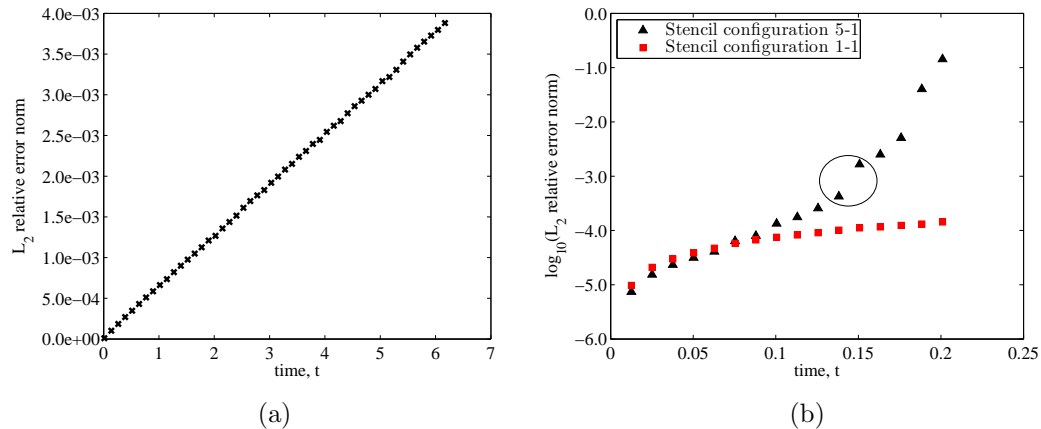


Figure 4.11: (a) -  $L_2$  error norm at 10 time step intervals as an  $\alpha_g = 100$  Gaussian packet is convected one revolution using a 1-1 stencil configuration. The quadtree dataset is graded from level 3-7 with 600 points (b) - Initial time steps of the same Gaussian packet convection using two different stencil configurations. The circle highlights two poor  $\hat{L}$  reconstructions.

average can be undertaken in a partition of unity sense, whereby different weights are given to surrounding stencils based on their distance from the nodal point. However, in the case of the quadtree dataset, there exist several overlapping stencils of differing nodal discretisations and accuracy, and hence the coarser stencils can weaken the  $\hat{L}$  reconstruction and skew the weighted average to be less accurate. These stencils can be removed from the reconstruction algorithm, but it is not always obvious which stencils are causing the inaccuracies.

Using a stencil configuration that allows crossover stencils to have different nodal discretisations within them (such as the 5-1 configuration), creates overlapping stencils that have different accuracies of reconstruction within the stencil. In areas of the stencil where there are many nodal points, the reconstruction is generally strong, but in the coarser regions reconstruction can be weaker.

If several of these crossover stencils overlap a node where the  $\hat{L}$  value is being reconstructed, the reconstructions from these stencils can vary quite dramatically. This means that the  $\hat{L}$  can be approximated poorly for the next time step and the accuracy of the scheme is reduced. This is highlighted by the circle encompassing two points in Figure 4.11(b) in which two poor  $\hat{L}$  reconstructions in the domain have led to a step jump in the  $L_2$  error, which eventually leads to the error spiralling up. These poor reconstructions can be avoided by selecting the higher resolution overlapping stencils

and stencils that are not crossover stencils for the nodal reconstruction. However, this requires selective biasing of the reconstruction, and can lead to using stencils purely in the upwind or downwind direction, removing the implicit upwinding feature of the centrally defined stencils.

The most effective technique to maintain the accuracy of the  $\hat{L}$  reconstruction is to use the most basic 1-1 stencils throughout the domain (stencils shown in Figures 4.7 and 4.8). Although there are less overlapping stencils for each node, the  $\hat{L}$  reconstruction is much more consistent for the stencils that do overlap, and hence a straightforward weighted average can be used, rather than selective biasing of stencils. The global solution error at each time step is slightly higher than the larger stencil configurations (as can be seen in Figure 4.11(b) in the first 5 time steps), but the  $\hat{L}$  reconstruction is significantly more accurate meaning that consistent errors are obtained at each time step. The error grows linearly with time, as can be seen in Figure 4.11(a), which is expected due to the inhomogeneous boundary value problem being solved at each successive time step.

Temporal convergence studies are now presented for two Gaussian packet convection cases, with  $\alpha_g = 100$  and  $\alpha_g = 500$ . These cases were run using the 1-1 stencil configuration (crossover stencil 1 and T-junction stencil 1 in Figures 4.7 and 4.8 respectively), and various band thickness values to generate a suitable grading, the results of which are shown in Figures 4.12 and 4.13.

In Figure 4.12 it can be seen that all quadtree datasets outperform the corresponding uniform datasets, providing lower error for the same number of points. The Quadtree grading from level 5-7 uses 1260 points, but exhibits the same error at small time step sizes as the uniform level 6 data set with 3969 solution centres, a factor of three greater. This trend continues with higher resolution datasets, where a factor of three fewer points can be used to generate the same level of error using a quadtree dataset.

A similar trend can be seen in the  $\alpha_g = 500$  graph, however due to the much sharper Gaussian packet, the quadtree datasets perform much better relative to the uniform datasets. Using a uniform data set with level 8 cells throughout, giving  $N = 65025$  points the same error is produced as the quadtree dataset graded from level 5-9 with only 3825 points. This is a factor of 17 less in the total number of points, but with the same level of error.

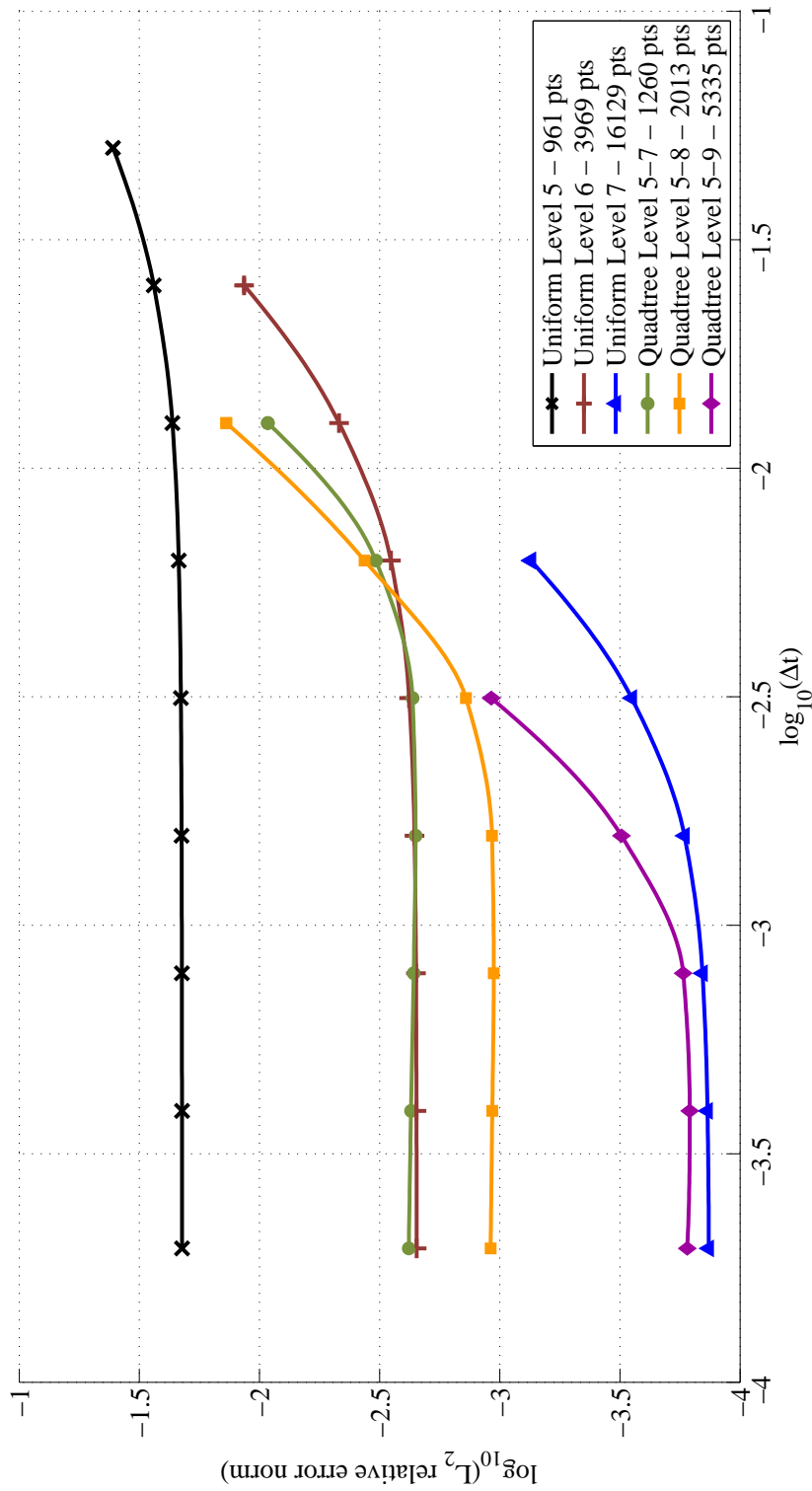


Figure 4.12: Gaussian packet temporal convergence with  $\alpha_g = 100$  for various uniform and Quadtree datasets.

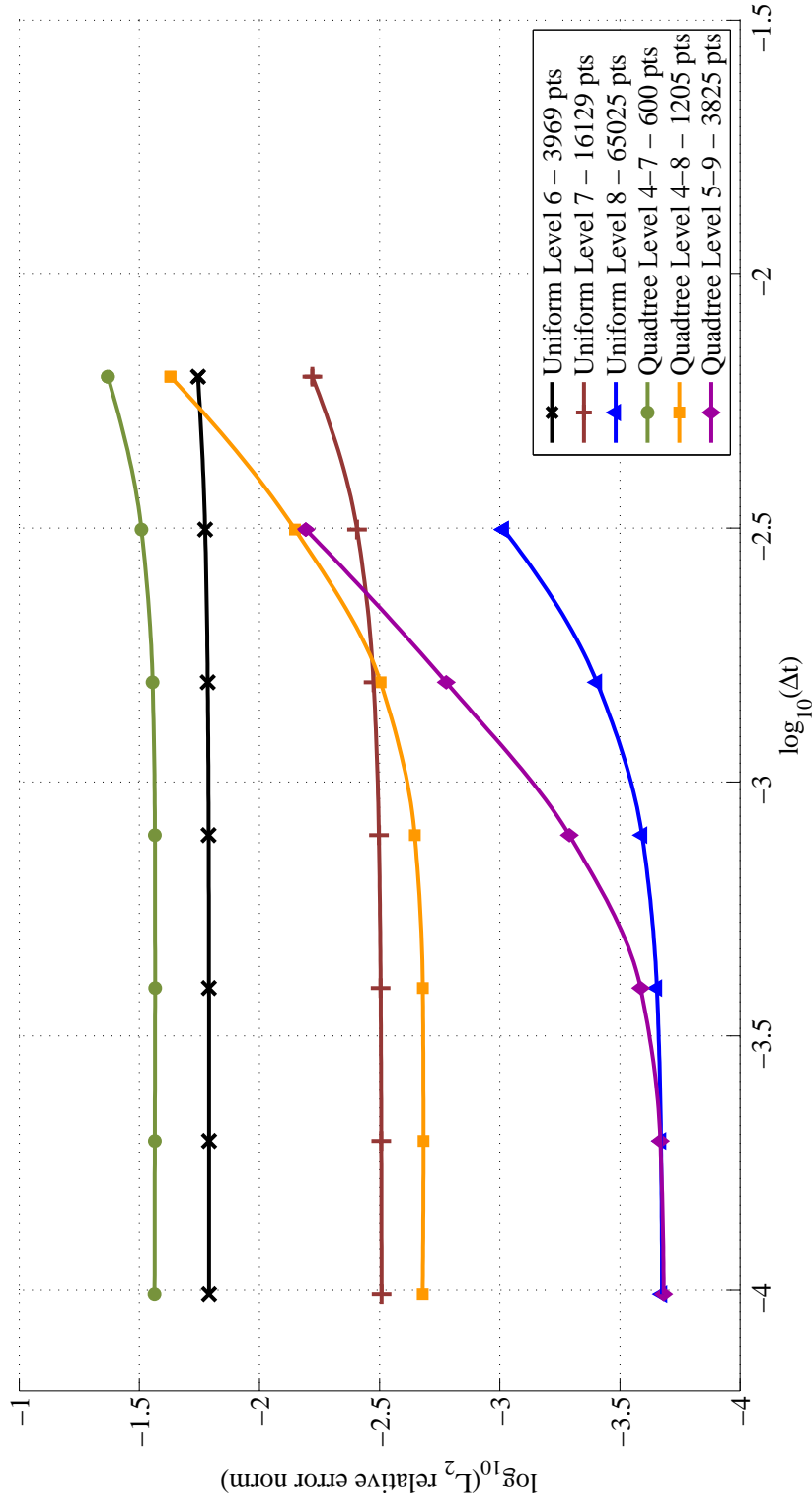


Figure 4.13: Gaussian packet temporal convergence with  $\alpha_g = 500$  for various uniform and Quadtree datasets.

Between the uniform datasets in both Figure 4.12 and 4.13 there is roughly a 4<sup>th</sup> order spatial convergence between the datasets. Using the 2<sup>nd</sup> order Crank-Nicholson scheme for the time derivatives, 2<sup>nd</sup> order temporal convergence is exhibited when the datasets have a fine enough spatial resolution to allow the temporal resolution to be the limiting factor in the error.

It is worth noting that some of the plots in Figure 4.12 and 4.13 do not extend all the way to the first time step size being tested using the coarsest spatial resolutions. This is due to instability that can occur using the RBF-FC scheme with very fine spatial resolutions and very coarse temporal resolutions. Although the 2<sup>nd</sup> order Crank-Nicholson method is an implicit method and is unconditionally stable for several PDEs (notably the heat equation), oscillations can occur which grow with time when using a very large time step size and fine spatial resolution with infinite Peclet number flows, for more details about this anomaly in the RBF interpolation see [115]. This instability is exacerbated when using the quadtree data set, as the spatial resolution can vary throughout the domain, meaning oscillations can occur within the very refined parts of the domain and be magnified in the coarser regions later in time. However, using a large time step size and fine spatial resolution is generally not considered in practical applications, as the error will be limited by the large time step size. The oscillations can also be damped by using an artificial diffusion term, demonstrated in [115].

The quadtree datasets demonstrate clear improvement over uniform datasets for capturing sharp functions through time. Using a 1-1 stencil configuration ensures consistent and accurate  $\hat{L}$  reconstruction at each time step, allowing effective propagation of previous time step information.

To further demonstrate the robustness of the adaptive RBF-FC method, specific solution contours can be extracted at time increments through the simulation. A specific contour value can be found using a Taylor expansion with nearby grid points, shown in Figure 4.14.

The function,  $\phi(x_1, x_2)$  can be represented through a Taylor series as:

$$\phi(\mathbf{x}) = \phi(a_1, b_1) + (x_1 - a_1) \frac{\partial \phi(a_1, b_1)}{\partial x_1} + (x_2 - b_1) \frac{\partial \phi(a_1, b_1)}{\partial x_2} + \mathcal{O}(\delta^2) \quad (4.33)$$

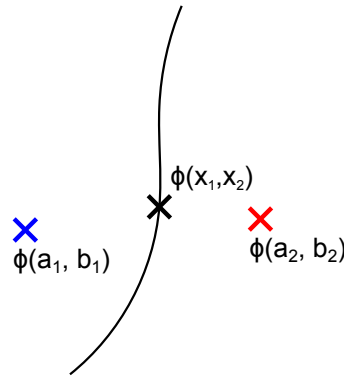


Figure 4.14: Diagram showing known test points,  $(a_1, b_1)$ ,  $(a_2, b_2)$  and unknown contour point for extraction  $(x_1, x_2)$ .

$$\phi(\mathbf{x}) = \phi(a_2, b_2) + (x_1 - a_2) \frac{\partial \phi(a_2, b_2)}{\partial x_1} + (x_2 - b_2) \frac{\partial \phi(a_2, b_2)}{\partial x_2} + \mathcal{O}(\delta^2) \quad (4.34)$$

In equations (4.33) and (4.34),  $\delta$  represents the distance between the points. Through substitution of the known function values and spatial derivatives at the test points, equations (4.33) and (4.34) can be solved to find the location  $(x_1, x_2)$  of the contour.

The derivatives at the test points  $(a_1, b_1)$ ,  $(a_2, b_2)$  can be calculated using the overlapping RBF local Hermitian systems. Applying the derivative operators to equation (4.11), the existing local systems can be used to obtain the spatial derivative values at the test points. It is worth noting that the Taylor expansion above could be extended to include second order and mixed spatial derivatives to extend the order of approximation, however, in practice with suitably close test points, the first order Taylor series is sufficient. Candidate test points can be found by choosing existing nodal points whose solution falls within a suitably small tolerance of the contour value.

In Figure 4.15 the  $\phi(x, y) = 0.1$  contours from the  $\alpha_g = 100$  Gaussian profile can be seen. Here, a quadtree level 5-7 dataset is used with 2000 time steps, with the contour output every 200 time steps. Figure 4.15 shows that the  $\phi(x, y) = 0.1$  contour remains circular throughout the simulation. There is no oscillation or change in shape of the contour, and the circle retains a constant area as the Gaussian packet is advected. The contour remains centred on the analytical centrepoint of the Gaussian packet, with the solution showing no lag or change in shape, meaning the initial condition has been almost perfectly advected along the curve  $dx_1/dx_2 = u_1(x_1, x_2, t)/u_2(x_1, x_2, t)$ .

In more traditional polynomial based FD or FV approaches where upwinded stencils

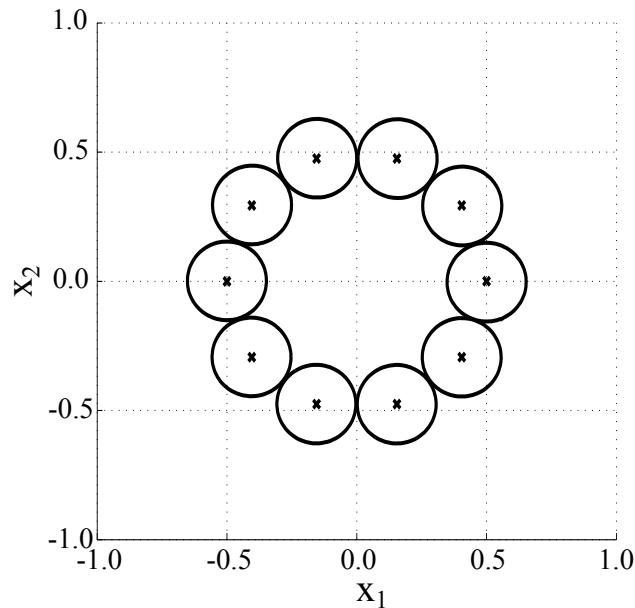


Figure 4.15:  $\phi = 0.1$  contour evolution with time. Solid lines represent the  $\phi = 0.1$  contour at 200 time step intervals. The crosses are the analytical centerpoints of the Gaussian packet.

are used, the solutions tend to lose mass with time, and the contour reduces in size as the Gaussian packet is advected. Using centrally defined stencils can also result in a deformed contour, as oscillations at the solution front can change the profile. The contour extraction demonstrates the robustness of the RBF-FC scheme with a quadtree dataset, showing that stable, non-diffusive solutions can be obtained with centrally defined stencils on infinite Peclet number problems

## 4.6 Multi-zone verification

The adaptive quadtree dataset has been verified in the previous sections on single-zone convection-diffusion cases, which was necessary to assess the quality of the adaptive quadtree method in the RBF-FC context and the appropriate stencil and PDE update configurations to use. In the next sections, the embedded and auxiliary multi-zone methods are verified on three test case to demonstrate the robustness of the proposed multi-zone schemes and their accuracy on some well known test cases. The following examples are presented: a fixed interface steady-state multi-zone case, a fixed interface

transient case and a moving interface transient case to verify the performance for problems similar to those in the full viscous fingering problem.

#### 4.6.1 Steady-state fixed interface

Here, a steady-state convection-diffusion problem is considered with a discontinuous flux across the interface. The problem is solved using a two-dimensional Cartesian coordinate system assuming zero lateral flux and Dirichlet temperatures at the outer walls, shown in figure 4.16. The convection-diffusion problem in each zone  $l$  can be expressed in Cartesian form as:

$$D_l \left( \frac{\partial^2 \phi_l}{\partial x_1^2} + \frac{\partial^2 \phi_l}{\partial x_2^2} \right) + \frac{D_l}{x_1} \left( \frac{\partial \phi_l}{\partial x_1} \right) = 0 \quad l = 1, 2 \quad (4.35)$$

The matching conditions of solution and flux at the zone interface are given by:

$$\phi_1 = \phi_2 \quad (4.36)$$

$$D_1 \frac{\partial \phi_1}{\partial x_1} + \frac{D_1}{x_1} \phi_1 = D_2 \frac{\partial \phi_2}{\partial x_1} + \frac{D_2}{x_1} \phi_2 \quad (4.37)$$

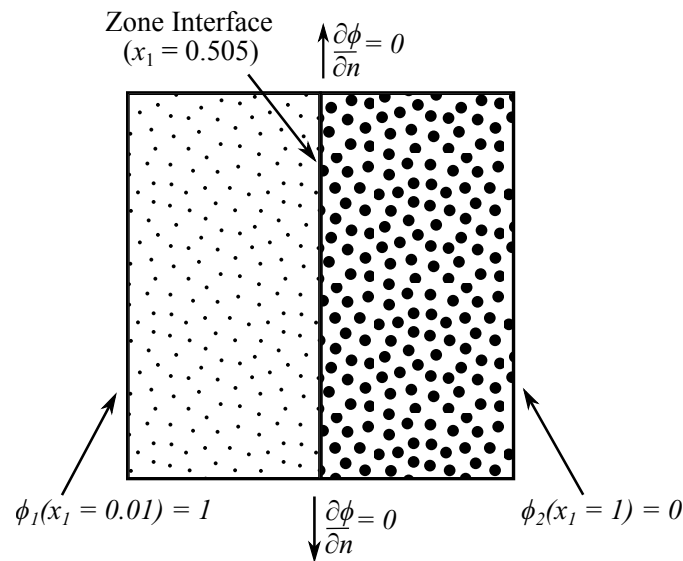


Figure 4.16: Two-dimensional Cartesian setup for the multi-zone convection-diffusion problem. The zone interface marks the transition between different material properties.

The flux in equation (4.37) is discontinuous across the zonal interface, since the diffusivities in each zone differ. Equation (4.35), subject to the interface matching conditions (4.36, 4.37) and boundary conditions in Figure 4.16 represents a 1D convection-diffusion problem, which has the following analytical solution [121]:

$$\phi_l = A_l + B_l \ln(x_1) \quad (4.38)$$

where  $A_l$  and  $B_l$  can be found using the appropriate boundary and interface conditions. Equation (4.35) is solved on a square problem domain, with  $0.01 \leq x_1 \leq 1$ ,  $0.01 \leq x_2 \leq 1$ . The zonal interface is located at  $x_1 = 0.505$ . Since there is a strong convective field near  $x_1 = 0.01$ , and a discontinuous flux at the interface, a uniform distribution of nodes are used in the relatively small domain to test the RBF-FC multi-zone methods.  $c^* = 70$  throughout.

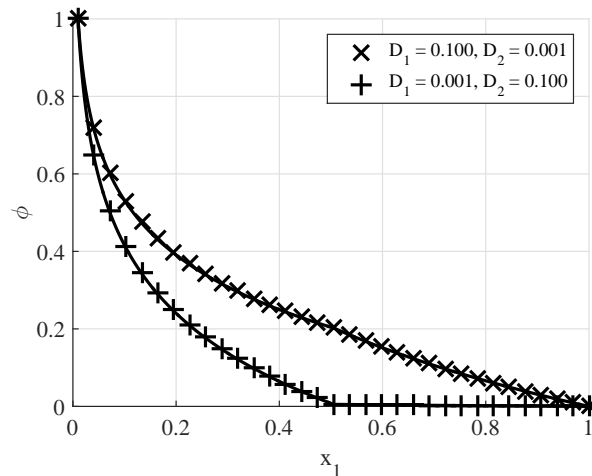


Figure 4.17: Solution profiles for the fixed interface steady state problem at  $x_2 = 0$ . Solid lines represent the analytical solution, crosses and plus signs are the numerical solution with  $\Delta x = 0.0309375$ ,  $\log_{10}(\Delta x) = -1.50951$ .

With 31 interior nodes in both the  $x_1$  and  $x_2$  directions ( $\Delta x = 0.0309375$ ), the solution profiles with two different diffusivity combinations can be seen in Figure 4.17 for the embedded method (note, the auxiliary method data points would be indistinguishable from the embedded method points if displayed). With a relatively small dataset, the RBF-FC embedded multi-zone method is able to accurately reproduce the solution profiles in Figure 4.17. The solution profile is only  $C_0$  continuous at the interface due to the discontinuous diffusivities (a factor of 100 difference) and the associated jump in flux. The numerical method has accurately captured this discontinuity, without any

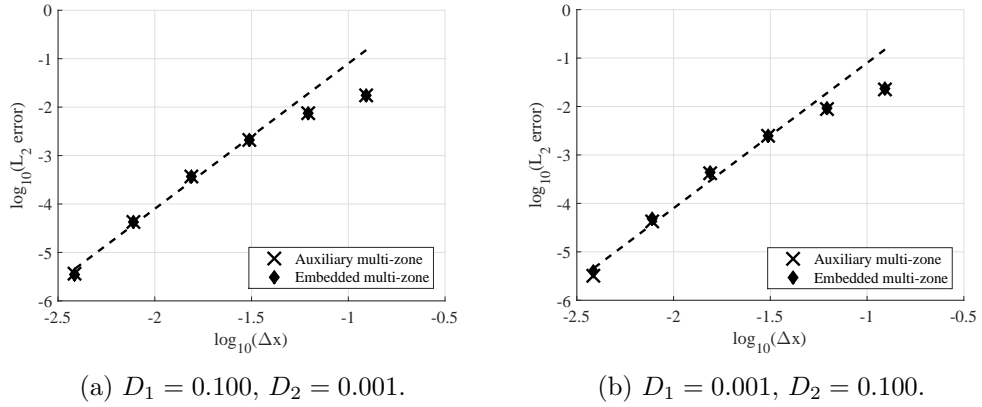


Figure 4.18: Solution errors for the auxiliary and embedded multi-zone methods for the steady state fixed interface problem. Dashed lines show theoretical  $3^{rd}$  order convergence.

refinement around the interface and with a relatively coarse dataset. The velocity field, which is a factor of 50.5 times higher at the start of the domain, has not caused any spurious oscillations. The Peclet number using a global lengthscale ( $L = 1$ ) ranges from 100 at the start of the domain, to 1 at the end of the domain.

The convergence properties of both the embedded and auxiliary methods are displayed in Figure 4.18, in which the  $L_2$  errors are plotted against the nodal separation. Both multi-zone methods in Figure 4.18 exhibit remarkably similar accuracies and both follow similar  $3^{rd}$  order convergence trends. As the methods only differ in the implementation of the multi-zone matching conditions at the interface, it is not unexpected that the solution accuracies are very similar for this test case where the solution changes significantly away from the interface. Both methods accurately represent the solution and flux matching conditions, with the auxiliary method being very slightly more accurate at the finest nodal discretisations in case (b). This test case demonstrates the high convergence of the multi-zone schemes and their applicability for steady-state cases.

#### 4.6.2 Transient fixed interface

Here, a transient fixed interface test case is presented detailing the embedded and auxiliary multi-zone RBF-FC methods. A problem presented in [113] is considered, using linear superposition to form a suitable analytical solution valid over a discontinuous

interface. The one dimensional convection-diffusion in each fluid domain  $l$  is given as:

$$\frac{\partial \phi_l}{\partial t} = D_l \frac{\partial^2 \phi_l}{\partial x_1^2} - u \frac{\partial \phi_l}{\partial x_1} \quad l = 1, 2 \quad (4.39)$$

Where  $D_l$  is the thermal diffusivity,  $u$  is the fluid velocity and  $l$  is the zone. Continuity of solution and flux are enforced at the zone interface:

$$\phi_1 = \phi_2 \quad (4.40)$$

$$D_1 \frac{\partial \phi_1}{\partial x_1} = D_2 \frac{\partial \phi_2}{\partial x_1} \quad (4.41)$$

In each zone a cosine or sinusoidal general solution to (4.39) can be formed, which when combined over the two zones lead to the following analytical solution valid when  $u = 1$  and the fixed interface is located at  $x_1 = 0$  [113]:

$$\phi(\mathbf{x}, t) = \begin{cases} \left( \cos\left(\frac{x_1}{2D_1D_2}\right) + \sin\left(\frac{x_1}{2D_1D_2}\right) \right) e^{\frac{x_1}{2D_1} - \frac{D_1+D_2}{4D_1D_2}t}, & \text{if } x_1 \leq 0. \\ \left( \cos\left(\frac{x_1}{2D_1D_2}\right) + \frac{D_1}{D_2} \sin\left(\frac{x_1}{2D_1D_2}\right) \right) e^{\frac{x_1}{2D_2} - \frac{D_1+D_2}{4D_1D_2}t}, & \text{if } x_1 > 0. \end{cases} \quad (4.42)$$

Equation (4.39) is solved on a square 2D domain, with  $-2 \leq x_1 \leq 2$ ,  $-2 \leq x_2 \leq 2$ , using zero flux conditions at the top and bottom boundaries to ensure a 1D solution profile. For the  $x_1$  direction boundary conditions, the analytical solution is used to prescribe the Dirichlet condition at time  $t$ . For fluid parameters,  $D_1 = 0.1$ ,  $D_2 = 10$ ,  $u = 1$ . For initial conditions, the analytical solution (4.42) is prescribed with  $t = 0$ . Under these conditions, the Peclet number for zone 1 and 2 using a global lengthscale ( $L = 4$ ) are  $Pe_1 = 40$  and  $Pe_2 = 0.4$  respectively.

Both auxiliary and embedded methods use a  $2^{nd}$  order Crank-Nicholson time stepping scheme ( $\theta = 0.5$ ) using  $\Delta t = 1 \times 10^{-5}$  for  $0 \leq t \leq 0.2$ ,  $c^* = 50$ . The solution of (4.39) behaves as a decaying exponential solution which very quickly becomes temporally independent as  $\Delta t$  is lowered. When temporal convergence studies were performed, the convergence was very quick, and did not allow the  $2^{nd}$  order (or  $1^{st}$  order if  $\theta = 1$ ) nature of the convergence to become prominent with the solution depending much more on the spatial discretisation and multi-zone scheme. For this reason a small time step is used to ensure that all datasets are temporally independent and the spatial properties of the schemes can be explored. In all quadtree cases, a constant  $B_t$  value of 4 is used

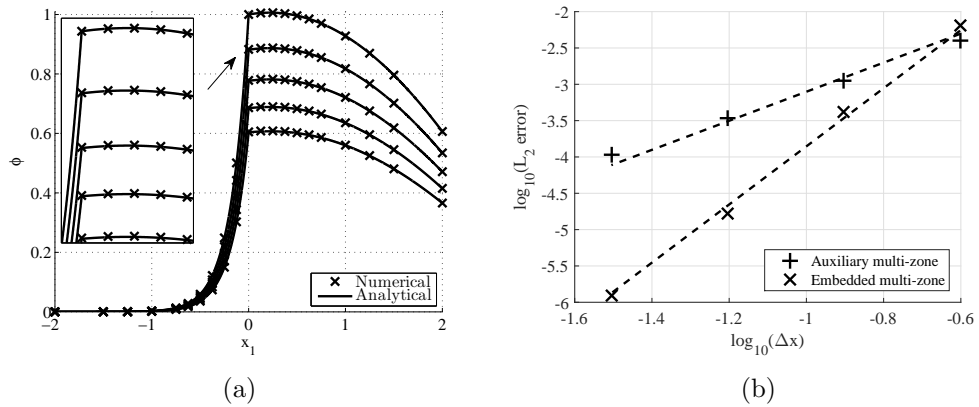


Figure 4.19: (a) Solution profile for the transient fixed interface problem at  $x_2 = 0$ . Numerical solution uses the auxiliary method with quadtree cell level 3-5. (b) Solution errors for the two multi-zone methods using uniform datasets. Dashed lines show theoretical  $2^{\text{nd}}$  and  $4^{\text{th}}$  order convergence.

to ensure several nodes appear in each refinement banding.

In Figure 4.19(a) the numerical solution profile using the auxiliary method with a quadtree cell level 3-5 dataset can be seen. This coarse dataset is able to very accurately capture the sharp solution profile around the interface and appears indistinguishable from the analytical solution. The zoomed in plot in figure 4.19(a) more clearly shows the matching flux condition, in which both zone solution gradients ( $\partial\phi_l/\partial x$ ) are positive at the interface. In Figure 4.19(b) corresponding  $L_2$  solution errors are presented, which show the consistent spatial convergence of the auxiliary and embedded schemes with uniform nodal distributions. The embedded method shows greater solution accuracy and near to  $4^{\text{th}}$  order convergence, whereas the auxiliary method shows only  $2^{\text{nd}}$  order spatial convergence. The methods only differ in the local system formation on stencils directly falling on the interface, meaning the difference in solution accuracy must come from the multi-zone representation.

In the auxiliary method, there are no PDE operators placed on the interface (in anticipation of extrapolation problems in moving interface cases), with local flux and solution matching conditions collocated instead. The embedded method on the other hand has two PDE operators at each interface location, one for each zone, as well as the globally enforced matching conditions. This creates a stronger representation of the underlying PDE at the interface, and means that the transient PDE operator update is applied directly to the interface, yielding a better representation of the transiently

evolving solution. PDE operators could be included in the auxiliary method here to have a like for like comparison with the embedded method, however the auxiliary method is designed with moving interface problems in mind where PDE operators cannot be placed on the interface if extrapolation is to be avoided.

By presenting the auxiliary method without PDE operators on the interface, it is shown that the method still exhibits  $2^{nd}$  order convergence on transient problems, and can still very accurately represent a sharp solution profile in a transient convection-diffusion problem. It is worth noting that without PDE operators on the interface, the embedded method performs very poorly as it does not contain any other local collocation at the interface (the auxiliary method has flux and solution matching collocation). It only reconstructs the solution at the global level, but does not have an underlying collocation point applied at the local level, severely limiting solution accuracy.

Quadtree cell level	Average $Nx$	$\log_{10}(\Delta x)$	Auxiliary $\log_{10}(L_2 \text{ err})$	Embedded $\log_{10}(L_2 \text{ err})$
Uniform level 4	15	-0.6021	-2.397	-2.192
Uniform level 5	31	-0.9031	-2.953	-3.380
Uniform level 6	63	-1.2041	-3.468	-4.778
Quadtree level 2-4	13.96	-0.5730	-2.364	-2.161
Quadtree level 3-5	22.20	-0.7635	-2.834	-3.219
Quadtree level 4-6	33.54	-0.9363	-3.251	-3.581

Table 4.2: Transient fixed interface solution errors with dataset density for the auxiliary and embedded multi-zone methods.

Examples of uniform and quadtree dataset solution errors are shown in table 4.2. The quadtree cases show comparable solution error to the uniform dataset at the corresponding maximum level, with the quadtree datasets exhibiting marginally more error but with significantly reduced nodal points. The difference between the embedded and auxiliary methods using the quadtree dataset is less pronounced as in the uniform datasets. The solution error in the fine quadtree datasets starts to drift further from the uniform datasets as the spatial resolution is increased. This suggests the quadtree has limited the convergence of the spatial schemes, meaning the representation of the outer solution field must be key to maintaining consistent convergence properties in this case. As both multi-zone methods use the same local systems in in the outer domain, the drop in accuracy must be due to the coarseness of the datasets in these areas (especially as  $x \Rightarrow 2$  where the solution is still varying significantly).

The auxiliary and embedded multi-zone methods both perform well on the transient fixed interface problem presented in this section. They demonstrate good spatial convergence properties ( $2^{nd}$  order and  $4^{th}$  order for the auxiliary and embedded methods respectively) and high accuracy using coarse quadtree datasets when compared to the analytical solution. These results provide excellent verification of the methods for transient, multi-zone convection diffusion problem that will be further supported by a moving interface example in the next section.

### 4.6.3 Transient moving interface

In this section, the auxiliary method is verified on a transient convection-diffusion problem with a moving interface. The 1D transient convection-diffusion equation is again solved in each fluid zone i.e.:

$$\frac{\partial \phi_l}{\partial t} = D_l \frac{\partial^2 \phi_l}{\partial x_1^2} - u \frac{\partial \phi_l}{\partial x_1} \quad l = 1, 2 \quad (4.43)$$

Where  $D_l$  is the thermal diffusivity,  $u$  is the fluid velocity and  $l$  is the zone. Continuity of flux and solution are enforced at the interface, which is convected with the fluid velocity  $u$ :

$$\phi_1 = \phi_2, \quad (4.44)$$

$$D_1 \frac{\partial \phi_1}{\partial x_1} = D_2 \frac{\partial \phi_2}{\partial x_1} \quad (4.45)$$

At the boundaries ( $-L \leq x_1 \leq L$ ), Dirichlet boundary conditions are enforced:

$$\phi_1(x_1 = -L, t) = 1 \quad (4.46)$$

$$\phi_2(x_1 = L, t) = 0 \quad (4.47)$$

The initial conditions for the problem, with the interface located at  $-L/2$  are:

$$\phi_1(x_1 \leq -L/2, 0) = 1 \quad (4.48)$$

$$\phi_2(x_1 > -L/2, 0) = 0 \quad (4.49)$$

The auxiliary multi-zone method can be used to solve the above problem, with the nodal points near the interface displaced at each time step to lie directly on the interface. PDE operators close to the interface are similarly displaced so that at each time step they have available data from the same zone at the previous time step. Since there are also no PDE operators directly on the interface, no extrapolation has to be performed for any PDE operators, with the nodal points being suitably displaced due to the meshless nature of the scheme.

The above problem was tested using the embedded multi-zone method with 1<sup>st</sup> and 2<sup>nd</sup> order Taylor series extrapolation (since PDE points have to exist on the interface for global accuracy), however, the extrapolation severely limited the accuracy of the scheme and made it ineffective for moving interface problems in its current form. Unless impractically small time step values were used, so that the interface movement was very small between each time step, the solution error would blow up over the course of the simulation. Since the problems under consideration have high Peclet numbers, the extrapolation schemes presented in [98] did not perform well in these cases, with small errors produced in the extrapolation propagating through the solution. For this reason, only results using the auxiliary method without extrapolation are presented here.

Although analytical solutions exist for various transient convection-diffusion type problems, the solutions are typically hard to construct and involve complex functions of exponentials, Fourier series and infinite sums (see for example [122, 123]). These solutions become even harder to construct for moving interface, multi-zone transient convection-diffusion problems, even with constant coefficients. Therefore, to verify the performance of the auxiliary problem, the above moving multi-zone convection-diffusion problem may be transformed to a static linear diffusion problem using a moving reference system with velocity  $u$  [124]. The transformed variables are introduced as:

$$X^* = x_1 - ut, \quad t^* = t \quad (4.50)$$

Using these variables, the convection-diffusion problem (4.43) reduces to the following diffusion problem:

$$\frac{\partial \phi_l}{\partial t^*} = D_l \frac{\partial^2 \phi_l}{\partial X^{*2}} \quad l = 1, 2 \quad (4.51)$$

Typically, closure of equation (4.51) involves boundary and matching conditions that move with time, equivalent to those in (4.44) to (4.47) since these are on a fixed domain. Also, the domain range for equation (4.51) would also change with time. However, since the interface in the original problem is moving (with positive velocity), the two zones are effectively moving reference frames that displace with the interface velocity  $u$ . The inner zone size increases with time, whilst the outer zone decreases with time. Therefore an approximate solution to equation (4.43) can be sought by solving (4.51) on a fixed domain, and mapping the results back, in a reverse fashion to what is classically done. As long as certain conditions are held, these solutions are equivalent for a finite amount of time until the mapping passes beyond the original domain.

Equation (4.51) is solved on a static frame from  $(-L \leq X^* \leq L)$ , with the results then mapped back to the original  $x$  domain. Since the newly mapped points in  $x$  will be displaced to the right of the original domain, i.e.  $-L + ut \leq x_1 \leq L + ut$ , any points that lie  $-L \leq x_1 \leq -L + ut$  are set to the boundary condition at  $x_1 = -L$ . This is valid as long as the Peclet number is much greater than 1 meaning the solution near the left boundary at  $x_1 = -L$  will remain at the Dirichlet boundary condition and simply be convected into the domain. Any points that map to the region outside of the original domain, i.e.,  $x_1 \geq L$  are not used. The mapped and original results will only be comparable if the solution at the points  $X^* \geq L - ut$  is equal to the boundary condition at  $x_1 = L$ . As long as the solution profile is sharp, the solution at the right of the domain remains near zero for a long time, allowing the solutions to be compared. For this procedure to work, the boundary conditions for the fixed  $X^*$  domain have to be interpolated from the mapped domain, i.e.:

$$\phi_1(X^* = -L, t^*) = \phi_1(x_1 = -L + ut, t) \quad (4.52)$$

$$\phi_2(X^* = L, t^*) = \phi_2(x_1 = L + ut, t) = 0 \quad (4.53)$$

Since the interface is displacing in time with position  $x_1 = -L/2 + ut$ , the transformed matching conditions are:

$$\phi_1 = \phi_2, \quad (4.54)$$

$$D_1 \frac{\partial \phi_1}{\partial X^*} = D_2 \frac{\partial \phi_2}{\partial X^*} \quad \text{at} \quad X^* = -L/2 \quad (4.55)$$

Finally the initial conditions for the transformed problem are:

$$\phi_1(X^* \leq -L/2, 0) = 1 \quad (4.56)$$

$$\phi_2(X^* > -L/2, 0) = 0 \quad (4.57)$$

Solving equation (4.51) subject to boundary, matching and initial conditions (4.52) to (4.57) and mapping the results to the domain  $x_1 = X^* + ut$  following the assumptions above, is equivalent to solving (4.43) subject to boundary, matching and initial conditions (4.44) to (4.49) on the original  $x$  domain.

Although the solution to equation (4.51) can be sought analytically (e.g. [125, 126]), the analytical solutions typically involve eigenvalue problems, whose solution is usually sought numerically. To this end, a very fine resolution finite difference scheme is used to solve the governing equation (4.51) directly. Equation (4.51) is solved using finite differences on the domain  $(-2 \leq X^* \leq 2)$ .  $2^{nd}$  order central differencing is used for the spatial derivatives, and a  $1^{st}$  order fully implicit time stepping procedure for the temporal derivatives. A fictitious node either side of the interface is used to close the system of equations arising from the extra flux and solution matching conditions at the interface. Initially the interface is located at  $x_1 = -1$ , which with a velocity of  $u = 1$  and simulation time of  $t = 1$  results in an end location at  $x_1 = 0$ . To achieve a spatial and temporally independent solution, 511 solution nodes are used in the  $X^*$  domain with a time step size of  $\Delta t = 1 \times 10^{-7}$ . Even though implicit time stepping is used, the boundary conditions must be taken at the previous time step where the mapped solution is known (it is not known at the current time when the solution is sought).

Equation (4.43) is solved in a square 2D domain  $-2 \leq x_1 \leq 2$ ,  $-2 \leq x_2 \leq 2$  using the auxiliary multi-zone RBF-FC method, with zero flux Neumann conditions at the top and bottom boundaries to ensure a 1D solution. Several different nodal discretisations are tested, with a time step size of  $\Delta t = 1 \times 10^{-3}$ . The same velocity field and starting interface location are used as above with  $c^* = 50$ .

In the results that follow, the finite difference and RBF solutions are compared at the time  $t$  and spatial locations  $x_1$  set by the original convection-diffusion problem, meaning the finite difference solution has been mapped to the original domain, i.e.  $x_1 = X^* + ut$ , with the approximations above. By ensuring that the simulations only run until  $t = 1$ ,

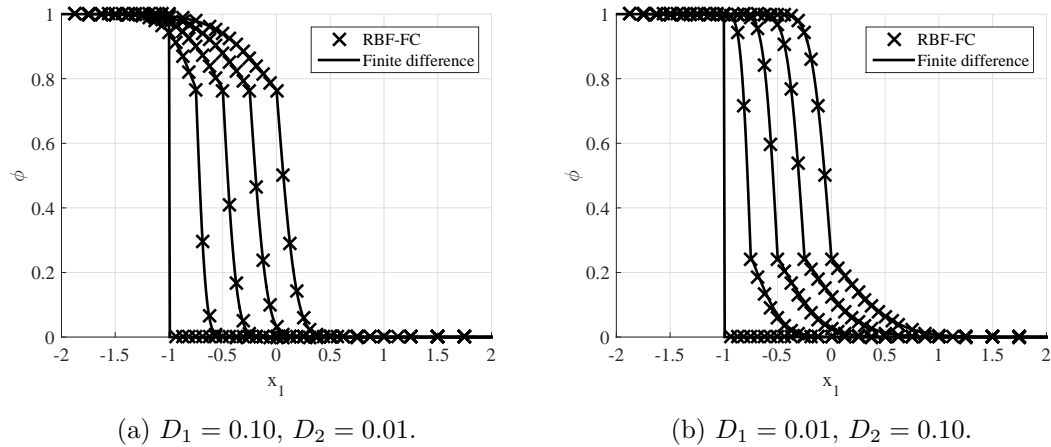


Figure 4.20: Moving interface solution profiles. RBF-FC solutions taken using quadtree cell level 4-6 dataset at the centreline  $x_2 = 0$ , average 40.37 nodes in  $x_1$  direction. Solutions shown at  $\Delta t = 0.25$  increments from  $0 \leq t \leq 1$ .

the solution at the outer nodes in the FD scheme never rises above the outer boundary condition in the original domain.

Figure 4.20 shows the auxiliary RBF-FC and FD method solution profiles for two diffusivity regimes with time. Both solutions show sharp multi-zone interfaces where the diffusivity ratio causes a corresponding transition in the solution gradient. Since the interface moves with the convective field, the transient profile does not show the usual solution trapping at the discontinuity common in fixed interface problems [113]. In the cases here, it can be seen that as the inner zone expands, the solution cannot stagnate near the interface and increase with time, instead the solution is ‘swept’ along with the interface. In this way, once the transient profile has been setup after  $t = 0.25$ , the solution at the interface does not change significantly, as any increase through convection/diffusion is matched by an expanding zone acting to lower the solution value.

The Peclet number in both zones is high for each diffusivity case presented in Figure 4.20, with the solution dominated by convection. Using a global lengthscale ( $L = 4$ ), the Peclet numbers in each zone for the two cases are: (a)  $Pe_1 = 40, Pe_2 = 400$  (b)  $Pe_1 = 400, Pe_2 = 40$ .

The RBF solution in Figure 4.20 shows a highly accurate solution profile that is indistinguishable from the FD profile, with over 12 times fewer nodal points. The FD profile represents a highly accurate solution to the problem, since it solves a simple diffusion problem with changing boundary conditions that is then simply mapped to the

original domain. The RBF method has to update the interface location and displace the nodal points at every step, but is able to accurately capture the solution with very few points.

Quadtree cell Level	Average $Nx$	Average $\Delta x$	$L_2$ difference Case 1	$L_2$ difference Case 2
Uniform level 5	31	0.1250	$4.01 \times 10^{-3}$	$5.69 \times 10^{-3}$
Uniform level 6	63	0.0625	$1.27 \times 10^{-3}$	$2.14 \times 10^{-3}$
Quadtree level 4-6	40.37	0.0967	$1.59 \times 10^{-3}$	$2.60 \times 10^{-3}$

Table 4.3: Moving interface relative errors between the auxiliary multi-zone RBF-FC method and the FD method at  $t = 1$ .

The solution differences taken at  $t = 1$  between the FD and RBF-FC method for different datasets are shown in table 4.3. As expected, the uniform level 6 RBF dataset shows the lowest difference, with a significantly refined mesh. Due to the relatively coarse time step size used, the errors do not drop significantly with an increase in the maximum cell level, since the error is controlled by the  $2^{nd}$  order Crank-Nicholson time marching scheme. The error in the level 4-6 RBF dataset is very close to the uniform level 6 dataset, despite the significantly reduced number of nodes. Since the solution field changes sharply at the interface, very few nodes can be used in the outer domain, whilst nodes are clustered around the interface.

These results highlight the highly robust auxiliary multi-zone method for moving multi-zone problems. The solutions errors are low when compared to a transformed FD solution using only very few nodal points. Without extrapolation the scheme is also able to accurately capture the interface and surrounding solution profile, that make it very robust and not limited in spatial convergence to the extrapolation order. This represents a large improvement over fixed mesh schemes that have to use extrapolation when the interface moves over the nodes, and makes it highly suited for the moving interface problems that are tackled in this work.

## 4.7 Conclusion

In this chapter, a new multi-zone RBF-FC method utilising adaptive quadtree datasets has been developed and validated using various steady-state and transient convection-diffusion problems, showcasing the accuracy and robustness of the method.

Single-zone test cases were used to understand the stencil configuration behaviour when using a non-uniform adaptive quadtree dataset that evolved with time. Results showed that the local stencil configuration and the location of PDE points played a crucial role in reconstructing the previous time step data,  $\hat{L}_l$ , and the resulting solution accuracy. Interior, crossover and T-junction stencils were analysed, with optimal results obtained using a 1-1 stencil configuration, allowing accurate PDE reconstruction and low global solution error for use within the adaptive dataset RBF-FC framework.

These stencil configurations were then used with the new multi-zone methods to test several well known multi-zone problems. Both methods exhibited very low solution error on steady-state fixed interface problems, with high 3<sup>rd</sup> order convergence. In the moving multi-zone problem, only the auxiliary method could be used effectively as the extrapolation procedure for the embedded method rendered the scheme inaccurate unless impractically small time step sizes are used. The auxiliary method demonstrated accurate solution profiles when compared to a very high-resolution finite difference scheme, without the need for extrapolation, using a fraction of the nodal points to capture the sharp, discontinuous solution profile.

From the testing presented in this chapter, it is clear that the new adaptive, auxiliary multi-zone RBF-FC scheme is effective at solving moving multi-zone problems, in which the PDE being solved is itself transient. The ability to accurately compute solutions without the need for extrapolation makes the scheme highly suited to transient PDEs where the inhomogeneous  $\hat{L}_l$  must be computed at each time step. The embedded method has proved more effective for the solution of steady-state multi-zone problems, where there can be a greater linking between stencils along the interface, increasing the solution accuracy. This general methodology for the multi-zone RBF-FC method can be used in subsequent chapters to solve the cases of inhomogeneous mobility in immiscible viscous fingering.

# 5. Immiscible displacement with inhomogeneous mobility

## Summary

In this chapter, the previously presented BE and RBF-FC methods are coupled to track the radial displacement and viscous fingering between two immiscible fluids with inhomogeneous mobility in a Hele-Shaw cell. The fluid mobility is a function of the cell plate separation, which is varied spatially in order to explore the effects of inhomogeneous mobility on immiscible viscous fingering. The analogy between Hele-Shaw and porous media flow can again be used to draw conclusions about the immiscible viscous fingering regime during  $CO_2$  injection and storage.

Systematic numerical experiments with uniformly converging radial cells confirm recent analytical and experimental results under low capillary number regimes, in which stabilising effects become prominent and perturbations can be damped. By increasing the capillary number a transition point is identified, after which the effect of the converging geometry reverses. At high capillary numbers, the stabilising capillary pressure is overcome by the increased pressure gradient through the converging aperture and finger growth is promoted.

In sharply varying geometries at the late stages of interfacial growth, the finger fronts create a bottleneck and could detach into separate bubbles when entering regions of sharply expanding geometry. In corresponding converging cases, the finger fronts spread azimuthally creating a highly stabilised interface with fingers separated by thin lubrication layers. Investigations into highly anisotropic Hele-Shaw cells reveal

the fingering complexity that can occur in periodic and channelled Hele-Shaw cells, demonstrating the robustness of the numerical scheme.

## 5.1 Introduction

A typical subsurface aquifer will have an inhomogeneous permeability that varies in space as a consequence of the way it has been formed and re-shaped over many millions of years, altering the natural stress state of the aquifer [17]. Abrupt changes in aquifer permeability can exist due to fault lines and changes in the aquifer material [17]. As well as pre-existing variations in permeability, the  $CO_2$  injection process itself can alter the permeability of the aquifer. During  $CO_2$  injection, formation dry-out and precipitation of minerals (such as salt from pre-existing brine) near the injection well can reduce the porosity and permeability of the aquifer [18]. The formation of carbonic acids in the brine due to reactions with the injected  $CO_2$  can dissolve the calcite in sandstone aquifers, increasing the permeability [19]. Injection pressures over the formation pressure of the aquifer can also induce fracturing and fault slip, which can increase the permeability in a region surrounding the injection well [20]. Understanding the effect of these permeability variations on the flow regime and interfacial evolution of injected  $CO_2$  is critical in understanding the long term storage capabilities of supercritical  $CO_2$  and forms the motivation behind this chapter.

A spatially varying permeability can be considered in a Hele-Shaw cell context as a variation in the plate separation, in effect altering the cell's intrinsic permeability ( $k = b^2/12$ ) analogous to that in a porous medium. This also gives rise to an inhomogeneous fluid mobility that varies spatially. The fluid mobility can also vary with the viscosity, which can be spatially dependent (due to an imposed temperature field) within the fluids. The mathematical model is general and can be applied to any form of spatially varying mobility, however, in this chapter, the case of an inhomogeneous fluid mobility arising purely from the spatial variation in plate separation is studied. The case of a spatially varying viscosity is analysed in the next chapter.

Recently, several analytical and experimental works have shown that small changes in the plate separation in a Hele-Shaw cell can have significant effects on the interface evolution, allowing the control and suppression of fingering instabilities [127]. Using

a rectilinear Hele-Shaw cell set-up, [128] investigate secondary tip-splitting instabilities occurring under high capillary number regimes when the cell has a small gradient in the plate separation in the flow direction. Experiments show that a small positive gradient flattens the finger tip, making it easier for the finger to bifurcate. In the converging cell case, the finger sharpens, and remains stable for a much longer period compared to the flat plate configuration. Physically, with an almost constant curvature around the finger front in the rectilinear set-up, the finger tip is accelerated first by the converging geometry, creating a sharper tip. The analytical stability analysis of [128] reveals a large dependence of the growth rate of instabilities with the magnitude of the plate separation, but no dependence on the sign of the separation gradient, contrary to experimental results.

[129] use a similar stability analysis to [128] but employ mode coupling theory to provide analysis into the slightly non-linear regime of finger tip splitting in a rectilinear cell. They find dependence on the sign of the plate separation gradient on the finger tip growth in contrast to [128]. Their findings agree with the experimental findings published by [128] for the case of high capillary numbers in the weakly non-linear stage of finger growth.

In contrast to [128] and [129], [130] present results in a rectilinear cell with a gradually varying plate separation under much smaller capillary number regimes, looking at the onset and subsequent control of the fingering instability. In very low capillary number flows, the gradually converging cell can completely stabilise the flow due to the variation in transverse curvature around the interface. Areas of the interface displaced further into the cell have a larger transverse curvature, resulting in a larger capillary pressure and stabilising action from the surface tension. The large capillary pressure helps to stabilise the front and can produce a completely flat interface if the capillary number is below a critical value. [130] predict a critical capillary number through experimental testing and analytically using an equation derived from a linear stability analysis (LSA) of the governing Darcy flow regime. This analysis gives a critical capillary number under which perturbations of any wavelength can be stabilised, depending on the viscosity contrast, contact angle and plate gradient. The analytical predictions agree remarkably well with the experimental findings, with small discrepancies likely due to dynamic wetting effects [130].

Utilising a radial Hele-Shaw cell set-up, [27] provides early insight into the case of a slightly diverging cell, showing that viscous fingering is initially delayed. This was later confirmed analytically by [127], who show that the radial growth of a finger has an offset given by  $-ar_0/b_0$ , where  $\alpha$  is the gap gradient,  $r_0$  is the interface position and  $b_0$  is the plate separation respectively. This offset is negative in the diverging geometry causing the interface to be slowed and viscous fingering delayed. [127] also analyse how the radial set-up is affected by converging geometry, showing a similar capillary number limit for which viscous fingering can be completely suppressed.

Another strategy to suppress the fingering instability is the use of a Hele-Shaw cell with an elastic upper membrane, replacing the classic rigid plate. The elastic membrane displaces vertically upon the injection of the less viscous fluid, creating a profile that converges to a uniform plate separation far from the injection site. The expansion of the elastic upper membrane occurs at a rate much faster than the displacement of the outer fluid, meaning the viscous fingering stability can be modelled in a similar vane to the radial case presented by [127], i.e. in a static manner. [131] and [132] show that the converging geometry caused by the rapid cell expansion helps to stabilise the interface between the fluids. This is also demonstrated experimentally by [133], where the interface can be completely stabilised using an elastic membrane for short time periods under low capillary number regimes. At higher capillary numbers, the interface proceeds to form short stubby fingers, also identified by the numerical model in [132].

More recent studies by [134] and [135] analyse single and two-phase axisymmetric radial flow in a Hele-Shaw cell with an elastic upper membrane. [134] perform experiments and direct numerical simulations using a Navier-Stokes and lubrication theory model; both of which agree very well with experimental results for the profile evolution of the upper membrane. However, the lubrication model shows some discrepancy with the experimental results for the radial evolution of the injection plume, due to the omission of the dynamic-wetting layer in the capillary pressure jump formulation. This is later incorporated by [135], with results showing remarkable agreement with the experimental. Due to the large expansion of the upper membrane and hence significant volume of trailing fluid left behind, incorporating the dynamic wetting layer is crucial to accurately predict the radial front evolution.

As well as static cell geometries and the use of elastic membranes, time dependent strategies can be used to control the growth of instabilities and the resulting interfacial evolution. [136], [137] and [138] use Hele-Shaw cells with time dependent lifting or squeezing rigid upper plates. With a diverging lifting plate, [136] find that the growth rate of unstable modes can be reduced, helping to stabilise a system that would be unstable in a parallel plate situation. Using a plate separation  $b$  that scales in time with  $b(t) = b_1 t^{1/7}$ , [138] are also able to suppress the onset of fingering instabilities, or maintain non-splitting self-similar fingers throughout time. Similarly, using a time dependent injection rate that scales with the inverse of the fastest growing fingers ( $Q(t) = Q_1 t^{-1/3}$ ), [139] show that self-similar finger morphologies can be created that do not split or form highly branched structures.

These theoretical and experimental findings confirm that the evolution of viscous fingering has a large dependence on the plate separation variation (and hence inhomogenous mobility) in both rectilinear and radial Hele-Shaw flows. Although a significant amount of previous work exists on the linear growth and early stages of the tip splitting instability with a variable plate separation, analysis of the long term non-linear evolution is lacking. Research has focused on control of the fingering instability, where linear stability theory can be effectively used to analyse the growth rate and finger morphology if the instabilities are suppressed early in time. However, to fully understand the non-linear finger interactions and late stage interfacial evolution in radial Hele-Shaw flow, subject to a variable plate separation, requires extensive numerical simulation [129].

The contrasting results at low and high capillary numbers in rectilinear cells mentioned previously (in converging cells, fingers are smoothed at low capillary numbers and sharpened at high capillary numbers) indicate a transition in fingering mechanisms with capillary number. This transition has not been explored in detail, with previous authors generally focusing on one region due to the application of their study. However, in the present work the transition region is explicitly explored, in order to provide detail on the regimes that could occur under the flow regimes present in  $CO_2$  sequestration. Here, the capillary number is initially high, but decreases with time, indicating that both high and low capillary number regimes may be experienced by the advancing plume.

This work aims to numerically model the long time scale interfacial evolution between two fluids in a radial Hele-Shaw cell with a spatial variation in the plate separation.

To this end, a coupled boundary element - radial basis function method is developed to accurately track the interfacial displacement of fluids with inhomogeneous mobility in Hele-Shaw cells. Unlike previous studies, this work does not aim to provide a control strategy for the fingering instabilities, instead presenting analysis and discussion on the long term effects of plate separation variation on the interfacial evolution.

In the following chapter, the mathematical model is first formulated in section 5.2 followed by an overview of the numerical methods (which have mainly been introduced in the previous chapters). Mass conservation verification is performed in section 5.4 followed by numerical results with detailed discussion and comparison with previous work in section 5.5. This chapter concludes with final remarks and findings in section 5.6.

## 5.2 Mathematical model

A circular Hele-Shaw cell of infinite radius is again considered, in which high viscosity fluid is displaced by the injection of a less viscous fluid. The initial interface has a perturbation given in Figure 5.1, where  $\epsilon_0$  and  $\theta$  are the perturbation amplitude and the azimuthal angle around the interface.

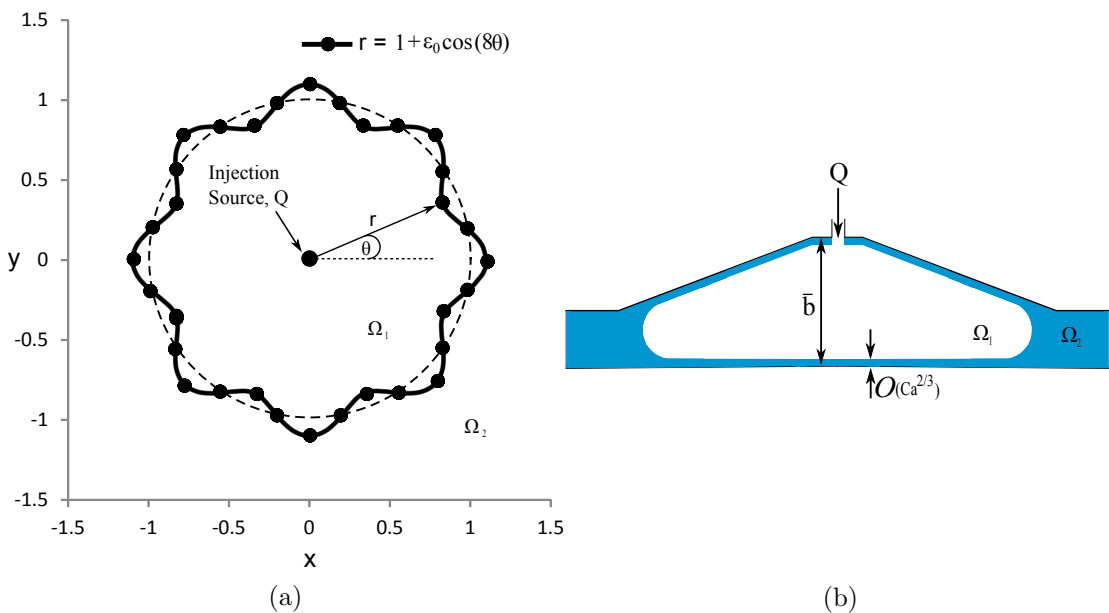


Figure 5.1: (a) Planar view of the 2D radial injection problem, with 8 finger symmetric perturbation. (b) Side view of a radially symmetric converging Hele-Shaw cell.

The governing equations of the flow follow from Darcy's law and conservation of mass with suitable matching conditions, given in section 2.2.1 in chapter 2. These equations are repeated here for convenience, firstly the conservation of mass with substituted Darcy velocity:

$$\frac{\partial}{\partial x_i} \left( b(\mathbf{x}) M_l(\mathbf{x}) \frac{\partial P_l}{\partial x_i} \right) = 0 \quad \mathbf{x} \in \Omega_l, \quad l = 1, 2 \quad (5.1)$$

The kinematic condition requires the continuity of normal velocity  $u_i(\boldsymbol{\xi}) n_i(\boldsymbol{\xi})$ , i.e.

$$-M_1(\boldsymbol{\xi}) \frac{\partial P_1(\boldsymbol{\xi})}{\partial n} = -M_2(\boldsymbol{\xi}) \frac{\partial P_2(\boldsymbol{\xi})}{\partial n} \quad (5.2)$$

The dynamic condition describes the pressure jump across the interface:

$$P_1(\boldsymbol{\xi}) - P_2(\boldsymbol{\xi}) = \gamma \left( \frac{2}{b(\boldsymbol{\xi})} + \frac{\pi}{4} k(\boldsymbol{\xi}) \right) \quad (5.3)$$

Note that here the original Young-Laplace condition is used without dynamic wetting effects. This is because the dynamic wetting effect adds significant extra computation to the numerical schemes, and in this chapter the focus is solely on inhomogeneous mobility effects. The final conditions to close the problem are the near and far field asymptotic conditions, i.e.:

$$\frac{\partial P_1(\mathbf{x})}{\partial r} \Big|_{\mathbf{x} \rightarrow 0} \rightarrow -\frac{Q}{2\pi M_1 r} \quad (5.4)$$

$$P_2(\mathbf{x}) \Big|_{\mathbf{x} \rightarrow \infty} \rightarrow -\frac{Q}{2\pi M_2(\mathbf{x})} \ln \left( \frac{r}{r_0} \right) \quad (5.5)$$

Equation (5.1), subject to matching conditions (5.2, 5.3), and asymptotic conditions (5.4) and (5.5) represents a well posed problem that can be solved with the previously developed numerical methods. In this chapter, in order to characterise the specific effects of the varying plate separation in comparison to the uniform cell case (which has been discussed in chapter 2), the variables that depend on the plate separation are decomposed into homogeneous and perturbed components. In this way, the homogeneous components can be solved with the BEM in a similar fashion to chapter 2 and the perturbed components using the RBF-FC method in chapter 4 in order to characterise the effect of the variable plate separation from the homogeneous case.

Firstly, the plate separation can be represented with homogeneous and perturbed components as:

$$b(\mathbf{x}) = \bar{b} + \tilde{b}(\mathbf{x}) \quad (5.6)$$

The perturbed component,  $\tilde{b}(\mathbf{x})$  represents the variation in  $b(\mathbf{x})$  with respect to the homogeneous separation (the characteristic value defined at the origin) and the corresponding variation in permeability from the homogeneous base value in a porous medium. This gives the mobility of the fluid in zone  $l$  as:

$$M_l(\mathbf{x}) = \frac{(\bar{b} + \tilde{b}(\mathbf{x}))^2}{12\mu_l} = \bar{M}_l(\mathbf{x}) + \tilde{M}_l(\mathbf{x}) \quad (5.7)$$

$$\bar{M}_l = \frac{\bar{b}^2}{12\mu_l}, \quad \tilde{M}_l(\mathbf{x}) = \frac{\tilde{b}^2(\mathbf{x}) + 2\bar{b}\tilde{b}(\mathbf{x})}{12\mu_l} \quad (5.8)$$

From equation (5.1) the plate separation  $b(\mathbf{x})$  can now be incorporated into a new modified mobility term:

$$m_l(\mathbf{x}) = b(\mathbf{x})M_l(\mathbf{x}) = \frac{(\bar{b} + \tilde{b}(\mathbf{x}))^3}{12\mu_l} = \bar{m}_l + \tilde{m}_l(\mathbf{x}) \quad (5.9)$$

$$\bar{m}_l = \frac{\bar{b}^3}{12\mu_l}, \quad \tilde{m}_l(\mathbf{x}) = \frac{\tilde{b}^3(\mathbf{x}) + 3\bar{b}\tilde{b}^2(\mathbf{x}) + 3\bar{b}^2\tilde{b}(\mathbf{x})}{12\mu_l} \quad (5.10)$$

Non-dimensional variables can be introduced utilising the characteristic length, time, velocity, pressure and mobility of the problem, given by:

$$(\mathbf{x}, r, b) = r_0 (\mathbf{x}', r', b'), \quad t = \frac{r_0^2}{Q} t', \quad (5.11)$$

$$u_i^l = \frac{Q}{r_0} u_i'', \quad P_l = \frac{Q}{\bar{M}_2} P_l', \quad (M_l, m_l) = \bar{M}_2 (M_l', m_l') \quad l = 1, 2 \quad (5.12)$$

In equalities (5.11) - (5.12), apostrophes identify non-dimensional variables with  $t$  as time and  $\bar{M}_2$  as the the homogeneous mobility of the displaced fluid (corresponding to the homogeneous thickness  $\bar{b}$ ). From this point onwards in the chapter, the apostrophe of all non-dimensional variables will be dropped, and all variables will be assumed to be in their non-dimensional form unless otherwise stated.

Consistent with the above representation of the mobility, in order to analyse the flow effects arising from the perturbed plate separation  $\tilde{b}(\mathbf{x})$ , the total pressure can be

represented as a sum of homogeneous and perturbed components:

$$P_l(\mathbf{x}) = \bar{p}_l(\mathbf{x}) + \tilde{p}_l(\mathbf{x}) \quad (5.13)$$

Expanding (5.1), noting that  $\partial \bar{m}_l / \partial x_i = 0$ , the following equation is obtained:

$$m_l(\mathbf{x}) \frac{\partial^2 \bar{p}_l}{\partial x_i^2} + m_l(\mathbf{x}) \frac{\partial^2 \tilde{p}_l(\mathbf{x})}{\partial x_i^2} + \frac{\partial \tilde{m}_l(\mathbf{x})}{\partial x_i} \frac{\partial \tilde{p}_l(\mathbf{x})}{\partial x_i} = - \frac{\partial \tilde{m}_l(\mathbf{x})}{\partial x_i} \frac{\partial \bar{p}_l(\mathbf{x})}{\partial x_i} \quad (5.14)$$

The homogeneous pressure is constrained to satisfy Laplace's equation, in order to characterise the case of uniform plate separation and the effects of variable plate separation:

$$\frac{\partial^2 \bar{p}_l(\mathbf{x})}{\partial x_i^2} = 0; \quad (5.15)$$

To derive the correct matching and boundary conditions for the pressure field at the interface and the far field, the homogeneous and perturbation pressures can be substituted into (5.2) and (5.3). The homogeneous pressure is subject to the following matching and asymptotic conditions:

$$\bar{p}_1(\boldsymbol{\xi}) - \bar{p}_2(\boldsymbol{\xi}) = \frac{1}{Ca_g} \left( \frac{2}{b(\boldsymbol{\xi})} + \frac{\pi}{4} k(\boldsymbol{\xi}) \right) \quad \text{for } \boldsymbol{\xi} \in S \quad (5.16)$$

$$\bar{M}_1(\boldsymbol{\xi}) \frac{\partial \bar{p}_1(\boldsymbol{\xi})}{\partial n} = \bar{M}_2(\boldsymbol{\xi}) \frac{\partial \bar{p}_2(\boldsymbol{\xi})}{\partial n} \quad \text{for } \boldsymbol{\xi} \in S \quad (5.17)$$

$$\frac{\partial \bar{p}_1(\mathbf{x})}{\partial r} \Big|_{\mathbf{x} \rightarrow 0} \rightarrow -\frac{1}{2\pi r} \quad (5.18)$$

$$\bar{p}_2(\mathbf{x}) \Big|_{\mathbf{x} \rightarrow \infty} \rightarrow -\frac{1}{2\pi} \ln(r) \quad (5.19)$$

Here,  $Ca_g$  is the global capillary number, appearing due to the non-dimensional scaling of the problem. The global capillary number in (5.16) describes the ratio of viscous driving forces to surface tension forces in terms of the characteristic mobility  $\bar{M}_2$  and plate separation  $\bar{b}$  at the origin:

$$Ca_g = \frac{12\bar{\mu}_2 Q}{\gamma r_0} \left( \frac{r_0}{\bar{b}} \right)^2 = \frac{r_0 Q}{\gamma \bar{M}_2} \quad (5.20)$$

where  $r_0$  is the initial unperturbed interface radius. By considering the global conditions given by (5.2), (5.3) and (5.5), equation (5.14) is then subject to the following matching

conditions at the interface and asymptotic conditions near the origin and in the far field:

$$\tilde{p}_1(\boldsymbol{\xi}) - \tilde{p}_2(\boldsymbol{\xi}) = 0 \quad \text{for } \boldsymbol{\xi} \in S \quad (5.21)$$

$$m_1(\boldsymbol{\xi}) \frac{\partial \tilde{p}_1(\boldsymbol{\xi})}{\partial n} = m_2(\boldsymbol{\xi}) \frac{\partial \tilde{p}_2(\boldsymbol{\xi})}{\partial n} \quad \text{for } \boldsymbol{\xi} \in S \quad (5.22)$$

$$\frac{\partial \tilde{p}_1(\boldsymbol{x})}{\partial r} \Big|_{\boldsymbol{x} \rightarrow 0} \rightarrow 0 \quad (5.23)$$

$$\tilde{p}_2(\boldsymbol{x}) \Big|_{\boldsymbol{x} \rightarrow \infty} \rightarrow 0 \quad (5.24)$$

Asymptotic conditions (5.18), (5.19), (5.23) and (5.24) ensure that the total pressure and total velocity tend toward that arising solely from the injection source near the origin and in the far field. Since  $b(\boldsymbol{x} \rightarrow 0) = \bar{b}$ , the velocity field is defined solely by the homogeneous solution arising from  $\bar{p}(\boldsymbol{x})$  near the origin; see for example Figure 5.10, where  $\frac{\partial \bar{p}(\boldsymbol{x})}{\partial x} \approx 0$  around the origin.

The perturbed pressure flux matching condition (5.22) is scaled by the plate variation  $b(\boldsymbol{x})$  in order to maintain consistency with the effective diffusion in equation (5.14). In this way, the homogeneous pressure evaluates the flow in a constant plate separation, and the perturbed pressure the effect due to changes in geometry of the flow path.

The obtained values of  $\bar{p}_l$  and  $\tilde{p}_l$  can be used to reconstruct the normal velocity at an interface point,  $\boldsymbol{\xi}$ , in order to track the fluid:

$$U_n(\boldsymbol{\xi}) = \bar{u}_n(\boldsymbol{\xi}) + \tilde{u}_n(\boldsymbol{\xi}) \quad (5.25)$$

$$U_n(\boldsymbol{\xi}) = -M_1(\boldsymbol{\xi}) \frac{\partial \bar{p}_1(\boldsymbol{\xi})}{\partial n} - M_1(\boldsymbol{\xi}) \frac{\partial \tilde{p}_1(\boldsymbol{\xi})}{\partial n} \quad (5.26)$$

The evaluation of the perturbed and homogeneous pressure requires discretisation of the domain and interface as well as the use of a coupled BE-RBF-FC numerical method, discussed in the next section.

### 5.3 Numerical methods

Here, the solution procedures to evaluate the perturbed and homogeneous pressure components are described, along with the reconstruction of the interface velocity with equation (5.26). The homogeneous pressure is solved using a boundary element method

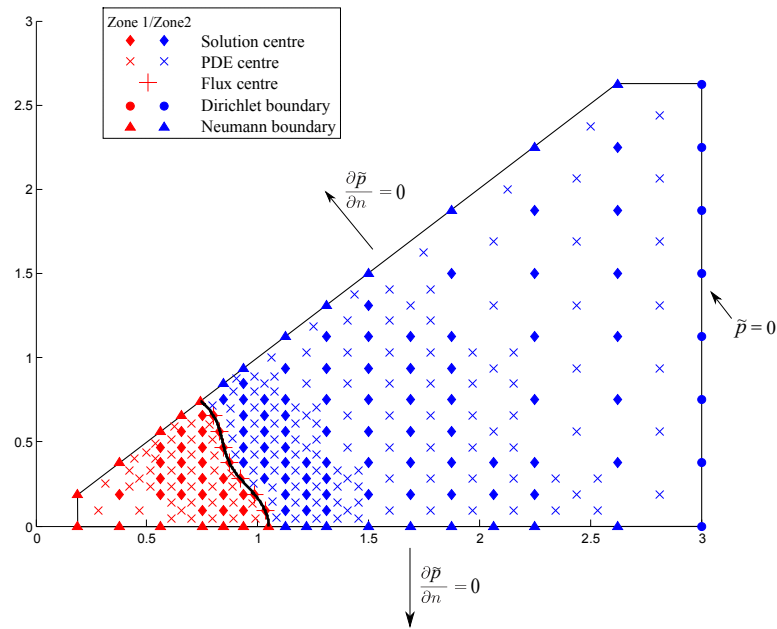


Figure 5.2: Solution domain showing different operator types. The curved solid black line indicates the fluid-fluid interface over which the boundary elements are formed. Note only 1/8th of the interface is shown here for the RBF-FC method, but the BEM evaluates the full interface.

similar to that shown in chapter 2 utilising an indirect formulation instead of a direct formulation.

The perturbed pressure equation (5.14) is solved via the strong form radial basis function finite collocation method presented in chapter 4 utilising the embedded multi-zone method. This requires both internal and boundary nodes as seen in Figure 5.2.

To decrease the solution cost for the methods an 8 finger symmetric interface is used throughout the numerical simulations. This enables the RBF-FC method to make use of symmetry in the domain and solve only 1/8<sup>th</sup> of the entire domain (shown in Figure 5.2). The boundary element method still solves the full interface, since it is typically an order of magnitude faster to solve than the RBF-FC method, and the formulation requires a closed interface. The perturbed velocities reconstructed by the RBF-FC method can be copied to the unsolved 7/8<sup>ths</sup> of the domain utilising symmetry, to reconstruct the full interface velocity to displace the interface.

### 5.3.1 Homogeneous pressure solution

The homogeneous pressure can be represented as a sum of the pressures due to an injection potential source,  $Q$ , and the double layer potential density,  $W(\mathbf{x}, \psi)$ .

$$\bar{p}_1(\mathbf{x}) = W(\mathbf{x}, \psi) - \frac{1}{2\pi\beta} \ln(r) \quad (5.27)$$

$$\bar{p}_2(\mathbf{x}) = \beta W(\mathbf{x}, \psi) - \frac{1}{2\pi} \ln(r) \quad (5.28)$$

where  $\psi$  is the double layer potential density. In equations (5.27) and (5.28)  $\beta$  is the mobility ratio between the two fluids,  $\beta = \bar{M}_1/\bar{M}_2$  and  $W(\mathbf{x}, \psi)$  is the double layer potential, defined as:

$$W(\mathbf{x}, \psi) = \int_s K(\mathbf{x}, \mathbf{y}) \psi(\mathbf{y}) dS_y \quad (5.29)$$

The regular kernel,  $K(\mathbf{x}, \mathbf{y})$  is the normal derivative of the fundamental solution of Laplace's equation. Substituting the homogeneous pressures (5.27) and (5.28) into (5.16) and taking the limit at the interface of the two fluids, the following 2<sup>nd</sup> kind Fredholm equation is obtained:

$$-\frac{1}{2}\psi(\boldsymbol{\xi}) + \lambda \int_s K(\boldsymbol{\xi}, \mathbf{y}) \psi(\mathbf{y}) dS_y = f_s(\boldsymbol{\xi}) \quad (5.30)$$

where:

$$\lambda = \frac{1 - \beta}{\beta + 1} \quad (5.31)$$

$$f_s(\boldsymbol{\xi}) = \frac{1}{Ca_g(1 + \beta)} \left( \frac{2}{b(\boldsymbol{\xi})} + \frac{\pi}{4} k(\boldsymbol{\xi}) \right) + \left( \frac{\lambda}{2\pi\beta} \right) \ln(r) \quad (5.32)$$

The indirect formulation here has produced equation (5.30) which is the adjoint of equation (2.49) formed in the direct method. For this reason, the solution procedure can be formed in a very similar way, using the convergent series, i.e.:

$$\psi(\boldsymbol{\xi}) = \psi_0(\boldsymbol{\xi}) + \lambda\psi_1(\boldsymbol{\xi}) + \cdots + \lambda^m\psi_m(\boldsymbol{\xi}) \quad (5.33)$$

The terms in equation (5.33) can be calculated recursively, via the following formulae:

$$\psi_0(\boldsymbol{\xi}) = -2f(\boldsymbol{\xi}) \quad (5.34)$$

$$\psi_m(\boldsymbol{\xi}) = 2 \int_s K(\boldsymbol{\xi}, \mathbf{y}) \psi_{m-1}(\mathbf{y}) dS_y \quad \text{for } m \neq 0 \quad (5.35)$$

Once  $\psi$  has been calculated around the interface, the spatial derivatives of the double layer potential can be found to reconstruct the homogeneous normal velocity at the interface (and the source term for the perturbation pressure equation (5.14) in the corresponding zone):

$$\bar{u}_n(\boldsymbol{\xi}) = -M_1(\boldsymbol{\xi}) n_i \frac{\partial \bar{p}_1(\boldsymbol{\xi})}{\partial x_i} = -M_1(\boldsymbol{\xi}) n_i \left( \frac{\partial W(\boldsymbol{\xi}, \psi)}{\partial x_i} - \frac{x_i}{2\pi\beta r^2} \right) \quad (5.36)$$

The reconstruction of the derivative of the double layer potential in (5.36) requires the evaluation of a hypersingular integral. The hypersingular integral evaluation is performed in exactly the same way as that in the direct formulation in equation (2.49), using the semi-analytical subtraction technique. The only major difference between the two hypersingular integral evaluations, is that the evaluation is used for the inhomogeneous source term on the RHS of the direct equation, whilst the evaluation is done as a post-processing stage with the indirect method.

The indirect method is preferred here since the derivatives of the homogeneous pressure (needed for equation (5.14)) are easily reconstructed anywhere in the domain using the double layer potential, i.e.:

$$\frac{\partial \bar{p}_1(\mathbf{x})}{\partial x_i} = \frac{\partial W(\mathbf{x}, \psi)}{\partial x_i} - \frac{x_i}{2\pi\beta r^2} \quad (5.37)$$

$$\frac{\partial \bar{p}_2(\mathbf{x})}{\partial x_i} = \beta \frac{\partial W(\mathbf{x}, \psi)}{\partial x_i} - \frac{x_i}{2\pi r^2} \quad (5.38)$$

In the direct method, the constant for the no-flux condition  $k_{as}$  must be found before the surface potentials can be reconstructed in equations (2.43) and (2.44) to find the spatial derivatives of the pressure. This introduces extra computation that is not necessary with the indirect method. The direct method is preferred for solutions that only require the interface velocity (since only one equation has to be solved), whereas the indirect method is preferred when domain velocities must also be calculated.

The boundary element representation for equation (5.30) uses the same cubic B-spline

formulation as in chapter 2. When solving the homogeneous velocity on the interface, the direct and indirect methods give exactly the same solution (down to the double precision implementation), with identical mesh and time step characteristics due to the equivalence of the adjoint equations being solved.

The spatial derivatives of the double layer potential for the domain source terms in (5.14) can exhibit near hypersingularities when the domain point is very close to the interface. This only occurs on PDE points from cells that coincide with the interface, since solution points from the cell will be directly displaced onto the interface. When this happens, the PDE points are simply removed from the formulation, since the regular integration scheme will be poor. If the PDE point is close to the interface due to the deformed vertices of a cell, but not from a cell directly coinciding with the interface, the integration scheme can subdivide nearby elements and use many integration points to accurately resolve the near singular integration.

### 5.3.2 Perturbed pressure solution

In this section, the RBF-FC method is formulated to evaluate the perturbed pressure in equation (5.14). The solution method uses the embedded multi-zone method presented in chapter 4 utilising the quadtree dataset based on the 1-1 stencil configuration. Nodal points close to the interface are deformed to lie directly on the interface so that flux and field variable matching conditions can be applied consistently. The cell centroids (where the PDE nodal points are placed) are also deformed so that they lie in the geometric centre of the cell.

An example problem domain is presented in Figure 5.2 for the perturbed pressure solution, showing an example nodal discretisation generated by the quadtree dataset. The quadtree is initialised using a distance based scheme to cluster cells around the boundary element interface, in which a cell will split if the following equality is met:  $D_c B_t > R_c$ . Here,  $D_c$  refers to the diagonal length of the cell,  $R_c$  is the distance from the cell centre to the closest point on the interface and  $B_t$  is the band thickness. After initialisation, the cells closest to the interface are deformed such that their vertices lie directly on the interface and the centres lie at the geometric centre of the cell. Vertices move in a purely orthogonal direction to maintain spatial consistency. After the quadtree

has been generated, the nodal points for the 1-1 RBF-FC local systems can be created based on the vertices and cell centres of the leaf cells.

As the present Darcy formulation is quasi-static, the perturbed pressure equation (5.14) can be described generally as a steady-state multi-zone transport boundary value problem of the form:

$$L_{l,x}[\tilde{p}_l(\mathbf{x})] = -S_l(\mathbf{x}) \quad \mathbf{x} \in \Omega_l \quad (5.39)$$

$$B_{l,x}[\tilde{p}_l(\mathbf{x})] = g_l(\mathbf{x}) \quad \mathbf{x} \in \partial\Omega_l \quad (5.40)$$

$$Q_{l,x}[\tilde{p}_l(\mathbf{x})] = f_l(\mathbf{x}) \quad \mathbf{x} \in \partial\Omega_{int} \quad (5.41)$$

where:

$$L_{l,x} = m_l(\mathbf{x}) \frac{\partial^2}{\partial x_i^2} + \frac{\partial \tilde{m}_l(\mathbf{x})}{\partial x_i} \frac{\partial}{\partial x_i} \quad \mathbf{x} \in \Omega_l \quad (5.42)$$

$$S_l(\mathbf{x}) = \frac{\partial \tilde{m}_l(\mathbf{x})}{\partial x_i} \frac{\partial \tilde{p}_l(\mathbf{x})}{\partial x_i} \quad \mathbf{x} \in \Omega_l \quad (5.43)$$

$$B_{l,x}^{DU} = B_{l,x}^{DK} = 1, \quad B_{l,x}^N = n_i \frac{\partial}{\partial x_i} \quad \mathbf{x} \in \partial\Omega_l \quad (5.44)$$

$$g_l^{DU}(\mathbf{x}) = \tilde{p}_l(\mathbf{x}), \quad g_l^{DK}(\mathbf{x}) = 0, \quad g_l^N(\mathbf{x}) = 0 \quad \mathbf{x} \in \partial\Omega_l \quad (5.45)$$

$$Q_{l,x} = \tilde{m}_l(\mathbf{x}) n_i \frac{\partial}{\partial x_i} \quad \mathbf{x} \in \partial\Omega_{int} \quad (5.46)$$

$$f_l(\mathbf{x}) = \tilde{m}_l(\mathbf{x}) n_i \frac{\partial \tilde{p}_l(\mathbf{x})}{\partial x_i} \quad \mathbf{x} \in \partial\Omega_{int} \quad (5.47)$$

In equations (5.39) to (5.47), subscript  $l$  refers to the zone.  $L_l$ ,  $B_l$  and  $Q_l$  are linear partial differential operators on the domain  $\Omega_l$ , the boundary  $\partial\Omega_l$  and the fluid-fluid interface  $\partial\Omega_{int}$  respectively. The operator  $Q_{l,x}$  refers to the flux operator in zone  $l$  acting on node  $x$ .  $S_l(\mathbf{x})$  is the source term coming from the homogeneous pressure  $\bar{p}(\mathbf{x})$  in domain  $\Omega_l$ . Superscript  $DU$ ,  $DK$  and  $N$  refer to Dirichlet unknown, Dirichlet known and Neumann boundary operators respectively.

The value of the perturbed pressure  $\tilde{p}_l(\mathbf{x})$  can be reconstructed as a weighted sum of partial differential operators applied to a set of radial basis functions that are centred on nodes  $\mathbf{y}_j$ . At nodes lying on the domain boundary the boundary operator  $B$  is applied to the corresponding RBF, and at nodes within the domain interior the governing PDE operator  $L$  is applied. For nodes which exist on the fluid-fluid interface, both the solution

operator  $C$  and the flux operator  $Q$  are applied:

$$\begin{aligned} \tilde{p}_l(\mathbf{x}) = & \sum_{j=1}^{NB} \tau_j B_{l,y} \Psi(\|\mathbf{x} - \mathbf{y}_j\|) + \sum_{j=NB+1}^{NB+NI+1} \tau_j \bar{L}_{l,y} \Psi(\|\mathbf{x} - \mathbf{y}_j\|) \\ + & \sum_{j=NB+NI+2}^{NB+NI+NF+2} \tau_j C_{l,y} \Psi(\|\mathbf{x} - \mathbf{y}_j\|) + \sum_{j=NB+NI+NF+3}^{NB+NI+2NF+3} \tau_j Q_{l,y} \Psi(\|\mathbf{x} - \mathbf{y}_j\|) \end{aligned} \quad (5.48)$$

In equation (5.48),  $NB$  is the number of boundary nodes,  $NF$  is the number of flux (interface) nodes and  $NI$  is the number of internal nodes,  $\tau_j$  are the unknown weights. The RBF operators  $\Psi$  in equation (5.48) are Hardy Multiquadric RBF interpolants. Enforcing the PDE system (5.39 - 5.41) at a set of test locations, equal to the set of functional centres in a local stencil in zone  $l$ , a collocation matrix can be formed. These collocation matrices can be formed at every interior node, creating  $N$  local RBF collocation systems.

To link the systems together,  $\tilde{p}_l(\mathbf{x})$  is reconstructed at each system centrepoint using the RBF reconstruction formula (5.48). By performing the reconstruction of  $\tilde{p}_l(\mathbf{x})$  at the centrepoint of each local system  $k$ , a series of  $N$  simultaneous equations are formed for the  $N$  unknown values of  $\tilde{p}_l(\mathbf{x})$  and  $Q_x(\tilde{p}_l(\mathbf{x}))$  at the system centrepoints. For each node that lies on the interface between the fluids, two reconstructions are performed in the embedded multi-zone method, one for each RBF system with a centrepoint at that node. By solving this sparse global system the values of  $\tilde{p}_l(\mathbf{x})$  and  $Q_x(\tilde{p}_l(\mathbf{x}))$  are obtained at the  $N$  internal nodes.

After the solution of the sparse global system, the normal perturbation velocity  $\tilde{u}_n(\boldsymbol{\xi})$ , at a location  $\boldsymbol{\xi}$  on the interface can be reconstructed using the nearest overlapping system, i.e.:

$$\tilde{u}_n(\boldsymbol{\xi}) = -M_1(\boldsymbol{\xi}) \frac{\partial \tilde{p}_1(\boldsymbol{\xi})}{\partial n} \quad (5.49)$$

### 5.3.3 Coupled solution algorithm

To solve the coupled homogeneous and perturbed pressure problem, the following algorithm is used:

1. Initialise the interface with an 8 finger perturbation and discretise into B-Spline boundary elements.

2. Initialise the quadtree dataset, deforming it around the initial interface position.
3. Solve the double layer potential density around the interface, equation (5.30).
4. Reconstruct the normal homogeneous velocity at every boundary element node around the interface using equation (5.36). Reconstruct the spatial derivatives of the homogeneous pressure at every internal (RBF) node in the domain, for use in the source term for equation (5.14).
5. Solve equation (5.14) using the RBF-FC method. Reconstruct the normal perturbation velocity at every boundary element node using using the nearest overlapping systems with equation (5.49).
6. Find the total normal velocity at the interface nodes using equation (5.25).
7. Advance the interface nodes using a forward Euler time stepping scheme:  $\Delta x_i = n_i U_n \Delta t$ .
8. Re-form the boundary elements around the new interface position. Adapt the quadtree dataset to the new interface position. Increase time by  $\Delta t$ .
9. Repeat steps 1 to 8 until the simulation end time has been reached.

## 5.4 Mass conservation verification

In this section, the coupled numerical scheme is used to solve the displacement of an initially circular interface, with zero perturbation. Perturbations will only grow after a long period of time due to numerical error, meaning that the interface should propagate as a growing circle with an increasing volume equal to that injected at the origin. The numerical volume of the growing plume and the volume of fluid injected at the origin can be compared to verify that the numerical scheme is mass conservative (since the density is constant) and that the governing equation of the flow (5.1) is being satisfied. The total volume of fluid in the cell is given in non-dimensional form as:

$$V_a = V_0 + \bar{b}t \quad (5.50)$$

Where  $V_0$  is the initial volume of fluid in the cell. If the interface displaces as an unperturbed circle with radius  $r(t)$  in a uniform cell with  $b(\mathbf{x}) = \bar{b}$ , the volume can be expressed as:

$$V_a = \pi \bar{b} r(t)^2 = \bar{b}(\pi + t) \quad (5.51)$$

$$r(t) = \sqrt{\frac{\pi + t}{\pi}} \quad (5.52)$$

To ensure that mass has been conserved in the numerical method, the volume of fluid can be calculated through numerical integration of the evolving interface (using the average interface position  $\bar{r}$ ) and compared to the value given by equation (5.50). Although there are no fingering effects present due to the constant curvature, the problem still provides validation of the coupling of the RBF method and the BEM. The BEM has been validated for homogenous mobility cases in chapter 2, meaning the mass conservation tests presented here will validate that the RBF-FC method is contributing a correct velocity to displace the interface. The RBF method still solves the full multi-zone steady-state pressure problem, but with the interface given by a simple circle instead of the convoluted interface usually found in viscous fingering problems.

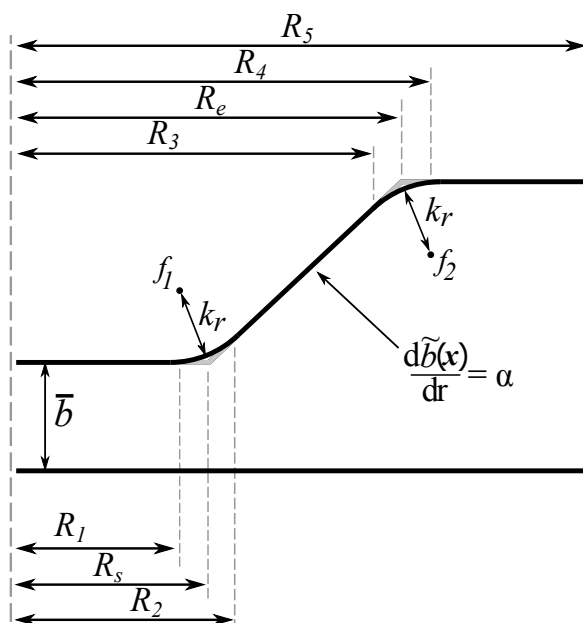


Figure 5.3: Gradually diverging Hele-Shaw cell diagram (gradient exaggerated for display purposes). The dashed line at the far left of the domain shows the line of symmetry at the origin.

For an inhomogeneous test case, a gradually varying cell geometry is studied, shown in

Figure 5.3. The cell is axisymmetric around the origin, with values of  $\tilde{b}(\mathbf{x})$  and  $\partial\tilde{b}(\mathbf{x})/\partial x_i$  at the different radial locations  $r = |\mathbf{x}|$  in Figure 5.3 as:

$$\tilde{b}(\mathbf{x}) = 0, \quad \frac{\partial\tilde{b}(\mathbf{x})}{\partial x_i} = 0 \quad r < R_1, r > R_4 \quad (5.53)$$

$$\tilde{b}_l(\mathbf{x}) = \pm (R_w^2 - (r - f_l(1))^2)^{\frac{1}{2}} + f_l(2) - \bar{b}, \quad \frac{\partial\tilde{b}(\mathbf{x})}{\partial x_i} = \mp \left( \frac{\left(\frac{x_i}{r}\right)(r - f_l(1))}{(R_w^2 - (r - f_l(1))^2)^{\frac{1}{2}}} \right) \\ R_1 < r < R_2, R_3 < r < R_4 \quad (5.54)$$

$$\tilde{b}(\mathbf{x}) = \alpha(r - R_s), \quad \frac{\partial\tilde{b}(r)}{\partial x_i} = \alpha \left( \frac{x_i}{r} \right) \quad R_2 < r < R_3 \quad (5.55)$$

In equation (5.54), subscript  $l$  refers to fillet 1 or 2 in Figure 5.3.  $f_l$  is the centrepoint of fillet  $l$  with coordinates  $(f_l(1), f_l(2))$ , with radius of curvature  $k_r$ . The  $+/-$  sign in  $\tilde{b}_l(\mathbf{x})$  refers to a converging/diverging fillet ( $2^{nd}/1^{st}$  fillet in Figure 5.3).  $R_w$  is the length of the fillet, i.e.,  $R_w = R_s - R_1$ . The fillet is defined by inputs of  $R_s, R_e, R_w$  and simple trigonometric identifies. In the simulations in this section  $\bar{b} = 0.01$ , the gradient of the slope  $|\alpha| = 0.001$ ,  $R_s = 0.6$ ,  $R_e = 5$  and  $R_w = 0.1$ . These parameters ensure that plate separation varies gradually through the cell and that the circular interface, with an unperturbed radius of  $r = 1$ , exists entirely in the constant gradient section from  $t = 0$  to the end of the simulation.

Given the symmetry of the problem, a triangular solution domain is used for the RBF-FC method, similar to that shown in Figure 5.2, with an outer boundary at  $x = 32$ . For the validation cases the maximum quadtree cell level (MQL) is varied from 8 - 10 whilst maintaining a minimum quadtree cell level of 3. The band thickness values  $B_t$  are varied for each cell level, in contrast to the constant values used in chapter 4. Varying  $B_t$  with each level allows greater control of the individual band thickness and fine-tuning for the specific problems. Here, the maximum cell level has  $B_t = 3$ , which is increased in increments of 0.5 up to the minimum cell level. A constant non-dimensional shape parameter value of  $c^* = 70$  is used for all simulations. The time step size is varied to showcase the temporal convergence properties. In the boundary element method the full interface is solved, around which a target element size is maintained throughout the

simulations at  $\Delta x \approx 0.06$ , ensuring a mesh-independent boundary element solution (see chapter 2, section 2.4.6).

Property	Value (SI Units)
$\mu_{Brine}$	$1 \times 10^{-3}$ Pa.s
$\mu_{CO_2(sc)}$	$1 \times 10^{-4}$ Pa.s
$\mu_{MineralOil}$	$2.5 \times 10^{-2}$ Pa.s
$\mu_{Air}$	$2 \times 10^{-5}$ Pa.s
$\beta_{CO_2(sc)/brine}$	10
$\beta_{Air/Mineral Oil}$	1250
$\gamma(CO_2-Brine) \ \& \ \gamma(Air-Mineral Oil)$	$0.03 \text{ kg/s}^2$

Table 5.1: Fluid properties used in the numerical experiments

The fluid properties used for the numerical experiments in both this section and the results section are summarised in table 5.1. The properties are taken at suitable aquifer conditions, with mineral oil and air properties used in results that compare with corresponding previous works. In this validation study,  $CO_2$  and brine are used as the working fluids, with a global capillary number  $Ca_g = 1000$ .

The results showing the relative error between the numerical and analytical volumes of fluid in the Hele-Shaw cells at a time  $t = 10$  are displayed in table 5.2. It can be seen that the relative errors for all time step and mesh discretisations shown are relatively low, with the largest error being only  $3.97 \times 10^{-3}$ . The dataset with MQL = 8 shows the largest error generally, due to the very coarse discretisation around the interface. With MQL = 8, the RBF dataset is roughly 2x coarser than the boundary element mesh, meaning that several elements can exist between RBF nodes. This is undesirable as the interface could curve significantly between data points, meaning the interface matching conditions are not adequately represented in the RBF dataset. As the nodal points are ‘snapped’ to the nearest position on the boundary element mesh, the resulting RBF dataset is not as uniform if the nodal discretisation is very much larger than the boundary element discretisation.

When the MQL is increased from 8 through to 10, the relative error drops significantly, especially at the smaller time step sizes. At the lowest time step size of  $\Delta t = 0.005$ , the error is 9 to 16 times lower than at MQL = 8, representing close to  $2^{nd}$  order spatial convergence. The increased solution quality is due to the MQL = 10 dataset being twice as refined as the boundary element mesh around the interface. This means that in

between the RBF nodes, the interface is much closer to a linear approximation, making the strong form RBF collocation of matching conditions more consistent, leaving less space for the flux and solution matching conditions to vary between points. At  $\text{MQL} = 10$ , the time stepping scheme exhibits 1<sup>st</sup> order convergence as expected due to the forward Euler implementation.

In some instances of the diverging cases with the larger time step sizes, the  $\text{MQL} = 9$  dataset performs slightly better than the  $\text{MQL} = 10$  dataset. This is because at these larger time step values in the diverging case, the scheme has reached the limit of solution accuracy, and needs a further decrease in the time step size to see a significantly reduced error. This is not seen in the converging case since the error is generally larger and has not reached the limit of spatial accuracy at the large time step values.

Hele-Shaw cell case	Time step size, $\Delta t$	MQL = 8	MQL = 9	MQL = 10
		$\Delta x = 0.125$	$\Delta x = 0.0625$	$\Delta x = 0.03125$
		Relative error	Relative error	Relative error
Converging, $\alpha = -0.001$	0.040	$3.97 \times 10^{-3}$	$2.14 \times 10^{-3}$	$1.29 \times 10^{-3}$
	0.020	$3.35 \times 10^{-3}$	$1.51 \times 10^{-3}$	$6.60 \times 10^{-4}$
	0.010	$3.05 \times 10^{-3}$	$1.18 \times 10^{-3}$	$3.45 \times 10^{-4}$
	0.005	$2.90 \times 10^{-3}$	$1.04 \times 10^{-3}$	$1.87 \times 10^{-4}$
Diverging, $\alpha = 0.001$	0.040	$3.02 \times 10^{-3}$	$9.46 \times 10^{-4}$	$1.56 \times 10^{-3}$
	0.020	$2.22 \times 10^{-3}$	$1.77 \times 10^{-4}$	$7.57 \times 10^{-4}$
	0.010	$1.83 \times 10^{-3}$	$2.02 \times 10^{-4}$	$3.67 \times 10^{-4}$
	0.005	$1.64 \times 10^{-3}$	$4.02 \times 10^{-4}$	$1.78 \times 10^{-4}$
Uniform, $\alpha = 0.000$	0.040	$1.43 \times 10^{-3}$	$1.43 \times 10^{-3}$	$1.43 \times 10^{-3}$
	0.020	$7.16 \times 10^{-4}$	$7.16 \times 10^{-4}$	$7.16 \times 10^{-4}$
	0.010	$3.58 \times 10^{-4}$	$3.58 \times 10^{-4}$	$3.58 \times 10^{-4}$
	0.005	$1.79 \times 10^{-4}$	$1.79 \times 10^{-4}$	$1.79 \times 10^{-4}$

Table 5.2: Relative errors between the numerical and analytical volumes of fluid in the cell at  $t = 10$  with different mesh and time step discretisations.  $\text{MQL} =$  maximum quadtree cell level.

The time evolution of the relative errors between the numerical and analytical volume of fluid can be seen in Figure 5.4. For a fixed low time step of  $\Delta t = 0.005$  in Figure 5.4(a), the error for the different nodal discretisations becomes much more consistent as  $\Delta x$  is lowered. The coarse discretisation of  $\Delta x = 0.125$  ( $\text{MQL} = 8$ ), shows fairly erratic behaviour due to the interface representation. However, the error evolution becomes much smoother as  $\Delta x \rightarrow 0.03125$ . As time progresses the error drops since the interfacial velocity becomes lower and the fixed Euler time stepping scheme becomes more accurate.

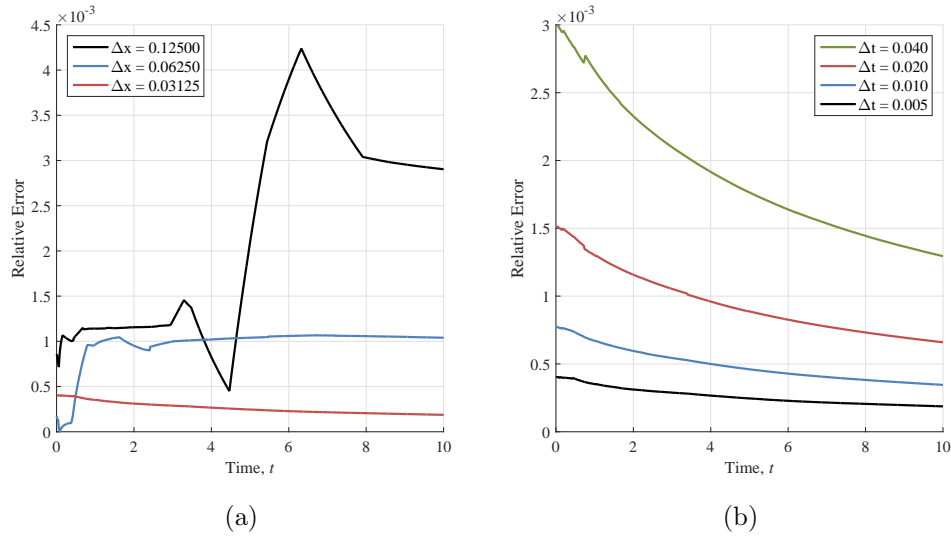


Figure 5.4: Time evolution plots of the relative error between analytical and numerical volume of fluid in the converging Hele-Shaw cell  $\alpha = -0.001$ . (a) Different nodal discretisations,  $\Delta t = 0.005$ . (b) Different time step discretisations,  $\Delta x = 0.03125$ .

The first order temporal convergence can be seen in Figure 5.4(b), where the time step size is varied for the finest spatial discretisation ( $\Delta x = 0.03125$ ). Due to the smoothness of the error evolution and the generally low relative error, the finest dataset ( $\Delta x = 0.03125$ , MQL = 10) is chosen for simulations in the following results sections. For practicality,  $\Delta t = 0.02$  is used to provide a good balance between solution accuracy and simulation running times.

## 5.5 Numerical results and discussion

In this section, results are presented from several numerical experiments exploring the variable plate separation problem. In order to compare with previous work, studies based on air injection into mineral oil are presented, corresponding to the cases of negligible viscosity of the injected fluid considered by [128], [130] and [133]. In the current formulation, the low viscosity of the injected fluid is included in the model, resulting in a (high) finite mobility ratio between the air and mineral oil. As well as the high mobility ratio regime, a low mobility ratio regime is also considered in order to analyse the injection of supercritical  $CO_2$  into brine. The fluid properties used for the numerical experiments are summarised in the previous section in table 5.1.

Throughout the numerical simulations, an 8 finger symmetric pattern is used as the initial interface condition, given in Figure 5.1(a) as:

$$r = 1 + \epsilon_0 \cos(8\theta) \quad (5.56)$$

where  $\epsilon_0$  and  $\theta$  are the perturbation amplitude and the azimuthal angle around the interface respectively. A symmetric 8 finger perturbation is used in contrast to the 6 finger perturbation in chapter 2 and 3 so that a reduced  $1/8^{th}$  domain can be implemented simply using the quadtree nodal arrangement. In a  $1/6^{th}$  domain representation using the 6 finger perturbation, points have to be deformed to lie on the symmetric boundary, producing sub optimal boundary systems in the RBF-FC method.

### 5.5.1 Uniformly converging/diverging Hele-Shaw cells

This section explores the immiscible displacement in a uniformly varying cell geometry with a small constant gradient  $\alpha$  in the radial direction, as shown in Figure 5.3 in the previous section. In the simulations in this section  $\bar{b} = 0.01$ ,  $R_s = 0.6$ ,  $R_e = 5$  and  $R_w = 0.1$ . The initial perturbation amplitude  $\epsilon_0 = 0.05$ . These parameters ensure that plate separation varies gradually through the cell and that the interface, with an unperturbed radius of  $r = 1$ , exists entirely in the constant gradient section from  $t = 0$  to the end of the simulation.

Given the symmetry of the problem, a triangular solution domain can be used for the RBF-FC method, similar to that shown in Figure 5.2, with an outer boundary at  $x = 32$ . The minimum quadtree cell level is 3 with a maximum level of 10,  $B_t$  varies uniformly from 3 at cell level 10 to 6.5 at cell level 3,  $c^* = 70$ . In the boundary element method the full interface is solved, around which a target element size is maintained throughout the simulations at  $\Delta x \approx 0.06$  and time step size of  $\Delta t = 0.02$ . This ensures that the RBF-FC nodal refinement is around twice that of the BEM around the interface, and that both solutions are mesh and time step independent.

In Figure 5.5, results are presented for different capillary number and mobility ratio flows in uniform, converging and diverging cell geometries.  $\beta = 1250$  corresponds to air injection into mineral oil, and  $\beta = 10$  corresponds to supercritical  $CO_2$  injection into brine. In the converging cases in Figures 5.5(a) and 5.5(d), the interfaces have

been stabilised in the low capillary number regimes, where the bases of the fingers have been pushed outwards, resulting in more circular interfaces. The lower mobility ratio in Figure 5.5(d) has stabilised the interface even further compared to Figure 5.5(a). This is due to the higher finger base velocities present in low mobility ratio cases, as the inner fluid has a non-negligible viscosity. This, coupled with the converging cell geometry, produces a very stable interface that shows almost no signs of the usual viscous fingering regime. The stabilising effect of the converging geometry is also present in Figures 5.5(b) and 5.5(e), however, with an increasing capillary number the stabilisation becomes less prominent.

The stabilisation in the low capillary number regime in the converging cases is due to the dominating effect of the transverse curvature in the capillary pressure jump condition. Here, as  $Ca_g$  is taken lower, the  $2/b(\mathbf{x})$  transverse curvature term has more effect. Parts of the interface which are further back in the plane of the cell are at a larger plate separation than those further forward, and hence the  $2/b(\mathbf{x})$  term is smaller. The capillary pressure is smaller, meaning it is easier for the viscous forces to overcome capillary forces. However, at the finger front where the plate separation is smaller, the capillary pressure is higher which stabilises the interface.

At higher capillary numbers, the effects of the stabilisation due to the transverse curvature are smaller, and the interfaces in the converging cases can actually be seen to displace beyond the uniform cases in Figures 5.5(c) and 5.5(f). The stabilisation from the transverse curvature is weakened, and the velocity is increased due to the converging geometry. The magnitude of the pressure gradient  $|\partial P(\mathbf{x})/\partial r|$  increases in the converging section to ensure mass conservation, accelerating the interface. This acceleration effect directly competes with the stabilisation from the capillary pressure and the reduction in fluid mobility through the converging section. The converging cell therefore induces the following effects that control the stability of the displacing interface:

1. Stabilisation through an increased transverse curvature.
2. Deceleration due to a reduced fluid mobility.
3. Acceleration due to an increased pressure gradient.

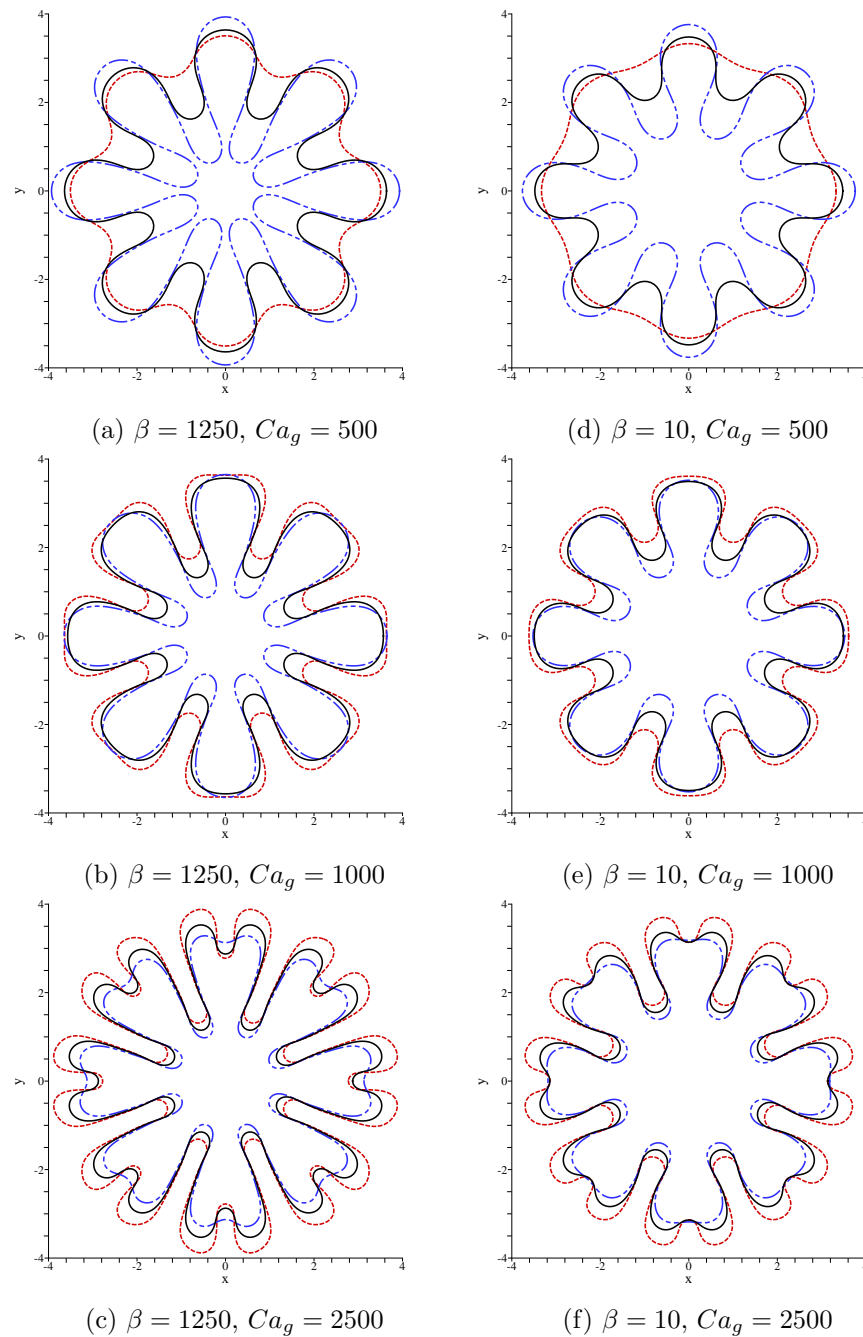


Figure 5.5: Interface plots at  $t = 24$  for different cell geometries.  $|\alpha| = 0.001$ . — Uniform cell, - - - Converging cell, - - - Diverging Cell

These effects can be thought of as aperture effects, as they result directly from the spatial change in cell aperture (plate separation). In Figure 5.5 it can be seen that the combined effects of the converging geometry appears to transition from stabilising at a low capillary number (aperture effect 1 and 2 dominate), to destabilising at a high capillary number (aperture effect 3 dominates). These effects are relative in relation to the uniform cell cases, i.e., at lower capillary numbers the interface is stabilised in

comparison to the uniform cell, but it may still be ‘unstable’ in an absolute sense and exhibit viscous fingering instabilities.

In contrast to the converging cases, the aperture effects listed above are exactly opposite for the diverging cases. The diverging cells in Figures 5.5(a) and 5.5(d) create a more convoluted interface with a high surface area in the low capillary number regime. The finger bases remain closer to the injection source, and the fingers are elongated from their original Saffman-Taylor shape. The lower mobility ratio regime in Figure 5.5 damps the effects of the diverging cell in a similar manner to the converging cases. There also appears to be a transition in the high capillary number regime whereby the diverging cell smooths the interface in Figures 5.5(c) and 5.5(f).

The transition in relative stability for the converging/diverging cases between low and high capillary numbers can be analysed by considering the growth rate of the finger front perturbation. In the converging cases, the fronts lag behind those of the uniform case at low capillary numbers, representing a more stable interface. At higher capillary numbers, the fronts extend beyond those of the uniform case. The reverse is true of the diverging cases, meaning the growth rate of the front perturbation can highlight the relative stability between cases. The dimensionless non-linear growth rate of a perturbation with radial position  $r$  is given by:

$$\sigma_t = U_n(r, t) - U_{n0}(r, t) \quad (5.57)$$

Where,  $U_n(r, t)$  is the normal velocity at the perturbed interface and  $U_{n0}(r, t)$  is the normal velocity at the unperturbed interface (in a uniform cell). The velocity of the unperturbed interface with time is given purely by the source injection velocity at the corresponding radius given by equation (5.52). The non-linear growth rate (5.57) subtracts the linear velocity of the base growth giving the non-linear growth of the perturbation with time. The non-linear growth rate for the finger fronts (using the rightmost finger in each plot in Figure 5.5 along  $y = 0$ ) has been plotted with time for the  $Ca_g = 500, 1000$  and  $2500$  cases in Figure 5.6.

Figure 5.6 shows that the converging cell has a smaller growth rate than the uniform cell at  $Ca_g = 500$ , supporting the stabilising mechanism of the transverse curvature highlighted by Figure 5.5(d). Increasing the capillary number to  $Ca_g = 1000$ , the growth

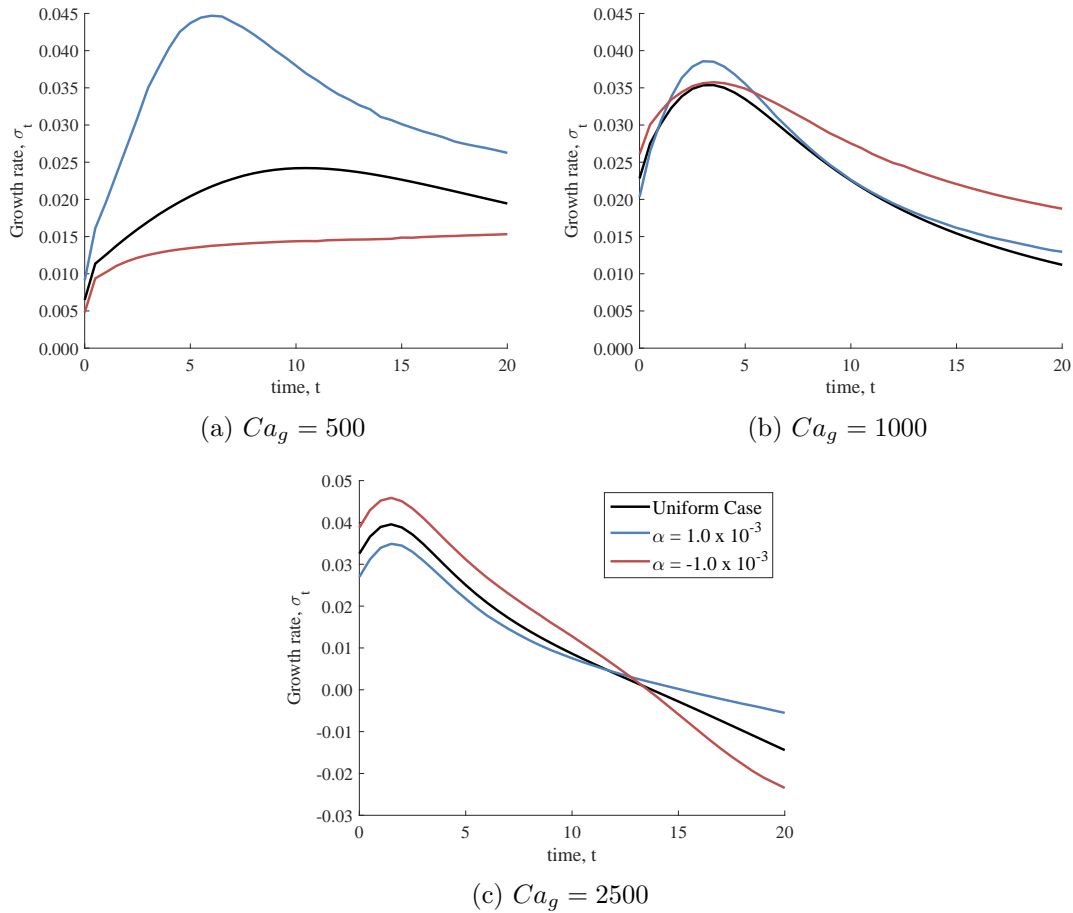


Figure 5.6: Plots showing the non-linear growth rates with time for uniform, converging and diverging cells.  $\beta = 10$

rate increases beyond that of the uniform cell, as the front becomes more unstable. Interestingly, the diverging case at  $Ca_g = 1000$  also exhibits a very slightly higher growth rate than the uniform, with remnants from the destabilising mechanism of the transverse curvature still apparent (see the resemblance of the fronts in Figures 5.5(b) and 5.5(e)). In this transition regime, the growth rates show similar profiles due to the combined magnitude of the aperture effects. Prediction of the relative stabilisation compared to the uniform case in the transition regime therefore becomes very difficult in the full non-linear state.

At the highest capillary number of  $Ca_g = 2500$  in Figure 5.6, the cases all show post-transition properties, whereby the converging case has a higher growth rate than the uniform, and the diverging case has a smaller growth rate than the uniform. This relationship holds until  $t \approx 14$  in the figure, at which point bifurcation starts to occur. After this, due to the increased destabilisation of the converging case, the growth rate

drops below that of the uniform case, as it bifurcates sooner and the front velocity drops. The reverse is true of the diverging case.

The low capillary number results in converging cases in the figures above show similar stabilising attributes to those presented by [130], in which air is injected into wetting mineral oil, with similar fluid properties to the high mobility ratio case presented here. They inject with a constant volumetric injection into a gradually converging rectilinear cell. As is the case with our converging cell, at low capillary numbers, [130] find that the interface can be almost completely stabilised to form a flat front.

Further work by [127] formulates the analytical growth rate for a circular fluid-fluid interface subject to an initial perturbation  $\epsilon_0$  with a constant radial injection flux and a constant radial gradient in the cell separation. For this linear stability analysis to be valid at early times, the length scale of interface perturbation  $r_0/n$  should be much smaller than the variation of the cell separation  $|b_0/\alpha|$ . The non-dimensional growth rate  $\sigma_a$  is given by [127] as:

$$\sigma_a = - \left( \frac{\beta + 1}{\beta} \right) \left( 1 + \frac{\alpha r_0}{b_0} \right) + \left( \frac{\beta - 1}{\beta} + \frac{2\alpha + (\pi/4)b_0^2/r_0^2}{Ca_{la}} \right) n - \frac{(\pi/4)b_0^2/r_0^2}{Ca_{la}} n^3 \quad (5.58)$$

$$Ca_{la} = \frac{12\mu_2 Q U_n(r_0)}{\gamma r_0} \quad (5.59)$$

In equations (5.58) and (5.59),  $U_n(r_0)$  refers to the non-dimensional normal interface velocity at a radial location  $r_0$  with corresponding plate separation  $b_0$ .  $n$  is the non-dimensional wavenumber of the perturbation (8 in the current work).  $Ca_{la}$  is the local capillary number used by [127], with slightly different scalings to those in  $Ca_l$  in this work. The parameter  $Q/r_0$  in (5.59) appears due to the non-dimensional velocity  $U_n(r_0)$ . Note the mobility ratio  $\beta$  has been included instead of the viscosity ratio originally used by [127] as well as a correction of  $\pi/4$  to be consistent with the Young-Laplace matching condition used in this work.

To compare the early time frame linear stability of the numerical system with that given by the equation (5.58), a linear numerical growth rate  $\sigma_i$  may be formed:

$$\sigma_i = \left( \frac{U_n(r_0 + \epsilon) - U_n(r_0)}{\epsilon_0 U_n(r_0)} \right) \left( \frac{\beta + 1}{\beta} \right) \quad (5.60)$$

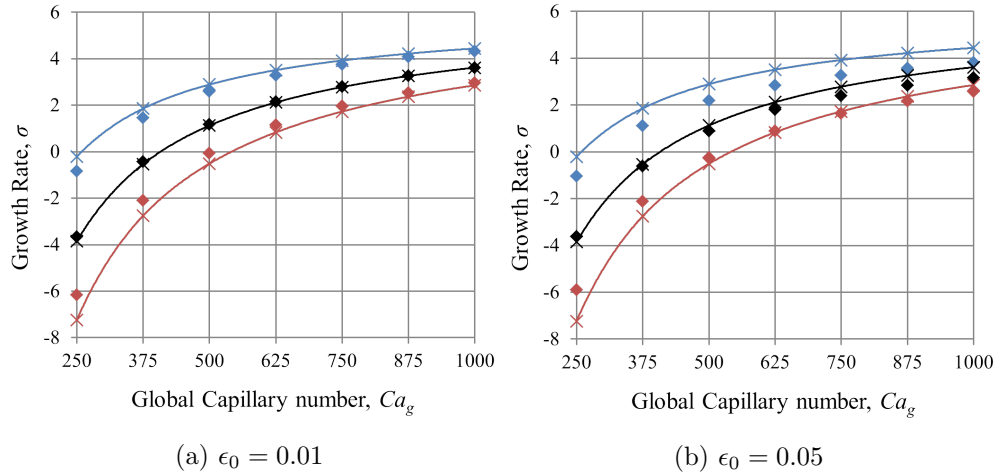


Figure 5.7: Plots showing the linear analytical and numerical growth rates for different initial perturbations  $\epsilon_0$  at the initial state.  $\beta = 10$ . Solid lines and crosses represent the analytical solution, diamonds represent the numerical solution. — Uniform cell, — Converging cell, — Diverging Cell

The linear numerical growth rate in (5.60) represents the growth rate of the interface at the perturbed initial state minus the growth rate at the unperturbed initial state. This growth rate differs from (5.57) in that it subtracts the non-linear velocity of the unperturbed interface as opposed to linear velocity in (5.57). The non-linear growth rate includes a component due to the changing geometry, meaning at small initial amplitudes (5.60) gives a linearised approximation to the growth rate. Using corresponding scalings  $\epsilon_0$ ,  $\beta$  and  $U_n(r_0)$ , the linear numerical growth rate in (5.60) is comparable to the analytical linear stability given in (5.58) at small initial perturbations  $\epsilon_0$  and at early time stages.

The linear analytical and numerical growth rates have been plotted for two different perturbation amplitudes in Figure 5.7. The growth rate is plotted against the global capillary number, rather than the local capillary number in (5.58) to be consistent with the numerical simulations in this work. The local capillary number in (5.58) can be found from the appropriate initial values, in order work out the growth rate for a specific global capillary number.

In Figure 5.7 it can be seen that the numerical growth rate at the initial state shows very good agreement with that given by the analytical rate in (5.58). As the perturbation value is lowered to  $\epsilon_0 = 0.01$  the numerical and analytical values become closer, as the

numerical growth rate becomes more linear and closer to the approximation given by the LSA.

The initial state growth rates can be used to give insight into the front evolution when the capillary number is low. For the  $Ca_g = 500$  cases, the growth rate is negative when the plates are converging in Figure 5.7, meaning the interface will be stable to perturbations of wave number  $n$ . This is clearly demonstrated in Figure 5.5(a) and 5.5(d), where the interfaces are almost completely stable. The reverse is also true of the uniform cell, in which the growth rate is positive, and clearly defined fingers form. In the simulation set-up, the ratio of length scale of interface perturbation to the variation of the cell separation is  $|\alpha r_0/nb_0| = 0.013$ . This is the same order of magnitude as the initial perturbation,  $\epsilon_0 = 0.05$ , making the linear stability analysis valid in the early stages of the simulations presented here.

In Figure 5.7, the initial state growth rates of the converging cases are always below that of the uniform cases, i.e. they are always more stable in the range  $250 \leq Ca_g \leq 1000$ , with the reverse true for the diverging cases. However, in the non-linear simulations with  $Ca_g = 1000$  at  $t = 24$  in Figure 5.5(e), the front is further displaced in the converging case compared to the uniform case, so must have a higher growth rate. The initial state linear stability therefore cannot accurately predict the transition at high capillary numbers. Although the converging and uniform curves in Figure 5.7 will eventually cross and transition, (i.e the converging case has a larger growth rate and becomes more unstable than the uniform), this does not occur until  $Ca_g > 1300$ , much higher than the transition in the numerical simulations.

To better predict the capillary number at which the converging case stops being more stable than the uniform case and transitions to have a relatively more unstable front, the non-linear numerical growth rate at the initial state can be used. The non-linear growth rate is plotted at the initial state for various values of  $\alpha$  in Figure 5.8. There exists a clearly defined transition region at  $Ca_g \approx 640$ , where the growth rate of the converging cases increases over the uniform case, and the growth of the diverging cases decreases below the uniform cases. In this plot, at  $Ca_g = 1000$ , the converging cases have larger growth rates than the uniform cases, exhibiting the same behaviour that can be seen from the numerical simulation in Figure 5.5(e). The non-linear growth rate at the initial state therefore provides a better prediction of the late stage displacement of

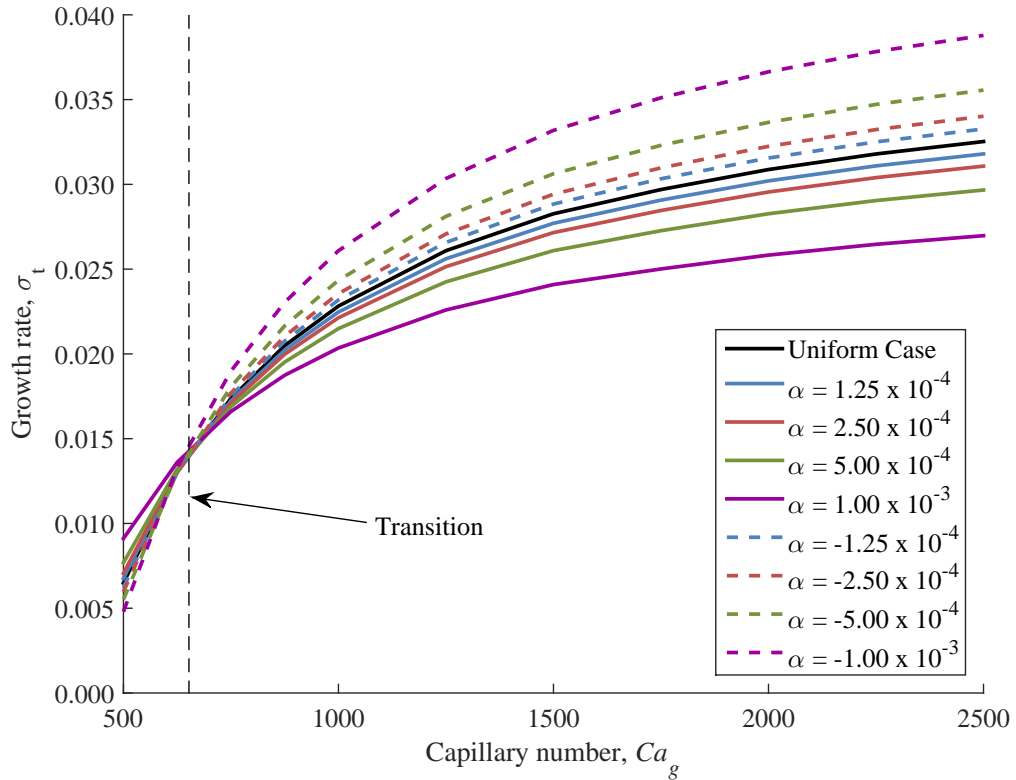


Figure 5.8: Non-linear numerical growth rate at the initial state.  $\beta = 10$ . The transition occurs at  $Ca_g \approx 640$ .

the finger front at higher capillary numbers than the linear growth rate, demonstrating the clear transition point at  $Ca_g \approx 640$ .

At  $Ca_g \approx 640$  in Figure 5.8, the different  $\alpha$  all have the same growth rate, i.e. the combination of stabilising and destabilising aperture effects result in the same finger front displacement regardless of  $\alpha$ . This appears counter-intuitive, as varying  $\alpha$  changes the magnitude of the three aperture effects. However, at the transition point for any  $\alpha$ , due to the competing effects, the combined result is to create an equal growth rate. In converging cases for example, the larger magnitude  $\alpha$  will cause more stabilisation from the transverse curvature (aperture effect 1) and a greater reduction in mobility (effect 2), but the pressure gradient is also significantly increased (aperture effect 3). Whereas for the smaller magnitude  $\alpha$ , there is less transverse curvature stabilisation and reduction in mobility, but also less increase in pressure gradient, resulting in the same growth rate.

The aperture effects of the converging/diverging Hele-Shaw cells are further highlighted by the different components of the solution in Figure 5.9. The difference between the

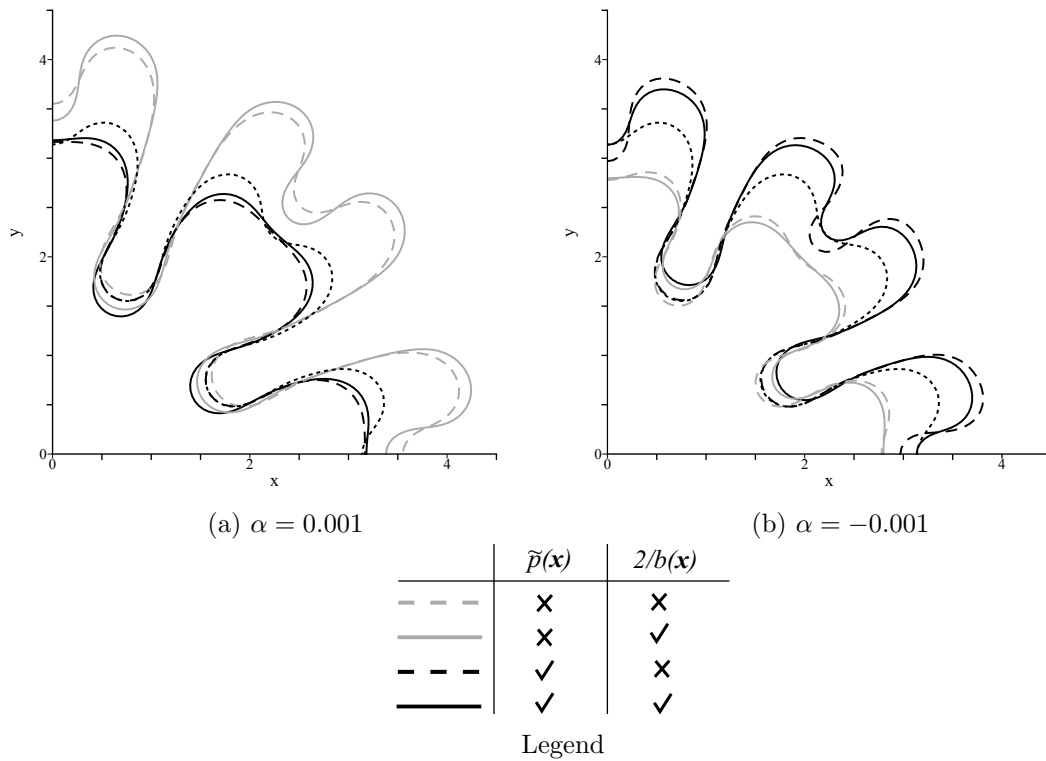


Figure 5.9: (a) and (b) - Solution component plots at  $t = 24$ . Ticks in the legend indicate which interfacial displacements in (a) and (b) include the curvature term  $2/b(\mathbf{x})$  and the perturbed pressure  $\tilde{p}(\mathbf{x})$ . The dotted lines represent the uniform cell case.  $\beta = 10$ ,  $Ca_g = 2500$ .

solid lines and the dashed lines shows the effect of the stabilising  $2/b(\mathbf{x})$  term. The solid lines have the transverse curvature term included in the capillary pressure jump, and as such the interface is smoothed from the dashed lines in the converging case 5.9(b). In diverging geometry, the transverse curvature destabilises the interface, leading to more ramified structures in figure 5.9(a). The capillary pressure is smaller at the finger fronts in the diverging case, and as such viscous forces overwhelm capillary forces, and the interface is more unstable to small perturbations.

The effect of the change in pressure gradient can also be seen in Figure 5.9 by considering the solution with and without the perturbed pressure component. Without the perturbed pressure component, the change in pressure gradient due to the converging/diverging geometry (aperture effect 3) is not included. This means the interface velocity consists of the uniform cell pressure gradient with a variable mobility and transverse curvature (solely aperture effects 1 and 2). Figure 5.9(b) shows that the black interfaces have all been displaced beyond the grey interfaces which do not

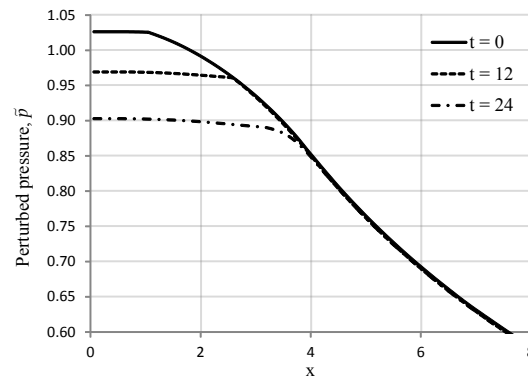


Figure 5.10: Graph showing the perturbed pressure along  $y = 0$  at various times for  $\beta = 10$ ,  $Ca_g = 2500$ ,  $\alpha = -0.001$

include the perturbed pressure. The converging geometry creates a decreasing perturbed pressure, whose gradient accelerates the interface. Without the perturbed pressure, the grey interfaces are not displaced even as far as the uniform cases, showing the dramatic effect that the increased pressure gradient has on the interfacial evolution at this high capillary number. The inclusion of the perturbed pressure has only significantly affected the finger fronts, with the base position remaining relatively unchanged, being affected more significantly by the transverse curvature. The accelerating flow from the perturbed pressure in the converging case has made the finger bifurcate earlier. In the diverging case, the perturbed pressure gradient slows the interface, helping to stabilise it and hinder bifurcation; clearly visible in Figure 5.9(a).

A 1D slice of the perturbed pressure solution taken at various times along  $y = 0$  with  $x \geq 0$  is shown in Figure 5.10. As the effective diffusivity in equation (5.14) is much higher in the inner zone due to the higher mobility of the fluid, the perturbed pressure is almost constant as it is rapidly diffused and convected to fill the inner zone. The pressure then quickly drops as the diffusivity and velocity reduce by a factor of  $\beta$  at the interface and act to bottleneck the perturbed pressure; see Figure 5.10. The perturbed pressure decreases to zero at the outer boundary to satisfy the constraint that the total pressure tends towards the pressure arising from the injection flux.

Using the effective diffusivity and velocity from equation (5.14), with the initial unperturbed interface radius  $r_0$  as the global lengthscale, the Peclet number varies from 0 to 0.5 in the domain, indicating that both diffusivity and convection are important in the perturbed pressure solution.

The increased flattening and bifurcation present in the converging cases here is in contrast to the findings of [128] in a rectilinear converging cell, whereby the finger shape was found to sharpen. This contrast is due to the rectilinear geometry, where one long prominent finger is produced with a uniform width throughout its length, roughly equal to half the cell width. In [128], the plate separation varies solely along the length of the cell. When the long finger is formed in a converging cell, the front is sharpened, since the tip is accelerated more strongly in comparison to the rest of the finger. However, in the case of a constant radial variation in the plate separation, the sides of the fingers are accelerated in a similar manner to the finger tips, and the front becomes flatter promoting bifurcation. The contrast in results is due to the variation in the plate separation with respect to the flow path of the fingers. In radial displacement, the finger tips and sides displace into pathways of similar convergence, whereas in rectilinear flow, the tip evolves in a much more converging pathway than the sides, sharpening the finger. These differences are discussed in more detail in section 5.5.2.

The results presented in this section link the linear stability analysis works of [127, 130] and the experimental results of [128], detailing the explicit mechanisms that cause the transition in aperture effects when the capillary number is increased. The aperture effects here would also be present in more ‘random’ geometries in real subsurface aquifers. The aperture effects could be experienced by an advancing  $CO_2$  plume at the scale of the representative element volume (REV) as is consistent with the Darcy approximation here, meaning that similar transitions could occur in the aquifer. The plume would initially be at a very high capillary number, indicating that it would be subject to aperture effect 2 and 3 most significantly, but after time as the velocity drops, aperture effect 1 would become prominent and the plume could be stabilised in areas of decreasing permeability.

### 5.5.1.1 Sharply converging/diverging geometry

To analyse low capillary number aperture effects on the fingering regime once defined fingers have formed, a uniform cell with a sharply varying section occurring far downstream of the initial interface position is used. A constant gradient variance from the same homogeneous separation as before,  $\bar{b} = 0.01$  is utilised; however, the magnitude of the gradient is larger at  $|\alpha| = 0.0025$ . The constant gradient section begins at  $r = 4$

and finishes at  $r = 5$ , allowing the late stage exploration of secondary tip-splitting instabilities.

Figure 5.11 shows the late stage interfacial evolution of the converging case for  $Ca_g = 500$ . Here, the rapid stabilisation of the interface causes it to form a very flat front, with the finger sides almost merging into one continual interface. The finger bases have remained entirely unaffected, as they exist in regions of uniform geometry and have almost stagnated.

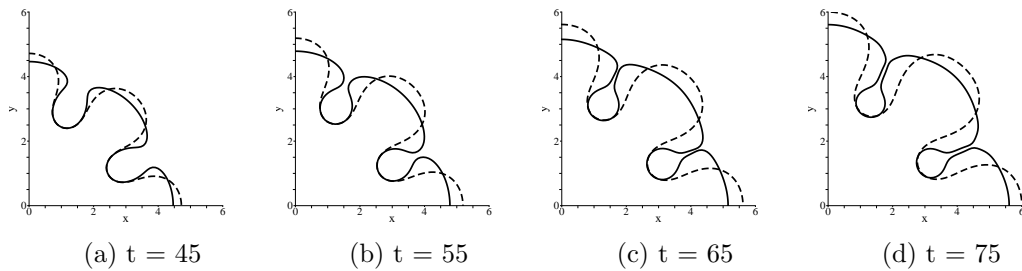


Figure 5.11: Time evolution plots for the converging cell case,  $\alpha = -0.0025$ ,  $Ca_g = 500$ . — Converging cell, ---- Uniform cell.  $\beta = 10$

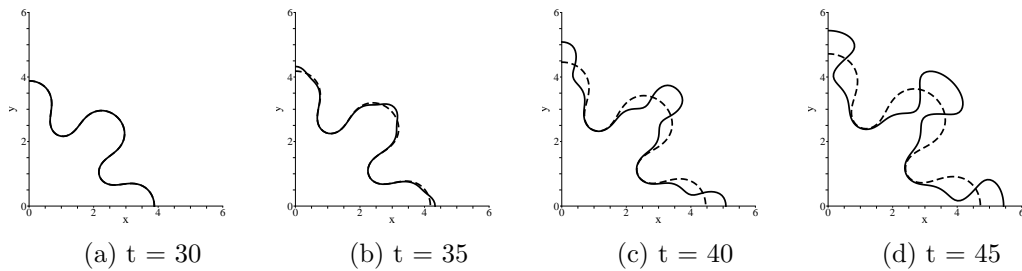


Figure 5.12: Time evolution plots for the diverging cell case,  $\alpha = 0.0025$ ,  $Ca = 500$ . — Diverging cell, ---- Uniform cell.  $\beta = 10$

Although the front is relatively flat and has been accelerated by the converging geometry in Figure 5.11, the stabilisation given by the large capillary pressure at the finger front keeps the interface from bifurcating into many smaller fingers. The fingers proceed to spread and expand under the stabilising aperture effect 1 of the converging geometry, with small lubrication layers forming between the fingers. Due to the complete immiscibility of the fluids in these simulations, there will always exist a small layer of the outer fluid separating the advancing fingers, meaning that droplets of the external fluid inside the moving plume never completely form. The lubrication layer formed in Figure 5.11 is fully resolvable with both the BEM and RBF-FC methods, in which several overlapping local systems exist within the layer itself.

In the diverging geometry case in Figure 5.12, the front is rapidly destabilised as it enters a region of very large plate separation. This causes a sudden decrease in capillary pressure, meaning it is much easier for the interface to displace in this region. The interface quickly forms a throat of very small radius at the entrance to the diverging section at  $r = 4$ , which becomes thinner and thinner with time. After  $t = 45$ , the throat continues to shrink until it reaches a stage where it is so thin that it collapses and the finger downstream of the throat detaches to form a separate bubble.

The simulation ends before the breaking effect, as the throat size is too small to fit sufficient nodal points inside to form suitable local systems in the RBF-FC method. Also, the model cannot accurately predict the bubble detachment and surface tension snapping effect. However, the model can predict up until a time very close to the ‘breaking’, where it can be fairly accurately predicted that the throat will collapse and the finger will detach. After this, the same process will likely occur again, as the remaining interface that forms the main plume will enter the expanding region, where the same destabilising effects would be felt. In this way, it can be inferred that the expansion acts as a barrier breaking the plume into a succession of droplets that will be convected by the displaced fluid.

Physically, a sudden change in cell geometry is analogous to a sharp change in porous medium permeability. For the diverging case, the interface effectively travels from a region of low permeability (such as sandstone), to a region of very large permeability (such as fractured shale). The periodic shedding of the interface would be highly desirable in  $CO_2$  sequestration, as the interface surface area would be effectively increased, meaning the rate of dissolution and total amount of dissolution trapping would increase significantly. For the converging case, the interface hits a permeability barrier, where the permeability decreases rapidly. This could represent an area of porous medium under greater compression than at the origin of the injection, where the interface would stabilise and the amount of trapping would decrease.

### 5.5.2 Highly anisotropic Hele-Shaw cells

In this final results section, immiscible displacement is analysed in Hele-Shaw cells with highly anisotropic geometry in order to demonstrate the robustness of the numerical

scheme, and provide insight into the fingering complexity present in periodic and channelled cells. Before proceeding, it is worth discussing the validity of the lubrication approximation in Hele-Shaw cells when the plate separation varies sharply. This is done in order to provide some justification for the use of the model in the work presented here, whereby the spatial derivatives of plate separation can be quite large.

In the works of [140],[141] and [142], the validity of the lubrication approximation for fractures is discussed when the fractures are small and surface roughness may affect the flow regime. Under certain conditions, [142] finds that the difference in fluxes predicted between the lubrication and Stokes models can vary by a factor of two. [140] and [141] provide quantitative limits for the validity of the lubrication theory, based on the profile of the fractures. [140] find that the wavelength  $\gamma_h$  of the aperture variation must exceed fifty times the standard deviation of the aperture height distribution  $\sigma_h$  for the lubrication model to be valid. This ensures that the velocity gradients along the length of the fracture are much smaller than perpendicular to the fracture. [141] later refine this limit to only  $5\sigma_h$ .

Applying the ratio  $r_l = \gamma_h/\sigma_h$  to the cases here, the validity of the lubrication model can be assessed. The largest variation in plate separation with respect to flow path in this work is the channel case shown in Figure 5.18. Here, the sharpest variation occurs in the lateral direction with respect to the channel length. The ratio of the wavelength of the variation of the plate separation to the standard deviation of the plate separation profile here is  $r_l = 442$ . This is much greater than the lower limit of 5 given by [141], validating the use of the lubrication model in this work. In the case of the sharp, uniformly converging profiles in the previous section, the ratio is even larger at  $r_l = 1384$ . The very large values here are due to the fact that although the spatial derivatives in the plate separation are quite large, the absolute change in the cell profile is small, meaning the velocity gradients in the plane of the cell will still be much smaller than those in the perpendicular direction.

For the rest of this section the results for three anisotropic Hele-Shaw cell cases are discussed. For brevity the analytical functions used to define the plate separations are not presented, instead contour plots are shown of the associated variations.

### 5.5.2.1 Radially periodic cells

Firstly, a radially periodic cell is considered with a cosine geometrical perturbation (variation shown in the contour plot in Figure 5.14). In Figure 5.13, interfacial plots at  $t = 60$  are presented for the radially periodic and uniform geometries. The periodic cases show oscillations that occur along the sides of the fingers, with much more pronounced oscillation occurring in the  $Ca_g = 500$  case. As the fingers progress through the peaks and troughs of the cell, the interface is repeatedly spread and stabilised by the converging sections, and destabilised by the diverging sections. The oscillations have a frequency equal to that of the cosine function applied to the plate separation.

It is apparent that increasing the capillary number reduces the magnitude of the oscillations that appear along the finger sides in Figure 5.13(b). The transverse curvature has less effect, and the periodic oscillations appear as noise around the interface. The bifurcation mode has not been altered by the introduction of the periodically varying geometry, and the overall shape remains remarkably similar to the uniform case.

These oscillations can be viewed with regards to aquifer permeability as a small spatial variability due to inconsistencies in the rock structure and flow path [17]. These imperfections and inconsistencies in the material structure do not alter the homogeneous permeability and macro-scale interfacial evolution, but do create small micro-scale perturbations around the interface when the capillary number is high.

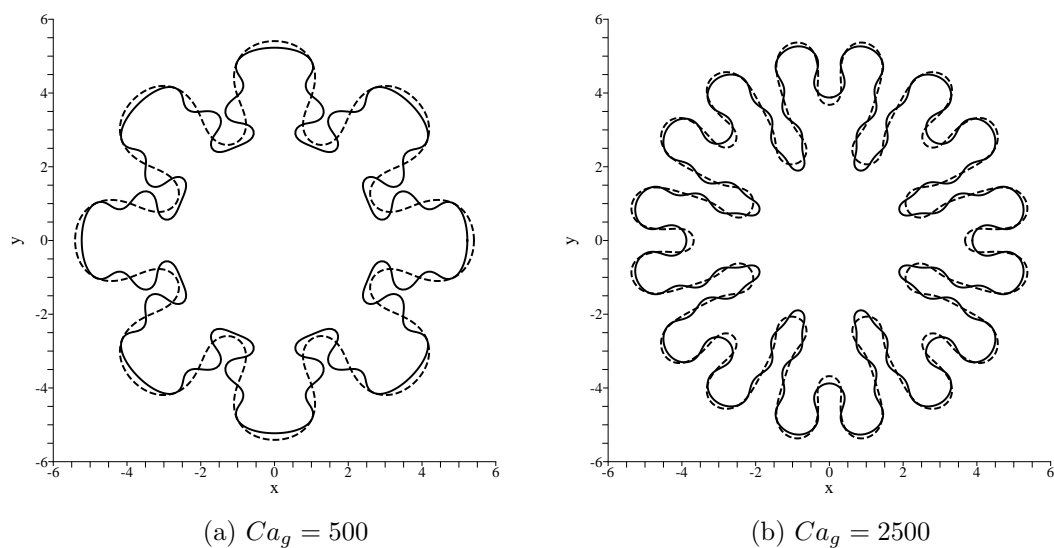


Figure 5.13: Interface plots at  $t = 60$  for the radially periodic and uniform cells at different capillary numbers.  $\beta = 10$ . — Radially periodic cell, ---- Uniform cell

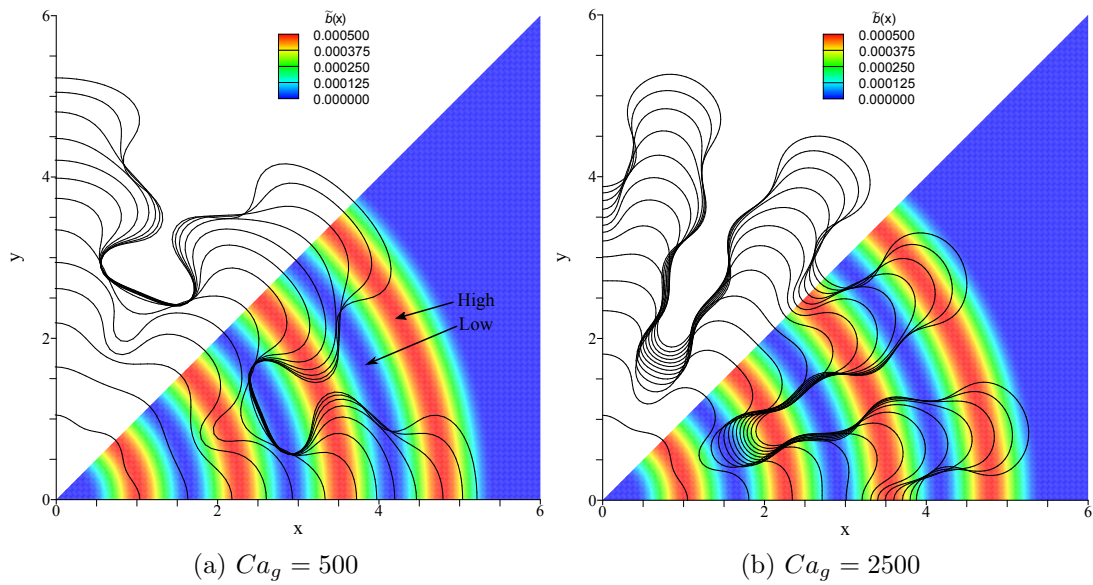


Figure 5.14: Interface plots at  $\Delta t = 5$  increments from  $t = 0$  to  $t = 60$  for the  $Ca_g = 500$  and  $Ca_g = 2500$  radially periodic cases. The interfaces overlay a contour plot of the plate separation variation,  $\tilde{b}(\boldsymbol{x})$ .

The long term evolution of the radially periodic cases are plotted over the change in plate separation  $\tilde{b}(\boldsymbol{x})$  in Figure 5.14. In the  $Ca_g = 500$  case, the transverse curvature is able to significantly stabilise or destabilise the interface based on whether the cell is locally converging or diverging respectively. The interface starts in a converging section in Figure 5.14, and is initially stabilised, almost forming a circle. The small residual perturbation around the interface is then destabilised by the diverging section, forming a sharper front. This process repeats, with the interface continually stabilising, forming flatter fingers, followed by destabilisation creating sharper fingers.

When  $t > 25$  in Figure 5.14(a), the fingers' base evolution virtually stops, and they remain stationary in converging cell sections. The bases are stabilised significantly by the converging section, with the normal velocity dropping to near zero, forming stagnation points. This is in contrast to the bases in Figure 5.14(b), which continually displace with time. In this case the capillary pressure is much smaller and does not stabilise the base enough to cause complete stagnation in the converging sections.

The finger fronts after  $t = 25$  in Figure 5.14(a) undergo a series of elongations and stabilisations, which act like a form of bifurcation. The fingers are split into three distinct parts: the finger tip which is displaced radially, and the two sides of the finger front which displace in an azimuthal direction. The fingers periodically 'extrude' the

sides of the finger fronts producing defined protrusions in the azimuthal direction. These protrusions remain fixed in position in converging sections of the cell. As the front is continually deformed and stabilised, the chance of a classical tip splitting bifurcation occurring is reduced significantly in the lower capillary number regime. The front cannot become flat enough in a converging section to conventionally split before it is accelerated and sharpened in a diverging section, reducing the length scale of bifurcation. It can therefore reasonably be predicted that the periodic pattern presented in Figure 5.14(a) will continue indefinitely as long as the cell plate separation varies periodically. The finger front will never bifurcate in a classical manner, instead evolving in a self-similar pattern akin to dendrite growth with side branching fingers.

### 5.5.2.2 Cartesian periodic cells

In this example, results from a Hele-Shaw cell with a plate separation that varies periodically in both Cartesian coordinates are presented. The same eight finger starting interface is used as in previous simulations, however, the plate separation now exhibits quarter-fold symmetry (requiring a quarter domain RBF-FC solution with corresponding symmetry conditions). The separation variation contour is shown in the background of Figure 5.16.

In Figure 5.15, the interface plots for the periodic cell and a corresponding uniform cell can be seen at  $t = 40$ . The finger evolving in the periodic cell at  $45^\circ$  to the horizontal has a completely different bifurcation mode to the fingers travelling parallel to the x- and y-axis. The fingers travelling parallel to the axes have been sharpened significantly due to continued acceleration of the finger tips, whereas the  $45^\circ$  finger evolves in a very similar manner to the uniform case.

The evolution of the fingers and the direction of displacement with regards to the variation in plate separation are shown in Figure 5.16. The capillary number is large in the case presented here ( $Ca_g = 2500$ ), meaning the transverse curvature (aperture effect 1) has very little effect on the overall finger evolution. The fingers parallel to the axes generally have their tips in regions of higher mobility compared to the sides of finger fronts as the interface displaces, with aperture effect 2 causing the finger sharpening. As

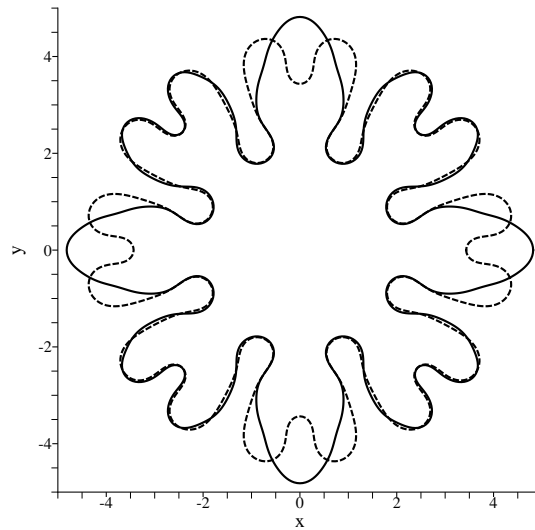


Figure 5.15: Interface plots at  $t = 40$  for the Cartesian periodic cell and uniform cell. — Cartesian periodic cell, - - - Uniform cell

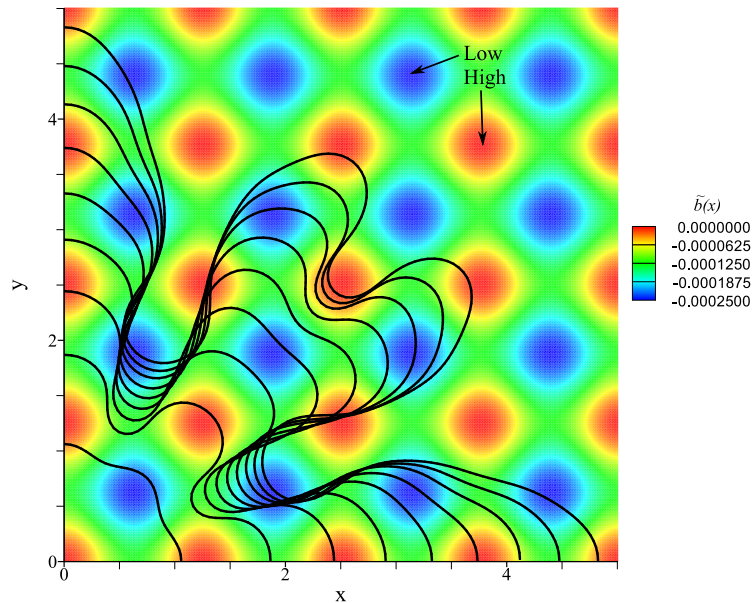


Figure 5.16: Interface plots at  $\Delta t = 5$  increments from  $t = 0$  to  $t = 40$  for the Cartesian periodic case. The interfaces overlay a contour plot of the plate separation variation,  $\tilde{b}(x)$ .

the overall change in plates separation is small, the change in pressure gradient (aperture effect 3) is relatively small.

The sharpening behaviour is similar in nature that in the rectilinear case presented by [128]. In [128], a gradually converging rectilinear cell was found to sharpen the fingers, as the tip would be accelerated more significantly than the sides of the finger fronts.

The pressure gradient at the finger tip would be increased locally, with aperture effect 3 causing the increased tip velocity (the mobility variation is small around the finger front). However, in the present case, a locally high mobility (aperture effect 2) causes the increased velocity. The result in both cases is that the finger tip experiences a higher velocity than the sides of the finger front, and the finger is sharpened. This result is in contrast to what has been seen in previous sections using radially symmetric cases, in which the finger tip and the sides of the finger front exist in areas of similar mobility and spatial variation in mobility.

For the finger that is displacing at  $45^\circ$  to the x-axis a morphology very similar to the uniform case is seen. The bifurcation is only slightly different to the uniform case as the finger travels through both a peak and a trough in the cell separation before bifurcating. This means the finger tip and sides of the finger front both experience regions of acceleration and deceleration in relation to each other, somewhat reducing the overall effects.

The  $45^\circ$  degree finger evolves in a cell whose plate spacing can be considered homogeneous in the direction of finger displacement, with a small perturbation term slightly altering the finger shape. The fingers parallel to the axes evolve in a highly inhomogeneous environment, where the tip travels through a region of high permeability (like a fracture or channel) compared to the sides, resulting in the highly sharpened finger.

### 5.5.2.3 Channelled cells

In this final example, results from Hele-Shaw cells with channelled geometry are presented. The plate separation is increased in a direction parallel to the finger fronts, creating highly preferential flow paths, similar to that seen in fractured porous media. Two examples are provided, one where there exists a channelled section parallel to each finger in the domain (see the contour in Figure 5.18(b)) and another where there is a channelled section on every other finger (see the contour in Figure 5.18(a)).

The interface plots at  $t = 35$  for the two channelled case can be seen in Figure 5.17. The fingers have been strongly accelerated through the channel pathways, exhibiting highly sharpened profiles in comparison to the uniform case. In the 4 channel case, the

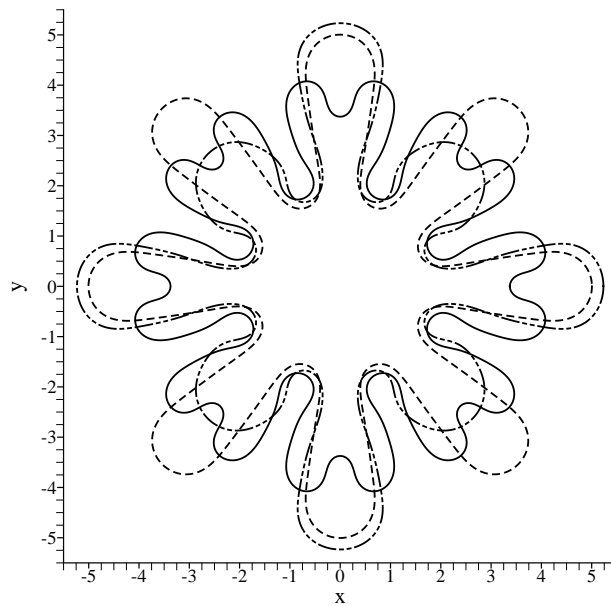


Figure 5.17: Interface plots at  $t = 35$  for the two channelled cells and uniform cell.  $Ca_g = 2500$ ,  $\beta = 10$ . — Uniform cell, - - - 4 channel cell, - . - 8 channel cell.

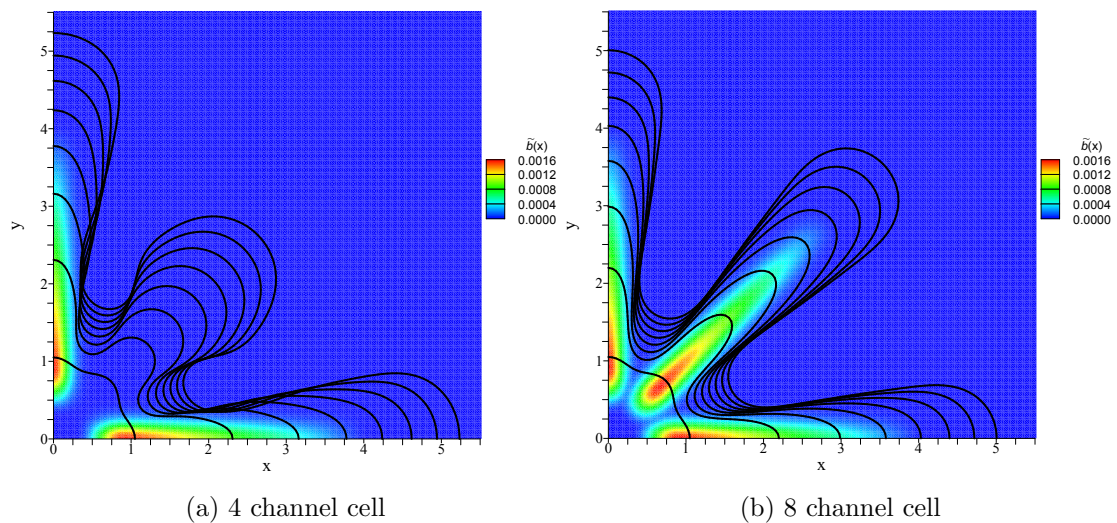


Figure 5.18: Interface plots at  $\Delta t = 5$  increments from  $t = 0$  to  $t = 35$  for the two channelled cells. The interfaces overlay a contour plot of the plate separation variation,  $\tilde{b}(\mathbf{x})$ .

fingers that displace into uniform regions have a reduced volume due to the fluid being displaced preferentially through the channelled regions.

The channelled cases here show very similar displacements to the rectilinear cases presented by [128]. As the channels here create a large fluid mobility directly at the finger fronts they experience much more acceleration from the converging geometry

than the finger sides, creating the sharp profile. The fingers in the channelled sections exhibit no signs of bifurcation, even at this very high capillary number. Aperture effect 2 becomes the dominating effect, as the fluid mobility is increased very locally around the finger tip. The fingers travelling parallel to the channels displace in effectively rectilinear regimes.

The temporal evolution of the channel cases can be seen in Figure 5.18. It is interesting to observe that whilst  $\Delta t \leq 10$ , the fingers are confined to the geometry of the channel, i.e. the finger sides do not displace significantly outside of the channelled section. The front pulls the finger through the channel, hindering the displacement of the remaining finger outside of the channel. When  $\Delta t > 10$ , the fronts enter a region where the channel profile starts to tail off towards the homogeneous plate separation, reducing the acceleration effects. After this point, the fingers start to displace in a more uniform cell whereby the finger fronts can spread in a conventional radial fingering regime.

These final result sections demonstrate the effect of local variations in cell plate separation (and intrinsic cell permeability). This can also be viewed in the sense of aquifer permeability, with large permeability changes such as cracks and fractures resulting in highly directional flow paths. In the results presented here, small changes in permeability result in largely the same interfacial displacement if the capillary number is high enough. The perturbations in the cell permeability create small local oscillations around the interface, but do not change the overall displacement (see the  $45^\circ$  finger in Figure 5.16). This infers that in the  $CO_2$  injection cases, small variations in aquifer permeability across the whole plume are unlikely to alter the resulting displacement regime in the early stages of injection when the capillary number is high.

However, when the capillary number is very small or local variations in the cell permeability are large, the finger displacement can change significantly. When the local capillary number is low and the cell permeability is decreasing the capillary pressure becomes larger. This makes it very difficult for the fluid to displace and it can become trapped (see the bases in Figure 5.14(a)). In an aquifer context, this locally high capillary pressure can lead to capillary trapping, where globules of the plume can become disjointed and remain trapped in the aquifer pores. This is highly desirable, as capillary trapping represents a very secure form of trapping in which the  $CO_2$  can remain for many years.

## 5.6 Conclusion

In this chapter, a coupled BE-RBF numerical method has been developed to track the interfacial displacement between two immiscible fluids with inhomogeneous mobility in a Hele-Shaw cell. The focus in this chapter was on cases where the Hele-Shaw cell had a spatially varying plate separation, creating an inhomogeneous mobility in the fluids.

The onset of fingering and late stage tip splitting instabilities were examined for different cell geometries under various capillary number regimes. Numerical experiments with uniformly converging/diverging Hele-Shaw cells revealed a large dependence on the capillary number for the stability of the system. Three aperture effects were identified that control the interfacial stability, for converging cells these were:

1. Stabilisation through an increased transverse curvature.
2. Deceleration due to a reduced fluid mobility.
3. Acceleration due to an increased pressure gradient.

In diverging cases, the effects were reversed. At low capillary numbers, effect 1 and 2 dominate, stabilising the interface in converging cases and destabilising in diverging cases. At higher capillary numbers, the result of the combined effects reverse, and converging cells destabilise the interface in comparison to uniform cells, with diverging cases being more stable. This transition point using the non-linear numerical growth rate was found at  $Ca_g \approx 640$ .

The enhanced spreading and bifurcation at higher capillary numbers in gradually converging cells was in contrast to the converging rectilinear cell cases in [128]. In rectilinear converging cells, the tip evolves in a much more converging pathway than the sides, sharpening the finger. However, in radially converging cells, the finger tips and sides displace into pathways of similar convergence, enhancing the spreading and bifurcation mechanisms.

For late stage interfacial growth the effect of sharply varying geometries occurring far downstream of the injection source was explored. When the fingers were fully formed and entered a sharply expanding region, the finger fronts created a bottleneck and could detach into separate bubbles, increasing the surface area of the injected plume. For

sharply converging sections, the fronts were spread azimuthally and remained separated only by very fine lubrication layers, stabilising the fingering regime.

Finally, anisotropic Hele-Shaw cells were explored to demonstrate the fingering complexity that can occur when the fluid mobility is highly inhomogeneous. In radially periodic geometry at low capillary numbers, classical tip-splitting could be avoided as the finger was continually stabilised and then accelerated, producing secondary side branching fingers that formed periodically. Under Cartesian periodic geometry, different fingers would form around the initially symmetric interface. The fingers were sharpened when they were aligned with the periodic grid, in much the same way as the rectilinear converging case in [128]. Fingers travelling at  $45^\circ$  to the axes evolved in a very similar manner to the uniform case due to the homogeneity of the plate separation in the flow path.

The analysis of the governing mechanisms and aperture effects in this chapter provides a good link between previous works focusing on either low or high capillary number regimes, furthering understanding of the underlying fingering mechanism in inhomogeneous mobility flows at both the early stages of finger growth and the late stages of tip splitting.

## 6. Immiscible thermo-viscous fingering

### Summary

In this chapter, immiscible radial displacement in a Hele-Shaw cell with a temperature dependent viscosity is investigated using the coupled boundary element - radial basis function methods. Thermal gradients created in the domain through the injection of a low viscosity fluid at a different temperature to the resident high viscosity fluid can lead to the formation of unstable thermo-viscous fingers, which are explored in the context of immiscible flows. The transient, multi-zone heat transfer is evaluated using the newly developed auxiliary multi-zone RBF-FC method, which locally captures variation in flux and field variable over the moving interface, without the need for ghost node extrapolation. The viscosity couples the transient heat transfer to the Darcy pressure/velocity field, which is solved using the BE-RBF-FC method as in the previous chapter, providing an accurate and robust interface tracking scheme for the full thermo-viscous problem.

The thermo-viscous problem space is explored using systematic numerical experiments, revealing that the early stage finger growth is controlled by the pressure gradient induced by the varying temperature and mobility field. In hot injection regimes, negative temperature gradients normal to the interface act to accelerate the interface, promoting finger bifurcation and enhancing the viscous fingering instability. Correspondingly, cold injection regimes stabilise the flow compared to isothermal cases, hindering finger formation. The interfacial mobility distribution controls the late stage bifurcation mode, with non-uniformities induced by the thermal diffusivity creating alternate bifurcation modes. Further numerical experiments reveal the neutral stability of the thermal

effects on the fingering evolution, with classical viscous fingering dynamics eventually dominating the evolution.

## 6.1 Introduction

The injection of supercritical  $CO_2$  in sequestration processes will typically occur at a temperature different to that of the resident brine, creating temperature gradients in the domain that will alter mechanical fluid quantities such as diffusivity, viscosity, density and surface tension. The  $CO_2$  can be injected at a colder temperature than the resident brine, due to heat loss en-route to the downhole injection site [12], or through very deep subsurface injection where the resident brine temperature is very high (typically at depths  $> 3\text{km}$ ), e.g. the In Salah formation in Algeria [13].  $CO_2$  can also be used for combined storage and extraction in geothermal reservoirs, in which very high temperature brine ( $T > 150^\circ\text{C}$ ) can be extracted for energy use [14]. The  $CO_2$  may also be injected at a higher temperature than the resident brine, for pre-conditioning purposes [15] or for plume evolution monitoring [16]. Another immiscible displacement regime where thermal effects are prominent is that of thermal enhanced oil recovery, in which high temperature water (or steam) is used to mobilise trapped oil and increase well production [143].

Understanding how temperature gradients affect the fluid properties and resulting interfacial displacement is key to understanding the key physical mechanisms in the immiscible displacement regimes above and in the fundamental study of moving multi-zone problems in classical fluid dynamics. In this chapter, the changes in the immiscible viscous fingering regime due to a thermally dependent viscosity are analysed, often termed thermo-viscous fingering. In order to examine the effects coming purely from the variable viscosity, constant surface tension and diffusivity are used for each fluid, with density driven buoyancy effects negligible in the lateral fluid flow. This simplification allows the thermo-viscous fingering process to be quantified for immiscible regimes without the complication of additional Marangoni and variable diffusivity effects.

To analyse the fully coupled thermal problem involves the solution of a different set of non-linear equations requiring inclusion of viscous shear stresses around the interface and a non-linear diffusion term in the heat transfer. The solution of these coupled

equations would require more complex numerical techniques that are beyond the scope of this work. The reader is directed towards the following works that focus on the other thermal processes mentioned above: [144, 145] for Marangoni type effects and [146] for the solution of non-linear diffusivity problems.

In order to model the immiscible displacement regimes the analogy between Hele-Shaw and porous media flows is again used. As the thermal diffusivities of the two fluids can be very low, the thermal Peclet number describing the ratio of convective to diffusive heat transfer can be large ( $>1000$ ). Therefore, the full convection-diffusion heat equation has to be solved in order to track the heat transfer in the domain.

During thermo-viscous fingering, generally, two fronts are established in the domain: ‘solutal’ and thermal. The solutal front is defined here as the point at which the fluid composition transitions from the injected fluid to the resident fluid. In immiscible displacement this is a sharp front controlled by capillary forces, where the mechanical fluid properties exhibit discontinuous profiles, whereas in miscible displacement the front is smoothed as dispersion and molecular diffusion mix the fluid properties of the injected and resident fluid [5]. In miscible flows the viscosity of the fluid is determined by both the solute concentration and the temperature. However, in immiscible flows, the viscosity depends only on the fluid being considered and the temperature that the fluid exists at.

The solutal and thermal fronts do not necessarily propagate with the same velocity due to a difference in mass and thermal diffusivities and the fact that heat may diffuse away from the fluid into surrounding solid media. This is the case in porous media flow, where the thermal front is diffused into the solid matrix and ‘lags’ behind the solutal front, creating a double advective displacement [147]. This lag is a pre-multiplier of the temperature transport velocity and is determined by the solid matrix porosity, density and the specific heat capacity of solid and fluid phases. In the case of a thermally insulated Hele-Shaw cell, there is no thermal lag, as the cell remains an open channel with an effective porosity of one. The solutal and thermal fronts advance with the same velocity, creating a single or iso-advective regime, that is governed purely by the fluid velocity [147].

The miscibility of the fluids controls the mass diffusivity, and when considered with the thermal diffusivity determines whether the flow is iso- or double-diffusive. In miscible

flows, the concentration and temperature scalars necessarily diffuse at different rates, governed by the fluid properties, creating a double diffusive displacement [148]. However, in the case of immiscible flows, the solutal front is determined purely by the advective motion of the fluids and capillary forces at the sharp interface; there are no diffusive or dispersive mechanisms acting on the concentration field. To this extent, the immiscible thermo-viscous fingering problem is one of iso-diffusion (i.e. there is only thermal diffusion, no mass diffusion). When considered in a thermally insulated Hele-Shaw cell, the problem becomes one of iso-advection and iso-diffusion for each specific fluid. The immiscible limit has introduced a true multi-zone representation of the problem, taking away the double diffusive effects that are apparent in miscible flows [148].

There exists a very limited number of studies on immiscible thermo-viscous fingering, with most previous research focusing on miscible cases. One notable work in the immiscible regime by Sheorey and Muralidhar finds that non-isothermal, high temperature injection of water into resident oil promotes the formation of viscous fingers and increases the sweep efficiency of the water [149]. The fluid front can temporarily displace beyond the thermal front into a region of low temperature (and high viscosity), where the front velocity drops. The sides of the front can then bypass this region, forming fingers around the sides of the domain. The finger evolution here is a result of the interplay between the thermal and fluid fronts, which despite the exclusion of a thermal lag parameter, have different diffusive regimes and hence affect the advancing front on different time scales. It is also worth noting, that due to the constitutive relationship for the capillary pressure based on the water saturation alone (without temperature variation), and the Darcy flow approximation that is used, thermocapillary and Marangoni effects are not included in their model [149].

For miscible flows, there are several previous works concerning the linear stability of the problem [5, 147, 148, 150, 151]. These analyses focus on the interaction and time-scale effects of the different scalar diffusive fronts. In the analysis of radial double-diffusive fronts, Pritchard finds that even for strongly stabilising temperature fields (i.e. they form a decreasing viscosity profile across the interface), a destabilising viscosity profile can be maintained over the front due to a strongly advective solute regime [5], unless the thermal lag is near unity and the thermal viscosity contrast is many times higher than the viscosity contrast across the solutal front.

Mishra *et al.* [148] and Pritchard [147] show that localised unstable zones across the interface may develop with time if the solutal front is destabilising, and the thermal front is sufficiently diffusive. The aggregate viscosity profile is not sufficient to predict the overall stability at late stages, as diffusive effects become more prominent, and early stage stabilisation of the flow may diminish. It is not enough to state that if one of the scalar components promotes fingering, then fingering will eventually occur in the late stage regime [147].

Numerical studies of various miscible displacements regimes agree qualitatively with the stability analyses above [3, 152–155]. In general, at the late stages of interfacial growth, they find that at sufficiently low values of thermal lag, or if the thermal regime is highly diffusive, the evolution depends entirely on the solutal viscosity ratio. The (de)stabilising effects of the thermal front are reduced with an increase in diffusivity or thermal lag [152, 154]. It should also be noted, that the fingering processes generated through an equivalent thermal front or solutal front (i.e. the same absolute viscosity profile) are identical, due to their additive nature on the viscosity and the equivalence of the PDEs being solved.

Experimentally, thermo-viscous fingering is typically hard to quantify under laboratory conditions. Nagatsu *et al.* [156] and Holloway and de Bruyn [8] track the injection of hot glycerine (glycerine-water solutions in [156]) into colder more viscous glycerine in a Hele-Shaw cell. Nagatsu *et al.* [156] find that in a small range of mobility ratios, around  $\beta = 10$ , injection at a higher temperature than the resident fluid promotes the onset of fingering, with bifurcation occurring at a smaller interface radius. The results have good agreement with Holloway and de Bruyn [8]. However, more specific thermal effects are hard to gauge due to the insulation of the Hele-Shaw cell and resulting heat loss through the glass plates [156].

In this current work, the immiscible thermo-viscous fingering process is analysed in a Hele-Shaw cell due to the radial injection of a low viscosity fluid with injection temperature different to that of the high viscosity resident fluid. The work analyses the case of Hele-Shaw flow to study the effects of thermo-viscous fingering in an immiscible regime with a true multi-zone representation of the fluid flow and heat transfer. To the authors knowledge, this work represents the first comprehensive numerical study of

immiscible thermo-viscous fingering in a Hele-Shaw cell, and hopes to shed light on the effects of multi-zone heat transfer on the purely advective immiscible fluid flow regime.

The boundary element and radial basis function methods from the previous chapters can be used here to track the fluids' pressure, velocity and temperature through the solution of Darcy flow and the multi-zone convection-diffusion of heat through the domain. This chapter is organised as follows; firstly, the mathematical model is presented followed by a summary of the numerical methods. After this, mass conservation verification is performed for the coupled thermo-viscous problem. Results are then presented for immiscible thermo-viscous fingering under different capillary number, temperature and diffusivity regimes, concluding with a discussion and summary of the results.

## 6.2 Mathematical model

In the thermo-viscous problem, a radial Hele-Shaw cell of infinite radius is again considered, in which high viscosity fluid is displaced by the radial injection of a low viscosity fluid. The low viscosity invading fluid with temperature  $T_0$  occupies the inner region  $\Omega_1$ , whilst a high viscosity fluid with temperature  $T_\infty$  occupies the external region  $\Omega_2$ , shown in Figure 6.1.

The interface separating the internal and external region has an initial 8 finger perturbation given by  $r = 1 + \epsilon \cos(8\theta)$ . The initial temperature  $T_{in}(\mathbf{x})$  at a point  $\mathbf{x}$  is given by a smoothed step function, i.e.

$$T_{in}(\mathbf{x}) = T_\infty + 0.5(T_0 - T_\infty) \left( 1 + \tanh \left( \frac{\hat{r}}{\delta} \right) \right) \quad (6.1)$$

Where,  $\hat{r}$  is the radial distance from a point  $\mathbf{x}$  to the corresponding interface point.  $\delta$  is the sharpness of the smoothed step function, see Figure 6.1. For the flow in a Hele-Shaw cell, the depth averaged pressure  $P_l$  and 2D Darcy velocity  $u_i^l$  in each fluid region  $l$  can be expressed through Darcy's law:  $u_i^l(\mathbf{x}) = -M_l(\mathbf{x}) \frac{\partial P_l}{\partial x_i}$ . The mobility  $M_l$  is related to the spatially dependent fluid viscosity  $\mu_l(\mathbf{x})$  and plate spacing  $b$  by:  $M_l(\mathbf{x}) = b^2/12\mu_l(\mathbf{x})$ . The conservation of mass, interface matching conditions and asymptotic conditions for

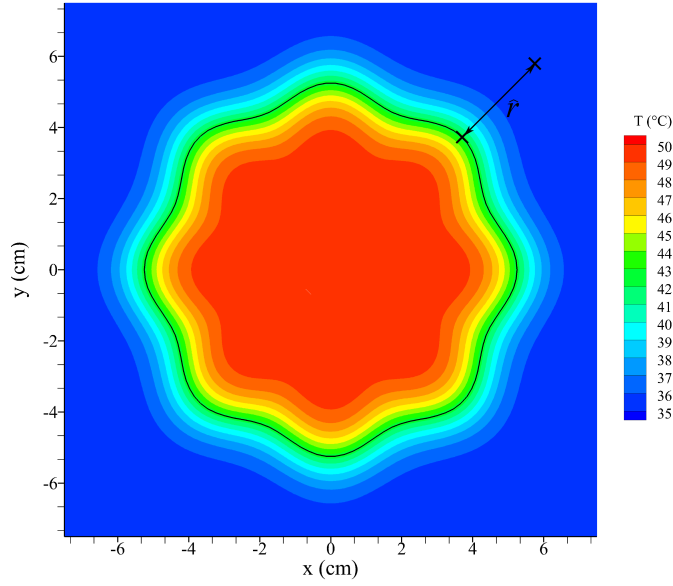


Figure 6.1: Initial setup of the immiscible thermo-viscous fingering problem in a Hele-Shaw cell. The black fluid-fluid interface marks the transition from the inner zone  $\Omega_1$  to the outer zone  $\Omega_2$  and overlays a contour plot of the initial temperature field. The radial distance used in the smoothed step function  $\hat{r}$  is highlighted.

the depth averaged pressure  $P_l$  in a Hele-Shaw cell are repeated here for clarity:

$$\frac{\partial}{\partial x_i} \left( M_l(\mathbf{x}) \frac{\partial P_l}{\partial x_i} \right) = 0 \quad \mathbf{x} \in \Omega_l, \quad l = 1, 2 \quad (6.2)$$

$$-M_1(\boldsymbol{\xi}) \frac{\partial P_1(\boldsymbol{\xi})}{\partial n} = -M_2(\boldsymbol{\xi}) \frac{\partial P_2(\boldsymbol{\xi})}{\partial n} \quad \boldsymbol{\xi} \in S \quad (6.3)$$

$$P_1(\boldsymbol{\xi}) - P_2(\boldsymbol{\xi}) = \gamma \left( \frac{2}{b} + \frac{\pi}{4} k(\boldsymbol{\xi}) \right) \quad \boldsymbol{\xi} \in S \quad (6.4)$$

$$\frac{\partial P_1(\mathbf{x})}{\partial r} \Big|_{r \rightarrow 0} \rightarrow -\frac{Q}{2\pi M_1(\mathbf{x})r} \quad (6.5)$$

$$P_2(\mathbf{x}) \Big|_{r \rightarrow \infty} \rightarrow -\frac{Q}{2\pi M_2(\mathbf{x})} \ln \left( \frac{r}{r_0} \right) \quad (6.6)$$

In equation (6.2), the plate separation  $b$  has been dropped from the equation since it is taken as a constant in the thermo-viscous problem studied here. In order to characterise effects coming from the non-isothermal regime, the variables that relate to the viscosity are decomposed into homogeneous and perturbed components. Firstly, the viscosity of each fluid  $l$  can be represented through an exponential dependence on the temperature

[5][151].

$$\mu_l(\mathbf{x}) = \bar{\mu}_l \exp \left[ \mp a_l \left( 1 \pm \frac{T(\mathbf{x}) - T_\infty}{|T_0 - T_\infty|} \right) \right] \quad \mathbf{x} \in \Omega_l, \quad l = 1, 2 \quad (6.7)$$

Here, the homogeneous viscosity  $\bar{\mu}_l$  is that of fluid  $l$  at the injection temperature  $T_0$ .  $T_\infty$  is the resident fluid temperature,  $a_l$  is the rate of change of viscosity for fluid  $l$  with temperature. The minus/plus sign in  $\mp a_l$  is used for when the injecting fluid is hotter (+) or colder (−) than the resident fluid. This gives the mobility of the fluid in zone  $l$  as:

$$M_l(\mathbf{x}) = \frac{b^2}{12\mu_l(\mathbf{x})} = \bar{M}_l + \tilde{M}_l(\mathbf{x}) \quad (6.8)$$

$$\bar{M}_l = \frac{b^2}{12\bar{\mu}_l}, \quad \tilde{M}_l(\mathbf{x}) = \frac{b^2}{12\mu_l(\mathbf{x})} - \bar{M}_l \quad (6.9)$$

Non-dimensional variables are now introduced utilising the characteristic length, time, velocity, pressure, temperature and mobility of the problem, given by:

$$(\mathbf{x}, r, b) = r_0 (\mathbf{x}', r', b'), \quad t = \frac{r_0^2}{Q} t', \quad (6.10)$$

$$M_l = \bar{M}_2 M'_l, \quad u_l = \frac{Q}{r_0} u'_l, \quad P_l = \frac{Q}{\bar{M}_2} P'_l, \quad (6.11)$$

$$T_l = |T_0 - T_\infty| T'_l + T_\infty, \quad D_l = Q D'_l \quad l = 1, 2 \quad (6.12)$$

In equalities (6.10) - (6.12), apostrophes identify non-dimensional variables with  $t$  as time and  $\bar{M}_2$  as the homogeneous mobility of the displaced fluid (corresponding to the homogeneous viscosity  $\bar{\mu}_2$ ).  $D_l$  is the thermal diffusivity of fluid  $l$ . From this point onwards in the chapter, the apostrophe of all non-dimensional variables will be dropped, and all variables will be assumed to be in their non-dimensional form unless otherwise stated. The pressure can again be represented as a sum of homogeneous and perturbed components:

$$P_l(\mathbf{x}) = \bar{p}_l(\mathbf{x}) + \tilde{p}_l(\mathbf{x}) \quad (6.13)$$

Using the above form of the pressure, equation (6.2) can be expanded, noting that  $\partial \bar{M}_l / \partial x_i = 0$ , to obtain the following equation:

$$M_l(\mathbf{x}) \frac{\partial^2 \tilde{p}_l}{\partial x_i^2} + \tilde{M}_l(\mathbf{x}) \frac{\partial^2 \tilde{p}_l(\mathbf{x})}{\partial x_i^2} + \frac{\partial \tilde{M}_l(\mathbf{x})}{\partial x_i} \frac{\partial \tilde{p}_l(\mathbf{x})}{\partial x_i} = - \frac{\partial \tilde{M}_l(\mathbf{x})}{\partial x_i} \frac{\partial \bar{p}_l(\mathbf{x})}{\partial x_i} \quad (6.14)$$

The homogeneous pressure is constrained to satisfy Laplace's equation, in order to characterise the case of isothermal displacement, i.e.:

$$\frac{\partial^2 \bar{p}_l(\mathbf{x})}{\partial x_i^2} = 0; \quad (6.15)$$

The homogeneous pressure is then subject to the following matching and asymptotic conditions:

$$\bar{p}_1(\boldsymbol{\xi}) - \bar{p}_2(\boldsymbol{\xi}) = \frac{1}{Ca_g} \left( \frac{2}{b} + \frac{\pi}{4} k(\boldsymbol{\xi}) \right) \quad \text{for } \boldsymbol{\xi} \in S \quad (6.16)$$

$$\bar{M}_1(\boldsymbol{\xi}) \frac{\partial \bar{p}_1(\boldsymbol{\xi})}{\partial n} = \bar{M}_2(\boldsymbol{\xi}) \frac{\partial \bar{p}_2(\boldsymbol{\xi})}{\partial n} \quad \text{for } \boldsymbol{\xi} \in S \quad (6.17)$$

$$\frac{\partial \bar{p}_1(\mathbf{x})}{\partial r} \Big|_{\mathbf{x} \rightarrow 0} \rightarrow -\frac{1}{2\pi r} \quad (6.18)$$

$$\bar{p}_2(\mathbf{x}) \Big|_{\mathbf{x} \rightarrow \infty} \rightarrow -\frac{1}{2\pi} \ln(r) \quad (6.19)$$

The perturbed pressure equation (6.14) is subject to the following matching conditions at the interface,  $S$ , and asymptotic conditions near the origin and in the far field:

$$\tilde{p}_1(\boldsymbol{\xi}) - \tilde{p}_2(\boldsymbol{\xi}) = 0 \quad \boldsymbol{\xi} \in S \quad (6.20)$$

$$M_1(\boldsymbol{\xi}) \frac{\partial \tilde{p}_1(\boldsymbol{\xi})}{\partial n} = M_2(\boldsymbol{\xi}) \frac{\partial \tilde{p}_2(\boldsymbol{\xi})}{\partial n} + \left( \beta \tilde{M}_2(\boldsymbol{\xi}) - \tilde{M}_1(\boldsymbol{\xi}) \right) \frac{\partial \bar{p}_1(\boldsymbol{\xi})}{\partial n} \quad \boldsymbol{\xi} \in S \quad (6.21)$$

$$\frac{\partial \tilde{p}_1(\mathbf{x})}{\partial r} \Big|_{\mathbf{x} \rightarrow 0} \rightarrow 0 \quad (6.22)$$

$$\tilde{p}_2(\mathbf{x}) \Big|_{\mathbf{x} \rightarrow \infty} \rightarrow 0 \quad (6.23)$$

Where  $\beta$  is the mobility ratio between the fluids,  $\beta = \bar{M}_1/\bar{M}_2 = \bar{\mu}_2/\bar{\mu}_1$ . The jump in flux in equation (6.21) is given by:

$$\left( \beta \tilde{M}_2(\boldsymbol{\xi}) - \tilde{M}_1(\boldsymbol{\xi}) \right) \frac{\partial \bar{p}_1(\boldsymbol{\xi})}{\partial n} = \frac{b^2}{12\bar{\mu}_1} \left( e^{\pm a_2(1 \pm T)} - e^{\pm a_1(1 \pm T)} \right) \frac{\partial \bar{p}_1(\boldsymbol{\xi})}{\partial n} \quad (6.24)$$

Therefore, if  $a_1 = a_2$  the flux in equation (6.21) is continuous, however, in all cases the interfacial flux (6.3) is always satisfied, i.e. continuous. This can be observed by adding equations (6.17) and (6.21) and using the definitions (6.8) and (6.13) with  $\beta = \bar{M}_1/\bar{M}_2$ , which is valid for any value of  $a_1$  and  $a_2$ . The obtained values of  $\bar{p}_l$  and  $\tilde{p}_l$  can be used

to reconstruct the normal velocity at an interface point  $\boldsymbol{\xi}$  in order to track the fluid:

$$U_n(\boldsymbol{\xi}) = \bar{u}_n(\boldsymbol{\xi}) + \tilde{u}_n(\boldsymbol{\xi}) = -M^1(\boldsymbol{\xi}) \frac{\partial \bar{p}_1(\boldsymbol{\xi})}{\partial n} - M^1(\boldsymbol{\xi}) \frac{\partial \tilde{p}_1(\boldsymbol{\xi})}{\partial n} \quad (6.25)$$

To evaluate the flow and pressure in the domain and calculate the interfacial velocity with equation (6.25) the temperature is required in order to calculate the viscosity and its spatial derivatives. To track the temperature (and viscosity) evolution through the domain in order to calculate the resulting pressure/flow field, the multi-zone convection diffusion heat equation may be solved:

$$\frac{\partial T_l(\boldsymbol{x}, t)}{\partial t} = D_l \frac{\partial^2 T_l(\boldsymbol{x}, t)}{\partial x_i^2} - u_i^l(\boldsymbol{x}, t) \frac{\partial T_l(\boldsymbol{x}, t)}{\partial x_i} \quad \boldsymbol{x} \in \Omega_l, \quad l = 1, 2 \quad (6.26)$$

Equation (6.26) is valid in each fluid region  $l$ , subject to the following matching, boundary and initial conditions:

$$T_1(\boldsymbol{\xi}, t) = T_2(\boldsymbol{\xi}, t) \quad \text{for } \boldsymbol{\xi} \in S \quad (6.27)$$

$$D_1 \frac{\partial T_1(\boldsymbol{\xi}, t)}{\partial n} = D_2 \frac{\partial T_2(\boldsymbol{\xi}, t)}{\partial n} \quad \text{for } \boldsymbol{\xi} \in S \quad (6.28)$$

$$T_1(\boldsymbol{x}, t) \xrightarrow{\boldsymbol{x} \rightarrow 0} T_0 \quad T_2(\boldsymbol{x}, t) \xrightarrow{\boldsymbol{x} \rightarrow \infty} T_\infty \quad (6.29)$$

$$T_l(\boldsymbol{x}, 0) = T_{in}(\boldsymbol{x}) \quad \boldsymbol{x} \in \Omega_l, \quad l = 1, 2 \quad (6.30)$$

In equations (6.27) and (6.28), continuity of temperature and flux are enforced respectively, noting that the fluid velocity  $u_i^l$  is continuous across the interface. The initial temperature in each fluid zone (6.30) follows a prescribed, smoothed step initial condition  $T_{in}$  given by equation (6.1).

The heat transfer completes the mathematical formulation of the problem. In order to evaluate the pressure field in equation (6.14), and the temperature field in equation (6.26), the domain, interface and boundaries must be discretised with suitable numerical methods, discussed in the following sections.

### 6.3 Numerical methods

Here, the solution procedures to evaluate the transient temperature field and quasi-static pressure are described in order to reconstruct the interface velocity with equation (6.25). The steady-state pressure is solved in an almost identical fashion to that in chapter 5, using an indirect boundary element method for the homogeneous pressure, and the embedded multi-zone RBF-FC method for the perturbed pressure. The formulations will be presented below including the small changes needed in the interface matching conditions to account for the variable viscosity.

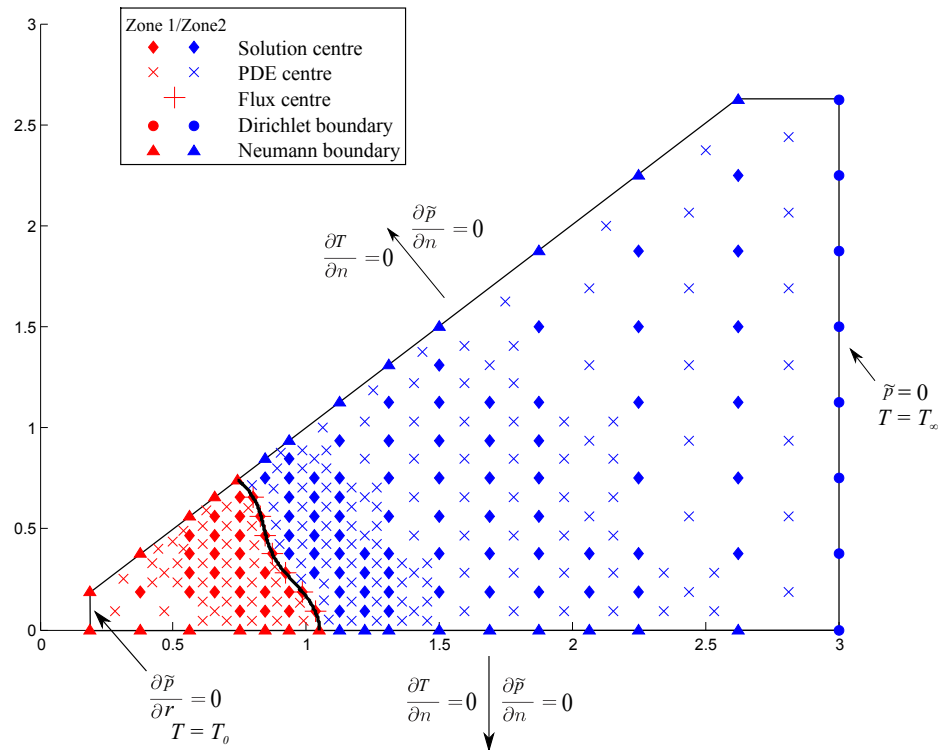


Figure 6.2: Thermo-viscous solution domain showing different RBF-FC operator types and boundary conditions. The curved solid black line indicates the fluid-fluid interface over which the boundary elements are formed. Note, only 1/8th of the interface is shown here for the RBF-FC method, but the BEM evaluates the full interface.

The heat transfer equation (6.26) is solved using the newly developed auxiliary multi-zone RBF-FC method presented in chapter 4, in which the temperature/flux matching conditions appear locally in the RBF systems. The heat transfer and pressure solutions are coupled through the thermally dependent viscosity, which links the two equations. The coupled solution procedure advances in a quasi-static fashion, described in more detail in section 6.3.3.

The boundary conditions, RBF-FC operator types and quadtree dataset structure are shown in Figure 6.2. The quadtree generation follows the same routine as that in chapter 5, splitting around the interface using a distance based algorithm, with nodal points displaced explicitly to the interface in order for matching conditions to be enforced.

### 6.3.1 Transient heat transfer solution

The heat transfer equation (6.26) can be described as a transient multi-zone boundary value problem of the form:

$$\bar{L}_{l,x}^{n+1}[T_l^{n+1}(\mathbf{x})] = \hat{S}_l^n(\mathbf{x}) \quad \mathbf{x} \in \Omega_l \quad (6.31)$$

$$B_{l,x}^{n+1}[T_l^{n+1}(\mathbf{x})] = g_l(\mathbf{x}) \quad \mathbf{x} \in \partial\Omega_l \quad (6.32)$$

$$C_{1,x}^{n+1}[T_1^{n+1}(\mathbf{x})] - C_{2,x}^{n+1}[T_2^{n+1}(\mathbf{x})] = h(\mathbf{x}) \quad \mathbf{x} \in \partial\Omega_{int} \quad (6.33)$$

$$Q_{1,x}^{n+1}[T_1^{n+1}(\mathbf{x})] - Q_{2,x}^{n+1}[T_2^{n+1}(\mathbf{x})] = f(\mathbf{x}) \quad \mathbf{x} \in \partial\Omega_{int} \quad (6.34)$$

Where:

$$\bar{L}_{l,x}^{n+1} = I - \theta\Delta t \left( D_l^{n+1} \frac{\partial^2}{\partial x_i^2} - u_l^{n+1}(\mathbf{x}) \frac{\partial}{\partial x_i} \right) \quad \mathbf{x} \in \Omega_l \quad (6.35)$$

$$\hat{S}_l^n(\mathbf{x}) = T_l^n(\mathbf{x})I + (1 - \theta)\Delta t \left( D_l^n \frac{\partial^2 T_l^n(\mathbf{x})}{\partial x_i^2} - u_{l,x}^n(\mathbf{x}) \frac{\partial T_l^n(\mathbf{x})}{\partial x_i} \right) \quad \mathbf{x} \in \Omega_l \quad (6.36)$$

$$B_{l,x}^{DU,n+1} = B_{l,x}^{DK,n+1} = 1, \quad B_{l,x}^{N,n+1} = n_i \frac{\partial}{\partial x_i} \quad \mathbf{x} \in \partial\Omega_l \quad (6.37)$$

$$g_{l,x}^{DU,n+1}(\mathbf{x}) = T_l^{n+1}(\mathbf{x}), \quad g_{1,x}^{DK,n+1}(\mathbf{x}) = T_0, \quad g_{2,x}^{DK,n+1}(\mathbf{x}) = T_\infty, \quad g_{l,x}^N(\mathbf{x}) = 0 \quad \mathbf{x} \in \partial\Omega_l \quad (6.38)$$

$$C_{l,x}^{n+1} = 1, \quad Q_{l,x}^{n+1} = D_l^{n+1} n_i \frac{\partial}{\partial x_i}, \quad h(\mathbf{x}) = 0, \quad f(\mathbf{x}) = 0 \quad \mathbf{x} \in \partial\Omega_{int} \quad (6.39)$$

In equations (6.31) to (6.39), subscript  $l$  refers to the zone and superscript  $n/n+1$  refers to the time step in question.  $L_l$ ,  $B_l$  and  $C_l/Q_l$  are linear partial differential operators on the domain  $\Omega_l$ , the boundary  $\partial\Omega_l$  and the fluid-fluid interface  $\partial\Omega_{int}$  respectively.  $I$

is the identity matrix (dimension 1 here). Superscript  $DU, DK$  and  $N$  refer to Dirichlet unknown, Dirichlet known and Neumann boundary operators respectively.

It is important to observe that according to the quasi-static approximation of the Hele-Shaw flow (Darcy flow), the convective velocity  $u_i^{n+1}(\mathbf{x})$  in equation (6.35) is equal to  $u_i^n(\mathbf{x})$ , since under such approximation the velocity at a given time step, i.e. between  $t$  and  $(t + \Delta t)$ , is defined by the position of the fluid interface at time  $t$ . This makes it appear that the finite difference approximation (6.31) with the terms at  $(t + \Delta t)$  given by equation (6.35) is semi-implicit, which is due to the quasi-static approximation of the Hele-Shaw flow formulation.

The auxiliary multi-zone RBF-FC method described previously is used to discretise the system of equations (6.31) to (6.34). After the solution of the resulting sparse global system for time step  $n+1$ , the newly computed temperature field can be used to compute the viscosity variation at time step  $n + 1$  using equation (6.7). After the pressure and velocity field have been calculated with equation (6.14) and the interface moved to its new position, the values of  $\hat{S}_l^n(\mathbf{x})$  can be calculated in the new domain using the updated velocity/diffusivity and the old local systems.

The issue of ghost nodes discussed in chapter 4 is alleviated in the the auxiliary method presented here by simply translating nodes out of the ghost zone, into the inner zone. This can be done since this method is truly meshless, and as long as a fairly regular nodal arrangement is maintained, the solution accuracy and convergence are not significantly affected. The required translation is typically very small (maximum  $\Delta t U_n$ ), since the interface displaces a very small amount at each time step.

After translation, all nodes apart from the interface nodes will exist in a region where they also existed at time step  $n$ , meaning all the data needed for the PDEs is known. As interface nodes only require reconstruction of the solution or flux, which do not depend on previous time step data, no extrapolation is needed for these even though they switch between zones at each time step. If PDE centres were placed on the interface as in the embedded method, extrapolation would be needed at each time step as interface nodes would also require  $\hat{S}_1^n(\mathbf{x})$  and  $\hat{S}_2^n(\mathbf{x})$ . By omitting them in the auxiliary method, no transport data is required at time step  $n$  along the new interface position at time step  $n + 1$ .

### 6.3.2 Steady-state pressure solution

For the steady-state pressure solution, the same numerical methods can be used as in the inhomogeneous mobility cases presented in chapter 5, replacing the definition for the mobility with that presented in this chapter. The homogeneous pressure can be found through the solution of the 2<sup>nd</sup> kind Fredholm equation:

$$-\frac{1}{2}\psi(\boldsymbol{\xi}) + \lambda \int_s K(\boldsymbol{\xi}, \mathbf{y})\psi(\mathbf{y})dS_y = f_s(\boldsymbol{\xi}) \quad (6.40)$$

where:

$$f_s(\boldsymbol{\xi}) = \frac{1}{Ca_g(1 + \beta)} \left( \frac{2}{b} + \frac{\pi}{4}k(\boldsymbol{\xi}) \right) + \left( \frac{\lambda}{2\pi\beta} \right) \ln(r) \quad (6.41)$$

The double layer potential  $W$  (defined in the previous chapter) can then be used to reconstruct the homogeneous normal interface velocity through:

$$\bar{u}_n(\boldsymbol{\xi}) = -M_1(\boldsymbol{\xi})n_i \frac{\partial \bar{p}_1(\boldsymbol{\xi})}{\partial x_i} = -M_1(\boldsymbol{\xi})n_i \left( \frac{\partial W(\boldsymbol{\xi}, \psi)}{\partial x_i} - \frac{x_i}{2\pi\beta r^2} \right) \quad (6.42)$$

The solution procedure for the homogeneous pressure and normal velocity are identical to that in the previous chapter, utilising a cubic B-spline boundary element method with hypersingular integral evaluation. The only difference is that the homogeneous mobility  $\bar{M}_l$  here is changed to represent the viscosity formulation, and  $b$  is used in equation (6.41) instead of  $b(\mathbf{x})$  since the plate separation is constant.

The perturbed pressure solution procedure is also very similar to that in chapter 5. Figure 6.2 shows the boundary conditions and an example nodal discretisation for the solution of the perturbed pressure in equation (6.14). As the present Darcy formulation is quasi-static, the perturbed pressure equation (6.14) can be described as a steady-state multi-zone transport boundary value problem of the form:

$$L_{l,x}[\tilde{p}_l(\mathbf{x})] = -S_l(\mathbf{x}) \quad \mathbf{x} \in \Omega_l \quad (6.43)$$

$$B_{l,x}[\tilde{p}_l(\mathbf{x})] = g_l(\mathbf{x}) \quad \mathbf{x} \in \partial\Omega_l \quad (6.44)$$

$$C_{1,x}[\tilde{p}_1(\mathbf{x})] - C_{2,x}[\tilde{p}_2(\mathbf{x})] = h(\mathbf{x}) \quad \mathbf{x} \in \partial\Omega_{int} \quad (6.45)$$

$$Q_{1,x}[\tilde{p}_1(\mathbf{x})] - Q_{2,x}[\tilde{p}_2(\mathbf{x})] = f(\mathbf{x}) \quad \mathbf{x} \in \partial\Omega_{int} \quad (6.46)$$

Where:

$$L_{l,x} = M_l(\mathbf{x}) \frac{\partial^2}{\partial x_i^2} + \frac{\partial \tilde{M}_l(\mathbf{x})}{\partial x_i} \frac{\partial}{\partial x_i}, \quad S_l(\mathbf{x}) = \frac{\partial \tilde{M}_l(\mathbf{x})}{\partial x_i} \frac{\partial \bar{p}_l(\mathbf{x})}{\partial x_i} \quad \mathbf{x} \in \Omega_l \quad (6.47)$$

$$B_{l,x}^{DU} = B_{l,x}^{DK} = 1, \quad B_{l,x}^N = n_i \frac{\partial}{\partial x_i} \quad g_l^{DU}(\mathbf{x}) = \tilde{p}_l(\mathbf{x}), \quad g_l^{DK}(\mathbf{x}) = g_l^N(\mathbf{x}) = 0 \quad \mathbf{x} \in \partial\Omega_l \quad (6.48)$$

$$C_{l,x} = 1, \quad Q_{l,x} = M_l(\mathbf{x}) n_i \frac{\partial}{\partial x_i}, \quad h(\mathbf{x}) = 0, \quad f(\mathbf{x}) = \left( \beta \tilde{M}_2(\boldsymbol{\xi}) - \tilde{M}_1(\boldsymbol{\xi}) \right) \frac{\partial \bar{p}_1(\boldsymbol{\xi})}{\partial n} \quad \mathbf{x} \in \partial\Omega_{int} \quad (6.49)$$

In equations (6.43) to (6.49), subscript  $l$  refers to the zone.  $L_l$ ,  $B_l$  and  $C_l/Q_l$  are linear partial differential operators on the domain  $\Omega_l$ , the boundary  $\partial\Omega_l$  and the fluid-fluid interface  $\partial\Omega_{int}$  respectively.  $S_l(\mathbf{x})$  is the source term coming from the homogeneous pressure  $\bar{p}(\mathbf{x})$  in domain  $\Omega_l$ . Superscript  $DU$ ,  $DK$  and  $N$  refer to Dirichlet unknown, Dirichlet known and Neumann boundary operators respectively. The system of equations in (6.43) to (6.49) are very similar to those in (5.39) to (5.47), with changes in the modified mobility  $m$ , which is replaced with the mobility  $M$ , and  $f(\mathbf{x})$  which is now non-zero due to the difference between  $a_1$  and  $a_2$  in the viscosity formulation.

The embedded multi-zone RBF-FC method described previously is utilised to discretise the system of equations (6.43) to (6.46). After the solution of the resulting sparse global system, the normal perturbation velocity  $\tilde{u}_n(\boldsymbol{\xi})$ , at a location  $\boldsymbol{\xi}$  on the interface can be reconstructed using the nearest overlapping system, i.e.,

$$\tilde{u}_n(\boldsymbol{\xi}) = -M_1(\boldsymbol{\xi}) n_i \frac{\partial \tilde{p}_1(\boldsymbol{\xi})}{\partial x_i} \quad (6.50)$$

With  $\tilde{u}_n(\boldsymbol{\xi})$ , the total velocity can be reconstructed using (6.42) and the interface displaced via a forward Euler time stepping scheme, using a time step size of  $\Delta t$ .

As well as the normal interface velocity to displace the interface in time, the velocity is also needed in the domain to solve the transient heat transfer problem in (6.31) to (6.39). The perturbed component of the velocity can be reconstructed using nearby overlapping systems (in a partition of unity sense using the radial distance from the centrepoint of the systems as the weighting factor), whilst the homogeneous component

can be reconstructed using the derivatives of the double layer potential in the boundary element formulation, i.e:

$$\begin{aligned} U_i^1(\mathbf{x}) &= -M_1(\mathbf{x}) \left( \frac{\partial W(\mathbf{x}, \psi)}{\partial x_i} - \frac{x_i}{2\pi\beta r^2} + \frac{\partial \tilde{p}_1(\mathbf{x})}{\partial x_i} \right) \\ U_i^2(\mathbf{x}) &= -M_2(\mathbf{x}) \left( \beta \frac{\partial W(\mathbf{x}, \psi)}{\partial x_i} - \frac{x_i}{2\pi r^2} + \frac{\partial \tilde{p}_2(\mathbf{x})}{\partial x_i} \right) \end{aligned} \quad (6.51)$$

As in chapter 5, any domain points (typically PDE points from cells that coincide with interface) that are very close to, but not coinciding with the interface are removed, to avoid near hypersingular integration. In the heat transfer formulation this is rare, since PDE points very close to the interface are generally displaced to avoid the ghost region, meaning that they are not close enough to the interface to generate near-hypersingular integrands. Point removal is more common in the evaluation of the source term for the perturbed pressure solution, in which PDE points can lie very close to the interface, since no ghost region exists in the steady-state pressure formulation.

A summary of the full numerical method for the solution of the immiscible thermo-viscous fingering problem is outlined in the next section.

### 6.3.3 Coupled solution algorithm

The coupled thermo-viscous problem uses the algorithm below:

1. Set-up the initial interface and boundary element mesh using the 8 finger symmetric perturbation  $r = 1 + \epsilon_0 \cos(8\theta)$  at  $t = 0$ , time step  $n = 0$ . Set-up the initial temperature field using a smoothed step function over the interface using equation (6.1) with  $\delta = 1$ . Generate the embedded RBF-FC nodal arrangement for the steady-state pressure solution.
2. Use the initial temperature field to calculate the viscosity using (6.7). Solve the initial pressure/velocity field using the initial interface position, through equations (6.42) and (6.50), to calculate the the total interface velocity with (6.25).
3. Displace the interface using a forward Euler time step, i.e  $\Delta x_i = n_i U_n \Delta t$ . Advance  $t = t + \Delta t$ ,  $n = n + 1$ .
4. Generate a new boundary element mesh at  $n + 1$ .

5. Generate and update the auxiliary RBF-FC nodes and the embedded RBF-FC nodes using the new interface position at  $n + 1$ . In both datasets, displace nearby nodes directly onto the interface to enforce the matching conditions. Displace any nodes that lie in the ghost region in the auxiliary dataset in an orthogonal manner so that they exist in the same zones at time step  $n$  and  $n + 1$ .
6. Generate the heat transfer PDE data  $\hat{S}_l^n(\mathbf{x})$  at the new auxiliary RBF-FC nodal positions, using the data from time step  $n$ . If  $n = 1$  this is a simple interpolation of the initial temperature field, using the velocity field calculated in step 2. If  $n > 1$  the local systems and calculated solution from time step  $n$  can be used to reconstruct  $\hat{S}_l^n(\mathbf{x})$  at the new nodal positions. The velocity field is reconstructed using the boundary element and embedded RBF-FC solutions at time step  $n$  with (6.51).
7. Generate the new local systems for the auxiliary RBF-FC method using the positions and diffusivity data from time step  $n + 1$  and the velocity data from time step  $n$ , to generate  $\bar{L}_{l,x}^{n+1}$ .
8. Reconstruct the temperature at the centrepoint of each local stencil using the auxiliary multi-zone Hermitian formulation, creating a sparse global matrix system. Solve the global matrix system using a sparse LU solver, generating the temperature everywhere in the domain  $T_l^{n+1}(\mathbf{x})$ .
9. Use the temperature field  $T_l^{n+1}(\mathbf{x})$  to calculate the viscosity everywhere using (6.7).
10. Generate the new local systems for the embedded RBF-FC method, based on the new nodal positions at  $n + 1$ , with corresponding mobility data from the viscosity in step 9. Solve the pressure/velocity field for the interface position at  $n + 1$  through equations (6.42) and (6.50). Calculate the total interface velocity with (6.25).
11. Repeat steps 3 - 10 until the end simulation time is reached.

$T(^{\circ}C)$	$CO_2$ viscosity $\bar{\mu}_1$ (Pa.s)	Brine viscosity $\bar{\mu}_2$ (Pa.s)	$\beta$
35	$8.411 \times 10^{-5}$	$7.542 \times 10^{-4}$	8.967
40	$7.858 \times 10^{-5}$	$6.865 \times 10^{-4}$	8.736
45	$7.376 \times 10^{-5}$	$6.283 \times 10^{-4}$	8.519
50	$6.893 \times 10^{-5}$	$5.779 \times 10^{-4}$	8.384
55	$6.456 \times 10^{-5}$	$5.338 \times 10^{-4}$	8.268
60	$6.019 \times 10^{-5}$	$4.952 \times 10^{-4}$	8.227
65	$5.664 \times 10^{-5}$	$4.610 \times 10^{-4}$	8.139
70	$5.309 \times 10^{-5}$	$4.306 \times 10^{-4}$	8.112

Table 6.1:  $CO_2$  and Brine fluid properties with temperature.

Case	$T_0(^{\circ}C)$	$T_{\infty}(^{\circ}C)$	$\bar{M}_1(m^3.s/kg)$	$\bar{M}_2(m^3.s/kg)$	$\beta$	$a_1$	$a_2$
1	35	70	$2.133 \times 10^{-7}$	$2.379 \times 10^{-8}$	8.967	0.4583	0.5390
2	35	50	$2.133 \times 10^{-7}$	$2.379 \times 10^{-8}$	8.967	0.1986	0.2627
3	35	35	$2.133 \times 10^{-7}$	$2.379 \times 10^{-8}$	8.967	0.0000	0.0000
4	50	35	$2.603 \times 10^{-7}$	$3.105 \times 10^{-7}$	8.384	0.1986	0.2627
5	70	35	$3.380 \times 10^{-7}$	$4.167 \times 10^{-7}$	8.112	0.4583	0.5390

Table 6.2: Summary of injection regimes and fluid properties

## 6.4 Fluid properties

Before proceeding to the main body of the thermo-viscous fingering verification and results, the fluid properties and temperature regimes that will be used in these sections are summarised in tables 6.1 and 6.2.  $CO_2$  viscosity data is interpolated at the specified temperatures with an injection pressure of 20MPa from [157]. The brine viscosity is calculated from sodium chloride solution data at the specified temperatures at 0.5Mol/Kg and 10MPa resident pressure using [61]. A suitable brine -  $CO_2$  surface tension of  $0.03 \text{ kg/s}^2$  is used at the resident temperature and pressure values [62]. Due to the lack of data concerning thermal diffusivity values for brine, a corresponding diffusivity value for water at the resident temperature and pressure is taken as  $0.0015 \text{ cm}^2/\text{s}$ . For supercritical  $CO_2$ , the diffusivity is  $0.0005 \text{ cm}^2/\text{s}$  [158].

The injection regimes in table 6.2 summarise the mobility values for each specific injection temperatures and the associated rate of change of viscosity with temperature for the specific regime. The values of  $a_i$  change, since the non-dimensional scalings change with the resident temperature, meaning that  $a_i$  must be varied to keep the same dimensional dependence on temperature. The plate separation  $b = 0.00146731 \text{ cm}$ , meaning the intrinsic permeable of the cell is  $1.8 \times 10^{-11} \text{ cm}^2$  (equivalent to oil reservoir

rock). This value of  $b$  is chosen so that it corresponds to suitable aquifer permeability and that the lowest global capillary number regime tested with the given physical viscosities comes to a round value of  $Ca_g = 2000$ .

## 6.5 Mass conservation verification

In this section, the fully coupled numerical scheme is verified on the case of the displacement of an initially circular interface, with zero perturbation. Perturbations will only grow after a long period of time due to numerical error, meaning that the interface should propagate as a growing circle with an increasing volume equal to that injected at the origin. By comparing the numerical volume of the growing plume and the volume of fluid injected at the origin, the mass conservativeness of the coupled scheme can be verified. The total volume of fluid is given in non-dimensional form as:

$$V_a = V_0 + \bar{b}t \quad (6.52)$$

Where,  $V_0$  is the initial volume of fluid in the cell. To ensure that mass has been conserved in the numerical method, the volume of fluid can be calculated through numerical integration of the evolving interface (using the average interface position  $\bar{r}$ ) and compared to the value given by equation (6.52). Mass conservation has already been verified for the coupled BE-RBF-FC method when solving purely the pressure/velocity field in inhomogeneous mobility flows in the previous chapter. The scheme was also compared to linear stability analyses, showing very similar growth rates at the early stages of the displacement. In this section, the tests presented will verify that the RBF-FC method is contributing a correct velocity from the perturbed pressure to displace the interface and that the corresponding temperature field transports accurately. The RBF method still solves the full multi-zone steady-state pressure and the transient heat transfer problem, but with the interface given by a simple circle instead of the convoluted interface usually found in viscous fingering problems.

Extra complexity is introduced in the scheme in comparison to the previous chapter, since the heat transfer in the domain must also be accurately resolved in order to evaluate the viscosity and inhomogeneous mobility. The inhomogeneous mobility now comes from a numerical approximation of the transient temperature field, rather than from a known

analytical function as in the previous chapter. Also the perturbed pressure flux at the interface is discontinuous due to the viscosity formulation, introducing extra complexity to the steady-state pressure solution.

Given the symmetry of the problem, a triangular solution domain is again used for the RBF-FC methods, similar to that shown in Figure 6.2. Two different nodal distributions are used for the perturbed pressure solution and the transient heat transfer solution. This ensures numerical accuracy and stability for both solutions, which do not necessarily need the same nodal distribution. As the temperature profile is sharper than the perturbed pressure, the outer boundary can be brought closer to the injection source and the number of nodal points increased in the domain. Also, as the resulting global matrix for transient problems is very sparsely populated, increasing the number of nodes does not significantly increase the solution cost.

For the heat transfer the outer boundary is taken at  $x = 8$ , with a maximum quadtree level of 8, and minimum 4. For the perturbed pressure the outer boundary is at  $x = 32$ , to ensure that the perturbed pressure has dropped to near zero in the far field where the boundary condition is applied. The temperature (needed for the viscosity) at any point  $x > 8$  is taken at the outer boundary value  $T_\infty$ . The maximum quadtree level for the perturbed pressure is set at 10, with a minimum of 3. This ensures that both RBF nodal distributions cluster points around the interface with a minimum nodal separation of  $\Delta x = 0.03125$ . The transient heat transfer problem uses a much denser distribution of nodal points, with the  $B_t$  value varying uniformly from 11 at the highest cell level to 6 at the lowest cell level. Nodes around the injection source are forced to be at the highest cell level (i.e. they are continuously split until they reach the maximum), to ensure numerical stability. This constant high level, fine clustering of nodes extends to a point  $r = 3$  in the temperature domain. With the perturbed pressure nodes,  $B_t$  is varied uniformly from 3 at the highest level, to 6 at the lowest cell level, creating a much coarser dataset that can still accurately capture the perturbed pressure.

A constant non-dimensional shape parameter value of  $c^* = 90$  is maintained for all simulations. In the boundary element method the full interface is solved, around which a target element size is maintained throughout the simulations at  $\Delta x \approx 0.06$ , ensuring a mesh-independent boundary element solution. Both RBF nodal distributions are therefore twice as refined around the interface as the BEM. These nodal distributions

have been thoroughly tested, and the cell levels increased by two levels beyond those quoted here, creating an 8 fold increase in the nodal density compared to the BEM. At these higher levels, no further gain in accuracy is achieved, without significantly reducing the time step size to impractically small values.

In table 6.3, the relative errors between the analytical and numerical volume of fluid testing is shown for different temperature regimes and time step sizes. All cases exhibit very low relative errors, with the largest error coming from the  $35^\circ C - 70^\circ C$  case which has the largest local capillary number. The lower temperature regimes exhibit  $1^{st}$  order convergence in the time stepping scheme as expected, however, in the high temperature cases the error plateaus. This is due to the solution accuracy reaching the limit imposed by the spatial discretisation, so no further reduction in time step increases the accuracy (at least when  $Q$  is high).

Injection Regime	Relative Error, $Q = 0.5 \text{ cm}^2/\text{s}$		Relative Error, $Q = 0.75 \text{ cm}^2/\text{s}$	
	$\Delta t = 0.02$	$\Delta t = 0.04$	$\Delta t = 0.02$	$\Delta t = 0.04$
$35^\circ C - 50^\circ C$	$7.27 \times 10^{-4}$	$1.47 \times 10^{-3}$	$7.70 \times 10^{-4}$	$1.44 \times 10^{-3}$
$50^\circ C - 35^\circ C$	$7.02 \times 10^{-4}$	$1.39 \times 10^{-3}$	$6.00 \times 10^{-4}$	$1.55 \times 10^{-3}$
$35^\circ C - 70^\circ C$	$2.34 \times 10^{-3}$	$2.32 \times 10^{-3}$	$2.57 \times 10^{-3}$	$3.16 \times 10^{-3}$
$70^\circ C - 35^\circ C$	$1.86 \times 10^{-4}$	$7.01 \times 10^{-4}$	$6.38 \times 10^{-4}$	$7.30 \times 10^{-4}$

Table 6.3: Relative errors between analytical and numerical volume of fluid for different injection regimes at  $t = 10$ .

Figure 6.3 shows the interfacial displacement and temperature field for the  $50^\circ C - 35^\circ C$  case with  $Q = 0.5 \text{ cm}^2/\text{s}$  at  $t = 10$ . This highlights the high Peclet number ( $> 1000$ ), as the temperate field shows very little diffusion and the interface lies at a temperature close to the initial temperature condition, i.e. the initial condition has been almost purely advected. The contour lines bunch in the inner region with the low diffusivity and high convection, showing the sharp drop in temperature at the interface that is then smoothly diffused in the outer region. The numerical solution still exhibits a circular interface, indicating that numerical error has not yet caused any perturbations to grow, being amplified by the viscosity contrast and transient temperature field.

These results validate the mass conservation of the scheme, and showcase the accuracy of the proposed numerical methods when solving the full thermo-viscous fingering problem. For the problem cases presented in the next sections, a time step size of  $\Delta t = 0.02$  is used to provide a balance between accuracy and practical solution times.

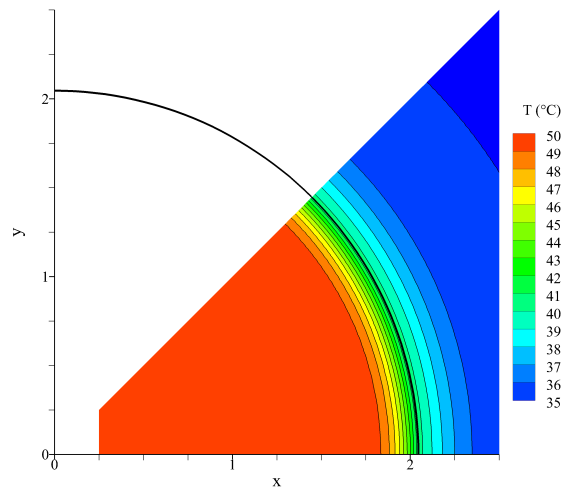


Figure 6.3: Temperature contour and interface plot at  $t = 10$  for the  $50^{\circ}\text{C} - 35^{\circ}\text{C}$ ,  $Q = 0.5 \text{ cm}^2/\text{s}$  case with  $\Delta t = 0.02$ . The bold black interface overlays a temperature contour plot with thin contour lines of the temperature field.

To maintain numerical stability with the numerical methods, a combination of smoothing algorithms are used that damp severe numerical oscillations. Brief summaries of these techniques are given below.

### 6.5.1 Artificial diffusion and smoothing

To ensure stability with the  $2^{\text{nd}}$  order Crank-Nicholson scheme for the the auxiliary RBF-FC heat transfer solution, artificial diffusion and selective smoothing are employed. In situations when the heat transfer is highly convective (i.e. when the thermal Peclet number is very high), the solution can sometimes briefly oscillate above/below the base values of the injection and resident temperatures, bringing numerical error into the solution. This occurs due to the relative instability of the RBF solution when high shape parameters are used, and the  $2^{\text{nd}}$  order time stepping scheme which is not unconditionally stable.

When the solution goes above/below a threshold of the base values (typically 0.1%), an artificially high diffusion is applied to the point for a single time step that is 100 times higher than the base diffusivity. This damps any severe numerical oscillations, whilst ensuring that there is negligible effect on the solution profile. Selective smoothing is also employed, whereby if a solution point differs from the average of its neighbours by a certain tolerance (this is set to a high value usually  $\approx 7.5\%$ ), then it is smoothed to

the average value of its neighbours. Artificial diffusion and selective smoothing occur very infrequently in the simulations due to the highly refined datasets, generally being applied to around 1-5 points every hundred time steps. This is enough to maintain numerical stability and allow the simulations to run for very long periods of time without affecting the solution accuracy. For example in the  $70^{\circ}\text{C} - 35^{\circ}\text{C}$  case in this section with  $\Delta t = 0.02$ , the percentage of total points (over the whole simulation time) where artificial diffusion and selective smoothing are applied is  $8.2 \times 10^{-4} \%$  and  $8.9 \times 10^{-3} \%$  respectively, indicating the sparse application of numerical smoothing.

### 6.5.2 Shape parameter relaxation

For the embedded RBF-FC pressure/velocity solution, shape parameter relaxation is employed to ensure smooth variation in the pressure/velocity field between time steps. The shape parameter is set to an initially high value of  $c^* = 90$  at each time step, and the residual change in interfacial velocity is compared to the previous time step. If the change between time steps is over 5% the shape parameter is dropped by 10% successively relaxing the solution (up to 30%) until the residual change is less than 5%. Since the nodal discretisation changes with each time step, some datasets show a more regular distribution around the interface (depending on its shape) and hence perform better. For poorer quality datasets, relaxing the shape parameter helps to ensure stability whilst maintaining solution accuracy and a smoothly varying velocity field. This process also occurs very infrequently, occurring on the order of 10 times in the whole simulation (of over 1500 time steps).

## 6.6 Thermo-viscous fingering results

The cases of non-isothermal displacement given in table 6.2 are now considered with an initial interface perturbation. All cases are run with the mesh/time step parameters discussed in the previous section. An isothermal case at  $35^{\circ}\text{C}$  is used as the base case to compare non-isothermal results with, since this represents the common temperature when raising the injection temperature for hot injection cases and raising the resident temperature for cold injection cases. The results sections are broken up into subsections

detailing the different characteristics of the flow, starting with the general system behaviour below.

### 6.6.1 General system behaviour

Here, the general system behaviour is described using interfacial plots and timeseries data of the key parameters. In Figure 6.4, the interfacial displacements at  $t = 30$  can be seen for the different temperature regimes at two different injection fluxes,  $Q = 0.5 \text{ cm}^2/\text{s}$  and  $Q = 0.75 \text{ cm}^2/\text{s}$ . These two injection fluxes will be used throughout to vary the effective capillary number.

The lower injection flux regimes, plotted in Figures 6.4(a) and (b) illustrate the effect of a non-isothermal temperature distribution in the domain. In the cold injection cases in Figure 6.4(a), the interfaces have been stabilised in comparison to the isothermal; the finger bases are more perturbed, whilst the fronts remain closer to the injection source, creating a less ramified structure. Increasing the resident temperature from  $35^\circ\text{C}$  to  $70^\circ\text{C}$  has more significantly stabilised the interface, delaying the onset of bifurcation.

In corresponding hot injection cases in Figure 6.4(b), the interfaces have been destabilised, with the fronts accelerated beyond the isothermal case. The larger temperature difference case of  $70^\circ\text{C} - 35^\circ$  has produced a more significant destabilisation, resulting in an earlier bifurcation and more perturbed finger front at  $t = 30$  in 6.4(b). Interestingly, the bases remain largely in the same position, indicating that the base position is controlled mainly by the outer fluid temperature.

Increasing the injection flux to  $Q = 0.75 \text{ cm}^2/\text{s}$  in Figure 6.4(c) and (d) results in more significant (de)stabilisation effects from the non-isothermal regimes due to the increased capillary number. In the cold non-isothermal cases, the interfaces are somewhat stabilised in Figure 6.4(c), with the bases all displaced further than the isothermal case. However the finger fronts now show different bifurcation regimes to the isothermal, due to the raised capillary number and increased thermal effects. Generally, raising the resident temperature has stabilised the front, with the  $35^\circ\text{C} - 70^\circ\text{C}$  case clearly showing a less advanced finger front than the isothermal case.

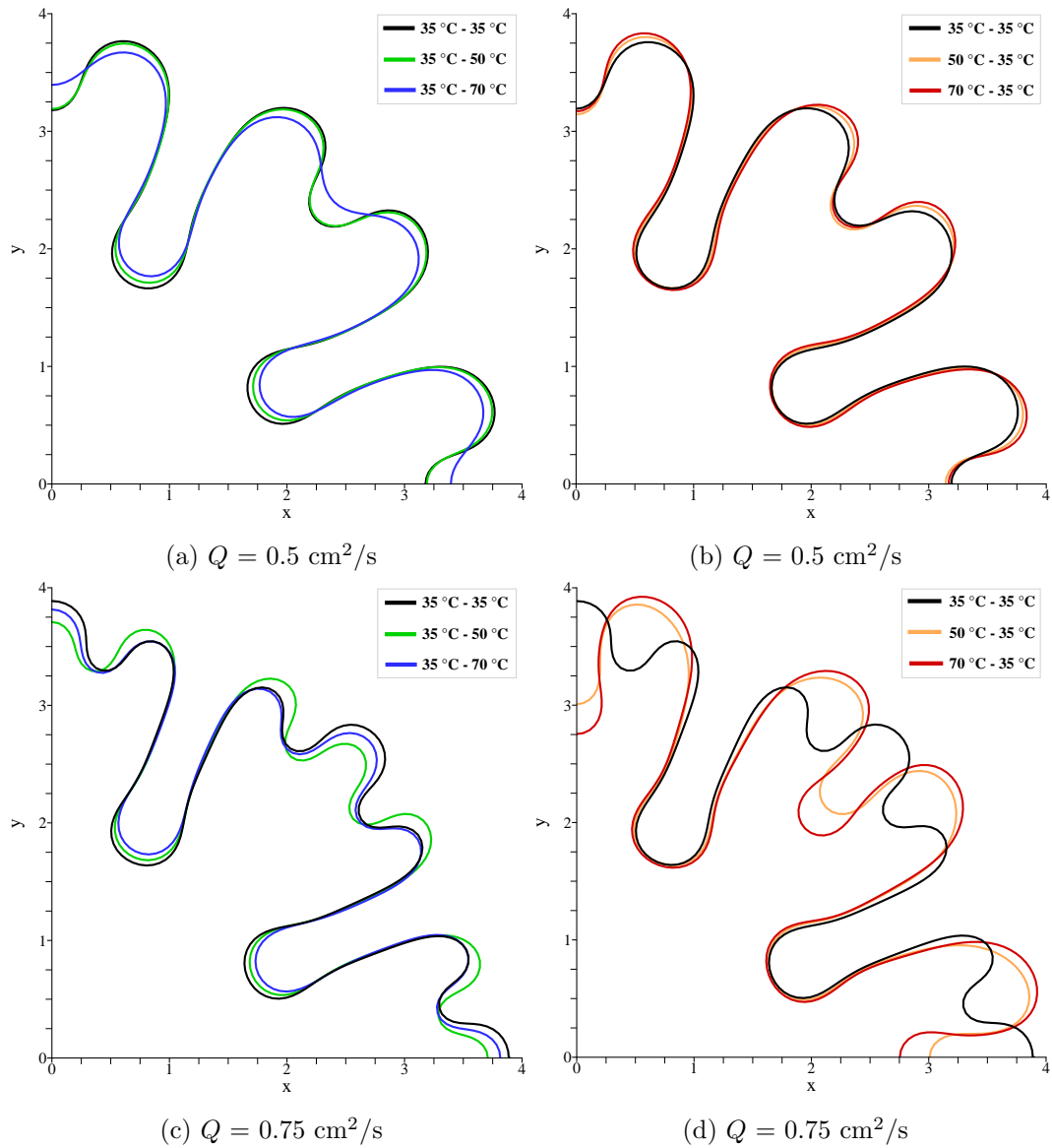


Figure 6.4: Interface plots at  $t = 30$  for several non-isothermal injection regimes; (a) and (c) show cold injection cases, (b) and (d) show hot injection cases.

For the hot injection cases at the higher flux of  $Q = 0.75 \text{ cm}^2/\text{s}$  in Figures 6.4(d), the interfaces have been accelerated and show elongated two finger split regimes. The two finger regime usually represents a more stable bifurcation than the three finger split, as viscous forces are lower in comparison to surface tension forces. However, in this case, the two finger split is caused by a different mechanism than in classical viscous fingering bifurcations, discussed in more detail in section 6.6.2.

The displacement regimes can be analysed quantitatively using time series data of the finger growth rate, pressure gradient and mobility, shown in Figure 6.5. The dimensional

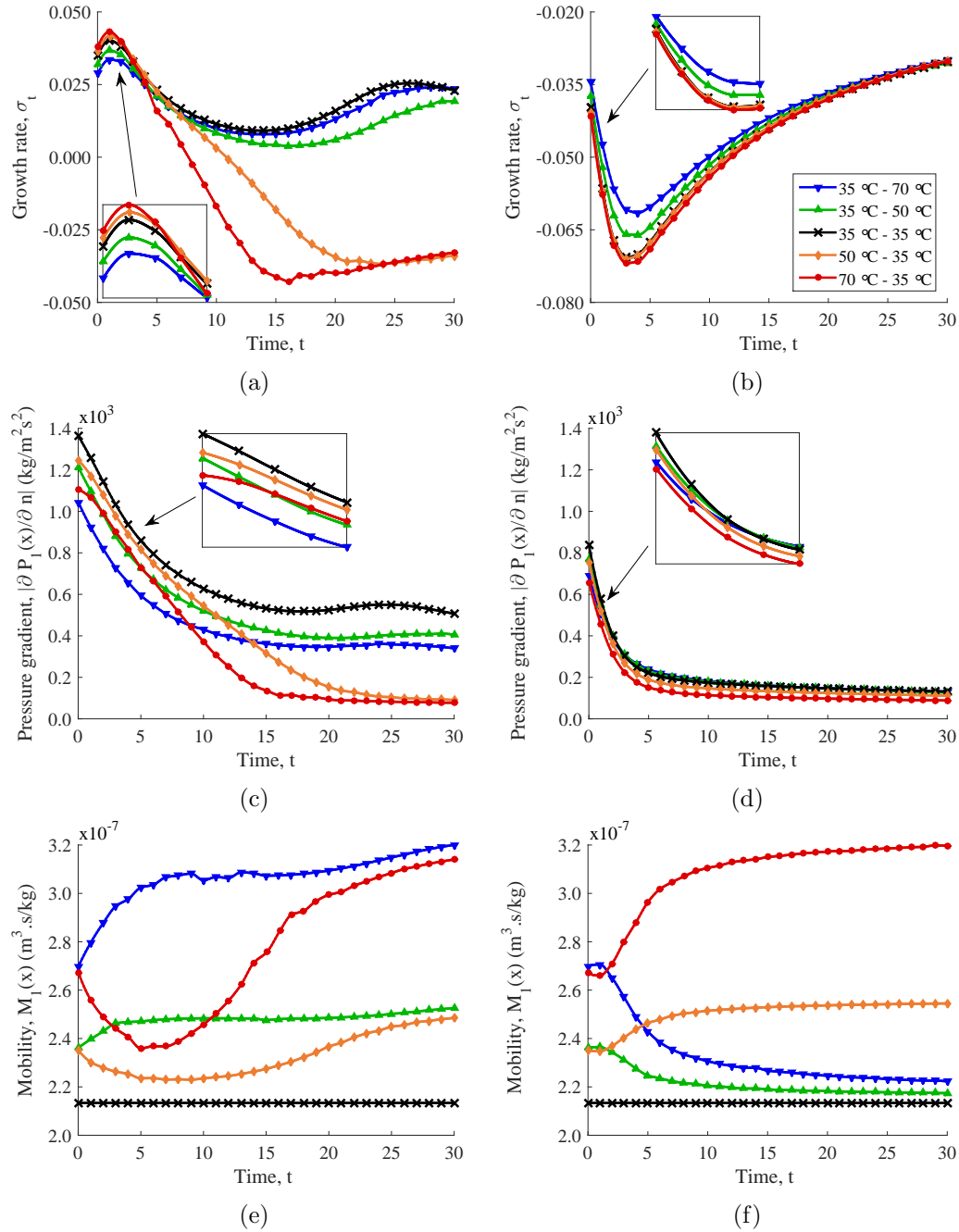


Figure 6.5: Plots of the growth rate, pressure gradient and mobility with time at the finger fronts (a, c, e) and finger bases (b, d, f) for different temperature regimes with  $Q = 0.75 \text{ cm}^2/\text{s}$ . Legend for each plot shown in (b).

pressure gradient and mobility are shown here (plotted against non-dimensional time), as the non-dimensional scalings change with each different injection temperature, which can be misleading with regards to the physical mechanisms that control the flow regime.

The growth rate shown in Figure 6.5(a) highlights the initial acceleration of the finger

fronts due to the high temperature injection and the initial deceleration of the front due to the low temperature injection. The growth rate is controlled by the evolution of the mobility and pressure gradient at the interface, shown in Figure 6.5(c) - (f). The initial difference in growth rate between the cases is due to the change in pressure gradient, as the hot and cold injection cases have the same mobilities for the same initial temperatures (i.e. the  $35^\circ\text{C} - 70^\circ\text{C}$  case has the same initial temperature and mobility at the interface as the  $70^\circ\text{C} - 35^\circ\text{C}$  case).

In cold injection cases, the pressure gradient is significantly reduced from the isothermal (see Figure 6.5(c)), as the perturbed pressure gradient component in equation (6.25) is positive, which reduces the velocity and hence growth rate. The magnitude of the total pressure gradient is initially reduced by 23.7% for the  $35^\circ\text{C} - 70^\circ\text{C}$  case compared to the isothermal, whereas the mobility is raised by only 20.9%, which results in the lower growth rate of the  $35^\circ\text{C} - 70^\circ\text{C}$  case. The reverse is true of the hot injection case, where a negative perturbed pressure gradient causes a reduction in magnitude of the total pressure gradient by only 19.0% for the  $70^\circ\text{C} - 35^\circ\text{C}$  case, with the mobility increasing by 20.9%, resulting in a higher growth rate.

At the finger bases, the growth rate behaviour is reversed, i.e. the cold cases have higher base growth rates than the hot cases (see Figure 6.5(b)). However, the mechanism for the increase/decrease in growth rate is the same as at the fronts. The cold injection cases have a higher growth rate at the finger bases, due to the increased pressure gradient (note the perturbed pressure gradient in equation (6.25) is negative at the base, increasing the velocity). With time, the base growth rates all tend to the same value, when the mobility and pressure gradient profiles have both reached near constant values. At this stage, the temperature fields are diffuse and the increase/decrease in pressure gradient due to the cold/hot injection is equalled by the decrease/increase of the temperature and mobility at the base, resulting in the same growth rate.

The negative growth rates that occur in Figure 6.5(a) and (b) are caused by bifurcations. At bifurcated points of the interface where the curvature is negative (for instance at the finger bases), the normal velocity is reduced significantly in comparison to an unperturbed interface, meaning the growth rate given by equation (5.57) becomes negative.

The pressure gradient represents the primary control for the initial growth of the interface, when the temperature field evolves in a highly convective regime. If the temperature field grew in a purely convective manner, this regime would hold for all time, with hot injection cases being relatively more unstable than isothermal and cold injection cases. However, with diffusion in the physical system, the temperature field evolves with different profiles around the interface for the hot and cold injection cases that alter the bifurcation mode. It is worth noting that in the lower injection flux regime at  $Q = 0.5 \text{ cm}^2/\text{s}$ , the same effects occur as detailed above but with reduced magnitude, resulting in the early timeframe acceleration/deceleration of the interface, but without alteration in the bifurcation mode.

The promotion of finger bifurcation in the hot injection cases here is similar to that reported experimentally by [156], albeit in the immiscible regime and at slightly lower injection fluxes than those stated in [156]. In a small range of mobility ratios  $\beta \approx 10$ , they find that bifurcation occurs earlier in the evolution for the hot non-isothermal regime. These results appear at least qualitatively very similar to those here, whereby the finger fronts are accelerated in hot injection regimes.

For the simulations presented here, at the late stage of displacement shown in Figure 6.4, the number of boundary elements is generally of the order  $N_b \approx 1500$ . The number of RBF-FC solution centers in the domain for the steady-state perturbed pressure is of the order  $N_B \approx 5000$ , and the number of solution centers in the domain for the transient heat transfer is of the order  $N_B \approx 10,000$ . The number of PDE centers ( $N_I$ ) in both RBF-FC schemes is generally slightly more (1000-2000) than the number of solution centers. These simulations all complete in under 1 week, using two cores of an Intel Core i3-4130 CPU with 8GB RAM.

### 6.6.2 Thermal evolution & bifurcation modes

After the initial growth at  $t = 5$  in the  $Q = 0.75 \text{ cm}^2/\text{s}$  regime, the growth rate of the two hot injection regimes in Figure 6.5(a) starts to vary significantly from the cold injection and isothermal cases as the bifurcation changes to a two finger mode. The difference in growth rate and bifurcation mode can be explained by considering the temperature and mobility evolution. In Figure 6.5(e) the front mobility (and temperature) drops

significantly when  $0 < t < 5$  in the hot injection cases, as the temperature is rapidly convected towards the finger tip and diffused into the surrounding media.

As the tip mobility drops, the base mobility rises in the hot cases in Figure 6.5(f). As the base develops a large negative curvature as time progresses, heat is diffused from the base and sides of the finger into the spacing between the fingers, creating a high temperature region. This raises the temperature of the base until it reaches a near constant value where the base convection matches the diffusion into the outer region. This difference in temperature evolution between the finger fronts and base results in the difference between the bifurcation regimes for the hot and cold injection cases at the high injection flux.

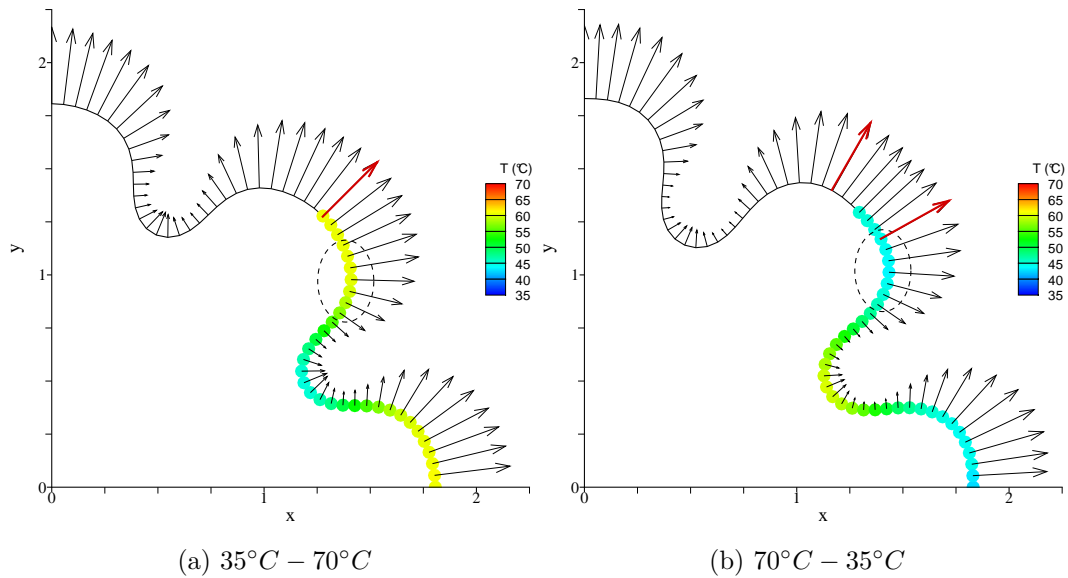


Figure 6.6: Temperature scatter plots around the interface for the hot and cold injection cases at  $t = 5$ ,  $Q = 0.75 \text{ cm}^2/\text{s}$ . The arrows show normal velocity vectors  $U_n$ , with red arrows highlighting the maximum velocity.

The temperature profile around the interface for the hot and cold injection regimes at  $t = 5$  in Figure 6.6 highlights the cause of the different bifurcation modes between the hot and cold cases with  $Q = 0.75 \text{ cm}^2/\text{s}$ . In the cold injection case in Figure 6.6(a), the temperature increases monotonically from the finger base to the tip, meaning the highest mobility (and hence velocity) is found at the finger tip. The interface proceeds to sharpen in time, and form the three finger bifurcation.

However, in the hot injection case, the temperature decreases monotonically from the finger base to the tip, meaning the finger sides have a higher mobility than directly at

the tip. This causes the velocity to be higher at the finger sides (highlighted by the red velocity vector in 6.6(b)) and the spreading mechanism is enhanced. This creates a ‘flatter’ finger front and leads to the two finger bifurcation later in time.

At the stage shown Figure 6.6, diffusion effects are becoming more significant and have altered the temperature profile around the interface enough to cause the change in bifurcation regime. From this, it can be inferred that the macroscopic temperature profile around the interface controls the late stage splitting mode of the interface, whilst the early time scale pressure gradient in the convective regime describes the general acceleration/deceleration effects of the hot/cold injection regimes.

Similar macroscopic temperature profiles can also be seen later on in the finger growth at  $t = 30$  in Figure 6.7(a) and (b). Here, after the first bifurcation, the finger tips in the hot injection case have lower temperatures than the sides and base, indicating that the spreading mechanism is again being enhanced. Likewise, the cold injection cases have the highest temperature at the finger tips, showing that the fingers will be sharpened and will likely split into more fingers on bifurcation. The temperature contour plots at  $t = 30$  in Figure 6.7(c) and (d) show the convective nature of the flow, with the temperature profile closely following that of the interface. Here, the thermal Peclet number is very large at  $Pe = Q/D_1 = 1500$ .

In the results presented here, only two and three finger bifurcations are seen due to the capillary number and temperature regimes that are considered. For a four or five finger bifurcation, the interface has to become much more unstable, requiring a larger injection flux and capillary number (i.e., the isothermal case needs to have  $Q > 1.75\text{cm}^2/\text{s}$ ,  $Ca_g > 7000$  to produce a different bifurcation mode). However, the general mechanisms that are presented here involving the bifurcation regime and acceleration/deceleration effects will still hold in these more unstable regimes, albeit with different variations in the bifurcation mode.

The temperature profiles across the finger front and base at  $t = 30$  can be seen in Figure 6.8. Here, the multi-zone nature of the temperature field is observable, where the gradient of the temperature profile decreases by a factor of three at the interface (highlighted by the crosses) due to the three fold increase in the diffusivity in the outer region ( $D_1 = 0.0005\text{cm}^2/\text{s}$ ,  $D_2 = 0.0015\text{cm}^2/\text{s}$ ). The temperature profile is very sharp in

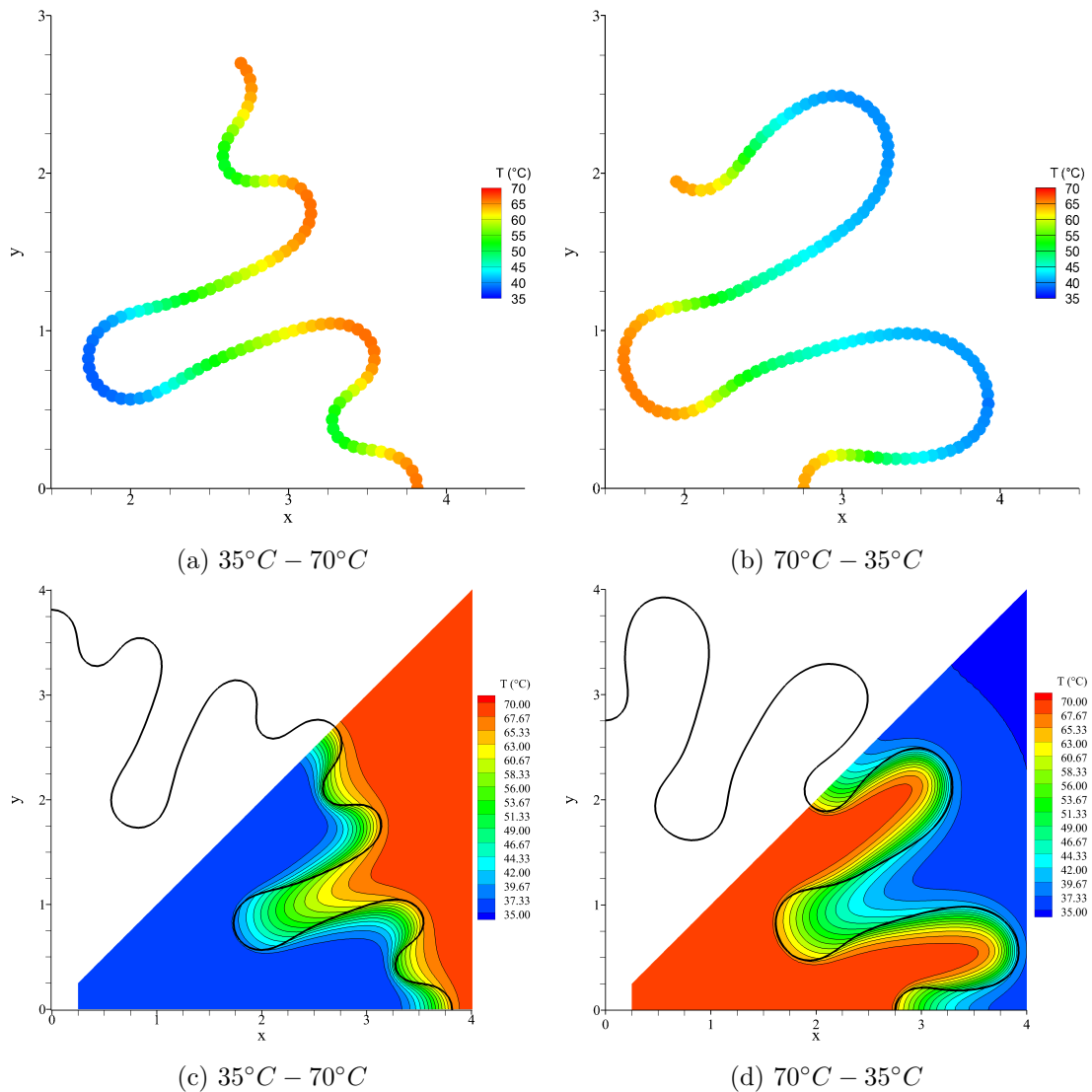


Figure 6.7: (a) and (b) Temperature scatter plots around the interface for the hot and cold injection cases at  $t = 30$ . (c) and (d) Temperature contour plots at  $t = 30$ . The bold black interfaces overlay temperature contour plots with thin contour lines of the temperature field.  $Q = 0.75 \text{ cm}^2/\text{s}$ .

the inner region in the hot injection case as the front has bifurcated and formed a near stagnation point, and the heat transfer is dominated by diffusion. The front and base profile therefore exhibit similar profiles at different locations in the domain, with the base being slightly more diffuse since it was formed earlier in time. In the cold injection case, the same change in temperature gradient is exhibited at the interface, but the inner zone temperature field is much more diffuse as the front has yet to bifurcate and stagnate.

The viscosity profiles in Figure 6.8(c) and (d) show the relative increase/decrease in local

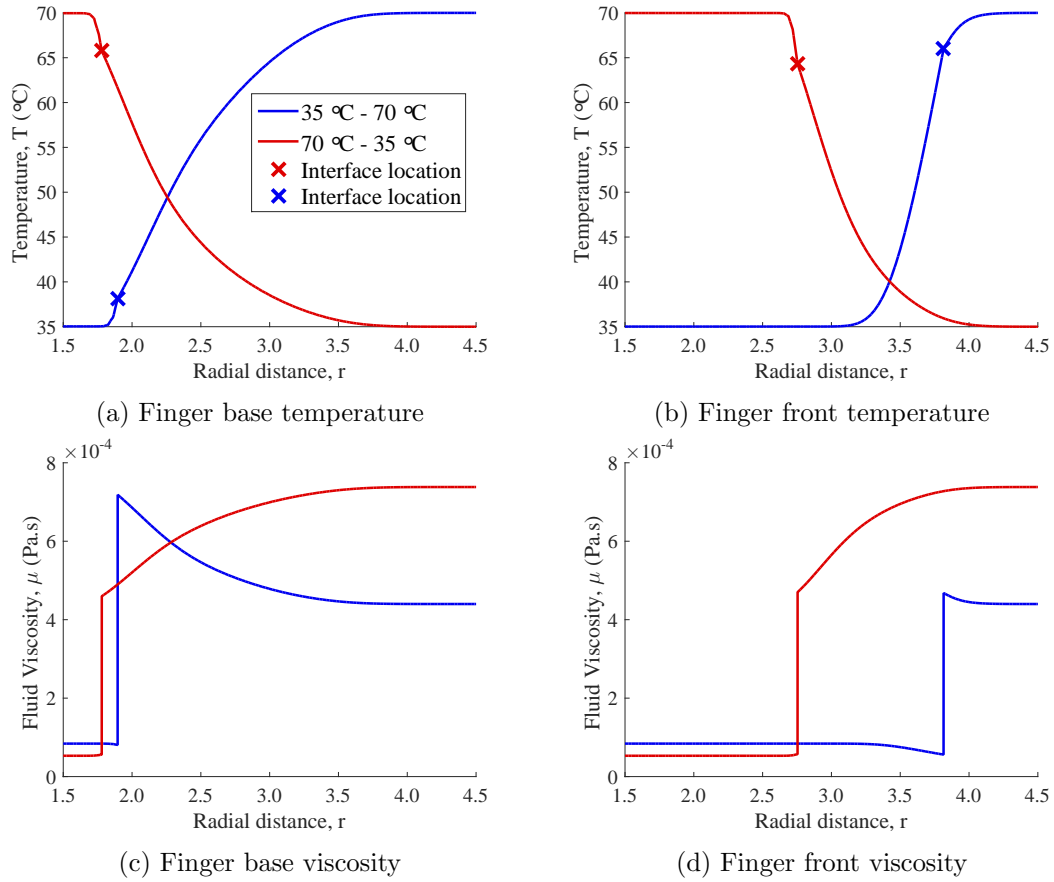


Figure 6.8: Temperature and viscosity profiles taken parallel to the finger front (along  $y = 0$ ) and base (along  $y = x \cdot \tan(\pi/8)$ ) at  $t = 30$ ,  $Q = 0.75 \text{ cm}^2/\text{s}$ . Legend for all plots shown in (a).

mobility ratio at the interface for the cold/hot injection regimes. As the temperature increases towards the interface for the cold injection case, the mobility ratio is increased due to the relative change in viscosity for the  $\text{CO}_2$  and brine. In contrast, the local mobility ratio is decreased for the hot injection case as the temperature drops at the interface.

In classical radial viscous fingering, as the mobility ratio is increased for a fixed global capillary number, the base should show more stagnation and perturb less into the domain. However, here the opposite effect is seen, where a more displaced finger base is observed in the cold injection case in comparison to the hot injection, with an associated *increase* in the local mobility ratio. Also, the hot injection cases all show near identical base movement to each other, even though the local mobility ratio (and capillary number) is changing. This indicates that the base movement in non-isothermal

regimes cannot be sufficiently described by only considering the *local* mobility ratio and capillary number, as is the case in isothermal displacements.

The increased base movement of the cold injection case in comparison to the hot injection case is due to the difference in homogeneous perturbed pressures. At the finger bases, the perturbed pressure gradient contributes only a small amount, with the primary movement being controlled by the homogeneous pressure gradient. At lower injection temperatures, the finger base homogeneous pressure gradient is larger (see Figure 6.5(d)), increasing the growth rate and displacement in comparison to hot injection cases.

In cases with equal injection temperatures (Figure 6.4(a) and (c)), the homogeneous pressure gradients are also equal. This means an increased base mobility in the  $35^\circ\text{C} - 50^\circ\text{C}$  and  $35^\circ\text{C} - 70^\circ\text{C}$  cases raises the growth rate and displaces the base further into the domain.

If the injection temperature is increased (Figure 6.4(b) and (d)), the homogeneous pressure gradient decreases. When this is coupled with a corresponding increase in mobility due to the higher temperature, very similar growth rates and base displacements are exhibited. The base movement in non-isothermal cases is therefore controlled mainly by the resident temperature; for equal resident temperatures the base movement is very similar and when the resident temperature is increased there is a corresponding increase in the growth rate and base displacement.

### 6.6.3 Thermo-viscous fingering with a continuous viscosity profile

To further explore the effect of hot/cold injection on the thermo-viscous fingering regime, immiscible displacement results are presented using injection and resident fluids with the same base viscosities,  $\bar{\mu}_1 = \bar{\mu}_2$  and the same dependence on the temperature field  $a_1 = a_2$ . This means that the viscosity profile is continuous across the immiscible interface, with variations coming purely from the continuous temperature field. There still exists surface tension between the fluids, but the effects of the thermal viscosity profile can be analysed independently from a discontinuous viscosity profile generated by the fluids.

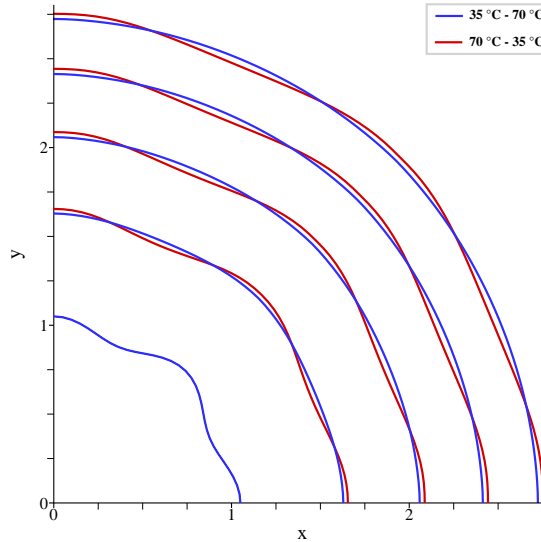
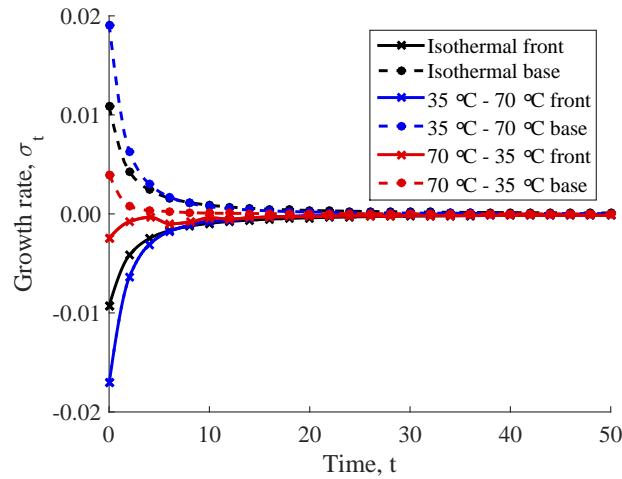


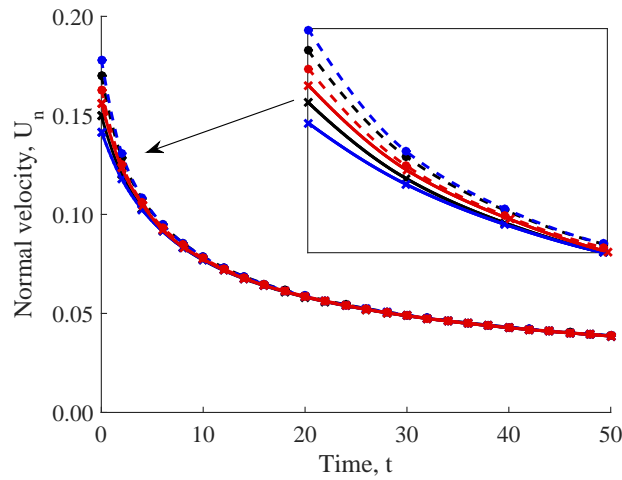
Figure 6.9: Interface plots at increments of  $\Delta t = 5$  from  $0 \leq t \leq 20$  for non-isothermal injection regimes using fluids with the same base viscosities and dependence on temperature.  $Q = 0.75 \text{ cm}^2/\text{s}$ .

In Figure 6.9, the interfacial displacement for the continuous viscosity profile regime can be seen for the different temperature cases. Here, the base viscosity and  $a_l$  values of brine are used at the corresponding injection temperatures for both fluids. The interfacial evolutions shows that the cold injection case quickly stabilises the initial perturbation and displaces as a circle. Without a discontinuous viscosity driving the growth of perturbations, the interface is stabilised by the surface tension and forms a circle. However, in the hot injection case the perturbation is not damped as significantly and appears to remain with a constant amplitude after  $t = 15$ . The perturbation amplitude changes initially on the first plots when  $t \leq 10$  but then seems to stabilise to a constant value afterwards.

The growth rate and velocity plots in Figure 6.10 show the short and long term behaviour of the different temperature regimes. Initially, the front of the cold injection case in Figure 6.10(a) experiences a smaller growth rate than the isothermal case, with the base experiencing a larger growth rate. This causes the interface to quickly stabilise whilst displacing to form a circle. However, the hot injection case exhibits a higher growth rate at the front and a lower growth rate at the base compared to the isothermal case, indicating that it maintains some of its initial perturbation and works against the surface tension to maintain the perturbed shape. With time, the growth rate of the fronts and bases for all cases drops to zero, and they evolve with equal velocity at the front and



(a)



(b)

Figure 6.10: Plots showing (a) Finger base and front growth rate with time. (b) Finger base and front normal velocity with time. Legend for both plots shown in (a).

base, shown in Figure 6.10(b). This means that the interfaces are simply convected with the shape they formed in the initial growth when  $0 \leq t \leq 10$ .

When the growth rate drops to zero in the hot injection case, there is still a contribution to the growth rate from the perturbed velocity; enough to maintain the perturbation amplitude. The source term velocity is larger at the finger base compared to the finger tip (since it is closer to the injection source), meaning the perturbed velocity component must be smaller at the base so that the total velocity is equal along the interface. If the perturbed velocity component was equal along the interface, or its sign reversed (as in the cold injection case), the interface would simply form a circle.

The non-isothermal temperature regimes when considered independently without a discontinuous viscosity profile are neutrally stable. The hot injection case is able to reduce the stabilisation effects from the surface tension around the interface, with some of the initial perturbation being maintained. However, the perturbation does not grow with time even at this high injection temperature, and the growth rate of the perturbation eventually falls to zero.

Thermal effects that vary the viscosity profile in a smooth manner act to promote or hinder the existing viscous fingering regime, but alone do not promote the onset of viscous fingering. This is exemplified in the previous section, where thermal effects enhanced the viscous fingering bifurcation in the hot cases and hindered the fingering in the cold cases. The stabilisation from the cold cases was never enough to completely hinder the finger growth, and once the temperature field had sufficiently diffused, the growth rate of features with similar curvatures tended to towards the same value.

#### 6.6.4 Thermal diffusivity effects

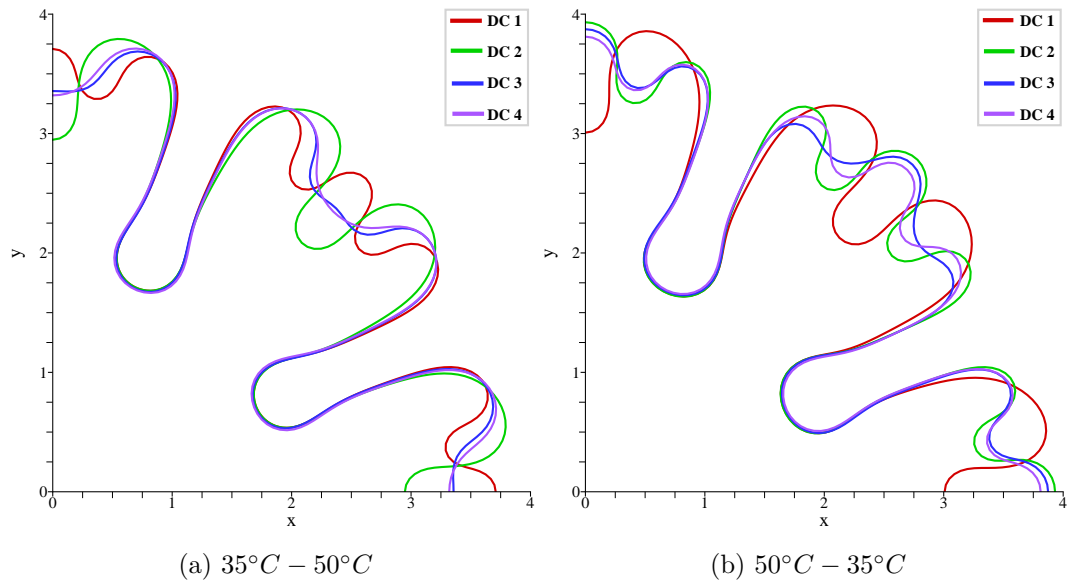
In this final section, the effect of thermal diffusivity on the thermo-viscous fingering problem is explored. Up until this point, the physical diffusivities of  $CO_2$  and brine have been used for all simulations. The diffusivity controls the sharpness of the mobility profile (affecting the acceleration/deceleration from the perturbed pressure) and the distribution of mobility around the interface controlling the bifurcation mode, meaning it is key to the entire thermo-viscous fingering process. Here, four diffusivity cases are presented using the  $50^\circ C - 35^\circ C$  and  $35^\circ C - 50^\circ C$  injection regime with  $Q = 0.75$ , summarised in table 6.4.  $\beta_d = D_1/D_2$  is the ratio of the diffusivities, and  $Pe = Q/D_1$  is the thermal Peclet number.

The fluid properties are equal between each diffusivity case for a given temperature regime, with only the diffusivity parameters varying. Diffusivity case 1 represents the base case with the physical  $CO_2$  and brine diffusivities. The diffusivities in each zone are swapped in diffusivity case 2, and in case 3 they are made equal representing a single-zone heat transfer problem. In case 4, the diffusivity is increased in each zone by a factor of 10 compared to case 1, to showcase a highly diffuse temperature field regime and its impact on the fingering morphology.

Diffusivity case (DC)	$D_1$ ( $cm^2/s$ )	$D_2$ ( $cm^2/s$ )	$\beta_d$	$Pe$
1	0.0005	0.0015	0.333	1500
2	0.0015	0.0005	3.000	500
3	0.0015	0.0015	1.000	500
4	0.0050	0.0150	0.333	150

Table 6.4: Thermal diffusivity cases with associated fluid properties.

The interfacial plots at  $t = 30$  for different diffusivity cases can be seen in Figure 6.11. In both temperature regimes, raising the inner diffusivity in cases 2, 3 and 4 has led to a change in the bifurcation mode compared to case 1. During cold injection, the bifurcation mode transitions to a two finger split, whereas in the hot injection case it transitions to a three finger split. As the resident temperature remains equal throughout all cases, the base positions have remained entirely unaffected by changing the diffusivity regime.

Figure 6.11: Interface plots at  $t = 30$  for hot and cold injection regimes with different diffusivity parameters.

When the thermal diffusivity is raised in both zones by a factor of 10 (compared to the base case) in DC4, the growth rates tend to that of the isothermal case, shown in Figure 6.12(a) and (b). In the early time frame, diffusivity cases 1, 2 and 3 (in which the diffusivities are in the same order of magnitude) show almost identical growth rates.

Diffusivity case 4 shows a very similar initial growth (and long term growth in the hot injection case) to the isothermal case, as the temperature (and hence mobility) field

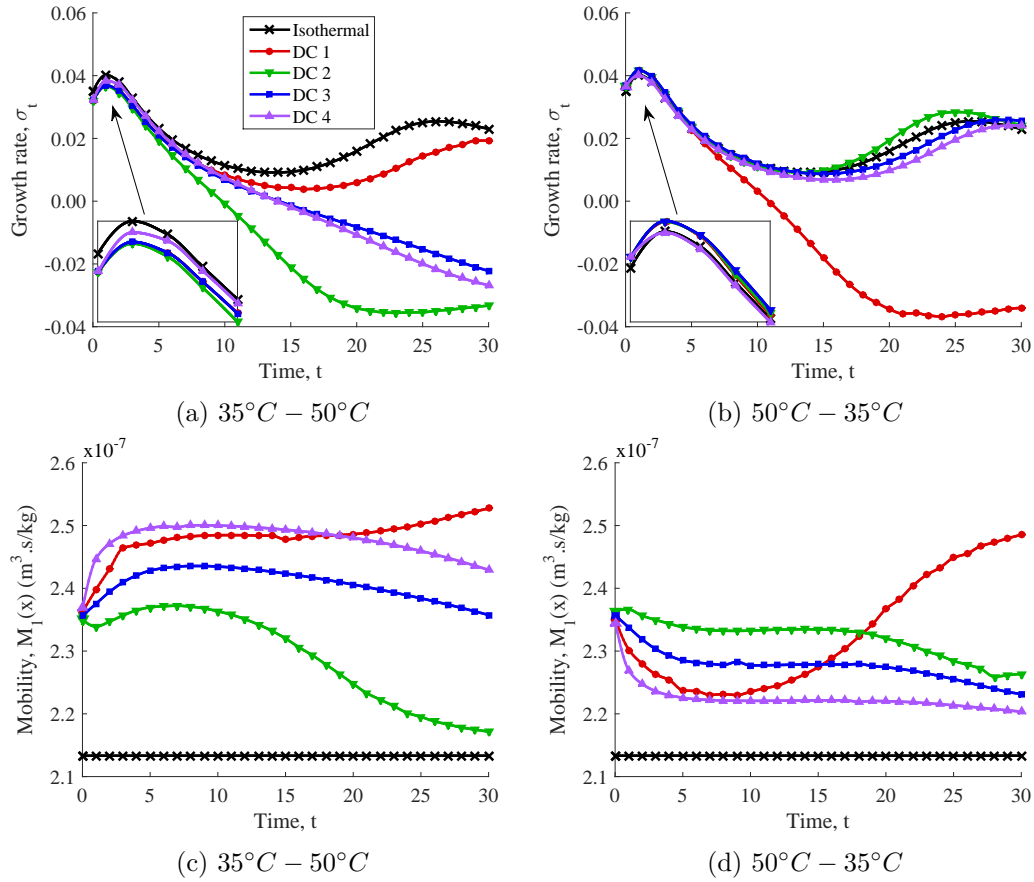


Figure 6.12: Timeseries plots of the growth rate and mobility at the finger fronts for the hot and cold injection regimes with different diffusivity parameters.  $Q = 0.75$ .

is highly diffuse causing only minor acceleration/deceleration effects with the induced perturbed pressure gradient. This is as expected, since the non-isothermal should tend towards the isothermal with highly diffuse temperature fields.

Although the growth rate is initially similar to the isothermal in the cold injection case DC4, after time the growth rate of the cold case drops, as the distribution of temperature in the domain causes the sides of the front to be accelerated more strongly than the tip. The temperature contours at the late stage show very little resemblance to the interfacial pattern, spreading radially from the injection source (see Figure 6.13(c)). Since the interface and the associated convective velocity field has little effect on the transport of the temperature field, the interface displaces with a radially diffusing temperature field, meaning the finger sides evolve in regions of higher mobility regions than the tip. This enhances the spreading mechanism and causing a two finger bifurcation. The reverse can be seen in Figure 6.13(d), where the finger sides in the hot injection cases evolve

into low mobility regions, promoting the growth of the finger tip and the three finger bifurcation.

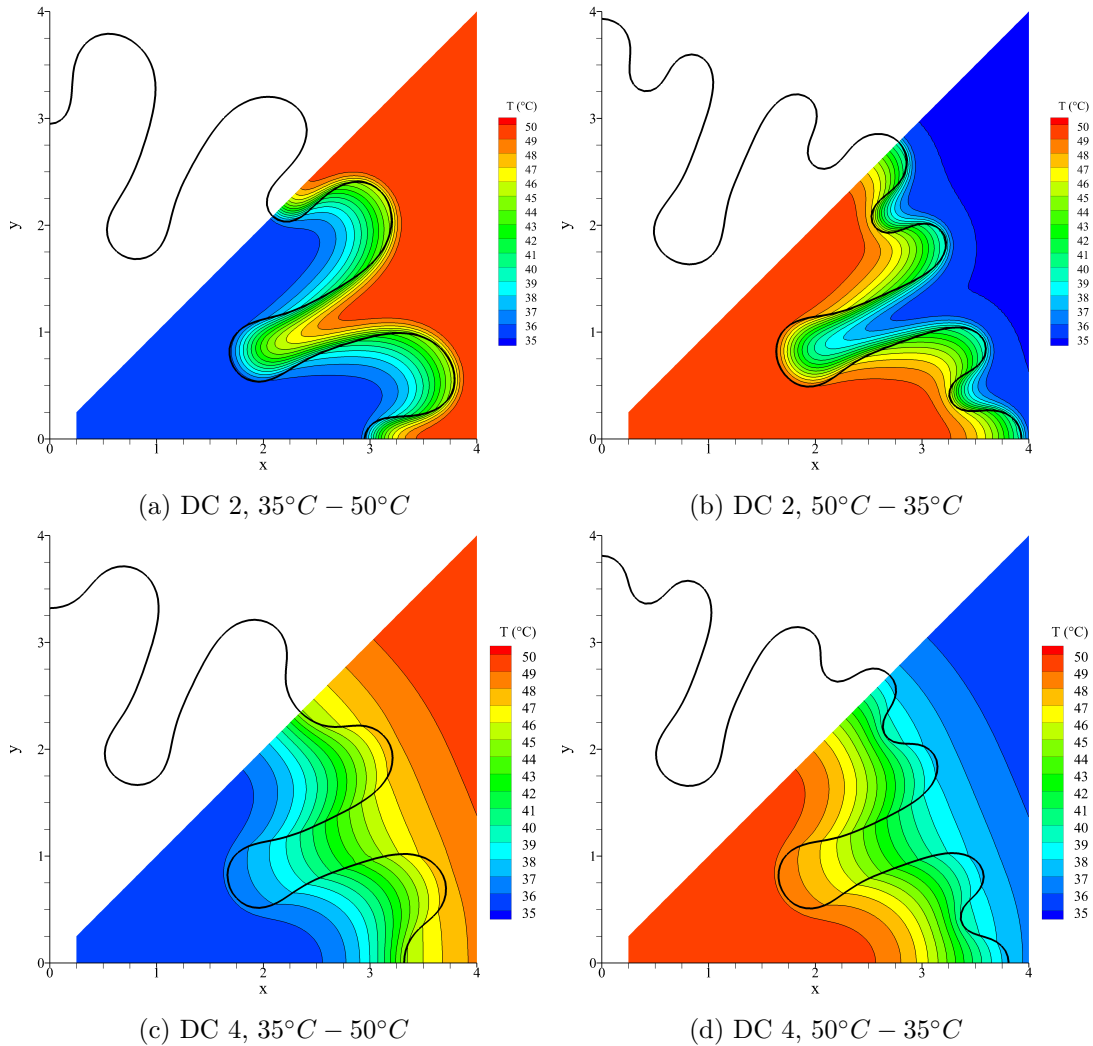


Figure 6.13: Temperature contour plots for diffusivity case 2 (top) and 4 (bottom) at  $t = 30$ . The thick black lines show the interface, with thin black lines representing contour lines.  $Q = 0.75$ .

The same mechanism also controls the bifurcation mode in diffusivity case 2 and 3, in which the increased diffusivity in the inner zone promotes heat transfer. Figure 6.13(a) and (b) show the diffuse inner regions for diffusivity case 2 at the two temperature regimes (note that very similar plots are obtained for diffusivity case 3, with a greater spacing between contour lines in zone 2). In the hot injection case, the temperature contours of the diffuse inner region follow the interface less closely in comparison to case 1, meaning that regions of the interface closer to the injection source displace with

a higher temperature and mobility. This causes the tip to be accelerated and the interface bifurcates into three fingers.

In contrast, the cold injection case with reversed diffusivities has a colder region near the injection source that propagates radially outwards (when the diffusivity is raised). This means the finger tips are closer to the low temperature source when the finger initially spreads and are decelerated in comparison to the finger sides, forming the two finger bifurcation. The bifurcation mode switches in the high inner diffusivity cases here as the temperature field less closely resembles the interface, instead propagating radially outwards from the source temperature, following a more circular evolution that produces non-uniformity around the interface.

Two effects are caused by the changing diffusivity, firstly, by raising the inner diffusivity (and lowering the Peclet number) the bifurcation mode is altered by forcing the temperature field to evolve in a more circular, radial fashion less closely resembling the interfacial pattern. This creates non-uniformities in the mobility field that don't match the interfacial advection, causing the bifurcation mode to switch from that given by the high Peclet number cases. Secondly, by changing the diffusivity ratio, the interfacial temperature can be raised/lowered without changing the bifurcation mode, instead changing the growth rate. In hot injection cases, by decreasing  $\beta_d$ , heat transfer is promoted in the outer zone and the temperature at the interface is lowered, delaying the three finger interfacial growth. In cold cases, decreasing  $\beta_d$  also enhances heat transfer in the outer region, but when coupled with the reversed temperature gradient, this increases the front temperature and hinders the two finger growth.

By lowering the thermal Peclet number, effects similar to those presented in [152] and [154] for miscible regimes are seen. By lowering the thermal Peclet number, the destabilising effects of a hot injection regime are reduced and the stabilising effects of the cold injection regime are reduced. [152] and [154] also generate similar results with the inclusion of thermal lag, which acts to slow the convective velocity in the heat transfer compared to that in the solutal regime. As well as changing the location of the thermal front, this also effectively reduces the thermal Peclet number, with very similar qualitative results to those presented here. These miscible results are discussed to provide some comparison to previous works in the area of thermo-viscous fingering, but

it must be noted that although qualitatively similar, the mechanism for their formation are entirely different.

## 6.7 Conclusion

In this final results chapter, the thermo-viscous fingering problem was investigated during the displacement of immiscible fluids using a high resolution BE-RBF-FC method. The numerical method utilised mesh reduction techniques to solve the coupled heat transfer and Darcy flow problem in an accurate and efficient manner. These new methods allowed the solution to moving multi-zone problems without extrapolation, utilising the truly meshless nature of the RBF-FC method to its full extent. The physical mechanisms that control the immiscible thermo-viscous fingering regime were investigated in a systemic manner, leading to the follow system behaviour:

- In high Peclet number flows, the early stage growth rate is governed by the pressure gradient at the interface. For hot injection cases, the magnitude of the pressure gradient is increased, due to an additive perturbed pressure gradient from the decreasing mobility field. When combined with an increased mobility, this enhances the growth rate. In cold injection cases, the growth rate is hindered due to a subtractive perturbed pressure gradient resulting from an increasing mobility field.
- The late stage bifurcation regime is controlled primarily by the mobility distribution around the interface. When the mobility decreases towards the finger tip, a two finger bifurcation is promoted, whereas when the mobility increases towards the tip a three finger bifurcation can be achieved if the injection flux is high enough.
- The diffusivity and diffusivity ratio control the mobility distribution around the interface. When the inner diffusivity is increased, the temperature field more closely resembles radial diffusion from a point source, which promotes two finger bifurcation in cold injection regimes and three finger bifurcations in hot regimes. By increasing the diffusivity ratio, the temperature and mobility are increased at the interface for hot injections, and decreased for cold injections.

- Finger base displacement is controlled by the resident fluid temperature. When the resident temperature is increased for a given flow rate, the finger base growth increases. For a fixed resident temperature with varying injection temperature, the base growth rates are equal.
- Thermal effects in the fingering evolution are neutrally stable. They act to enhance or inhibit existing perturbations that grow due to the fluids' homogeneous viscosity contrast. However, thermal effects are not enough alone to grow perturbations or cause a fingering instability without an existing viscosity contrast. Thermal effects diminish with time as the temperature field diffuses, with classical viscous fingering dynamics eventually overcoming any stabilisation from a smoothly decreasing mobility field.

The early stage mechanisms in thermo-viscous fingering are very similar to those in the uniformly converging/diverging cell cases presented in chapter 5. However, in the present chapter, the mobility field diffuses with time, meaning that aperture effect 3 diminishes. This is not the case in the uniformly converging/diverging cell, in which the mobility variation remains the same throughout the simulation. The early stage spreading mechanism found in the thermo-viscous cases here would be similarly enhanced/inhibited in rectilinear flows, since the inhomogeneous mobility here comes from the temperature field which follows the fingering evolution, not the profile of the cell itself.

With the findings presented in this chapter, careful variation of the fluid parameters and initial conditions could control the thermo-viscous fingering instability in a predictable manner, creating alternative bifurcation modes that cannot be predicted using classical viscous fingering theory at corresponding isothermal temperatures. This study represents the first of its kind in identifying the key mechanisms behind immiscible thermo-viscous fingering and hopes to provide a baseline for future research.

## 7. Conclusions & future work

### 7.1 Conclusions

In this work, the viscous fingering instability of immiscible displacement in Hele-Shaw cells has been explored numerically using several newly developed numerical methods. The methods were used to analyse the fingering regimes that could occur under conditions typical of  $CO_2$  injection and storage processes, i.e. with low mobility ratios, high capillary numbers, inhomogeneous mobilities and transient temperature fields.

The main novelty in this thesis lies in the development of the numerical methods that have allowed the late-stage exploration of the viscous fingering regime and associated non-linear finger interactions. Through systematic numerical experimentation, several key features of the immiscible fingering regime were revealed under the conditions mentioned above, which had not been reported before. This detailed analysis will increase the overall understanding of the late stage fingering mechanisms, and the processes governing the immiscible displacement of subsurface  $CO_2$  and brine.

To investigate the homogeneous, low mobility ratio regime, a boundary element method was implemented for the solution of the Laplace equation in a Hele-Shaw cell (possible with a constant plate separation  $b$  and a constant viscosity in each region  $\mu$ ). By non-dimensionalising the governing system of equations, the homogeneous problem was found to rely purely on the capillary number and mobility ratio of the fluids. Using a cubic B-spline boundary element scheme, the resulting integral equation involved the evaluation of a hypersingular integral which was performed semi-analytically in the sense of Hadamard finite parts. This, along with a 4<sup>th</sup> order Lagrangian approximation for the curvature allowed the accurate solution to the quasi-static pressure field and the normal interface velocity. A convergent series approach was used to solve the system of

equations with a solution time that scaled quadratically with the number of boundary elements instead of the cubic dependence found with traditional LU matrix solvers. This lifted the restriction of previous models on short time scale solutions.

Results in low mobility ratio regimes revealed significant differences with those predicted with previous high or infinite mobility ratio models. Finger base movement is much more prominent in low mobility ratio flows, resulting in generally more stable interfaces. Due to the non-negligible inner viscosity, secondary and side branching fingers can displace significantly into the domain, and aren't shielded by primary fingers as in high mobility ratio flows. This leads to the formation of more fingers in the domain, and much greater interaction. Raising the global capillary number was found to generally increase the number of fingers produced on bifurcation, but also lead to an increase in the number of side branching fingers.

Long time interface evolutions were run to showcase the BEM for predicting the large time scale dynamics of viscous fingering with homogeneous mobility. Using asymmetric initial interfaces, the increased finger interaction due to the low mobility ratio regime could lead to base thinning and eventual finger breaking. In very high mobility ratio flows, this did not occur, since the primary fingers shield the growth of secondary fingers meaning the interaction is insignificant. Due to the accuracy of the numerical method and explicit interface tracking scheme, the immiscible lubrication layer between competing fingers could be resolved to much greater detail than in previous models. This allowed finger breaking to be explored more explicitly than before, showing that in a sharp interface model, finger break-off should always occur in preference to coalescence since no fluid-fluid miscibility exists.

Using a Picard iteration scheme with relaxation factor, dynamic wetting could be incorporated into the boundary element method. The trailing wetting layer in the cell introduced a local capillary number term in the capillary pressure jump at the interface between the fluids, which was handled numerically using a Picard iteration scheme. At high capillary numbers the wetting layer is thickest, and could suppress the onset of viscous fingering and dramatically alter the bifurcation mode. The classical viscous fingering regime could never be fully suppressed since the wetting layer thickness reduced with time along with the interfacial velocity, however at high initial capillary numbers the bifurcation regime late in time could still be altered. In high mobility ratio flows,

finger shielding was also somewhat suppressed, since the primary growing fingers were stabilised and their velocity reduced. This allowed secondary and side branching fingers to be fed with more fluid and displace further into the domain, increasing the number of fingers present.

In order to explore the viscous fingering regimes that could occur with an inhomogeneous mobility, i.e. due to a varying cell permeability or viscosity present in  $CO_2$  injection problems, a meshless radial basis function-finite collocation method was developed for the general solution of moving multi-zone transport problems. The method was developed for use with an adaptive quadtree dataset that clustered nodal points around the interface. Local RBF-FC stencil configuration testing was performed on a steady-state boundary layer problem to identify the most robust stencil configuration and optimal PDE centre location. Further testing on the infinite Peclet number advection of a Gaussian packet identified the base 1-1 local stencil configuration as the most optimal to accurately reconstruct the PDE source term  $\hat{L}[\phi^n]$  at the end of each time step. The new method showed significant reductions in nodal points (17x less in some cases) compared to uniform dataset counterparts, achieving similar levels of global accuracy.

The adaptive RBF-FC scheme was then tested on several multi-zone problems using two new multi-zone formulations. The embedded method, in which the interface matching conditions appear at the global level was found to be more robust and accurate when solving steady-state and static interface problems, due to the more accurate representation of the governing PDE at the interface. The auxiliary method, in which the matching conditions appear locally in the RBF systems was found to perform significantly better for moving interface problems than the embedded method. The auxiliary method was verified against a moving multi-zone convection diffusion problem with a uniform fluid and interface velocity. Here, it demonstrated highly accurate solution profiles compared to a high resolution finite difference scheme solving the transformed static problem. Using a fraction of the nodal points it could accurately capture the discontinuous solution profile and high Peclet number flow as the interface moved through the domain.

The developed RBF-FC method was coupled with the BEM for the solution of inhomogeneous mobility flows arising from a spatially varying plate separation (and therefore intrinsic permeability) in chapter 5. The onset and late stage fingering

instabilities were examined under various cell geometries, revealing the key mechanisms behind the stability of the interface in variable permeability cases. Three aperture effects were identified that control the interfacial stability, for converging cells (decreasing permeability) these were:

1. Stabilisation through an increased transverse curvature.
2. Deceleration due to a reduced fluid mobility.
3. Acceleration due to an increased pressure gradient.

In diverging cases, the effects were reversed. At low capillary numbers, effect 1 and 2 dominate, stabilising the interface in converging cases and destabilising in diverging cases. At higher capillary numbers, the result of the combined effects reverse, and converging cells destabilise the interface in comparison to uniform cells, with diverging cases being more stable. The transition point at which the combined aperture effect result reverses was identified with the initial state numerical growth rate as  $Ca_g \approx 640$  for uniformly converging and diverging cells.

This analysis provided a useful bridge between the linear stability analyses (generally low capillary number) results in several works and the high capillary number results found experimentally in earlier works. The systematic numerical exploration of the problem allowed the transition to be identified and the mechanism behind the stability described. The mechanisms also explain the difference between uniformly varying radial and rectilinear cells, in which finger spreading or sharpening can be found depending on the aperture gradient.

Although the aperture effects were identified in uniformly converging/diverging cell simulations, the effects were also be found locally in more ‘random’ geometries controlling the overall interfacial evolution. In anisotropic cases at high capillary numbers, aperture effect 2 was found to become prominent as the finger evolution was dominated by local variations in the fluid mobility. The highly anisotropic cases demonstrated the robustness of the numerical scheme and the fingering complexity and richness that can be achieved with relatively small changes in the cell plate separation and permeability.

In the final results chapter 6, the fluid viscosity was allowed to vary spatially with a transient temperature field, inducing thermo-viscous fingering effects during the

displacement of the immiscible fluids. To this end, the transient moving multi-zone heat transfer problem was solved with the auxiliary multi-zone method to accurately reconstruct the viscosity field. The viscosity field could then be used to calculate the inhomogeneous mobility and the pressure/velocity could be solved as before using the BEM with the embedded RBF-FC method. The heat transfer and pressure/velocity solutions were coupled through the viscosity field, with the transient heat transfer evolving in a semi-implicit manner due to the quasi-static nature of the pressure field.

Systematic numerical exploration of the thermo-viscous fingering problem space identified several key parameters in predicting the fingering process from early to late stage evolution. During the early stages of finger growth, when the thermal Peclet number is high and defined fingers have yet to form, the process is controlled by the pressure gradient normal to the interface. This is in essence the same mechanism as aperture effect 3 identified in the permeability study. In hot injection regimes (high temperature fluid injected into a colder fluid), the magnitude of the pressure gradient was increased in comparison to isothermal cases at the same interfacial temperature. The increased pressure gradient causes acceleration of the interface, and promotes the onset of viscous fingering. Cold injection regimes caused a corresponding deceleration of the interface and an increase in the interfacial stability.

During the late stage of finger growth, the bifurcation mode was affected primarily by the interfacial distribution of mobility, which could be controlled by the thermal Peclet number of the inner fluid and the diffusivity ratio. Careful variation of these parameters could promote non-uniformity in the mobility distribution and lead to alternative bifurcation modes that cannot be predicted using classical viscous fingering theory at corresponding isothermal temperatures. The study of immiscible thermo-viscous fingering in chapter 6 represents a first step in identifying the key mechanisms behind immiscible thermo-viscous fingering that have yet to be explored in the literature.

In conclusion, this thesis provides a detailed analysis of several key mechanisms that control the immiscible viscous fingering process under flow regimes that have been previously unexplored. These flow regimes are encountered in several industrial processes, such as  $CO_2$  sequestration, and through increased understanding of the inherent fingering mechanisms these processes can be made more efficient and more reliably predicted. Efficient numerical methods were developed to allow exploration

into the late stage fingering processes that have been previously unattainable, providing insight into the governing mechanisms behind the viscous fingering instability.

As well as increased understanding of the complex nature of the viscous fingering instability, the numerical methods presented in this thesis also demonstrate significant advances in mesh-reduction and meshless techniques. These techniques have been developed generally, and can be applied to many other moving multi-zone transport problems found in natural and industrial flows, e.g. Stefan type problems or dendritic solidification. The adaptive RBF-FC method with auxiliary multi-zone representation has showcased highly desirable properties for the cases presented in this work, which when extended to parallel computing could make it a very useful tool for large scale transport problems.

## **7.2 Future work**

During the course of this work, it became apparent that there were several related areas of research and extensions to the current methods that were worthy of study. However, due to time constraints, not all of these areas could be investigated. This section highlights extensions and possible new research directions for the current work, based on developments of the numerical methods and the original mathematical models.

### **7.2.1 Parallelisation**

One of the most useful extensions to the current work would be the development of the numerical methods for parallel computing architectures. This would allow much larger datasets to be considered, and the non-linear stages of thermo-viscous finger growth to be investigated at later time stages with asymmetric initial conditions. Currently, the BEM and RBF-FC method have been tested on multi-cored workstations and shared-memory high performance computing architectures working on up to 16 computational cores. The base of the work in this thesis was performed on one/two cores with corresponding datasets that allowed analysis within a short time frame ( $< 1$  week). The OpenMP interface was tested for larger implementations that allowed up to 16 shared memory

cores to be used, however there was significant time spent passing data between cores which limited the scalability of the problem.

An alternative to the OpenMP interface, is the message passing interface (MPI). This is a standard message passing system and can work on distributed memory architectures, i.e. on high performance computing architecture with 100s of computational cores. Implementation of MPI directives requires significant alteration to the current code, with many features having to be re-designed to run efficiently. However, the RBF-FC method has the potential to be highly scalable; since a significant proportion of the computational time is spent on forming and factorising the small local systems, these could be distributed over many cores, with the calculation occurring in parallel.

Similarly, the sparse global matrix system (formed from the reconstruction of the centrepoint solution of each local system) could be solved using a standard direct sparse solver that has been explicitly developed for parallel computation, i.e. MUMPS [159]. The solution of the sparse global system only requires double precision, unlike the local systems (see [115]), and hence could make use of these standardised solvers that have been developed specifically for parallel computation.

The boundary element formulation makes use of a convergent series approach to reduce the computation down from a cubic scaling (i.e. solution time  $\propto N^3$ ) as in standard LU solvers to a quadratic scaling. The boundary element method when used solely (as in chapters 2 and 3) can therefore solve large datasets and run for significant periods of time. However, for very large implementations, the forming of the system (which takes  $N^2$  operations) can bottleneck the solution time. Also, when evaluating domain field variables (for example the velocity field in the heat transfer formulation), a large number of domain points  $N_i$  can significantly slow down the solution time, requiring  $N_i N$  operations.

An alternative fast multipole method (FMM) could be used, to reduce the computational time to  $O(N)$  [160]. Here multipole expansions of the original integral equation are employed, which effectively decouple the  $x, y$  collocation and field points [160]. Quadtree data cells are employed to cluster over the boundary elements, with the centroids being used to calculate the integrals on the locally expanded points. With appropriate translations, the original integral for a collocation point can then be calculated using

the integrals from the cells. Since the cell moments and integrals are only computed once, significant computation time is saved since each collocation point can use the same moments and integrals with simple translations. The FMM requires an iterative matrix solver (such as GMRES), which can be implemented in parallel on a computing cluster. Also, since the quadtree data structure already exists in the current formulation, it could be used for both the RBF-FC method and the FMM here.

With the  $O(N)$  scaling of the FMM, the solution time of the boundary element method could be significantly reduced and scaled to many cores (see for example [161]). The domain evaluation of the field variables from the BEM also use a significant amount of CPU time, and can sometimes bottleneck the solution (as in chapters 5 and 6 when evaluating the homogeneous pressure gradient). The FMM could significantly speed up the evaluation of domain field variables, which when implemented over several cores could dramatically reduce the overall time spent evaluating domain field variables.

Parallel implementation of both the BEM and RBF-FC method as described above could significantly increase the problem sizes that could be analysed. This would, for example, allow asymmetric problems to be considered in chapters 5 and 6, which could illustrate the effects of an inhomogeneous mobility on multiple finger modes simultaneously.

### 7.2.2 Interface capturing

The current boundary element method explicitly tracks the interface with a cubic B-spline representation. The interface has to be updated at each time step and re-meshed to maintain a consistent nodal arrangement, which can be difficult when the mesh is highly deformed or breaking/coalescence occurs. The boundary element method is very effective for the potential problems here, where there is a known fundamental solution. However, for more complex problems this is not always the case, meaning interface tracking is not always possible.

The RBF-FC method could be adapted for use in an interface capture scheme with level set or volume of fluid method implementations. Here, an indicator function is used to represent the interface in a continuous fashion, with a single value (usually 0.5 for VOF, or 0 for level set methods) representing the explicit interface. The indicator function is updated at each time step through the solution of an advection equation

(similar to that solved in the Gaussian advection problem in chapter 4). Since the function is continuous, it is easier to represent interfaces without complex re-meshing, and breaking/coalescence events are much easier to model. Also, the underlying PDE governing the advection velocity can be arbitrarily complex since there is no dependence on the existence of a fundamental solution (as in the BEM).

The RBF-FC method has proved very effective at solving pure advection (infinite Peclet number) problems in chapter 4, and with the contour extraction method could be used effectively to capture the interface in a level set or volume of fluid approach. Although global RBF implementations for interface capturing have been shown to be effective [84], local implementations could alleviate dataset size and ill-conditioning limitations. The RBF-FC method could then be used as a single tool for moving interface problems, solving both species transport and the interface advection, enabling the solution to more general moving interface problems with a variety of underlying PDEs, such as the Stefan problem or dendritic solidification.

### 7.2.3 Marangoni & other temperature effects

A natural extension to the problems addressed in chapter 6 are the inclusion of Marangoni effects and thermocapillarity. In [162] thermocapillarity was included in the potential flow model, using the temperature field to vary the surface tension around the interface in a point-wise manner. This significantly altered the interfacial evolution, with changes in the surface tension causing similar effects to point-wise changes in the plate separation  $b(x)$ . This used a simple single-zone model for the heat transfer which could be improved using the multi-zone formulation in this thesis. However, to include the full surface tension variation effects, the tangential derivative of the surface tension should induce movement, as in the Marangoni instability [144, 145]. The surface tension therefore requires a shear stress matching condition on the interface, i.e.:

$$\sigma_{ij}^1(\boldsymbol{\xi})s_i n_j - \sigma_{ij}^2(\boldsymbol{\xi})s_i n_j = -\frac{\partial \gamma(\boldsymbol{\xi})}{\partial s} \quad (7.1)$$

Where,  $\sigma^l(\boldsymbol{\xi})$  represents the stress tensor from region  $l$  at the interface, and  $\gamma(\boldsymbol{\xi})$  is the surface tension.  $s$  is the tangential vector along the interface and  $\partial/\partial s$  represents the tangential derivative along the interface. The normal stress balance must also be met

at the interface:

$$\sigma_{ij}^1(\boldsymbol{\xi})n_in_j - \sigma_{ij}^2(\boldsymbol{\xi})n_in_j = \gamma(\boldsymbol{\xi})k(\boldsymbol{\xi}) \quad (7.2)$$

Here,  $k$  is the interface curvature (both in and out of plane). The stress tensor has Cartesian components given by:

$$\sigma_{ij}(\boldsymbol{x}) = -P(\boldsymbol{x})\delta_{ij} + \mu \left( \frac{\partial u_i(\boldsymbol{x})}{\partial x_j} + \frac{\partial u_j(\boldsymbol{x})}{\partial x_i} \right) \quad (7.3)$$

In equation (7.3)  $P$  is the pressure,  $u_i$  the fluid velocity and  $\delta_{ij}$  the Kronecker delta function. As well as dynamic matching conditions, kinematic conditions are also required, enforcing continuity of normal and tangential velocity:

$$u_i^1 n_i = u_i^2 n_i \quad (7.4)$$

$$u_i^1 s_i = u_i^2 s_i \quad (7.5)$$

In order to incorporate the stress balance and kinematic matching conditions into the mathematical formulation, a Stokes based model must now be employed rather than the potential flow model from before. The stokes model takes the form:

$$\mu^l \frac{\partial^2 u_i^l(\boldsymbol{x})}{\partial x_j \partial x_j} = \frac{\partial P^l(\boldsymbol{x})}{\partial x_i} \quad \boldsymbol{x} \in \Omega_l, \quad l = 1, 2 \quad (7.6)$$

$$\frac{\partial u_i(\boldsymbol{x})}{\partial x_i} = 0 \quad (7.7)$$

The 3D stokes model with corresponding stress matching conditions (equation 7.1 and 7.2) at the interface, and suitable inlet and far field boundary conditions represents a closed second-kind boundary value problem that can be solved with a variety of numerical methods. With the calculated velocity, a quasi-static approach can be used to calculate the movement of the interface, equating the normal displacement of the interface in time to the normal interface fluid velocity.

To solve the above problem, a boundary integral approach could be used in a similar fashion to that developed for the potential flow problem. The Stokes velocity has the following Green's integral representation at a point  $\boldsymbol{x}$  in a closed domain [29]:

$$c(\boldsymbol{x})u_i(\boldsymbol{x}) - \int_s K_{ij}(\boldsymbol{x}, \boldsymbol{y})dS_y + \int_s u_i^j(\boldsymbol{x}, \boldsymbol{y})f_j = 0 \quad (7.8)$$

The constant  $c$  varies depending on the position of the source point ( $c = 1/2$  when on the interface). The surface tractions  $f_i$  are given by  $f_i = \sigma_{ij}n_j$ . The kernels in the above equation are given by the fundamental solutions to the Stokes equations; the stokeslet and stresslet:

$$u_i^j(\mathbf{x}, \mathbf{y}) = -\frac{1}{8\pi} \left[ \left( \frac{\delta_{ij}}{r} \right) + \frac{(x_i - y_i)(x_j - y_j)}{R^3} \right] \quad (7.9)$$

$$K_{ij}(\mathbf{x}, \mathbf{y}) = -\frac{3}{4\pi} \frac{(x_i - y_i)(x_j - y_j)(x_k - y_k)n_k(\mathbf{y})}{R^5} \quad (7.10)$$

$R$  is the distance between a collocation point  $\mathbf{x}$  and field point  $\mathbf{y}$ . The Green's representation for the Stokes velocity can be projected in the normal and tangential direction at the interface, in a similar manner as in [163], in which they use the formulation to apply a slip boundary condition. Applying the normal and tangential stress matching conditions at the interface as well as the kinematic condition (in a similar way to chapter 2), two integral equations could be formed for the solution of the Stokes problem. The numerical solution of the coupled system of equations would allow the velocity to be calculated everywhere in the 3D domain.

An alternative approach to resolve the shear and normal stress at the interface is through the use of a depth-averaged Brinkman model [164, 165]. In this approach, the same averaging across the cell separation is done as in chapter 2, but  $2^{nd}$  order terms ( $\delta^2$ ) are kept in the formulation. This results in the 2D Brinkman system of equations for the average velocity  $\bar{u}_i$ :

$$\mu^l \frac{\partial^2 \bar{u}_i^l(\mathbf{x})}{\partial x_j \partial x_j} + \frac{12\mu^l}{b^2} \bar{u}_i^l(\mathbf{x}) = \frac{\partial P^l(\mathbf{x})}{\partial x_i} \quad \mathbf{x} \in \Omega_l, \quad l = 1, 2 \quad (7.11)$$

$$\frac{\partial \bar{u}_i(\mathbf{x})}{\partial x_i} = 0 \quad (7.12)$$

Here, the system behaves as the Stokes system when the permeability (proportional to  $b^2$ ) is high, and the Darcy system when the permeability is low. A boundary integral formulation can be used in a similar fashion to the Stokes system above, with changes in the fundamental solution to reproduce the specific behaviour of the Brinkman solution [166]. The stress and kinematic conditions at the interface would be identical to those in the Stokes problem. It is worth noting that the singularities in the Stokes and Brinkman boundary integral equations would be of no greater order than those present in the

potential flow integral equation in this thesis (hypersingular), meaning similar evaluation techniques could be readily employed.

Brinkman flow has been applied to several Hele-Shaw problems, showing considerable agreement with the 3D Stokes solution when considering Marangoni type flows [165]. Using a Brinkman approach to the problems considered in this thesis would allow Marangoni instabilities to also be explored alongside viscous instabilities. These two interfacial instabilities can occur in parallel in many physical situations, especially  $CO_2$ -brine displacements where the temperature at the interface between the two fluids could vary quite significantly. The temperature field could be evaluated with the heat transfer model in chapter 6, in which the RBF-FC method could be used to calculate the point-wise and tangential derivatives of the temperature/surface tension. The full numerical simulation could provide insight into the long term interaction between Marangoni and viscous instabilities, and further understanding in the governing fingering mechanisms.

The Brinkman and Stokes flow models could also be used to evaluate the contribution of the tangential stress when considering uniform surface tension flows without temperature effects. The potential flow model used in this work does not evaluate the contribution of viscous stresses, but at larger values of  $\delta$  (approaching the high wavenumber limit) and  $Ca$ , viscous stresses can become the same order of magnitude as the pressure and the potential flow approximation may break down [167]. Recently, work from [167] has shown that a linear stability analysis using a Brinkman model for the flow in radial viscous fingering can provide a better agreement with experimental results for predicting the maximum wave number criteria at high capillary numbers. Although the limit for small capillary numbers agrees well with both potential and viscous potential models, investigating the non-linear stages of finger interaction using the Brinkman model would be a fundamentally important study. [167] state that a numerical simulation may provide a useful tool for analysing the full non-linear problem, which could be tackled in the way presented above.

# Bibliography

- [1] G.M. Homsy. Viscous fingering in porous media. *Annual Review of Fluid Mechanics*, 19:271–311, 1987.
- [2] A. Shafiei and M.B. Dusseault. Geomechanics of thermal viscous oil production in sandstones. *Journal of Petroleum Science and Engineering*, 103:121 – 139, 2013.
- [3] S.J. Zarrouk A. McDowell and R. Clarke. Modelling viscous fingering during reinjection in geothermal reservoirs. In *Proceedings World Geothermal Congress 2015*, Melbourne, Australia, 2015.
- [4] Y. Wang, C. Zhang, N. Wei, M. Oostrom, T.W. Wietsma, X. Li, and A. Bonneville. Experimental study of crossover from capillary to viscous fingering for supercritical  $CO_2$  - water displacement in a homogeneous pore network. *Environmental Science and Technology*, 47:212 – 218, 2013.
- [5] D. Pritchard. The instability of thermal and fluid fronts during radial injection in a porous medium. *Journal of Fluid Mechanics*, 508:133 – 163, 2004.
- [6] G. Lovoll, Y. Meheust, K.J. Maloy, E. Aker, and J. Schmittbuhl. Competition of gravity, capillary and viscous forces during drainage in a two-dimensional porous medium, a pore scale study. *Energy*, 30:861 – 872, 2005.
- [7] R. Lenormand, E. Touboul, and C. Zarcone. Numerical models and experiments on immiscible displacements in porous media. *Journal of Fluids Mechanics*, 189: 165 – 187, 1988.
- [8] K.E. Holloway and J.R. de Bruyn. Viscous fingering with a single fluid. *Canadian Journal of Physics*, 83:551 – 564, 2005.
- [9] S. Holloway. Storage of fossil fuel-derived carbon dioxide beneath the surface of the earth. *Annual Review of Energy and the Environment*, 26:145 – 166, 2001.
- [10] J.E. Garcia and K. Pruess. Flow instabilities during injection of  $CO_2$  into saline aquifers. In *TOUGH symposium 2003*, Lawrence Berkeley National Laboratory, Berkeley, California, May 2003.
- [11] J.W. Johnson, J.J. Nitao, and K.G. Knauss. Reactive transport modelling of  $CO_2$  storage in saline aquifers to elucidate fundamental processes, trapping mechanisms and sequestration partitioning. *Geological Society, London, Special Publications*, 233:107 – 128, 2004.
- [12] V. Vilarrasa, S. Olivella, J. Carrera, and J. Rutqvist. Long term impacts of cold  $CO_2$  injection on the caprock integrity. *International Journal of Greenhouse Gas Control*, 24:1 – 13, 2014.

- [13] R.C Bissell, D.W. Vasco, M. Atbi, M. Hamdani, M. Okwelegbe, and M.H. Goldwater. A full field simulation of the In Salah gas production and  $CO_2$  storage project using a coupled geo-mechanical and thermal fluid flow simulator. *Energy Procedia*, 4:3290 – 3297, 2011.
- [14] H. Liu, Z. Hou, P. Were, X. Sun, and Y. Gou. Numerical studies on  $CO_2$  injection – brine extraction process in a low – medium temperature reservoir system. *Environmental Earth Science*, 73:6839 – 6854, 2015.
- [15] F. Moller, A. Liebscher, S. Martens, C. Schmidt-Hattenberger, and M. Streibel. Injection of  $CO_2$  at ambient temperature conditions – Pressure and temperature results of the ‘cold injection’ experiment at the Ketzin pilot site. *Energy Procedia*, 2014:6298 – 6297, 63.
- [16] A. Kopp, A. Bielinski, A. Ebigbo, H. Class, and R. Helmig. Numerical investigation of temperature effects during the injection of carbon dioxide into brine aquifers. In *The Eighth International Conference on Greenhouse Gas Control Technologies, Trondheim, Norway.*, 2006.
- [17] J. Bear and A.H.-D. Cheng. *Modeling Groundwater Flow and Contaminant Transport (Theory and Applications of Transport in Porous Media)*. Springer Netherlands, 2010.
- [18] K. Pruess and N. Müller. Formation dry-out from  $CO_2$  injection into saline aquifers: 1. Effects of solids precipitation and their mitigation. *Water Resources Research*, 45:W03402, 2009.
- [19] B. Lamy-Chappuis, D. Angus, Q. Fisher, C. Grattoni, and B.W.D. Yardley. Rapid porosity and permeability changes of calcareous sandstone due to  $CO_2$  - enriched brine injection. *Geophysical Research Letters*, 41:399 – 406, 2014.
- [20] D.C. Thomas and S.M. Benson. *Carbon Dioxide Capture for Storage in Deep Geologic Formations - Results from the  $CO_2$  Capture Project: Vol 2 - Geologic Storage*, chapter Predicting and Monitoring Geomechanical Effects of  $CO_2$  injection, pages 751 – 766. Elsevier, 2015.
- [21] P.G. Saffman and G.I. Taylor. The penetration of a fluid into a porous medium or Hele-Shaw cell containing a more viscous liquid. *Proceedings of the Royal Society of London. Series A: Mathematical and Physical Sciences*, 245(1242):312 – 329, 1958.
- [22] L. Patterson. Radial fingering in a Hele-Shaw cell. *Journal of Fluid Mechanics*, 113:513 – 529, 1981.
- [23] S.D. Howison. Fingering in Hele-Shaw cells. *Journal of Fluid Mechanics*, 167(3): 439–453, 1986.
- [24] R.L Chouke, P. Meurs, and C. Van der Poel. The instability of slow, immiscible, viscous liquid-liquid displacements in permeable media. *Transactions of the American Institute of Mining, Metallurgical and Petroleum Engineers*, 216:188 – 194, 1959.
- [25] S. Chen, B. Merriman, S. Osher, and P. Smereka. A simple level set method for solving Stefan problems. *Journal of Computational Physics*, 135:8 – 29, 1997.

- [26] S. Tanveer. Surprises in viscous fingering. *Journal of Fluid Mechanics*, 409:273 – 308, 2000.
- [27] T. Maxworthy. Experimental study of interface instability in a Hele-Shaw cell. *Physical Review A*, 39(11):5863 – 5866, 1989.
- [28] J.A. Miranda and M. Widom. Radial fingering in a Hele-Shaw cell: A weakly nonlinear analysis. *Physica D*, 120:315 – 328, 1998.
- [29] H. Power and L.C. Wrobel. *Boundary Integral Methods in Fluid Mechanics*. Computational Mechanics Publications, Southampton, 1995.
- [30] D.A. Weitz, J.P. Stokes, R.C. Ball, and A.P. Kushnick. Dynamic capillary pressure in porous media: Origin of the viscous fingering length scale. *Physics Review Letters*, 59:2967 – 2970, 1987.
- [31] A. Riaz and H.A. Tchelepi. Numerical simulation of immiscible two-phase flow in porous media. *Physics of Fluids*, 18:014104, 2006.
- [32] S.B. Gorell and G.M. Homsy. A theory of optimal policy of oil recovery by secondary displacement process. *SIAM Journal of Applied Mathematics*, 43:79 – 98, 1983.
- [33] F.J. Hickernell and Y.C. Yortsos. Linear stability of miscible displacement processes in porous media in the absence of dispersion. *Studies in Applied Mathematics*, 74:93 – 115, 1986.
- [34] K.X.H Zhao, L.C. Wrobel, and H. Power. Numerical simulation of viscous fingering using B-spline boundary elements. *Transactions on Modelling and Simulation*, 11: 1–10, 1995.
- [35] A.J. DeGregoria and L.W. Shwartz. A boundary-integral method for two-phase displacement in Hele-Shaw cells. *Journal of Fluid Mechanics*, 164:383–400, 1986.
- [36] S. Li, J.S. Lowengrub, and P.H. Leo. A rescaling scheme with application to the long-time simulation of viscous fingering in a Hele-Shaw cell. *Journal of Computational Physics*, 25(1):554–567, 2007.
- [37] H. Hadavinia, S.G. Advani, and R.T. Fenner. The evolution of radial fingering in a Hele-Shaw cell using  $C^1$  continuous Overhauser boundary element method. *Engineering Analysis with Boundary Elements*, 16:183–195, 1995.
- [38] E.B. Hansen. A numerical study of unstable Hele-Shaw flow. *Computers & Mathematics with Applications*, 38:217–230, 1999.
- [39] M.A. Jaswon and G.T. Symm. *Integral Equations Methods in Potential Theory and Elastostatics*. Academic Press, New York, 1977.
- [40] H. Power. The evolution of radial fingers at the interface between two viscous liquids. *Engineering Analysis with Boundary Elements*, 14(4):297 – 304, 1994.
- [41] X. Guan and R. Pitchumani. Viscous fingering in a Hele-Shaw cell with finite viscosity ratio and interfacial tension. *Journal of Fluids Engineering*, 125:354–363, 2003.

- [42] Y. Sun and C. Beckermann. A two-phase diffuse-interface model for Hele-Shaw flows with large property contrasts. *Physica D*, 237:3089–3098, 2008.
- [43] T.Y. Hou, Z. Li, S. Osher, and H. Zhao. A hybrid method for moving interface problems with application to the Hele-Shaw flow. *Journal of Computational Physics*, 134:236–252, 1997.
- [44] M.G. Moore, A. Juel, J.M. Burgess, W.D. McCormick, and H.L. Swinney. Fluctuations and pinch-offs observed in viscous fingering. In *Proceedings of the Seventh Experimental Chaos Conference*, pages 189–194. Springer-Verlag, 2003.
- [45] C.W. Park and G.M. Homsy. Two phase displacement in Hele-Shaw cells: Theory. *Journal of Fluid Mechanics*, 139:291 – 308, 1984.
- [46] E. Alvarez-Lacelle, J. Ortin, and J. Casademunt. Relevance of dynamic wetting in viscous fingering patterns. *Physical Review E*, 74:025302(R), 2006.
- [47] P.H. Anjos and J.A. Miranda. Radial viscous fingering: Wetting effects on pattern-forming mechanisms. *Physical Review E*, 88:053003, 2013.
- [48] S.J. Jackson, D. Stevens, D. Giddings, and H. Power. Dynamic-wetting effects in finite-mobility-ratio Hele-Shaw flow. *Physical Review E*, 92:023021, 2015.
- [49] G.K. Batchelor. *An Introduction to Fluid Dynamics*. Cambridge University Press, 1967.
- [50] H. Power, D. Stevens, K.A. Cliffe, and A. Golin. A boundary element study of the effect of surface dissolution on the evolution of immiscible viscous fingering within a Hele-shaw cell. *Engineering Analysis with Boundary Elements*, 37:1318–1330, 2013.
- [51] J.J.S.P. Cabral, L.C. Wrobel, and C.A. Brebbia. A BEM formulation using B-splines: I - Uniform blending functions. *Engineering Analysis with Boundary Elements*, 7(3):136–144, 1990.
- [52] W.H. Press, B.P. Flannery, S.A. Teukolsky, and W.T. Vetterling. *Numerical Recipes in Fortran 90: The Art of Parallel Scientific Computing*. Cambridge University Press, 2nd edition edition, 1996.
- [53] A.J. Chorin. Curvature and solidification. *Journal of Computational Physics*, 57: 472 – 490, 1985.
- [54] M. Guigiani. Formulation and numerical treatment of boundary integral equations with hypersingular kernels. In V. Sladek and J. Sladek, editors, *Singular Intgerals in Boundary Element Methods*, pages 85–125. Computational Mechanics Publications, 1998.
- [55] S.G. Mikhlin. *Multidimensional singular integral and integral equations*. Pergamon Press, New York, 1957.
- [56] J. Hadamard. *Lectures on Cauchy's problem in linear partial differential equations*. Dover, New York, 1952.
- [57] E. Lajeunesse and Y. Couder. On the tip-splitting instability of viscous fingers. *Journal of Fluid Mechanics*, 419:125–149, 2000.

- [58] E. Alvarez-Lacelle, J. Ortin, and J. Casademunt. Low viscosity contrast fingering in a rotating Hele-Shaw cell. *Physics of Fluids*, 16(4):908–924, 2004.
- [59] A. De Wit and G.M. Homsy. Viscous fingering in reaction-diffusion systems. *Journal of Chemical Physics*, 110(17):8663–8675, 1999.
- [60] L. Ouyang. New correlations for predicting the density and viscosity of supercritical carbon dioxide under conditions expected in carbon capture and sequestration operations. *The Open Petroleum Engineering Journal*, 4:13–21, 2011.
- [61] J. Kestin, H.E. Khalifa, and R.J. Correia. Tables of the dynamic and kinematic viscosity of aqueous NaCl solutions in the temperature range 20-150°C and the pressure range 0.1-35 MPa. *Journal of Physical and Chemical Reference Data*, 10: 71 – 87, 1981.
- [62] S. Bachu and D.B. Bennion. Interfacial Tension between CO<sub>2</sub>, Freshwater, and Brine in the Range of Pressure from 2 to 27MPa, Temperature from 20 to 125°C, and Water Salinity from 0 to 334 000 mg/L. *Journal of Chemical Engineering Data*, 54:765–775, 2009.
- [63] Jacob Bear. *Dynamics of Fluids in Porous Media*. Dover, 1972.
- [64] B. Dong, Y.Y. Yang, W.Z. Li, and Y.C. Song. Simulation of the influence of surface wettability on viscous fingering phenomenon in porous media. *Journal of Bionic Engineering*, 7:267 – 275, 2010.
- [65] J.P. Stokes, D.A. Weitz, and J.P. Interfacial stability of immiscible displacement in a porous medium. *Physical Review Letters*, 57:1718 – 1721, 1986.
- [66] F. Fairbrother and A.E. Stubbs. Studies in electro-endosmosis. Part VI. The “bubble-tube” method of measurement. *J. Chem. Soc*, pages 527 – 529, 1935.
- [67] F.P. Bretherton. The motion of long bubbles in tubes. *Journal of Fluid Mechanics*, 10(166):166 – 188, 1961.
- [68] J. Ratulowski and H.-C. Chang. Marangoni effects of trace impurities on the motion of long gas bubbles in capillaries. *Journal of Fluid Mechanics*, 210:303–328, 1990.
- [69] P. Daripa and G. Pasa. The effect of surfactant on long bubbles rising in vertical capillary tubes. *Journal of Statistical Mechanics: Theory and Experiment*, 2: L02003, 2011.
- [70] L. Schwartz. Stability of Hele-Shaw flows: The wetting-layer effect. *Physics of Fluids*, 29:3086 – 3088, 1986.
- [71] D.A. Reinelt. The effect of thin film variations and transverse curvature on the shape of fingers in a Hele-Shaw cell. *Physics of Fluids*, 30:2617 – 2623, 1987.
- [72] L.M. Martyushev and A.I. Birzina. Specific features of the loss of stability during radial displacement of the fluid in the Hele-Shaw cell. *Journal of Physics: Condensed Matter*, 20:045201, 2008.
- [73] E. O. Dias and J.A. Miranda. Wavelength selection in Hele-Shaw flows: A maximum-amplitude criterion. *Physical Review E*, 88:013016, 2013.

- [74] L. Carillo, J. Soriano, and J. Ortin. Radial displacement of a fluid annulus in a rotating Hele-Shaw cell. *Physics of Fluids*, 11(4):778 – 785, 1999.
- [75] P.H.A. Anjos and J.A. Miranda. Influence of wetting on fingering patterns in lifting. *Soft Matter*, 10:7395 – 7670, 2014.
- [76] T. Ward and A.R. White. Gas-driven displacement of a liquid in a partially filled radial Hele-Shaw cell. *Physical Review E*, 83:046316, 2011.
- [77] C. Min and F. Gibou. A second order accurate level set method on non-graded adaptive cartesian grids. *Journal of Computational Physics*, 225:300 – 321, 2007.
- [78] V. John and E. Schmeyer. Finite element methods for time - dependent convection - diffusion - reaction equations with small diffusion. *Computer Methods in Applied Mechanics and Engineering*, 198:457 – 494, 2008.
- [79] F. Badrot-Nico, F. Brissaud, and V. Guinot. A finite volume upwind scheme for the solution of the linear advection - diffusion equation with sharp gradients in multiple dimensions. *Advances in Water Resources*, 30:2002 – 2025, 2007.
- [80] F. Gallerano, G. Cannata, and M. Tamburrino. Upwind WENO scheme for shallow water equations in contravariant formulation. *Computers and Fluids*, 62:1 – 12, 2012.
- [81] H. Chen, C. Min, and F. Gibou. A numerical scheme for the Stefan problem on adaptive Cartesian grids with supralinear convergence rate. *Journal of Computational Physics*, 228:5803 – 5818, 2009.
- [82] J. Papac, A. Helgadottir, C. Ratsch, and F. Gibou. A level set approach for diffusion and Stefan-type problems with Robin boundary conditions on quadtree/octree adaptive Cartesian grids. *Journal of Computational Physics*, 233: 241 – 261, 2013.
- [83] G. Beckett, J.A. Mackenzie, and M.L. Robertson. A moving mesh finite element method for the solution of two-dimensional Stefan problems. *Journal of Computational Physics*, 168:500 – 518, 2001.
- [84] L. Vrankar, E.J. Kansa, L. Ling, F. Runovc, and G. Turk. Moving-boundary problems solved by adaptive radial basis functions. *Computers and Fluids*, 39: 1480 – 1490, 2010.
- [85] M. Sussman, P. Smereka, and S. Osher. A level set approach for computing solutions to incompressible two-phase flow. *Journal of Computational Physics*, 114:146 – 159, 1994.
- [86] S.J. Jackson, D. R. Stevens, H. Power, and D. Giddings. A boundary element method for the solution of finite mobility ratio immiscible displacement in a Hele-Shaw cell. *International Journal for Numerical Methods in Fluids*, 78(9): 521 – 551, 2015.
- [87] V.G. Ferreira, R.A.B. de Quiroz, G.A.B. Lima, R.G. Cuenca, C.M. Oishi, J.L.F. Azevedo, and S. Mckee. A bounded upwinding scheme for computing convection-dominated transport problems. *Computers and Fluids*, 57:208 – 224, 2012.

- [88] S. Gottlieb and C-W Shu. Total variation diminishing Runge-Kutta schemes. *Mathematics of Computation*, 67:73 – 85, 1998.
- [89] J. Cheng and C-W. Shu. High order schemes for CFD: A review. *Chinese Journal of Computational Physics*, 26:633 – 655, 2009.
- [90] D. You, R. Mittal, M. Wang, and P. Moin. Analysis of stability and accuracy of finite-difference schemes on a skewed mesh. *Journal of Computational Physics*, 213(1):184 – 204, 2006.
- [91] D. Yang. A parallel nonoverlapping Schwarz domain decomposition method for elliptic interface problems. *IMA Journal of Numerical Analysis*, 16:75 – 91, 1996.
- [92] W-C. Wang. A jump condition capturing finite difference scheme for elliptic interface problems. *SIAM Journal of Scientific Computing*, 25(5):1479 – 1496, 2004.
- [93] P. A. Berthelsen and O.M. Faltinsen. A local directional ghost cell approach for incompressible viscous flow problems with irregular boundaries. *Journal of Computational Physics*, 227:4354 – 4397, 2008.
- [94] R. Mittal and G. Iaccarino. Immersed boundary methods. *Annual Review of Fluid Mechanics*, 37:239 – 261, 2005.
- [95] A. Wiegmann and K. P. Bube. The explicit-jump immersed interface method: Finite difference methods for PDEs with piecewise smooth solutions. *SIAM Journal of Numerical Analysis*, 37(3):827 – 862, 2000.
- [96] F. Gibou, R. Fedkiw, R. Caflisch, and S. Osher. A level set approach for the numerical simulation of dendritic growth. *Journal of Scientific Computing*, 19(1): 183 – 199, 2003.
- [97] F. Gibou and R. Fedkiw. A fourth order accurate discretization for the Laplace and heat equations on arbitrary domains, with applications to the Stefan problem. *Journal of Computational Physics*, 202(2):577 – 601, 2005.
- [98] T.D. Aslam. A partial differential equation approach to multidimensional extrapolation. *Journal of Computational Physics*, 193:349 – 355, 2003.
- [99] H. Chen, C. Min, and F. Gibou. A supra-convergent finite difference scheme for the poisson and heat equations on irregular domains and non-graded adaptive cartesian grids. *Journal of Scientific Computing*, 31:19 – 60, 2007.
- [100] R.L. Hardy. Multiquadric equations of topography and other irregular surfaces. *Journal of Geophysical Research*, 176:1905–1915, 1971.
- [101] M.J.D. Powell. *Advances in Numerical Analysis, Volume II: Wavelets, Subdivision Algorithms and Radial Functions*, chapter The theory of radial basis function approximation in 1990, pages 105 – 210. Oxford University Press, UK, 1992.
- [102] E. Larsson and B. Fornberg. A numerical study of some radial basis function based solution methods for elliptic PDEs. *Computers & Mathematics with Applications*, 46:891 – 902, 2003.

- [103] B. Fornberg, E. Larsson, and G. Wright. A new class of oscillatory radial basis functions. *Computers & Mathematics with Applications*, 51:1209 – 1222, 2006.
- [104] S.A. Sarra and E.J. Kansa. *Multiquadric radial basis function approximation methods for the numerical solution of partial differential equations*. Tech Science Press, 2010.
- [105] S.A. Sarra. Radial basis function approximation methods with extended precision floating point arithmetic. *Engineering Analysis with Boundary Elements*, 35:68 – 76, 2011.
- [106] B. Šarler. *Advances in Meshfree Techniques*, chapter From Global to Local Radial Basis Function Collocation Method for Transport Phenomena, pages 257 – 282. Springer Netherlands, 2007.
- [107] B. Šarler and R. Vertnik. Meshfree explicit local radial basis function collocation method for diffusion problems. *Computers & Mathematics with Applications*, 51: 1269 – 1282, 2006.
- [108] E. Divo and A. Kassab. An efficient local radial basis function meshless method for fluid flow and conjugate heat transfer. *Journal of Heat Transfer*, 129:124 – 136, 2007.
- [109] N Flyer, E Lehto, S Blaise, G.B Wright, and A St-Cyr. A guide to RBF-generated finite differences for nonlinear transport: Shallow water simulations on a sphere. *J. Comput. Phys.*, 231:4078–4095, 2012.
- [110] B. Fornberg, E. Lehto, and C. Powell. Stable calculation of Gaussian-based RBF-FD stencils. *Computers & Mathematics with Applications*, 65:627 – 637, 2013.
- [111] Y.V.S.S. Sanyasiraju and G. Chandhini. A note on two upwind strategies for the RBF-based grid-free schemes to solve steady convection-diffusion equations. *International Journal for Numerical Methods in Fluids*, 61:1053 – 1062, 2009.
- [112] Z. El Zahab, E. Divo, and A.J. Kassab. A localised collocation meshless method (LCMM) for incompressible flows CFD modelling with applications to transient hemodynamics. *Engineering Analysis with Boundary Elements*, 33:1045 – 1061, 2009.
- [113] D. Stevens, H. Power, M. Lees, and H. Morvan. A local Hermitian RBF meshless numerical method for the solution of multi-zone problems. *Numerical Methods for Partial Differential Equations*, 27(5):1201 – 1230, 2011.
- [114] D Stevens and H Power. A scalable and implicit meshless RBF method for the 3D unsteady nonlinear Richards equation, with single and multi-zone domains. *International Journal for Numerical Methods in Engineering*, 85:135–163, 2011.
- [115] D. Stevens and H. Power. The radial basis function finite collocation approach for capturing sharp fronts in time dependent advection problems. *Journal of Computational Physics*, 298:423 – 445, 2015.
- [116] D. Stevens, H. Power, C.Y. Meng, and D. Howard. An alternative local collocation strategy for high-convergence meshless PDE solutions, using radial basis functions. *Journal of Computational Physics*, 245:52 – 75, 2013.

- [117] D. Greaves. A quadtree adaptive method for simulating fluid flows with moving interfaces. *Journal of Computational Physics*, 194:35 – 56, 2004.
- [118] L. Vrankar, G. Turk, and F. Runovc. Solving two-dimensional moving-boundary problems with meshless and level set method. *Journal of Energy and Power Engineering*, 4:51 – 55, 2010.
- [119] J. Strain. Tree methods for moving interfaces. *Journal of Computational Physics*, 151:616 – 648, 1999.
- [120] D. Stevens, H. Power, M. Lees, and H. Morvan. The use of PDE centres in the local RBF Hermitian method for 3D convective-diffusion problems. *Journal of Computational Physics*, 228:4606–4624, 2009.
- [121] H.S. Carslaw and J.C. Jaeger. *Conduction of Heat in Solids*. Oxford at the Clarendon Press, Oxford, 1959.
- [122] M Van Genuchten and W Alves. Analytical solutions of the one-dimensional convective-dispersive solute transport equation. Technical report, United States Department of Agriculture, Agricultural research service, Technical bulletin number 1661, 1982.
- [123] D.K. Jaiswal, A. Kumar, and R.R. Yadav. Analytical solution to the one - dimensional advection - diffusion equation with temporally dependent coefficients. *Journal of Water Resource and Protection*, 3:76 – 84, 2011.
- [124] O.K Jensen and B.A. Finlayson. Solution of transport equations using a moving coordinate system. *Advances in Water Resources*, 3:9 – 18, 1980.
- [125] Y. Sun and I.S. Wichman. On transient heat conduction in a one-dimensional composite slab. *International Journal of Heat and Mass Transfer*, 47:1555 – 1559, 2004.
- [126] F. de Monte. Transient heat conduction in a one-dimensional composite slab. A natural analytic approach. *International Journal of Heat and Mass Transfer*, 43: 3607 – 3619, 2000.
- [127] T.T. Al-Housseiny and H.A. Stone. Controlling viscous fingering in tapered Hele-Shaw cells. *Physics of Fluids*, 25:092102, 2013.
- [128] H. Zhao, J. Casademunt, C. Yeung, and J.V. Maher. Perturbing Hele-Shaw flow with a small gap gradient. *Physical Review A*, 45:2455 – 2460, 1992.
- [129] E.O. Dias and J.A. Miranda. Finger tip behaviour in small gap gradient flows. *Physical Review E*, 82:056319, 2010.
- [130] T.T. Al-Housseiny, P.A. Tsai, and H.A. Stone. Control of interfacial instabilities using flow geometry. *Nature Physics*, 8:747 – 750, 2012.
- [131] T.T. Al-Housseiny, I.C. Christov, and H.A. Stone. Two-phase fluid displacement and interfacial instabilities under elastic membranes. *Physical Review Letters*, 111: 034502, 2013.
- [132] D. Pihler-Puzović, R. Périllat, M. Russell, A. Juel, and M. Heil. Modelling the supression of viscous fingering in elastic-walled Hele-Shaw cells. *Journal of Fluid Mechanics*, 731:162 – 183, 2013.

- [133] D. Pihler-Puzović, P. Illien, M. Heil, and A. Juel. Suppression of complex finger patterns at the interface between air and a viscous fluid by elastic membranes. *Physical Review Letters*, 108:074502, 2012.
- [134] D. Pihler-Puzović, A. Juel, G.G. Peng, J.R. Lister, and M. Heil. Displacement flows under elastic membranes. Part 1. Experiments and direct numerical simulations. *Journal of Fluid Mechanics*, 784:487 – 511, 2015.
- [135] G.G. Peng, D. Pihler-Puzović, A. Juel, M. Heil, and J.R. Lister. Displacement flows under elastic membranes. Part 2. Analysis of interfacial effects. *Journal of Fluid Mechanics*, 784:512 – 547, 2015.
- [136] E.O. Dias and J.A. Miranda. Taper-induced control of viscous fingering in variable-gap Hele-Shaw flows. *Physical Review E*, 87:053015, 2013.
- [137] S. Z. Zhang, E. Louis, O. Pla, and F. Guinea. Linear stability analysis of the Hele-Shaw cell with lifting plates. *The European Physical Journal B*, 1:123 – 127, 1998.
- [138] Z. Zheng, H. Kim, and H.A. Stone. Controlling viscous fingering using time - dependent strategies. *Physical Review Letters*, 115:174501, 2015.
- [139] S. Li, J.S. Lowengrub, J Fontana, and P. Palffy-Muhoray. Control of viscous fingering patterns in radial Hele-Shaw flow. *Physical Review Letters*, 102:174501, 2009.
- [140] S.R. Brown. Fluid flow through rock joints: The effect of surface roughness. *Journal of Geophysical Research*, 92(B2):1337 – 1347, 1987.
- [141] R.W. Zimmerman, S. Kumar, and G.S. Bodvarsson. Lubrication theory analysis of the permeability of rough-walled fractures. *International Journal of Rock Mechanics and Mining Sciences & Geomechanics Abstracts*, 28(4):325 – 331, 1991.
- [142] V. Mourzenko, J.-F. Thovert, and P. Adler. Permeability of a single fracture; validity of the Reynolds equation. *Journal de Physique II, EDP Sciences*, 5(3): 465 – 482, 1995.
- [143] M. Sajjadi and J. Azaiez. Thermo-viscous fingering in heterogeneous media. In *SPE Heavy Oil Conference Canada, 12-14 June, Calgary, Alberta, Canada*, 2012.
- [144] S.H. Davis. Thermocapillary instabilities. *Annual review in Fluid Mechanics*, 19: 403 – 435, 1987.
- [145] W. Boos and A. Thess. Thermocapillary flow in a Hele-Shaw cell. *Journal of Fluid Mechanics*, 352:305 – 330, 1997.
- [146] D Stevens, A LaRocca, H Power, and V LaRocca. *A Generalised RBF Finite Difference Approach to Solve Nonlinear Heat Conduction Problems, on Unstructured Datasets*, chapter 13, pages 281–296. InTech, 2011.
- [147] D. Pritchard. The linear stability of double - diffusive miscible rectilinear displacements in a Hele-Shaw cell. *European Journal of Mechanics B/Fluids*, 28:564 – 577, 2009.

- [148] M. Mishra, P.M.J Trevelyan, C. Almarcha, and A. De Wit. Influence of double diffusive effects on miscible viscous fingering. *Physical Review Letters*, 105:204501, 2010.
- [149] T. Sheorey and K. Muralidhar. Isothermal and non-isothermal oil-water flow and viscous fingering in a porous medium. *International Journal of Thermal Sciences*, 42:665 – 676, 2003.
- [150] M.C. Kim. Onset of radial viscous fingering in a Hele-Shaw cell. *Korean Journal of Chemical Engineering*, 29(12):1688 – 1694, 2012.
- [151] M.N. Islam and J. Azaiez. Miscible thermo-viscous fingering instability in porous media. Part 1: Linear stability analysis. *Transport in Porous Media*, 84:821 – 844, 2010.
- [152] M.N. Islam and J. Azaiez. Miscible thermo-viscous fingering instability in porous media. Part 2: Numerical simulations. *Transport in Porous Media*, 84:845 – 861, 2010.
- [153] M.N. Islam and J. Azaiez. Thermo-viscous fingering in quarter five-spot miscible displacements. *European Journal of Mechanics B/Fluids*, 30:107 – 119, 2011.
- [154] M. Sajjadi and J. Azaiez. Dynamics of fluid flow and heat transfer in homogeneous porous media. *The Canadian Journal of Chemical Engineering*, 91:687 – 697, 2013.
- [155] K.E. Holloway and J.R. de Bruyn. Numerical simulations of a viscous-fingering instability in a fluid with a temperature-dependent viscosity. *Canadian Journal of Physics*, 84:273 – 287, 2006.
- [156] Y. Nagatsu, N. Fujita, Y. Kato, and Y. Tada. An experimental study of non-isothermal miscible displacements in a Hele-Shaw cell. *Experimental Thermal and Fluid Science*, 33:695 – 705, 2009.
- [157] A. Fenghour, W.A. Wakeham, and V. Vesovic. The viscosity of carbon dioxide. *Journal of Physical and Chemical Reference Data*, 27(1):31 – 44, 1998.
- [158] E.W. Lemmon, M.O. McLinden, and D.G. Friend. *NIST Chemistry WebBook, NIST Standard Reference Database Number 69*, chapter Thermophysical Properties of Fluid Systems. National Institute of Standards and Technology, Gaithersburg MD.
- [159] MUMPS: a MULTifrontal Massively Parallel sparse direct Solver. <http://mumps.enseeiht.fr/>, 2016.
- [160] Y.J. Lui and N. Nishimura. The fast multipole boundary element method for potential problems: A tutorial. *Engineering Analysis with Boundary Elements*, 30:371 – 381, 2006.
- [161] I. Lashuk, A. Chandramowliswaran, H. Langston, T-A. Nguyen, R. Sampath, A. Shringarpure, R. Vuduc, L. Ying, D. Zorin, and G. Biros. A massively parallel adaptive fast-multipole method on heterogeneous architectures. In *Proceedings of the Conference on High Performance Computing Networking, Storage and Analysis*, Portland, Oregon, USA, 2009.

- 
- [162] S.J. Jackson, D. Stevens, D. Giddings, and H. Power. An adaptive RBF finite collocation approach to track transport processes across moving fronts. *Computers and Mathematics with Applications*, 71(1):278 – 300, 2016.
- [163] C. Nieto, H. Power, and M. Giraldo. Boundary elements solution of Stokes flow between curved surfaces with nonlinear slip boundary condition. *Numerical Methods for Partial Differential Equations*, 29:757 – 777, 2012.
- [164] J. Zeng, Y.C. Yortsos, and D. Salin. On the Brinkman correction in unidirectional Hele-Shaw flows. *Physics of Fluids*, 15:3829, 2003.
- [165] F. Gallaire, P. Meliga, P. Laure, and C.N. Baroud. Marangoni induced force on a drop in a Hele shaw cell. *Physics of Fluids*, 26:062105, 2014.
- [166] H. Yano and A. Kieda. The fundamental solution of Brinkman’s equation in two dimensions. *Fluid Dynamics Research*, 7:109 – 118, 1991.
- [167] M. Nagel and F. Gallaire. A new prediction of wavelength selection in radial viscous fingering involving normal and tangential stresses. *Physics of Fluids*, 25:124107, 2013.